

Ferromagnetic Semiconductor-Metal Transition in Heterostructures of Electron Doped Europium Monoxide

Dissertation
zur
Erlangung des Doktorgrades (Dr. rer. nat.)
der
Mathematisch-Naturwissenschaftlichen Fakultät
der
Rheinischen Friedrich-Wilhelms-Universität Bonn

vorgelegt von
Tobias Stollenwerk
aus
Troisdorf

Bonn 2013

Angefertigt mit Genehmigung der Mathematisch-Naturwissenschaftlichen Fakultät der
Rheinischen Friedrich-Wilhelms-Universität Bonn

1. Gutachter: Prof. Dr. Johann Kroha
2. Gutachterin: Prof. Dr. Corinna Kollath

Tag der Promotion: 16.9.2013
Erscheinungsjahr: 2013

Contents

1. Introduction	7
2. Properties of electron doped Europium Monoxide	9
2.1. Ultra thin films of electron doped Europium monoxide	12
3. Quantum impurities	15
3.1. The single impurity Anderson model	15
3.2. Pseudo-particle representation	16
3.3. Non-crossing approximation	18
3.4. Numerical solution of the NCA equations	23
4. Model	27
4.1. Bulk	27
4.2. Multilayer	28
5. Theory	31
5.1. Conduction band Green's function	31
5.1.1. Bulk conduction band Green's function	31
5.1.2. Multilayer conduction band Green's function	35
5.2. Impurities	42
5.2.1. Dilute impurities	42
5.2.2. Dynamical impurities	52
5.3. Heisenberg lattice	57
5.3.1. Mean field approximation in the bulk case	57
5.3.2. Mean field approximation in the multilayer case	59
5.3.3. Long range RKKY interaction	63
5.4. Electrostatics	66
5.4.1. Thomas-Fermi-approximation	66
5.4.2. Interfaces	69
5.5. Self consistent theory	70
5.5.1. Self consistent formulation	70
5.5.2. Numerical solution of the self-consistent theory	73
5.6. Conductivity	76
5.6.1. Linear response theory	76
5.6.2. Conductivity in the bulk system	78
5.6.3. Parallel and perpendicular conductivity in the multilayer system .	83
5.6.4. Numerical calculation	93

6. Bulk systems of electron doped Europium monoxide	97
6.1. Bulk $\text{Eu}_{1-x}\text{Gd}_x\text{O}$	97
6.2. Bulk EuO_{1-x}	102
6.3. Bulk $\text{Eu}_{1-x}\text{Gd}_x\text{O}$ with long range RKKY coupling	104
6.4. Conclusion	105
7. Thin films of Gadolinium doped Europium monoxide	109
7.1. Nearest neighbor case	109
7.2. Long range RKKY coupling case	116
7.3. Conclusion	117
8. Metal-$\text{Eu}_{1-x}\text{Gd}_x\text{O}$-metal heterostructures	119
8.1. Nearest neighbor case	120
8.1.1. Influence of the metal band filling	120
8.1.2. Influence of the $\text{Eu}_{1-x}\text{Gd}_x\text{O}$ film thickness	123
8.1.3. Further exploration of the parameter space	126
8.2. Long range RKKY coupling case	127
8.3. Conclusion	129
9. Ferromagnet-$\text{Eu}_{1-x}\text{Gd}_x\text{O}$-ferromagnet heterostructures	131
10. Prediction of STS spectra	135
11. Conclusion	141
A. Conductivity calculation	143
A.1. Current operator for the bulk model	143
A.2. Current operator for the multilayer model	145
A.3. Diagrammatic evaluation of the current-current correlation function	147
B. Local scattering	151
C. Mirror symmetric systems	153
D. Kramers-Kronig-relations	155
E. Numerical integration of multiple peaked functions	157
Publications	159
Bibliography	160

Abstract

In the present work, we develop and solve a self-consistent theory for the description of the simultaneous ferromagnetic semiconductor-metal transition in electron doped Europium monoxide. We investigate two different types of electron doping, Gadolinium impurities and Oxygen vacancies. Besides the conduction band occupation, we can identify low lying spin fluctuations on magnetic impurities as the driving force behind the doping induced enhancement of the Curie temperature. Moreover, we predict the signatures of these magnetic impurities in the spectra of scanning tunneling microscope experiments. By extending the theory to allow for inhomogeneities in one spatial direction, we are able to investigate thin films and heterostructures of Gadolinium doped Europium monoxide. Here, we are able to reproduce the experimentally observed decrease of the Curie temperature with the film thickness. This behavior is attributed to missing coupling partners of the localized $4f$ moments as well as to an electron depletion at the surface which leads to a reduction of the number of itinerant electrons. By investigating the influence of a metallic substrate onto the phase transition in Gadolinium doped Europium monoxide, we find that the Curie temperature can be increased up to 20%. However, as we show, the underlying mechanism of metal-interface induced charge carrier accumulation is inextricably connected to a suppression of the semiconductor-metal transition.

1. Introduction

Stoichiometric Europium monoxide (EuO) is a ferromagnetic semiconductor with a large band gap of 1.2 eV [1, 2] and a Curie temperature of 69 K [3]. The magnetization in the system is mainly due to localized magnetic moments in the Eu 4*f* orbitals. These moments interact via virtual excitations into the otherwise empty conduction band [3] and represent a prototype of a Heisenberg ferromagnet [4]. There is a strong exchange interaction between the localized moments and the conduction electron spins which results in a spin splitting of the conduction band [5]. Upon electron doping, the system becomes metallic in the low temperature phase and exhibits a simultaneous ferromagnetic semiconductor-metal transition in EuO_{1-x} [6–11] as well as Eu_{1-x}Gd_xO [12–16]. During the phase transition, the resistivity drops over several orders of magnitude. This giant magnetoresistance effect makes the material interesting for applications.

In the high temperature phase there is a gap between the conduction band above, and an impurity induced side band below the Fermi edge [17, 18], which renders the system insulating. During the ferromagnetic transition, the exchange splitting of the conduction band sets in, the gap is closed and the majority conduction electron states are populated. The system becomes half-metallic, i.e. there is nearly 100% spin polarization in the conduction band which make EuO a promising candidate for spintronics applications [19, 20].

Depending on whether most of the excess electrons are in a bound or in an itinerant state, the transition temperature increases with the doping concentration [15] due to the increased conduction electron mediated RKKY interaction. In that respect, Gadolinium impurities seem to be more efficient than Oxygen vacancies. Arnold and Kroha [18] found indications that this can be traced back to the magnetic nature of the Gadolinium impurities. If the impurity level lies slightly below the Fermi energy, strong on-site Coulomb repulsion will essentially lead to a singly occupied, and therefore magnetic impurity. If there is conduction electron spectral weight at the Fermi edge, low lying spin fluctuations at the impurity site lead to the formation of a Kondo resonance at the Fermi edge. Even though the Kondo temperature lies far below the ferromagnetic transition temperature, there is a tendency to transfer spectral weight towards the Fermi energy. This closes the semiconducting gap even at higher temperatures which results in an enhancement of the Curie temperature in Eu_{1-x}Gd_xO.

By Gadolinium doping, transition temperatures up to 130 K are possible [15]. Nevertheless, for possible applications a further increase would be desirable. In this respect, a coupling of an electron doped EuO film to a metallic substrate with a lower work function may prove beneficial. We conjecture that electrons will diffuse into the EuO and populate the conduction band, leaving a depletion region in the substrate. Therewith, the RKKY interaction near the surface is increased, which may outweigh the finite size

1. Introduction

effects in thin films and increase the Curie temperature. It is obvious that such surface effects are only relevant in thin films. Indeed, recent experiments on thin stoichiometric and Oxygen deficient EuO [19–24] have shown a huge impact of the film thickness on the phase transition.

In the present work, we develop and solve a self-consistent theory for thin films of electron doped EuO as well as for heterostructures of electron doped EuO and a metallic substrate. In the course of this, we extend the work of Arnold and Kroha [18,25] in several respects. First of all, we allow for broken translation symmetry in one direction in order to describe thin films. Besides Gadolinium impurities, we consider a model for Oxygen vacancies and go beyond the nearest neighbor approximation by incorporating long range RKKY interactions in our theory. For the sake of completeness and readability, we will not review the theory of Arnold and Kroha in a separate section but include them in our more general derivations.

The first chapter is concerned with a review of the properties of electron doped Europium monoxide. In the subsequent chapter, we review some aspects of quantum impurities. In particular, we derive the non-crossing approximation (NCA) which will be part of our theory for $\text{Eu}_{1-x}\text{Gd}_x\text{O}$. Here, we will present our improvements to the numerical solution of the NCA equations. Chapter 4 contains an introduction to our model for bulk and heterostructure systems. Afterward, in chapter 5, we derive the self-consistent theory and discuss the obstacles of its numerical solution. Hereafter, we present our results in the remaining chapters. We begin with the discussion of the differences between Gadolinium impurities and Oxygen vacancies in bulk systems in chapter 6. In chapters 7, 8 and 9, we present our results for the heterostructure theory. First, for isolated thin films of $\text{Eu}_{1-x}\text{Gd}_x\text{O}$ and then for heterostructures with metallic and ferromagnetic substrates. The presentation of our results is concluded by chapter 10, which is concerned with the prediction of STS spectra for electron doped Europium monoxide.

2. Properties of electron doped Europium Monoxide

Stoichiometric EuO has a rock salt crystal structure, i.e. a face-centered cubic lattice (FCC) with a lattice constant of $a = 5.143 \text{ \AA}$ and a diatomic basis of an Eu^{2+} and an O^{2-} ion. The two electrons from the Eu 6s shell fill up the 2p shell of the Oxygen atom. Therefore, the electronic structure of the Eu^{2+} ion is $4f^7 5d^0 6s^0$, while for O^{2-} we have $1s^2 2s^2 2p^8$ [3].

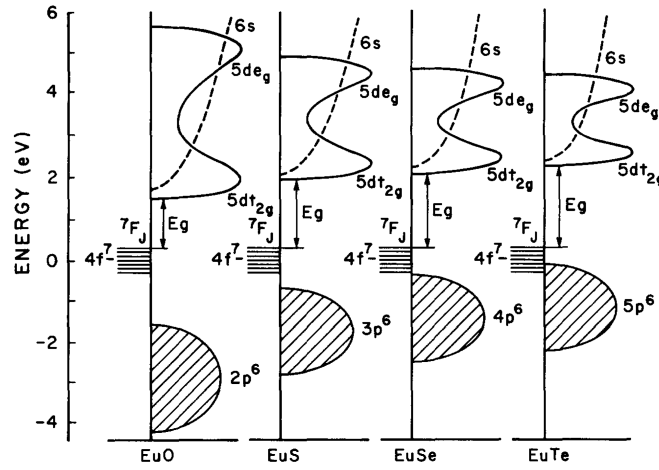


Figure 2.1.: Schematic representation of the energy levels in EuO, EuS, EuSe and EuTe. Taken from [3] or [26], respectively.

Figure 2.1 shows a schematic representation of the energy levels in EuO. The valence band is far below the Fermi energy and comprises the Oxygen 2p orbitals. In between the valence and the conduction band, there is as a flat 4f band which lies sufficiently far below the Fermi energy. Due to the localized nature of the 4f orbitals the influence of the crystal environment is small. Therefore, Hund's rule applies and all 7 spins in the 4f shell will align parallel. This leads to the formation of localized magnetic moments with spin $S = 7/2$ at the sites of the Eu ions. The conduction band is built out of the 5d and 6s orbitals and remains unoccupied in stoichiometric EuO.

Although the conduction band is empty, there is a ferromagnetic exchange interaction between the localized 4f moments, mediated by virtual excitations from the 4f levels to the conduction band [3]. This is why EuO is known as a prototype of a Heisenberg ferromagnet. Of course the indirect interaction between the 4f moments is much smaller than the direct exchange interaction with the empty conduction band. Steenenken et.

2. Properties of electron doped Europium Monoxide

al. [5] have found an exchange splitting of the conduction band of $\Delta \approx 0.6$ eV in nearly stoichiometric EuO by x-ray photoemission spectroscopy (XPS) [5] (see figure 2.2).

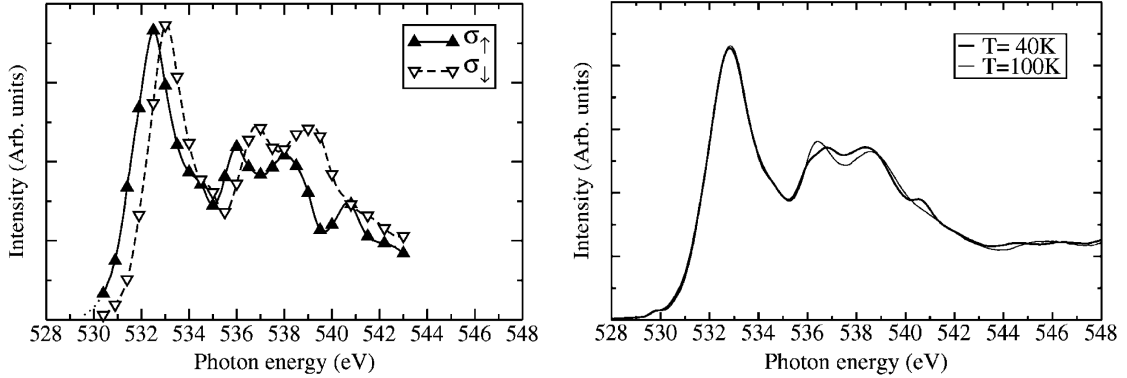


Figure 2.2.: Conduction band splitting in nearly stoichiometric EuO as seen in the spin resolved x-ray absorption spectrum at 20 K (left) and the x-ray absorption spectrum below and above the Curie temperature of 69 K (right). Taken from [5].

The exchange splitting can significantly affect the interaction between the localized $4f$ moments only if the conduction band is occupied. This can be achieved by electron doping, for example by using Oxygen deficient Europium monoxide, EuO_{1-x} . Each missing Oxygen ion effectively provides two excess electrons. Another common approach is the doping with Gadolinium, whose electronic structure differs from the one of Europium only by an additional electron in the d -shell, $4f^7 5d^1 6s^2$. Here, some of the Eu^{2+} ions are replaced by Gd^{2+} ions with $4f^7 5d^1 6s^0$. Therefore, in $\text{Eu}_{1-x}\text{Gd}_x\text{O}$ we have only one excess electron per unit cell. In both cases however, the lattice of localized magnetic moments is not changed significantly.

The fundamental question is whether the excess electrons are bound in a localized impurity state or if they are free to move and thereby mediate the magnetic interaction between the localized $4f$ moments. In the former case, no change of the Curie temperature is expected. In the latter case, an enhanced interaction between the localized moments will lead to an increase of the Curie temperature. This picture is supported and by experiments of Schoenes and Wachter [12] from the 1970s. Recently, Mairoser et. al. [15] found a direct relation between the conduction band occupation and the Curie temperature (see figure 2.6).

Concomitant with the population of the conduction band, the system can become metallic. A simultaneous semiconductor to metal and para- to ferromagnetic transition was observed in EuO_{1-x} [6–11, 20, 22, 23] (see figure 2.3) as well as in $\text{Eu}_{1-x}\text{Gd}_x\text{O}$ [12–16, 27] (see figure 2.4).

There are contradictory reports on the influence of the oxygen vacancy concentration on the Curie temperature in EuO_{1-x} . Early experiments [6–10] indicate that the Curie temperature remains constant at $T_C \approx 69$ K if the doping concentration is varied, a behavior which has recently been confirmed by Altendorf et. al. [11]. However, the

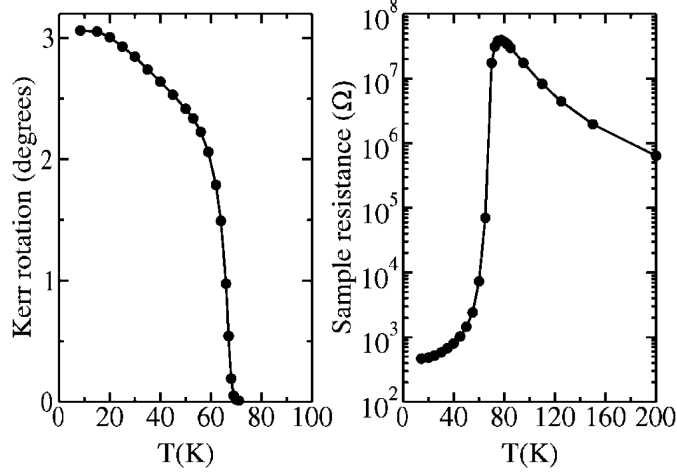


Figure 2.3.: Simultaneous ferromagnetic semiconductor-metal transition as seen in the Kerr rotation (left) and the sample resistance (right) of an oxygen deficient EuO sample. Taken from [5].

underlying reason for these results may be an insufficiently controlled stoichiometry and crystal structure [11,28]. In contrast, Barbagallo et. al. [22] reported a Curie temperature enhancement to around $T_C = 140K$ upon Oxygen deficiency. Theoretical investigations of Sinjukow and Nolting [17] found no increase of T_C . However, it should be noted that the model parameters were chosen such that the results match the experimental outcome of Oliver et. al. [7], who also found no T_C enhancement.

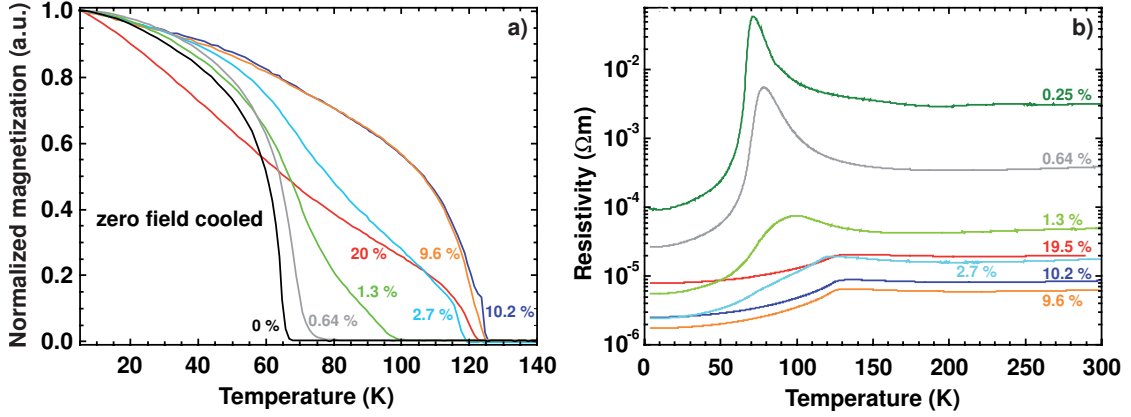


Figure 2.4.: Simultaneous ferromagnetic semiconductor-metal transition as seen in the normalized magnetization (left) and the resistivity (right) of $\text{Eu}_{1-x}\text{Gd}_x\text{O}$ samples with various doping concentrations x . Taken from [15].

In the $\text{Eu}_{1-x}\text{Gd}_x\text{O}$ case, the picture is more uniform. All experiments show an increase of T_C with the doping concentration [12–16,27] (see figures 2.4 and 2.6). Although the resistivity drop over several orders is present in both, the work of Altendorf [27] and

2. Properties of electron doped Europium Monoxide

Mairoser et. al. [15], there is a substantial difference in the magnitude of the measured resistivities between the experiments (see figure 2.5). The theory of Arnold and Kroha [18] for Gadolinium doped EuO correctly predicts the simultaneous phase transition. It serves as a basis for the present work and will be discussed in the subsequent chapters.

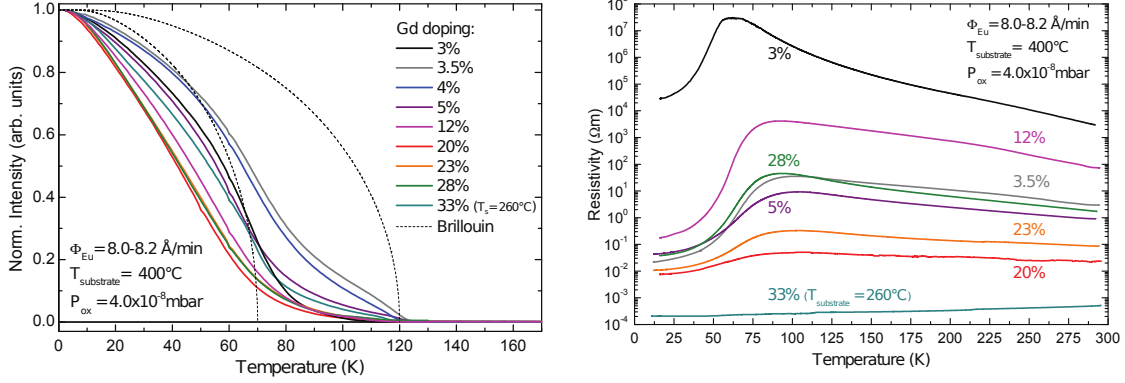


Figure 2.5.: Simultaneous ferromagnetic semiconductor-metal transition as seen in the normalized magnetization (left) and the resistivity (right) of $\text{Eu}_{1-x}\text{Gd}_x\text{O}$ samples with various doping concentrations x . Taken from [27]. According to [27] the exact doping concentration may not be very well controlled.

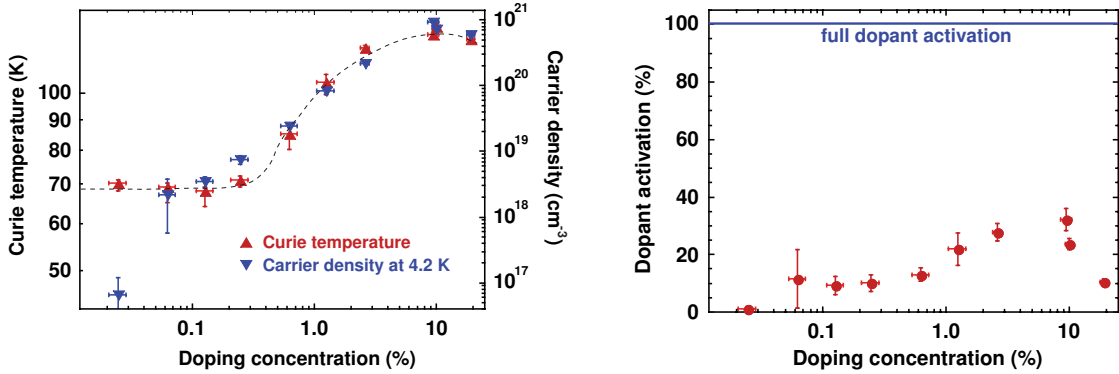


Figure 2.6.: Increase of the Curie temperature with the population of the conduction band in Gadolinium doped EuO as seen in the carrier density, the Curie temperature (left) and the dopant activation (right) plotted against the doping concentration. Taken from [15].

2.1. Ultra thin films of electron doped Europium monoxide

By decreasing the film thickness, the influence of the surfaces becomes more and more significant. Recent experiments on ultra thin films of stoichiometric or Oxygen deficient EuO show a reduction of the Curie Temperature with the film thickness [19, 21, 23, 24,

29] (see figure 2.7). Qualitatively, this reduction can be explained by the absence of neighboring magnetic moments at the surface [21, 23, 24, 30]. However, in [23], we argue that the observed increase of T_C at thicknesses of around 30 nm cannot be explained by the absence of neighboring spins, even in case one considers long range RKKY interaction. This indicates an influence of band bending effects and a resulting depopulation of the conduction band. This hypothesis is supported by the reduced magnetic moment in thin films which can be explained by a huge band bending and the resulting depopulation of the $4f$ band [23] (see figure 2.8).

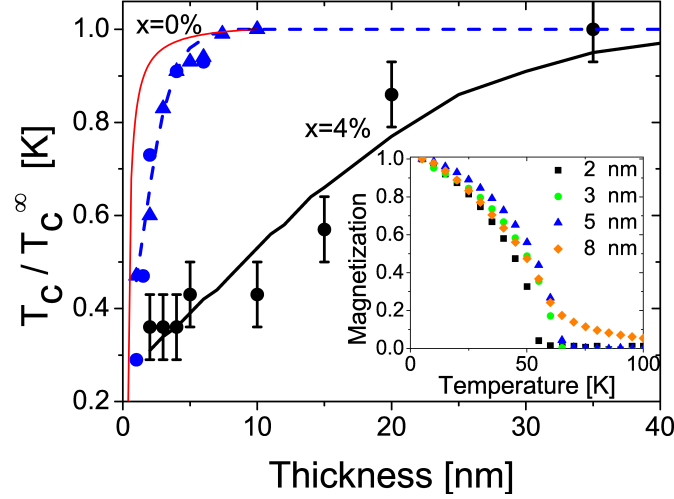


Figure 2.7.: Decreasing Curie temperature with the film thickness in stoichiometric and Oxygen deficient EuO. The blue dots and triangles indicate the normalized Curie temperature in stoichiometric EuO [19, 21]. The black dots are measurements for films with 4% Oxygen vacancies. The inset shows the corresponding magnetization curves. Taken from [23].

If one neglects effects like surface reconstruction, the direction of the band bending and resulting population or depopulation in the vicinity of the surface is determined by the difference of the work functions of both the EuO and the neighboring material. Therefore it should be possible to increase the transition temperature by a substrate with a smaller work function than EuO, which can be estimated by photoemission experiments to be $\sim 5\text{eV}$ [2]. Most recently, Klinkhammer et. al. [20] found an increased Curie temperature of $T_C \approx 75\text{K}$ in an ultra thin film of stoichiometric EuO on a substrate of Eu intercalated Graphene on top of Ir(111). The authors attribute the T_C enhancement to the influence of this substrate (see figure 2.9).

2. Properties of electron doped Europium Monoxide

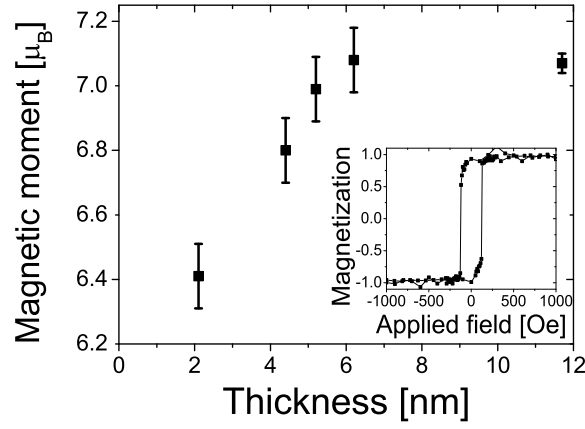


Figure 2.8.: Decreasing magnetic moment with the film thickness in $\text{EuO}_{0.96}$. Taken from [23]

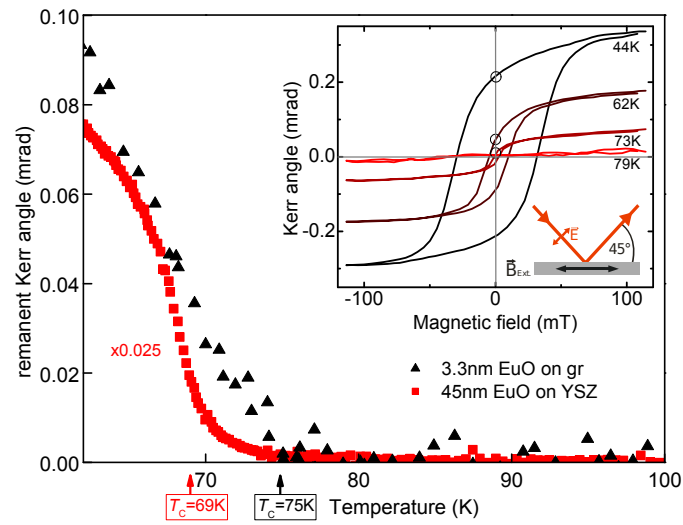


Figure 2.9.: Increased Curie temperature in an ultra thin film of stoichiometric EuO on a substrate of Eu intercalated Graphene on top of Ir(111). Taken from [20].

3. Quantum impurities

This chapter is concerned with quantum impurities which play a crucial role in the physics of electron doped Europium monoxide and constitute an integral part of our theory. In particular, we review the single impurity Anderson model [31,32], the pseudo-particle approach and the non-crossing approximation. In the course of this, we directly follow [33]. Afterwards, we discuss our improvements to the numerical solution of the non-crossing approximation in the case of a slightly filled conduction band in section 3.4.

3.1. The single impurity Anderson model

In the early sixties, P. W. Anderson developed a model for describing the interaction of itinerant conduction electrons with a localized magnetic impurity in a metal [31]. In general, the impurity can be N -fold degenerate and couple to M channels of conduction electrons. For instance, the former can be the spin degeneracy and the latter the angular momentum of the conduction electrons [34]. In this work, we will restrict ourselves to the simplest case of a doubly degenerate impurity (spin $S = \frac{1}{2}$) and a single conduction electron channel. In this case, the single impurity Anderson model (SIAM) Hamiltonian reads

$$H_{\text{SIAM}} = \sum_{\mathbf{k}\sigma} \varepsilon_{\mathbf{k}} c_{\mathbf{k}\sigma}^\dagger c_{\mathbf{k}\sigma} + E_d d_\sigma^\dagger d_\sigma + V \sum_{\mathbf{k}\sigma} (c_{\mathbf{k}\sigma}^\dagger d_\sigma + d_\sigma^\dagger c_{\mathbf{k}\sigma}) + U d_\uparrow^\dagger d_\uparrow d_\downarrow^\dagger d_\downarrow, \quad (3.1)$$

where the chemical potential is chosen to be $\mu = 0$ throughout this chapter. The model describes the interaction of a conduction band with dispersion $\varepsilon_{\mathbf{k}}$ and an impurity level at E_d . Due to the hybridization between the two, electrons can hop from the conduction band into the impurity level and vice versa. This is described by the term containing the hybridization energy V . The fourth term includes the on-site Coulomb repulsion U between two electrons with opposite spin at the impurity level.

Since there is no general solution to this model, the application of certain approximations is necessary. The kind of approximation is chosen in accordance with specific physical situations which correspond to special subsets of parameters in the Anderson model. We are particularly interested in the so-called Kondo limit [33,35], in which case, the impurity level lies sufficiently below the Fermi energy $E_d < 0$ and $\Gamma/E_d \ll 1$. Here we have introduced the width of the impurity level $\Gamma = \pi V^2 N_0$, where N_0 is the bare conduction electron density of states at the Fermi level $\omega = 0$. Furthermore, the on-site Coulomb repulsion should be sufficiently strong so that $E_d + U > 0$ and $\Gamma/(E_d + U) \ll 1$. This means that in the low temperature regime the impurity can be doubly occupied only by virtual processes. Therefore we are essentially left with a singly occupied, magnetic impurity. By treating the hybridization V as a small perturbation, one can apply a

3. Quantum impurities

Schrieffer-Wolff transformation [36] and map the Anderson Hamiltonian onto the Kondo Hamiltonian [35], which reads

$$H_K = \sum_{\mathbf{k}\sigma} \varepsilon_{\mathbf{k}} c_{\mathbf{k}\sigma}^\dagger c_{\mathbf{k}\sigma} + J_K \mathbf{S} \cdot \boldsymbol{\sigma}.$$

The anti-ferromagnetic interaction between the impurity spin \mathbf{S} and the conduction electron spin $\boldsymbol{\sigma}$ is given by $J_K = V^2(1/|E_d| + 1/(2E_d + U))$. For low temperatures, resonant spin flip scattering leads to the formation of a very sharp resonance at the Fermi energy, the so-called Kondo resonance. The width of the resonance is proportional to the Kondo temperature, which in the limit of $U \rightarrow \infty$ is given by [33]

$$T_K = \sqrt{2\Gamma} e^{-\pi \frac{E_d}{2\Gamma}}.$$

3.2. Pseudo-particle representation

The dynamics of an electron which encounters the impurity will strongly depend on whether the impurity is empty, singly occupied, or doubly occupied. Especially in the case of strong on-site Coulomb repulsion and low temperatures, double occupancy can only occur through virtual processes. In this case, it is reasonable to restrict the Hilbert space to empty and singly occupied states. The theoretical framework which accomplishes this task is the pseudo-particle representation [34], where new operators are introduced. First, two bosonic operators b^\dagger and a^\dagger , which create an empty impurity state $|0\rangle$ and a doubly occupied state $|2\rangle$ from the vacuum $|\text{vac}\rangle$. Second, fermionic operators f_σ^\dagger , which create a singly occupied state $|\sigma\rangle$ with spin σ .

$$\begin{aligned} b^\dagger |\text{vac}\rangle &= |0\rangle \\ f_\sigma^\dagger |\text{vac}\rangle &= |\sigma\rangle \\ a^\dagger |\text{vac}\rangle &= |2\rangle. \end{aligned}$$

The relation to the impurity creation operator is given by

$$d_\sigma^\dagger = f_\sigma^\dagger b + \eta_\sigma a^\dagger f_{-\sigma},$$

where $\eta_\uparrow = +1$ and $\eta_\downarrow = -1$. By this procedure, the Hilbert space is extended artificially. The physical subset of the Hilbert space is determined by the constraint

$$Q = \sum_{\sigma} f_\sigma^\dagger f_\sigma + b^\dagger b + a^\dagger a = 1.$$

which means that the number of pseudo-particles Q is conserved and restricted to $Q = 1$. We now restrict our discussion to the case of strong on-site Coulomb repulsion $U \rightarrow \infty$, where the operators a^\dagger will not show up in the equations anymore. If we write down the Anderson Hamiltonian (3.1) in terms of pseudo-particle creation and annihilation operators, we obtain

$$H_{\text{SIAM}} = \sum_{\mathbf{k}\sigma} \varepsilon_{\mathbf{k}} c_{\mathbf{k}\sigma}^\dagger c_{\mathbf{k}\sigma} + E_d f_\sigma^\dagger f_\sigma + V \sum_{\mathbf{k}\sigma} (c_{\mathbf{k}\sigma}^\dagger b^\dagger f_\sigma + f_\sigma^\dagger b c_{\mathbf{k}\sigma}). \quad (3.2)$$

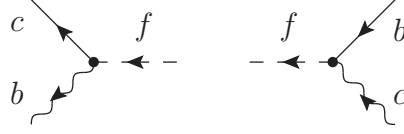


Figure 3.1.: Pseudo-particle vertices for the Anderson model with $U \rightarrow \infty$.

The corresponding vertices are shown in figure 3.1. In the considered limit, the pseudo-particle number constraint reads

$$Q = \sum_{\sigma} f_{\sigma}^{\dagger} f_{\sigma} + b^{\dagger} b = 1. \quad (3.3)$$

Note, that the conserved pseudo-particle number corresponds to a local gauge symmetry. This is reflected by the fact, that the pseudo-particle Anderson Hamiltonian (3.2) is invariant under $U(1)$ gauge transformations, $f_{\sigma}^{\dagger} \rightarrow e^{i\phi(\tau)} f_{\sigma}^{\dagger}$ and $b^{\dagger} \rightarrow e^{i\phi(\tau)} b^{\dagger}$, with an arbitrary time-dependent phase $\phi(\tau)$.

In order to fulfill (3.3), one has to project out the non-physical part of the Hilbert space in some way. To this end, we consider the grand canonical density operator

$$\rho_G = \frac{1}{Z_G} e^{-\beta(H + \lambda Q)},$$

with $Z_G = \text{tr}[\exp\{-\beta(H + \lambda Q)\}]$. Here, the chemical potential which corresponds to the pseudo-particle number Q is given by $-\lambda$. In the calculation of the grand canonical expectation value of some operator A ,

$$\langle A \rangle_G = \text{tr}[\rho_G A],$$

one has to sum over all pseudo-particle numbers $Q = 0, 1, 2, \dots$. In contrast to this, the physical expectation value $\langle A \rangle$ has to be evaluated in the canonical ensemble with $Q = 1$. It can be derived from the grand canonical expectation value by first taking the derivative with respect to the fugacity $\zeta = e^{-\beta\lambda}$, separately in numerator and the denominator, and subsequently taking the limit $\lambda \rightarrow \infty$:

$$\langle A \rangle = \lim_{\lambda \rightarrow \infty} \frac{\frac{\partial}{\partial \zeta} \text{tr}[A e^{-\beta(H + \lambda Q)}]}{\frac{\partial}{\partial \zeta} \text{tr}[e^{-\beta(H + \lambda Q)}]} = \lim_{\lambda \rightarrow \infty} \frac{\langle QA \rangle_G}{\langle Q \rangle_G} = \lim_{\lambda \rightarrow \infty} \frac{\langle A \rangle_G}{\langle Q \rangle_G}.$$

In the last step, we have assumed that the expectation of the operator A in the $Q = 0$ subspace is vanishing, $A|Q = 0\rangle = 0$. This is the case for most of the relevant operators here, like e.g. the physical impurity electron operator d_{σ}^{\dagger} . The physical impurity Green's function can be calculated from of the grand canonical impurity Green's function $\mathcal{G}_{d\sigma}(\omega, \lambda)$ via

$$G_{d\sigma}(\omega) = \lim_{\lambda \rightarrow \infty} \frac{\mathcal{G}_{d\sigma}(\omega)}{\langle Q \rangle_G}. \quad (3.4)$$

One cannot apply Wick's theorem and diagrammatic techniques to the physical Green's function $G_{d\sigma}(\omega)$ directly. In fact, this is possible only for the grand canonical Green's

3. Quantum impurities

function, $\mathcal{G}_{d\sigma}(\omega)$. In the next section, we will apply diagrammatic techniques in order to express $\mathcal{G}_{d\sigma}(\omega)$ in terms of the grand canonical pseudo-particle Green's functions

$$\begin{aligned}\mathcal{G}_{f\sigma}(\tau_1 - \tau_2) &= -\langle T\{f_\sigma(\tau_1)f_\sigma^\dagger(\tau_2)\}\rangle_G \\ \mathcal{G}_b(\tau_1 - \tau_2) &= -\langle T\{b(\tau_1)b^\dagger(\tau_2)\}\rangle_G,\end{aligned}$$

where T is the time-ordering operator. The Fourier transforms of those read

$$\mathcal{G}_{f\sigma}(i\omega_n) = \frac{1}{i\omega_n - E_d - \lambda - \Sigma_{f\sigma}(i\omega_n)} \quad (3.5)$$

$$\mathcal{G}_b(i\omega_n) = \frac{1}{i\omega_n - \lambda - \Sigma_b(i\omega_n)}. \quad (3.6)$$

During the evaluation of the Feynman diagrams, the projection procedure is carried out and the physical Green's functions are obtained. After analytic continuation $i\omega \rightarrow \omega - i0^+$, the poles of the pseudo-particle Green's functions in (3.5) and (3.6) will scale to infinity together with $\lambda \rightarrow \infty$. Therefore we shift the energy scale by λ before we apply the projection procedure and define the physical pseudo-particle Green's functions as

$$G_{f\sigma,b}(\omega - i0^+) = \lim_{\lambda \rightarrow \infty} \mathcal{G}_{f\sigma,b}(\omega + \lambda - i0^+).$$

This is feasible since the resulting impurity Green's function depends on the *difference* of the frequencies appearing as arguments in the pseudo-particle Green's functions.

3.3. Non-crossing approximation

The numerical calculation of the impurity Green's function for a given conduction electron Green's function is known as an impurity solver. In the following we will review the non-crossing approximation (NCA). The NCA is a well established impurity solver which is used for instance in DMFT calculations [37–39]. In particular, it is applicable to arbitrary conduction electron densities of states and its results are reliable for temperatures well above the Kondo temperature [33].

Our goal is to apply perturbation theory in the hybridization V , which is assumed to be small compared to the half conduction band width D_0 . A precondition for any perturbative approach is the compliance of the pseudo-particle number condition $Q = 1$ and the corresponding $U(1)$ symmetry. This is achieved by utilizing a conserving approximation [40, 41], which is determined by a generating functional Φ . It comprises all vacuum skeleton diagrams build out of full Green's functions and the approximation is defined by the choice of a subset of these diagrams. The simplest choice for the generating functional, as depicted in figure 3.2, defines the NCA. At the same time it equals the vacuum skeleton diagram with the lowest order in V , namely second order. Due to the absence of crossing conduction electron propagators, the approximation was named non-crossing approximation. Note that the depicted propagators correspond to the grand-canonical Green's functions of section 3.2. The grand canonical self-energies

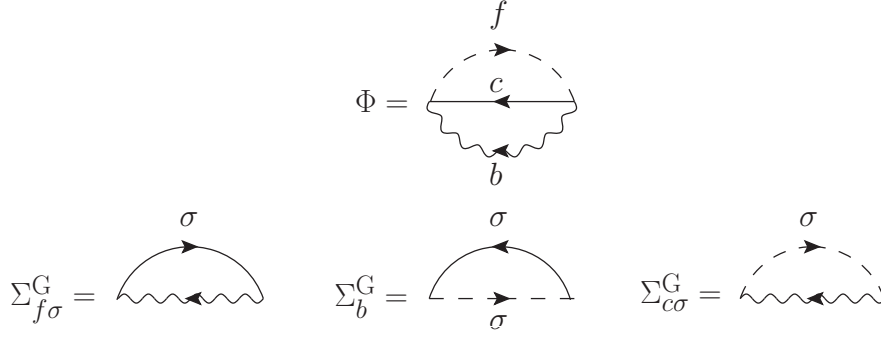


Figure 3.2.: Non-crossing approximation as seen in the generating functional (top) and the corresponding pseudo-fermion, slave-boson and conduction electron self-energies (bottom).

are then given by the functional derivative of the generating functional with respect to the corresponding Green's functions [40, 41]

$$\Sigma_{f\sigma, c\sigma, b}^G = \frac{\delta\Phi}{\delta\mathcal{G}_{f\sigma, c\sigma, b}},$$

which essentially corresponds to the removal of the corresponding propagator from the generating functional diagram (see figure 3.2). The grand canonical slave-boson self-energy reads

$$\begin{aligned} \Sigma_b^G(i\omega_n) &= \text{Diagram: } \omega_n \text{ wavy line, } \omega_l + \omega_n, \sigma \text{ dashed line, } \omega_l, \sigma \text{ solid line, } \omega_n \text{ wavy line} \\ &= (-1)^2 V^2 \frac{1}{\beta} \sum_{l\sigma} \underbrace{\left(-\mathcal{G}_{c\sigma}^0(i\omega_l)\right)}_{\int d\varepsilon \frac{\mathcal{A}_{c\sigma}^0(\varepsilon)}{i\omega_l - \varepsilon}} \underbrace{\left(-\mathcal{G}_{f\sigma}(i\omega_l + i\omega_n)\right)}_{\int d\alpha \frac{\mathcal{A}_{f\sigma}(\alpha)}{i\omega_l + i\omega_n - \alpha}} \\ &= V^2 \sum_{\sigma} \int d\varepsilon \int d\alpha \mathcal{A}_{c\sigma}^0(\varepsilon) \mathcal{A}_{f\sigma}(\alpha) \underbrace{\frac{1}{\beta} \sum_l \frac{1}{(i\omega_l - \varepsilon)(i\omega_l + i\omega_n - \alpha)}}_{\oint \frac{dz}{2\pi i} \frac{f(z)}{(z - \varepsilon)(i\omega_n + z - \alpha)} = \frac{f(\varepsilon)}{i\omega_n + \varepsilon - \alpha} + \frac{f(\alpha - i\omega_n)}{\alpha - i\omega_n - \varepsilon}} \\ &= V^2 \sum_{\sigma} \int d\varepsilon \int d\alpha \mathcal{A}_{c\sigma}^0(\varepsilon) \mathcal{A}_{f\sigma}(\alpha) \left(\frac{f(\varepsilon) + f(\alpha)}{i\omega_n + \varepsilon - \alpha} \right), \end{aligned} \quad (3.7)$$

where we have used the fermionic nature of ω_n in the last step and introduced the grand canonical spectral density $\mathcal{A}_{f\sigma}$. In order to obtain the physical slave-boson self-energy, we perform an analytic continuation to real frequencies, shift the energy by λ and take

3. Quantum impurities

the limit $\lambda \rightarrow \infty$:

$$\begin{aligned}
\Sigma_b(\omega - i0^+) &= \lim_{\lambda \rightarrow \infty} \Sigma_b^G(\omega - i0^+ + \lambda) \\
&= \lim_{\lambda \rightarrow \infty} V^2 \sum_{\sigma} \int d\varepsilon \int d\alpha \mathcal{A}_{c\sigma}^0(\varepsilon) \mathcal{A}_{f\sigma}(\alpha) \left(\frac{f(\varepsilon) + f(\alpha)}{\omega + \lambda + \varepsilon - \alpha - i0^+} \right) \\
&= \lim_{\lambda \rightarrow \infty} V^2 \sum_{\sigma} \int d\varepsilon \int d\alpha \mathcal{A}_{c\sigma}^0(\varepsilon) \mathcal{A}_{f\sigma}(\alpha + \lambda) \overbrace{\left(\frac{f(\varepsilon) + f(\alpha + \lambda)}{\omega + \varepsilon - \alpha - i0^+} \right)}^{\lambda \rightarrow \infty 0} \\
&= V^2 \sum_{\sigma} \int d\varepsilon f(\varepsilon) \mathcal{A}_{c\sigma}^0(\varepsilon) \int d\alpha \frac{\lim_{\lambda \rightarrow \infty} \mathcal{A}_{f\sigma}(\alpha + \lambda)}{\omega + \varepsilon - \alpha - i0^+} \\
&= V^2 \sum_{\sigma} \int d\varepsilon f(\varepsilon) \mathcal{A}_{c\sigma}^0(\varepsilon) G_{f\sigma}(\omega + \varepsilon - i0^+). \tag{3.8}
\end{aligned}$$

This formula represents the physical slave-boson self-energy in terms of the physical pseudo-fermion and conduction electron Green's functions. The evaluation of the pseudo-fermion self-energy diagram is performed similar to (3.7) and yields

$$\begin{aligned}
\Sigma_{f\sigma}^G(i\omega_n) &= \text{Diagram: A wavy line with an arrow pointing right, labeled ω_n, σ at the left end and ω_n, σ at the right end. Above the wavy line is a curved arrow pointing right, labeled ω_l, σ. The wavy line is part of a larger diagram structure involving vertices and other lines, but the focus is on this specific part.} \\
&= (-1) V^2 \frac{1}{\beta} \sum_l (-\mathcal{G}_{c\sigma}^0(i\omega_l)) (-\mathcal{G}_b(i\omega_n - i\omega_l)) \\
&= -V^2 \int d\varepsilon \int d\alpha \mathcal{A}_{c\sigma}^0(\varepsilon) \mathcal{A}_b(\alpha) \underbrace{\frac{1}{\beta} \sum_l \frac{1}{(i\omega_l - \varepsilon)(i\omega_n - i\omega_l - \alpha)}}_{\oint \frac{dz}{2\pi i} \frac{f(z)}{(z - \varepsilon)(i\omega_n - z - \alpha)} = \frac{f(\varepsilon)}{i\omega_n - \varepsilon - \alpha} - \frac{f(i\omega_n - \alpha)}{i\omega_n - \alpha - \varepsilon}} \\
&= -V^2 \int d\varepsilon \int d\alpha \mathcal{A}_{c\sigma}^0(\varepsilon) \mathcal{A}_b(\alpha) \left(\frac{f(\varepsilon) + b(-\alpha)}{i\omega_n - \varepsilon - \alpha} \right).
\end{aligned}$$

The physical pseudo-fermion self-energy reads

$$\begin{aligned}
 \Sigma_{f\sigma}(\omega - i0^+) &= \lim_{\lambda \rightarrow \infty} \Sigma_{f\sigma}^G(\omega - i0^+ + \lambda) \\
 &= - \lim_{\lambda \rightarrow \infty} V^2 \int d\varepsilon \int d\alpha \mathcal{A}_{c\sigma}^0(\varepsilon) \mathcal{A}_b(\alpha) \left(\frac{f(\varepsilon) + b(-\alpha)}{\omega + \lambda - \varepsilon - \alpha - i0^+} \right) \\
 &= - \lim_{\lambda \rightarrow \infty} V^2 \sum_{\sigma} \int d\varepsilon \int d\alpha \mathcal{A}_{c\sigma}^0(\varepsilon) \mathcal{A}_{f\sigma}(\alpha + \lambda) \left(\frac{f(\varepsilon) + \overbrace{b(-\alpha - \lambda)}^{\lambda \rightarrow \infty - 1}}{\omega + \varepsilon - \alpha - i0^+} \right) \\
 &= V^2 \sum_{\sigma} \int d\varepsilon [1 - f(\varepsilon)] \mathcal{A}_{c\sigma}^0(\varepsilon) \int d\alpha \frac{\lim_{\lambda \rightarrow \infty} \mathcal{A}_b(\alpha + \lambda)}{\omega - \varepsilon - \alpha - i0^+} \\
 &= V^2 \sum_{\sigma} \int d\varepsilon [1 - f(\varepsilon)] \mathcal{A}_{c\sigma}^0(\varepsilon) G_b(\omega - \varepsilon - i0^+). \tag{3.9}
 \end{aligned}$$

Finally, the grand canonical conduction electron self-energy is given by

$$\begin{aligned}
 \Sigma_{c\sigma}^G(i\omega_n) &= \text{Diagram: } \omega_n, \sigma \text{ (left), } \omega_n + \omega_l, \sigma \text{ (top), } \omega_l \text{ (middle), } \omega_n, \sigma \text{ (right)} \\
 &= (-1) V^2 \frac{1}{\beta} \sum_l (-\mathcal{G}_b(i\omega_l)) (-\mathcal{G}_{f\sigma}(i\omega_n + i\omega_l)) \\
 &= -V^2 \int d\varepsilon \int d\alpha \mathcal{A}_b(\varepsilon) \mathcal{A}_{f\sigma}(\alpha) \frac{1}{\beta} \sum_l \frac{1}{(i\omega_l - \varepsilon)(i\omega_n + i\omega_l - \alpha)} \\
 &\quad - \oint \frac{dz}{2\pi i} \frac{b(z)}{(z - \varepsilon)(i\omega_n + z - \alpha)} = -\frac{b(\varepsilon)}{i\omega_n + \varepsilon - \alpha} + \frac{b(\alpha - i\omega_n)}{i\omega_n + \varepsilon - \alpha} \\
 &= V^2 \int d\varepsilon \int d\alpha \mathcal{A}_b(\varepsilon) \mathcal{A}_{f\sigma}(\alpha) \left(\frac{b(\varepsilon) + f(\alpha)}{\varepsilon + i\omega_n - \alpha} \right) \\
 &= V^2 \int d\varepsilon b(\varepsilon) \mathcal{A}_b(\varepsilon) \int d\alpha \frac{\mathcal{A}_{f\sigma}(\alpha)}{\varepsilon + i\omega_n - \alpha} - V^2 \int d\alpha f(\alpha) \mathcal{A}_{f\sigma}(\alpha) \int d\varepsilon \frac{\mathcal{A}_b(\varepsilon)}{\alpha - i\omega_n - \varepsilon} \\
 &= V^2 \int d\varepsilon \{ b(\varepsilon) \mathcal{A}_b(\varepsilon) \mathcal{G}_{f\sigma}(\varepsilon + i\omega_n) - f(\varepsilon) \mathcal{A}_{f\sigma}(\varepsilon) \mathcal{G}_b(\varepsilon - i\omega_n) \}.
 \end{aligned}$$

The physical conduction electron self-energy can not be calculated from the above employing the limit $\lambda \rightarrow \infty$ since the expectation value of the conduction electron operator in the $Q = 0$ subspace does not vanish. Nevertheless, we consider this limit for later use.

3. Quantum impurities

It reads

$$\begin{aligned}
\lim_{\lambda \rightarrow \infty} \Sigma_{c\sigma}^G(\omega - i0^+) &\stackrel{\varepsilon = \tilde{\varepsilon} + \lambda}{=} \lim_{\lambda \rightarrow \infty} V^2 \int d\tilde{\varepsilon} \left\{ \overbrace{b(\tilde{\varepsilon} + \lambda)}^{\lambda \xrightarrow{\rightarrow} \infty} \mathcal{A}_b(\tilde{\varepsilon} + \lambda) \mathcal{G}_{f\sigma}(\tilde{\varepsilon} + \lambda + i\omega - i0^+) \right. \\
&\quad \left. - \overbrace{f(\tilde{\varepsilon} + \lambda)}^{\lambda \xrightarrow{\rightarrow} \infty} \mathcal{A}_{f\sigma}(\tilde{\varepsilon} + \lambda) \mathcal{G}_b(\tilde{\varepsilon} + \lambda - \omega + i0^+) \right\} \\
&= V^2 \left(\lim_{\lambda \rightarrow \infty} e^{-\beta\lambda} \right) \int d\tilde{\varepsilon} e^{-\beta\tilde{\varepsilon}} \left[A_b(\tilde{\varepsilon}) G_{f\sigma}(\tilde{\varepsilon} + i\omega - i0^+) \right. \\
&\quad \left. - A_{f\sigma}(\tilde{\varepsilon}) G_b(\tilde{\varepsilon} - \omega + i0^+) \right]. \quad (3.10)
\end{aligned}$$

In order to derive the impurity Green's function we consider the full grand canonical conduction electron Green's function

$$\begin{aligned}
\mathcal{G}_{c\sigma}(i\omega_n) &= \frac{c}{\longleftarrow} \\
&= \frac{c}{\longleftarrow} + \frac{c}{\longleftarrow} \cdot \frac{d}{\longleftarrow} \cdot \frac{c}{\longleftarrow} + \frac{c}{\longleftarrow} \cdot \frac{d}{\longleftarrow} \cdot \frac{c}{\longleftarrow} \cdot \frac{d}{\longleftarrow} \cdot \frac{c}{\longleftarrow} + \dots \\
&= \frac{c}{\longleftarrow} + \frac{c}{\longleftarrow} \cdot \frac{d}{\longleftarrow} \cdot \frac{c}{\longleftarrow} \\
&= \mathcal{G}_{c\sigma}^0(i\omega_n) [1 + V^2 \mathcal{G}_{d\sigma}(i\omega_n) \mathcal{G}_{c\sigma}^0(i\omega_n)].
\end{aligned}$$

By comparing this with $\mathcal{G}_{c\sigma}(i\omega_n) = \{[\mathcal{G}_{c\sigma}^0(i\omega_n)]^{-1} - \Sigma_{c\sigma}^G(i\omega_n)\}^{-1}$, we can express the grand canonical impurity Green's function in terms of the grand canonical conduction electron self-energy via

$$\mathcal{G}_{d\sigma}(i\omega_n) = \frac{\Sigma_{c\sigma}^G(i\omega_n)}{V^2 [1 - \Sigma_{c\sigma}^G(i\omega_n) \mathcal{G}_{c\sigma}^0(i\omega_n)]}. \quad (3.11)$$

Now, we can derive the physical impurity Green's function in the following way:

$$\begin{aligned}
G_{d\sigma}(\omega - i0^+) &\stackrel{(3.4)}{=} \lim_{\lambda \rightarrow \infty} \frac{\mathcal{G}_{d\sigma}(\omega - i0^+)}{\langle Q \rangle_G} \\
&= \lim_{\lambda \rightarrow \infty} \frac{e^{\lambda\beta} \mathcal{G}_{d\sigma}(\omega - i0^+)}{e^{\lambda\beta} \langle Q \rangle_G} \\
&= \lim_{\lambda \rightarrow \infty} e^{\lambda\beta} \mathcal{G}_{d\sigma}(\omega - i0^+) \\
&\stackrel{(3.11)}{=} \lim_{\lambda \rightarrow \infty} \frac{e^{\lambda\beta} \Sigma_{c\sigma}^G(\omega - i0^+)}{V^2 [1 - \underbrace{\Sigma_{c\sigma}^G(\omega - i0^+)}_{\text{with (3.10)} \xrightarrow{\lambda \rightarrow \infty} 0} \mathcal{G}_{c\sigma}^0(\omega - i0^+)]} \\
&\stackrel{(3.10)}{=} \int d\varepsilon e^{-\beta\varepsilon} [A_b(\varepsilon) G_{f\sigma}(\varepsilon + i\omega - i0^+) - A_{f\sigma}(\varepsilon) G_b(\varepsilon - \omega + i0^+)]. \quad (3.12)
\end{aligned}$$

In the third step, we have used

$$\lim_{\lambda \rightarrow \infty} e^{\beta\lambda} \langle Q \rangle_G = \lim_{\lambda \rightarrow \infty} \frac{\text{tr}(Q e^{-\beta[H + \lambda(Q-1)]})}{\text{tr}(e^{-\beta[H + \lambda Q]})} = 1. \quad (3.13)$$

3.4. Numerical solution of the NCA equations

For a given conduction electron Green's function, the equations (3.8), (3.9) and (3.12) constitute a self-consistent set of equations. They read

$$\Sigma_b(\omega - i0^+) = V^2 \sum_{\sigma} \int d\varepsilon f(\varepsilon) A_{c\sigma}^0(\varepsilon) G_{f\sigma}(\omega + \varepsilon - i0^+), \quad (3.8)$$

$$\Sigma_{f\sigma}(\omega - i0^+) = V^2 \sum_{\sigma} \int d\varepsilon [1 - f(\varepsilon)] A_{c\sigma}^0(\varepsilon) G_b(\omega - \varepsilon - i0^+), \quad (3.9)$$

$$G_{d\sigma}(\omega - i0^+) = \int d\varepsilon e^{-\beta\varepsilon} [A_b(\varepsilon) G_{f\sigma}(\varepsilon + i\omega - i0^+) - A_{f\sigma}(\varepsilon) G_b(\varepsilon - \omega + i0^+)]. \quad (3.12)$$

The numerical solution of the so-called NCA equations is subject of the next section.

3.4. Numerical solution of the NCA equations

For the numerical evaluation of the NCA equations (3.8), (3.9) and (3.12), two complications arise. The first problem is given by the fact that the pseudo-particle spectral densities diverge for $T = 0$ at a certain energy which can not be predicted [33]. This problem can be solved in the following way. We consider equation (3.13) and write

$$\begin{aligned} 1 &= \lim_{\lambda \rightarrow \infty} e^{\beta\lambda} \langle Q \rangle_G \\ &= \lim_{\lambda \rightarrow \infty} e^{\beta\lambda} \int d\omega \left[\sum_{\sigma} f(\omega) \mathcal{A}_{f\sigma}(\omega) + b(\omega) \mathcal{A}_b(\omega) \right] \\ &= \int d\omega e^{-\beta\omega} \left[\sum_{\sigma} A_{f\sigma}(\omega) + A_b(\omega) \right]. \end{aligned} \quad (3.14)$$

Next, we shift the energy scale in the pseudo-particle Green's functions by $\omega \rightarrow \omega + \lambda_0$ before the projection to the physical subspace by the transformation $\omega \rightarrow \omega + \lambda$ and the limit $\lambda \rightarrow \infty$ is performed [33]. With this, the pseudo-particle spectral densities read

$$A_{f\sigma,b}(\omega) = \lim_{\lambda \rightarrow \infty} \mathcal{A}_{f\sigma,b}(\omega + \lambda_0 + \lambda).$$

The position of the $T = 0$ divergence can be shifted by changing λ_0 . In each iteration of the self-consistent calculation, λ_0 is determined such that (3.14) is fulfilled. This is equivalent to the problem of finding the roots of the following function:

$$F(\lambda_0) = \int d\omega e^{-\beta\omega} \left[\sum_{\sigma} A_{f\sigma}(\omega) + A_b(\omega) \right] - 1 \stackrel{!}{=} 0.$$

With this, the $T = 0$ divergence is fixed to $\omega = 0$ which makes the numerical evaluation faster and more stable.

The second problem is that the Boltzmann factors $e^{-\beta\omega}$ in (3.14) diverge exponentially for $\omega < 0$. This means that the pseudo-particle spectral densities have to vanish exponentially $\sim e^{\beta\omega}$ for negative frequencies. One can circumvent the problem by separating

3. Quantum impurities

this behavior and defining modified pseudo-particle spectral densities [33] via

$$\begin{aligned} A_{f\sigma,b}(\omega) &= f(-\omega)\tilde{A}_{f\sigma,b}(\omega), \\ \Sigma_{f\sigma,b}(\omega) &= f(-\omega)\tilde{\Sigma}_{f\sigma,b}(\omega). \end{aligned}$$

The self-consistent NCA equations (3.8), (3.9) and (3.12) can now be formulated in terms of the modified spectral densities and the corresponding self-energies. They are given by

$$\text{Im}\tilde{\Sigma}_b(\omega - i0^+) = \Gamma \sum_{\sigma} \int d\varepsilon \frac{f(\varepsilon)(1 - f(\omega + \varepsilon))}{f(-\omega)} A_{c\sigma}^0(\varepsilon) \tilde{A}_{f\sigma}(\omega + \varepsilon), \quad (3.15)$$

$$\text{Im}\tilde{\Sigma}_{f\sigma}(\omega - i0^+) = \Gamma \int d\varepsilon \frac{f(-\varepsilon)(1 - f(\omega - \varepsilon))}{f(-\omega)} A_{c\sigma}^0(\varepsilon) \tilde{A}_b(\omega - \varepsilon), \quad (3.16)$$

$$A_{d\sigma}(\omega) = \int d\varepsilon [f(\omega + \varepsilon)f(-\varepsilon) + f(-\varepsilon - \omega)f(\varepsilon)] \tilde{A}_{f\sigma}(\omega + \varepsilon)\tilde{A}_b(\varepsilon), \quad (3.17)$$

and

$$\tilde{A}_b(\omega) = \frac{1}{\pi} \frac{\text{Im}\tilde{\Sigma}_b(\omega)}{[\omega + \lambda_0 - \text{Re}\Sigma_b(\omega)]^2 + [\text{Im}\Sigma_b(\omega)]^2}, \quad (3.18)$$

$$\tilde{A}_{f\sigma}(\omega) = \frac{1}{\pi} \frac{\text{Im}\tilde{\Sigma}_{f\sigma}(\omega)}{[\omega + \lambda_0 - E_d - \text{Re}\Sigma_{f\sigma}(\omega)]^2 + [\text{Im}\Sigma_{f\sigma}(\omega)]^2}. \quad (3.19)$$

The corresponding condition for λ_0 reads

$$F(\lambda_0) = \int d\omega f(\omega) \left[\sum_{\sigma} \tilde{A}_{f\sigma}(\omega) + \tilde{A}_b(\omega) \right] - 1 \stackrel{!}{=} 0. \quad (3.20)$$

These equations are solved as follows. One begins with a guess for the pseudo-particle self-energies (3.15) and (3.16), e. g. a Gaussian of width $2D_0$, where D_0 is the half width of the bare conduction band. Afterwards the spectral densities are calculated from the self-energies using (3.18) and (3.19). In the course of this, λ_0 is changed during a root finding algorithm until the condition (3.20) is fulfilled. Since $F(\lambda_0)$ is a monotonic function one can apply the following scheme to find its root. After starting at the value of λ_0 from the last iteration, its value is increased or decreased stepwise, depending on the sign of the function. In doing so, the step width is increased exponentially until a sign change in the function occurs. Afterwards a bisection method is applied for finding the root. Once the spectral densities which obey (3.20) are found, they are inserted into (3.15) and (3.16). The new self energies are mixed to the old ones by a small amount to ensure a careful relaxation of the solution. This process is repeated until the functions do not change anymore from one iteration to the next. Finally, the impurity spectral density is calculated with equation (3.17). As the bare conduction band density of states, we choose

$$A_{c\sigma}^0(\omega) = e^{-\left(\frac{\omega - \Delta}{D_0}\right)^2}$$

The filling of the conduction band is determined by the choice of the band center Δ . Figure 3.3 shows the results of the self-consistent solution of the NCA equations in the

case of a half filled Gaussian conduction band ($\Delta = 0$). The corresponding results for small conduction band fillings are depicted in figure 3.4.

In the following, we will discuss the details of the numerical solution of the NCA equations. In order to resolve the peaks in the spectral densities $\tilde{A}_b(\omega)$ and $\tilde{A}_{f\sigma}(\omega)$, a suitable integration grid is needed. The width and heights of these peaks are directly related to the imaginary part of the pseudo-particle Green's functions $\text{Im}\Sigma_b(\omega)$ and $\text{Im}\Sigma_{f\sigma}(\omega)$. Their position is determined by the real parts $\text{Re}\Sigma_b(\omega)$ and $\text{Re}\Sigma_{f\sigma}(\omega)$ and separated roughly by the impurity level energy E_d . If the conduction electron spectral weight around the Fermi energy is large enough, the peak in the pseudo-fermion spectral density may become very narrow for very low temperatures, but the slave-boson spectral density peak remains broad. In this case it is sufficient to use a fixed grid with a logarithmically dense cluster point at the Fermi energy, and a tangentially dense cluster point at E_d for $A_{d\sigma}(\omega)$ and at $-E_d$ for $A_b(\omega)$ [42].

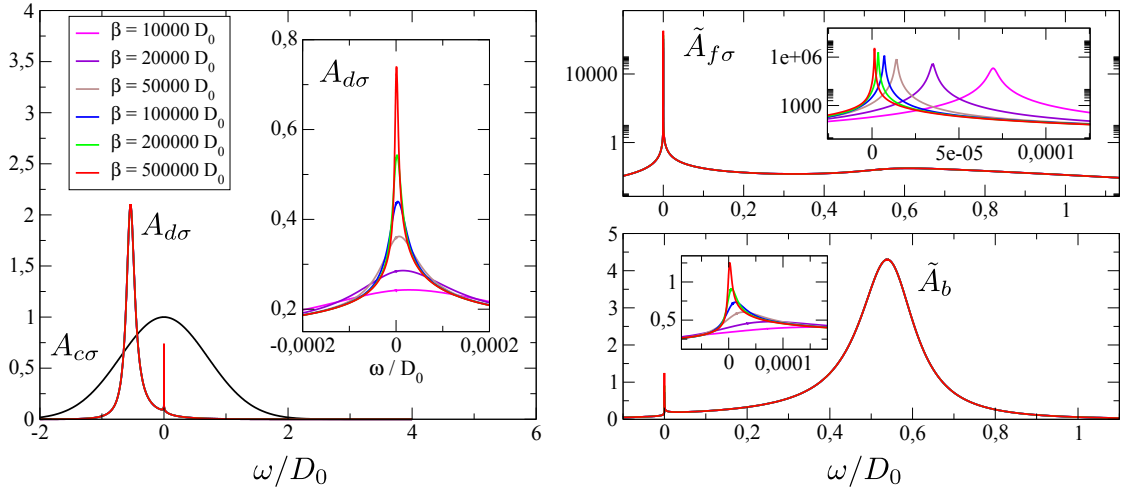


Figure 3.3.: Solutions of the NCA equations in the case of a half filled spin degenerate conduction band $\Delta = 0$. The impurity, pseudo-fermion and slave-boson spectral densities are shown for various temperatures through $\beta = \frac{1}{k_B T}$.

The numerical solution of the NCA equations becomes more demanding if the conduction band spectral weight at the Fermi energy is very small. For example, this is the case for the gaped conduction band in the high temperature phase of electron doped Europium monoxide (see chapter 5). Here, also the peak in the slave-boson spectral density can become very sharp. Moreover, there will be pronounced features in the slave-boson spectral density at the position of the pseudo-fermion spectral density peak and vice versa (see figure 3.4). In order to resolve multiple sharp peaks we developed a highly versatile integration grid library [43] which is capable of handling an arbitrary number of logarithmically and tangentially dense as well as equidistant grid regions. Moreover the position of these grid regions can also be chosen freely. It is even possible to resolve several neighboring sharp peaks with arbitrarily small distance to each other.

Even if all peaks are properly resolved, their position might change during the iteration

3. Quantum impurities

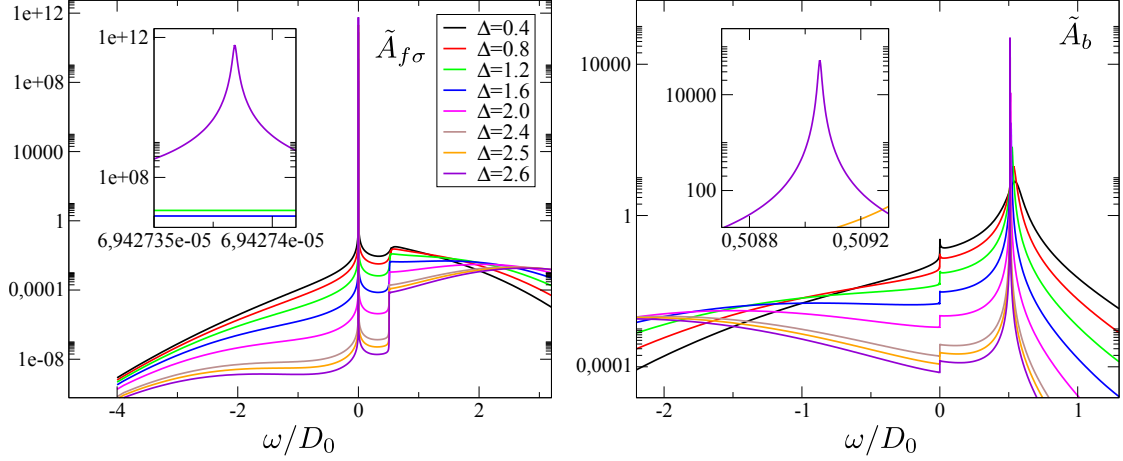


Figure 3.4.: Pronounced peaks in the pseudo-particle spectral densities in the case of a small filling in the conduction band. By increasing the band center Δ , which is given in units of the half conduction band width D_0 , the filling of the Gaussian conduction band decreases exponentially.

process. This problem can be overcome by a broad region of dense points only in the above case of sufficient conduction spectral weight at the Fermi energy. Otherwise, one has to adapt the integration grid whenever the peak is shifted away from the integration grid cluster point. For this purpose, we have developed a numerical method which tracks the peak of a given function during the iteration process. We use our integration grid [43] which makes it easy to create and change grid regions in an existing integration grid. The details of this adaptive peak resolution are explained in appendix E. The flexible integration grid proves beneficial also in the calculation of (3.17), where the integrand possesses four peaks or pronounced features whose positions will intersect each other while ω changes. The code of the NCA program can be found at [44].

In order to ensure that the width of these peaks does not fall below machine precision one can add an artificial constant imaginary part ζ to the pseudo-particle self energies:

$$\begin{aligned}\text{Im}\Sigma_{f\sigma}(\omega) &\rightarrow \text{Im}\Sigma_{f\sigma}(\omega) + \zeta \\ \text{Im}\Sigma_b(\omega) &\rightarrow \text{Im}\Sigma_b(\omega) + \zeta.\end{aligned}$$

The size of ζ dictates the accuracy of the resulting solution and should be adapted to the situation at hand. Note, that for the above results, we used $\zeta = 0$.

4. Model

In the next two chapters we develop a self-consistent theory for electron doped Europium monoxide. In doing so, we generalize the theory of Arnold and Kroha [18] for bulk $\text{Eu}_{1-x}\text{Gd}_x\text{O}$ in several ways. First of all, we allow for spatial invariance in one direction in order to describe heterostructures of electron doped EuO. This allows us to describe the influence of various capping materials on the phase transition. Moreover, different types of electron doping are realized. Besides $\text{Eu}_{1-x}\text{Gd}_x\text{O}$, the model covers oxygen deficient EuO and stoichiometric EuO. In order to properly describe long range spin coupling in heterostructures, we extend the theory of Arnold and Kroha to the second order in the coupling between the conduction electron spin and the 4f spins. For the sake of completeness, we include the derivation of the bulk $\text{Eu}_{1-x}\text{Gd}_x\text{O}$ case without long range coupling as it can be found in [25]. In the present chapter, we introduce the model Hamiltonians for the bulk and heterostructure case. The derivation of the self-consistent theory in part of the subsequent chapter 5.

4.1. Bulk

The theory of Arnold and Kroha for bulk $\text{Eu}_{1-x}\text{Gd}_x\text{O}$ is based on the work of Mauger and Godart [3] and has some similarities to the theory of Sinjukow and Nolting for Oxygen deficient EuO [17]. As discussed in chapter 2, the physics of electron doped EuO is mainly governed by three parts. Firstly the lattice of localized magnetic moments from the 4f shell, secondly the conduction band which mediates the interaction between the localized moments and thirdly, the impurities which provide the possibility of transport through excess electrons. For the bulk Hamiltonian we have

$$H = H_0 + H_{cd} + H_{cf}. \quad (4.1)$$

The conduction band part of the Hamiltonian is given by

$$H_0 = \sum_{\mathbf{k}\sigma} (\varepsilon_{\mathbf{k}} - \mu) c_{\mathbf{k}\sigma}^\dagger c_{\mathbf{k}\sigma}, \quad (4.2)$$

where $c_{\mathbf{k}\sigma}^\dagger$ is the conduction electron creation operator, $\varepsilon_{\mathbf{k}}$ is the conduction band dispersion and μ is the chemical potential. The impurity part describes Anderson impurities which are randomly distributed over the Eu sites in the FCC lattice (cf. chapter 3):

$$H_{cd} = E_d \sum_{\{i\}\sigma} d_{i\sigma}^\dagger d_{i\sigma} + V \sum_{\{i\}\sigma} (c_{i\sigma}^\dagger d_{i\sigma} + d_{i\sigma}^\dagger c_{i\sigma}) + U \sum_{\{i\}} d_{i\uparrow}^\dagger d_{i\uparrow} d_{i\downarrow}^\dagger d_{i\downarrow}, \quad (4.3)$$

4. Model

where $d_{i\sigma}^\dagger$ is the creation operator for an electron at the impurity site i , E_d is the impurity level, V is the hybridization between the conduction band and the impurity level, and U is the on-site Coulomb repulsion at the impurity sites. The notation $\{i\}$ indicates the sum over a fixed but random distribution of impurities over the Eu sites in the FCC crystal. Finally, the Heisenberg part of the Hamiltonian reads

$$H_{cf} = - \sum_{\langle ij \rangle} J_{ij} \mathbf{S}_i \mathbf{S}_j - J_{cf} \sum_i \boldsymbol{\sigma}_i \mathbf{S}_i, \quad (4.4)$$

where \mathbf{S}_i is the $4f$ spin operator at the Eu site i . J_{ij} is the coupling between the localized moments which is independent of the conduction band occupation and therefore responsible for the Curie temperature of 69 K in stoichiometric EuO. The second term of H_{cf} describes the exchange splitting between the localized $4f$ moments and the conduction electron spin $\boldsymbol{\sigma}_i$ at site i with the exchange coupling J_{cf} .

Instead of a specific conduction electron dispersion, we choose the following half circular bare conduction band density of states

$$N(\varepsilon) = \frac{1}{\pi D_0} \sqrt{1 - \left(\frac{\varepsilon - \Delta_0}{D_0} \right)^2}, \quad (4.5)$$

which reproduces the square root behavior at the band edges that is typical for three dimensional bands. Here, Δ_0 is the band center and D_0 the half band width. In the following we measure all energies in units of the half band width D_0 .

4.2. Multilayer

In order to describe thin films, we need to extend the bulk theory to allow for broken translational symmetry in one direction, which we call the z -direction. One can imagine the system as a number of atomic monolayers extended into the x - and y -direction that are stacked onto each other. Hence, we speak of a multilayer system. The z direction is called 'perpendicular' and any direction in the x - y planes is called 'parallel'. We split up the lattice vectors into parallel and perpendicular directions $\mathbf{R} = (\mathbf{R}_{\parallel}, \alpha)$. Likewise, the wavevectors read $\mathbf{k} = (\mathbf{k}_{\parallel}, q)$. The multilayer Hamiltonian is similar to the bulk Hamiltonian except for one additional term which takes the charge distribution in the z direction into account:

$$H = H_0 + H_{cd} + H_{cf} + H_\phi. \quad (4.6)$$

The conduction band part of the Hamiltonian in the basis of parallel momentum eigenstates and localized Wannier states in the perpendicular direction $|\alpha, \mathbf{k}_{\parallel}, \sigma\rangle$ reads [45]

$$\begin{aligned} H_0 &= \sum_{\substack{\alpha\beta \\ \mathbf{k}_{\parallel}\mathbf{p}_{\parallel} \\ \sigma\sigma'}} \langle \mathbf{k}_{\parallel}, \alpha, \sigma | H_0 | \mathbf{p}_{\parallel}, \beta, \sigma' \rangle c_{\mathbf{k}_{\parallel}\alpha\sigma}^\dagger c_{\mathbf{p}_{\parallel}\beta\sigma'} \\ &= H_{\parallel} + H_{\perp}, \end{aligned} \quad (4.7)$$

where H_\perp is the part containing the interlayer summation ($\alpha \neq \beta$) and H_\parallel incorporates the intralayer ($\alpha = \beta$) summation. The latter reads

$$\begin{aligned}
H_\parallel &= \sum_{\substack{\alpha \\ \mathbf{k}_\parallel \mathbf{p}_\parallel \\ \sigma \sigma'}} \underbrace{\langle \mathbf{k}_\parallel, \alpha, \sigma | H_0 | \mathbf{p}_\parallel, \alpha, \sigma' \rangle}_{\propto \delta_{\mathbf{k}_\parallel \mathbf{p}_\parallel} \delta_{\sigma \sigma'}} c_{\mathbf{k}_\parallel \alpha \sigma}^\dagger c_{\mathbf{p}_\parallel \alpha \sigma'} \\
&= \sum_{\alpha \mathbf{k}_\parallel \sigma} \underbrace{\langle \mathbf{k}_\parallel, \alpha, \sigma | H_0 | \mathbf{k}_\parallel, \alpha, \sigma \rangle}_{=:\varepsilon_{\mathbf{k}_\parallel}^\alpha} c_{\mathbf{k}_\parallel \alpha \sigma}^\dagger c_{\mathbf{k}_\parallel \alpha \sigma} \\
&= \sum_{\alpha \mathbf{k}_\parallel \sigma} \varepsilon_{\mathbf{k}_\parallel}^\alpha c_{\mathbf{k}_\parallel \alpha \sigma}^\dagger c_{\mathbf{k}_\parallel \alpha \sigma}, \tag{4.8}
\end{aligned}$$

where we have used the isotropy in the planes and the spin symmetry. The quantity $\varepsilon_{\mathbf{k}_\parallel}^\alpha$ denotes the dispersion of the conduction band electrons with parallel momentum \mathbf{k}_\parallel in layer α . We use the Fourier transform

$$|\mathbf{k}_\parallel, \alpha, \sigma\rangle = \frac{1}{\sqrt{N_\parallel}} \sum_i e^{-i\mathbf{k}_\parallel \mathbf{R}_{\parallel i}} |\mathbf{R}_{\parallel i}, \alpha, \sigma\rangle,$$

where N_\parallel is the number of lattice sites in each plane, to write down the perpendicular part of the conduction band Hamiltonian in real space:

$$\begin{aligned}
H_\perp &= \sum_{\substack{\alpha \neq \beta \\ \mathbf{k}_\parallel \mathbf{p}_\parallel \\ \sigma \sigma'}} \underbrace{\langle \mathbf{k}_\parallel, \alpha, \sigma | H_0 | \mathbf{p}_\parallel, \beta, \sigma' \rangle}_{\propto \delta_{\sigma \sigma'}} c_{\mathbf{k}_\parallel \alpha \sigma}^\dagger c_{\mathbf{p}_\parallel \beta \sigma'} \\
&= \sum_{\substack{\alpha \neq \beta \\ ij \\ \sigma}} \underbrace{\langle i, \alpha, \sigma | H_0 | j, \beta, \sigma \rangle}_{=:t_{\alpha\beta}^{ij}} \underbrace{\frac{1}{\sqrt{N_\parallel}} \sum_{\mathbf{k}_\parallel} e^{i\mathbf{k}_\parallel \mathbf{R}_{\parallel i}} c_{\mathbf{k}_\parallel \alpha \sigma}^\dagger}_{c_{i\alpha\sigma}^\dagger} \underbrace{\frac{1}{\sqrt{N_\parallel}} \sum_{\mathbf{p}_\parallel} e^{-i\mathbf{p}_\parallel \mathbf{R}_{\parallel j}} c_{\mathbf{p}_\parallel \beta \sigma}}_{c_{j\beta\sigma}} \\
&= \sum_{\substack{\alpha \neq \beta \\ ij \\ \sigma}} t_{\alpha\beta}^{ij} c_{i\alpha\sigma}^\dagger c_{j\beta\sigma}.
\end{aligned}$$

Here, $t_{\alpha\beta}^{ij}$ is the hopping matrix element from lattice site $(\mathbf{R}_{\parallel j}, \beta)$ to $(\mathbf{R}_{\parallel i}, \alpha)$. In nearest neighbor tight-binding approximation it reduces to

$$t_{\alpha\beta}^{ij} = \begin{cases} t_{\alpha\beta}^{ii} =: t_{\alpha\beta} & i = j \text{ and } \beta = \alpha \pm 1 \\ 0 & \text{else} \end{cases}.$$

If we use the symmetry $t_{\alpha\beta} = t_{\beta\alpha}$ and the notation $t_{\alpha\alpha-1} =: t_\alpha$ for the hopping from layer $\alpha - 1$ to layer α , we obtain

$$H_\perp = \sum_{\alpha i \sigma} \left(t_\alpha c_{i\alpha\sigma}^\dagger c_{i\alpha-1\sigma} + t_{\alpha+1} c_{i\alpha\sigma}^\dagger c_{i\alpha+1\sigma} \right). \tag{4.9}$$

4. Model

Note that as long as we are considering a single material, the interlayer hopping will not depend on the layer index and we have $t_\alpha =: t$.

The electrostatic potential at the perpendicular position α , φ_α , is determined by the charge density ρ_α over the Poisson equation

$$\frac{1}{\tilde{a}^2} \frac{\partial^2}{\partial \alpha^2} \varphi_\alpha = -\frac{\rho_\alpha}{\varepsilon_0},$$

where $\tilde{a} = a/2$ is the interlayer distance. The energy of an electron exposed to the electrostatic potential φ_α is given by $\phi_\alpha = -e\varphi_\alpha$. If we further express the charge density ρ_α by the charge carrier distribution Δn_α by $\rho_\alpha = -e \frac{\Delta n_\alpha}{\mathcal{V}}$, the Poisson equation reads

$$\frac{\partial^2}{\partial \alpha^2} \phi_\alpha = -\frac{e^2}{\varepsilon_0 a} \Delta n_\alpha, \quad (4.10)$$

where we have used that the FCC unit cell is given by $\mathcal{V} = a^3/4$. We assume that the electrostatic energy is not strong enough to affect the population of the valence band. Thus, it will only affect the conduction and impurity electrons and the corresponding contribution to the Hamiltonian reads

$$H_\phi = \sum_{i\alpha\sigma} \phi_\alpha c_{i\alpha\sigma}^\dagger c_{i\alpha\sigma} + \sum_{\{i\alpha\}\sigma} \phi_\alpha d_{i\alpha\sigma}^\dagger d_{i\alpha\sigma}. \quad (4.11)$$

The impurity and Heisenberg part of the Hamiltonian are equal to the bulk Hamiltonian parts. Written in the new basis, they read

$$H_{cd} = E_d \sum_{\{i\alpha\},\sigma} d_{i\alpha\sigma}^\dagger d_{i\alpha\sigma} + V \sum_{\{i\alpha\}} (c_{i\alpha\sigma}^\dagger d_{i\alpha\sigma} + d_{i\alpha\sigma}^\dagger c_{i\alpha\sigma}) + U \sum_{\{i\alpha\}} d_{i\alpha\uparrow}^\dagger d_{i\alpha\uparrow} d_{i\alpha\downarrow}^\dagger d_{i\alpha\downarrow}, \quad (4.12)$$

and

$$H_{cf} = - \sum_{\substack{ij \\ \alpha\beta}} J_{ij}^{\alpha\beta} \mathbf{S}_{i\alpha} \mathbf{S}_{j\beta} - J_{cf} \sum_i \boldsymbol{\sigma}_{i\alpha} \mathbf{S}_{i\alpha}. \quad (4.13)$$

Finally, the two dimensional bare density of states is chosen to be

$$N_\parallel(\varepsilon) = \begin{cases} \frac{1}{2D_\parallel} & \text{for } |\Delta_0 - \varepsilon| \leq D_\parallel \\ 0 & \text{else} \end{cases}, \quad (4.14)$$

where the half band width D_\parallel is chosen such that the half bandwidth of a non-interaction system of infinitely many layers would be D_0 . Similar to the tight binding model, we impose the relation of the half band width to the hopping matrix element to be $D_0 = 6t$ in the three dimensional case, and $D_\parallel = 4t$ in the two dimensional case. With this, we obtain $D_\parallel = \frac{2}{3}D_0$.

5. Theory

In this chapter, we develop a self-consistent theory for the solution of the bulk and the multilayer model, (4.1) and (4.6). As mentioned before, this theory includes the work of Arnold and Kroha [25] as the special case of bulk $\text{Eu}_{1-x}\text{Gd}_x\text{O}$ with nearest neighbor spin coupling. Again, we include this special case in our derivations below.

The self-consistent theory is formulated by diagrammatic Green's function techniques. A central part of the theory is the conduction band Green's function, whose calculation is non-trivial in the multilayer case. Hence, we begin with a detailed description on how this calculation is performed in the first section of this chapter. In the second section, for both the Gadolinium and the Oxygen case, we calculate the impurity contribution to the conduction band self-energy which stems from (4.3) and (4.12), respectively. The solution of the Heisenberg lattice ((4.4) and (4.13)) in mean field theory and its contribution to the conduction band self-energy is discussed in the third section. Afterwards, in the fourth section, the self-consistent theory is summarized and we discuss its numerical solution. The chapter is concluded by the derivation of transport properties in the fifth section.

5.1. Conduction band Green's function

In the following we discuss the calculation of the conduction band Green's function, first for the bulk case and then for the multilayer case. We assume that the interaction and therefore also the self-energy is local.

5.1.1. Bulk conduction band Green's function

We begin with the retarded Green's function for a conduction band electron with momentum \mathbf{k}

$$G_{c\sigma}^R(\mathbf{k}, t - t') = i\Theta(t - t')\langle\{c_{\mathbf{k}\sigma}(t), c_{\mathbf{k}\sigma}^\dagger(t')\}\rangle.$$

Since we want to apply diagrammatic techniques at finite temperatures, we take the time ordered Green's function, Fourier transform to frequency space and perform an analytic continuation

$$G_{c\sigma}(\mathbf{k}, z) = \frac{1}{z - \varepsilon_{\mathbf{k}} + \mu - \Sigma_{c\sigma}(z)}. \quad (5.1)$$

Note that we assumed the self-energy to be local, i.e. there is no momentum dependence. In section 5.2, 5.3 and 5.4 this assumption will be justified. The corresponding diagrammatic Dyson equation reads

$$\text{Diagram 1} = \text{Diagram 2} + \text{Diagram 3} \quad (5.2)$$

5. Theory

Real space conduction band Green's function

For the self-consistent theory, we need the real space conduction band Green's function. Due to translational invariance, the propagator between two positions \mathbf{r}' and \mathbf{r}'' depends only on the distance $\mathbf{r} = \mathbf{r}'' - \mathbf{r}'$ between the positions and we have

$$G_{c\sigma}(\mathbf{r}, z) = G_{c\sigma}(\mathbf{r}'', \mathbf{r}', z) = \frac{1}{N} \sum_{\mathbf{k}} e^{i\mathbf{k}\mathbf{r}} G_{c\sigma}(\mathbf{k}, z), \quad (5.3)$$

implying for the local Green's function ($\mathbf{r} = 0$)

$$G_{c\sigma}(z) = \frac{1}{N} \sum_{\mathbf{k}} G_{c\sigma}(\mathbf{k}, z). \quad (5.4)$$

Here, we assumed a finite crystal with N lattice sites. The momentum and frequency dependent Green's function $G_{c\sigma}(\mathbf{k}, z)$ is given by (5.1). Since it depends on \mathbf{k} only indirectly via the dispersion, i. e. $G_{c\sigma}(\mathbf{k}, z) = G_{c\sigma}(\varepsilon_{\mathbf{k}}, z)$, our goal is to convert the wavenumber summation into an energy integral. Due to the isotropy of the system we assume an isotropic dispersion

$$\varepsilon_{\mathbf{k}} = \varepsilon_{|\mathbf{k}|} = \varepsilon_k,$$

and go to the continuum limit

$$\frac{1}{N} \sum_{\mathbf{k}} \xrightarrow{\text{continuum}} \frac{\mathcal{V}}{(2\pi)^3} \int d^3k \xrightarrow{\text{isotropy}} \frac{\mathcal{V}}{(2\pi)^3} \int_0^{2\pi} d\phi \int_0^\pi d\theta \sin\theta \int_0^{k_{max}} dk k^2.$$

Here we have chosen the integral limits such, that the upper and lower band edges are reproduced, $\varepsilon_{k=0} = \Delta - D_0$ and $\varepsilon_{k_{max}} = \Delta + D_0$. The assumption of an isotropic dispersion is justified due to the sole use of local quantities in our theory and the usage of a model density of states. The non-local Green's function now reads

$$\begin{aligned} G_{c\sigma}(\mathbf{r}, z) &= \frac{\mathcal{V}}{(2\pi)^3} \int_0^{2\pi} d\phi \int_0^{k_{max}} dk k^2 \underbrace{\int_0^\pi d\theta \sin\theta e^{ikr \cos\theta}}_{\frac{2 \sin(kr)}{kr}} G_{c\sigma}(\varepsilon_k, z) \\ &= \frac{\mathcal{V}}{2\pi^2 r} \int_0^{k_{max}} dk k \sin(kr) G_{c\sigma}(\varepsilon_k, z), \end{aligned} \quad (5.5)$$

and for the local Green's function ($\mathbf{r} = 0$) we have

$$G_{c\sigma}(z) = \frac{\mathcal{V}}{2\pi^2} \int_0^{k_{max}} dk k^2 G_{c\sigma}(\varepsilon_k, z). \quad (5.6)$$

In order to convert the wavenumber integral into an energy integral we need to know the dispersion ε_k and its inverse mapping corresponding to the bare density of states

(4.5). To this end, we consider the definition of the density of states as an integral over equipotential surfaces and make use of the isotropy of the dispersion

$$\begin{aligned} N(\varepsilon) &= \frac{\mathcal{V}}{(2\pi)^3} \int d\mathbf{S} \frac{d\mathbf{k}}{d\varepsilon} \\ &= \frac{4\pi k^2 \mathcal{V}}{(2\pi)^3} \frac{dk}{d\varepsilon}. \end{aligned}$$

Hence, the dispersion reads

$$\frac{d\varepsilon}{dk} = \frac{\mathcal{V}k^2}{2\pi^2 N(\varepsilon)}. \quad (5.7)$$

In order to obtain the inverse mapping of the dispersion, we separate the variables and integrate both sides of the above equation from the lower band edge to an energy inside the band

$$\int_{\Delta_0 - D_0}^{\varepsilon'} d\varepsilon N(\varepsilon) = \frac{4\pi k^2 \mathcal{V}}{(2\pi)^3} \int_{k(\Delta_0 - D_0)}^{k(\varepsilon')} dk k^2 = \frac{\mathcal{V}}{6\pi^2} k(\varepsilon')^3,$$

where we have chosen $k(\Delta_0 - D_0) = 0$ in the second step. We insert (4.5), evaluate the integral [46] and solve for k :

$$\begin{aligned} k(\varepsilon') &= \left[\frac{6\pi^2}{\mathcal{V}} \left\{ \int_{\Delta_0 - D_0}^{\varepsilon'} d\varepsilon N(\varepsilon) \right\} \right]^{\frac{1}{3}} \\ &= \underbrace{\left[12\pi^2(\varepsilon' - \Delta_0)N(\varepsilon') + 24\pi \arcsin\left(\frac{\varepsilon' - \Delta_0}{D_0}\right) + 12\pi^2 \right]^{\frac{1}{3}}}_{=: \tilde{k}(\varepsilon')} \frac{1}{a}. \end{aligned} \quad (5.8)$$

In (5.8), we have introduced the dimensionless wavenumber $\tilde{k}(\varepsilon')$ and used the fact that the volume of an FCC unit cell is $\mathcal{V} = a^3/4$. Finally, we can convert the wavenumber integrals in (5.5) and (5.6) using

$$\int dk = \int d\varepsilon \frac{2\pi^2 N(\varepsilon)}{\mathcal{V}k(\varepsilon)^2}$$

which yields for the non-local Green's function

$$G_{c\sigma}(\mathbf{r}, z) = \int d\varepsilon \frac{N(\varepsilon) \sin(\tilde{k}(\varepsilon)\tilde{r})}{\tilde{k}(\varepsilon)\tilde{r}} G_{c\sigma}(\varepsilon, z), \quad (5.9)$$

and for the local Green's function

$$G_{c\sigma}(z) = \int d\varepsilon N(\varepsilon) G_{c\sigma}(\varepsilon, z). \quad (5.10)$$

Here, we have introduced the dimensionless position as $r = \tilde{r}/a$.

5. Theory

Numerical evaluation

For the self-consistent theory we need the spectral density

$$A_{c\sigma}(\mathbf{r}, \omega) = \frac{1}{\pi} \text{Im} G_{c\sigma}(\mathbf{r}, \omega - i0^+),$$

where we have chosen the advanced Green's function in order to make the imaginary part of the self-energy positive. The real part $\text{Re} G_{c\sigma}(\mathbf{r}, \omega - i0^+)$ is then calculated via the Kramers-Kronig-relation (see appendix D) and we are left with the task of calculating

$$A_{c\sigma}(\mathbf{r}, \omega) = \int d\varepsilon \frac{N(\varepsilon) \sin(\tilde{k}(\varepsilon)\tilde{r})}{\tilde{k}(\varepsilon)\tilde{r}} A_{c\sigma}(\varepsilon, \omega), \quad (5.11)$$

and

$$A_{c\sigma}(\omega) = \int d\varepsilon N(\varepsilon) A_{c\sigma}(\varepsilon, \omega). \quad (5.12)$$

According to (5.1) the momentum dependent spectral density reads

$$A_{c\sigma}(\varepsilon, \omega) = \frac{1}{\pi} \frac{\text{Im} \Sigma_{c\sigma}(\omega - i0^+)}{[\omega - i0^+ - \varepsilon + \mu - \text{Re} \Sigma_{c\sigma}(\omega - i0^+)]^2 + [\text{Im} \Sigma_{c\sigma}(\omega - i0^+)]^2}. \quad (5.13)$$

For slowly varying self-energies, this is approximately a Lorentz curve. Its width is given by the imaginary part of the conduction band self-energy. If the latter becomes small, we are left with an extremely narrow peak in the integrand of 5.11 and 5.12. The peak's position is given by $\omega - \varepsilon + \mu - \text{Re} \Sigma_{c\sigma}(\omega - i0^+) \approx 0$. In order to evaluate such an integral, one needs to ensure a proper resolution of the peak. It is a frequently used method to introduce an artificial imaginary part of the self-energy η to ensure a minimum width of the resonances in the spectral density.

$$\text{Im} \Sigma_{c\sigma}(\omega - i0^+) \rightarrow \text{Im} \Sigma_{c\sigma}(\omega - i0^+) + \eta \quad (5.14)$$

It is obvious that this will lead to exponential tails in regions where the spectral density would vanish otherwise. In our theory, spectral weight near the Fermi edge can have a huge impact on the physical quantities of the system, such as the conductivity. Therefore it is desirable to reduce the artificial imaginary part of the self-energy as much as possible. This can be achieved by using an integration grid with a logarithmic cluster point at the peak's position, which is given by the above equation. As mentioned before, we developed a highly versatile integration grid library for this task [43]. See appendix E for details.

If η is chosen to vanish and the imaginary part becomes very small, i.e. comparable to machine precision, one has to take the limit of (5.13) for vanishing imaginary part of the self-energy. This yields

$$A_{c\sigma}(\varepsilon, \omega) = \delta(\omega - \varepsilon + \mu - \text{Re} \Sigma_{c\sigma}(\omega - i0^+)) \quad (5.15)$$

and the integrals (5.11) and (5.12) can be calculated analytically.

5.1.2. Multilayer conduction band Green's function

In this section, we will derive an expression for the conduction band Green's function in the case of the inhomogeneous system defined by (4.6). For this purpose, we will use the Potthoff-Nolting approach [45, 47, 48], which is the standard technique for layer DMFT [49–52]. Nevertheless, due to increased requirements on the accuracy, a refinement of this technique became necessary. In the following we present a new approach, specially suited for the very accurate numerical calculation of the multilayer conduction band Green's function.

In 1999, Potthoff and Nolting [45] developed a technique for describing strongly correlated layered structures. They used a basis of momentum eigenstates parallel to the layers and spatially localized states in the direction perpendicular to the layers (see section 4.2). We will follow this approach to derive the retarded conduction electron Green's function with spin σ and parallel momentum \mathbf{k}_{\parallel} propagating between layer α and β ,

$$G_{c\sigma}^{\alpha\beta,R}(\mathbf{k}_{\parallel}, t - t') = i\Theta(t - t') \langle \{c_{\mathbf{k}_{\parallel}\alpha\sigma}(t), c_{\mathbf{k}_{\parallel}\beta\sigma}^{\dagger}(t')\} \rangle.$$

In order to apply Wick's theorem and diagrammatic techniques we need the time order conduction electron Green's function in frequency space. By Fourier transforming and analytically continuing to imaginary frequencies z we obtain the quantity of interest, i.e.

$$G_{c\sigma}^{\alpha\beta}(\mathbf{k}_{\parallel}, z) = \langle \mathbf{k}_{\parallel}, \alpha, \sigma | \hat{G}_c(z) | \mathbf{k}_{\parallel}, \alpha, \sigma \rangle,$$

with the Green's function operator

$$\hat{G}_c(z) = \frac{1}{z - \hat{H}_0 - \hat{\Sigma}(z)}, \quad (5.16)$$

where \hat{H}_0 is given by (4.7) and the self-energy $\hat{\Sigma}(z)$ stems from the interaction terms in (4.6). We take the matrix element of (5.16) between two basis states and insert an identity operator

$$\begin{aligned} \delta_{\alpha\gamma} &= \langle \mathbf{k}_{\parallel}, \alpha, \sigma | (z - \hat{H}_0 - \hat{\Sigma}(z)) \hat{G}_c(z) | \mathbf{k}_{\parallel}, \gamma, \sigma \rangle \\ &= \sum_{\beta \mathbf{p}_{\parallel} \sigma'} \langle \mathbf{k}_{\parallel}, \alpha, \sigma | (z - \hat{H}_0 - \hat{\Sigma}(z)) | \mathbf{p}_{\parallel}, \beta, \sigma' \rangle \underbrace{\langle \mathbf{p}_{\parallel}, \beta, \sigma' | \hat{G}_c(z) | \mathbf{k}_{\parallel}, \gamma, \sigma \rangle}_{\delta_{\mathbf{k}_{\parallel} \mathbf{p}_{\parallel}} \delta_{\sigma\sigma'} G_{c\sigma}^{\beta\gamma}(\mathbf{k}_{\parallel}, z)}, \end{aligned} \quad (5.17)$$

where we have implied that all interactions preserve the parallel momentum and spin. Moreover, if we assume all interactions to be local, i.e.

$$\langle \mathbf{k}_{\parallel}, \alpha, \sigma | \hat{\Sigma}(z) | \mathbf{p}_{\parallel}, \beta, \sigma' \rangle = \delta_{\alpha\beta} \delta_{\mathbf{k}_{\parallel} \mathbf{p}_{\parallel}} \delta_{\sigma\sigma'} \Sigma_{c\sigma}^{\alpha}(z), \quad (5.18)$$

the only remaining non-local contribution stems from the free Hamiltonian

$$\begin{aligned} \langle \mathbf{k}_{\parallel}, \alpha, \sigma | (z - \hat{H}_0) | \mathbf{p}_{\parallel}, \beta, \sigma' \rangle &= \delta_{\mathbf{k}_{\parallel} \mathbf{p}_{\parallel}} \delta_{\sigma\sigma'} \{ (z - \varepsilon_{\mathbf{k}_{\parallel}}^{\alpha} + \mu) \delta_{\alpha\beta} \\ &\quad + t_{\alpha} \delta_{\alpha\beta+1} + t_{\alpha+1} \delta_{\alpha\beta-1} \}, \end{aligned}$$

5. Theory

and equation (5.17) becomes

$$\sum_{\beta} \underbrace{\left[(z - \varepsilon_{\mathbf{k}_{\parallel}}^{\alpha} + \mu - \Sigma_{c\sigma}^{\alpha}(z)) \delta_{\alpha\beta} + t_{\alpha} \delta_{\alpha\beta+1} + t_{\alpha+1} \delta_{\alpha\beta-1} \right]}_{(G^{-1})_{c\sigma}^{\alpha\beta}(\mathbf{k}_{\parallel}, z)} G_{c\sigma}^{\beta\gamma}(\mathbf{k}_{\parallel}, z) = \delta_{\alpha\gamma}.$$

We have identified the expression for the inverse Green's function matrix in the layer indices as

$$\hat{G}_{c\sigma}^{-1}(\mathbf{k}_{\parallel}, z) = \begin{pmatrix} z - \varepsilon_{\mathbf{k}_{\parallel}}^1 + \mu - \Sigma_{c\sigma}^1(z) & -t_2 & 0 & \cdots \\ -t_2 & z - \varepsilon_{\mathbf{k}_{\parallel}}^2 + \mu - \Sigma_{c\sigma}^2(z) & -t_3 & \cdots \\ 0 & -t_3 & z - \varepsilon_{\mathbf{k}_{\parallel}}^3 + \mu - \Sigma_{c\sigma}^3(z) & \cdots \\ \vdots & \vdots & \ddots & \ddots \end{pmatrix}. \quad (5.19)$$

In order to obtain the Green's function itself, we need to invert this matrix. We introduce the following shorthand notation for the diagonal elements of (5.19)

$$d_{\alpha} := z - \varepsilon_{\mathbf{k}_{\parallel}}^{\alpha} + \mu - \Sigma_{c\sigma}^{\alpha}(z).$$

According to [53] the lower triangular matrix elements of the inverse of this tridiagonal symmetric matrix, $G_{c\sigma}^{\alpha\beta}(\mathbf{k}_{\parallel}, z)$, read

$$G_{c\sigma}^{\alpha\beta}(\mathbf{k}_{\parallel}, z) = \begin{cases} (-1)^{\alpha+\beta} t_{\beta+1} t_{\beta+2} \cdots t_{\alpha} \frac{\Theta_{\beta-1} \Phi_{\alpha+1}}{\Theta_N} & \text{for } \alpha > \beta \\ \frac{\Theta_{\alpha-1} \Phi_{\alpha+1}}{\Theta_N} & \text{for } \alpha = \beta \end{cases}. \quad (5.20)$$

where the Θ_{α} and Φ_{α} with $\alpha \in (1, \dots, N)$ are the minors of (5.19) and the following recursion relations hold:

$$\begin{aligned} \Theta_{\alpha} &= d_{\alpha} \Theta_{\alpha-1} - t_{\alpha}^2 \Theta_{\alpha-2} \\ \Theta_{-1} &= 0, \quad \Theta_0 = 1 \end{aligned}$$

and

$$\begin{aligned} \Phi_{\alpha} &= d_{\alpha} \Phi_{\alpha+1} - t_{\alpha+1}^2 \Phi_{\alpha+2} \\ \Phi_{N+1} &= 1, \quad \Phi_{N+2} = 0. \end{aligned}$$

Due to symmetry reasons, the upper triangular matrix elements are given by

$$G_{c\sigma}^{\beta\alpha}(\mathbf{k}_{\parallel}, z) = G_{c\sigma}^{\alpha\beta}(\mathbf{k}_{\parallel}, z), \quad \alpha > \beta. \quad (5.21)$$

In the case of mirror symmetric systems, one can simplify the above equations to some extent. This is part of appendix C. Note that with this technique, the inversion of the matrix is an operation of order N . Finally we can write down the diagrammatic Dyson equation in terms of the local self-energy. It reads

$$\overleftrightarrow{\alpha} \xrightarrow{z, \mathbf{k}_{\parallel}, \sigma} \overleftrightarrow{\beta} = \overleftrightarrow{\alpha} \xrightarrow{z, \mathbf{k}_{\parallel}, \sigma} \overleftrightarrow{\beta} + \overleftrightarrow{\alpha} \xrightarrow{z, \mathbf{k}_{\parallel}, \sigma} \text{bubble} \xrightarrow{z, \mathbf{k}_{\parallel}, \sigma} \overleftrightarrow{\beta} \quad (5.22)$$

γ

Real space conduction band Green's function

Due to the isotropy in the parallel direction, the conduction band propagator between two positions $\mathbf{r}' = (\mathbf{r}'_{\parallel}, \beta)$ and $\mathbf{r}'' = (\mathbf{r}''_{\parallel}, \alpha)$ depends only on the difference $\mathbf{r}_{\parallel} = \mathbf{r}''_{\parallel} - \mathbf{r}'_{\parallel}$ and reads

$$G_{c\sigma}^{\alpha\beta}(\mathbf{r}_{\parallel}, z) = G_{c\sigma}^{\alpha\beta}(\mathbf{r}''_{\parallel}, \mathbf{r}'_{\parallel}, z) = \frac{1}{N_{\parallel}} \sum_{\mathbf{k}_{\parallel}} e^{i\mathbf{k}_{\parallel}\mathbf{r}_{\parallel}} G_{c\sigma}^{\alpha\beta}(\mathbf{k}_{\parallel}, z). \quad (5.23)$$

Here, we have assumed a finite (100) FCC monolayer with N_{\parallel} lattice sites. For the diagonal elements, we introduce the shorthand notation $G_{c\sigma}^{\alpha}(\mathbf{r}_{\parallel}, z) = G_{c\sigma}^{\alpha\alpha}(\mathbf{r}_{\parallel}, z)$. In the following we will call this function the *parallel* Green's function. In contrast to that, for $\mathbf{r}_{\parallel} = 0$ we have

$$G_{c\sigma}^{\alpha\beta}(z) = \frac{1}{N_{\parallel}} \sum_{\mathbf{k}_{\parallel}} G_{c\sigma}^{\alpha\beta}(\mathbf{k}_{\parallel}, z), \quad (5.24)$$

which will be called *perpendicular* Green's function in the following. Note that (5.24) also includes the local Green's function in layer α , $G_{c\sigma}^{\alpha}(z) = G_{c\sigma}^{\alpha\alpha}(z)$. According to equation (5.19), the conduction band Green's functions depends on \mathbf{k}_{\parallel} only indirectly via the parallel dispersions in all layers, $G_{c\sigma}^{\alpha\beta}(\mathbf{k}_{\parallel}, z) = G_{c\sigma}^{\alpha\beta}(\varepsilon_{\mathbf{k}_{\parallel}}^1, \varepsilon_{\mathbf{k}_{\parallel}}^2, \dots; z)$. Therefore our goal is to convert the summation over wavenumbers into an energy integral. Due to the isotropy of the system in the parallel direction we assume

$$\varepsilon_{\mathbf{k}_{\parallel}}^{\alpha} = \varepsilon_{|\mathbf{k}_{\parallel}|}^{\alpha} = \varepsilon_k^{\alpha} \quad \forall \alpha,$$

and take the continuum limit

$$\frac{1}{N_{\parallel}} \sum_{\mathbf{k}_{\parallel}} \xrightarrow{\text{continuum}} \frac{\mathcal{V}_{2D}}{(2\pi)^2} \int d^2k \xrightarrow{\text{isotropy}} \frac{\mathcal{V}_{2D}}{(2\pi)^2} \int_0^{2\pi} d\phi \int_0^{k_{max}} dk k.$$

With this, we can write the parallel Green's function as

$$\begin{aligned} G_{c\sigma}^{\alpha\beta}(\mathbf{r}_{\parallel}, z) &= \frac{\mathcal{V}_{2D}}{(2\pi)^2} \int_0^{k_{max}} dk k \underbrace{\int_0^{2\pi} d\phi e^{ikr \cos \phi}}_{2\pi J_0(kr)} G_{c\sigma}^{\alpha\beta}(\varepsilon_k^1, \varepsilon_k^2, \dots; z) \\ &= \frac{\mathcal{V}_{2D}}{(2\pi)} \int_0^{k_{max}} dk k J_0(kr) G_{c\sigma}^{\alpha\beta}(\varepsilon_k^1, \varepsilon_k^2, \dots; z), \end{aligned} \quad (5.25)$$

and the perpendicular Green's function reads

$$G_{c\sigma}^{\alpha\beta}(z) = \frac{\mathcal{V}_{2D}}{2\pi} \int_0^{k_{max}} dk k G_{c\sigma}^{\alpha\beta}(\varepsilon_k^1, \varepsilon_k^2, \dots; z). \quad (5.26)$$

In equation (5.25), J_0 denotes the Bessel function of first kind and order zero. We are now able to perform the mentioned wavenumber integral substitution. Without loss of generality, we can choose the dispersion in an arbitrary layer with index β , $\nu = \varepsilon_{\mathbf{k}_{\parallel}}^{\beta}$ as an integration variable. This is feasible, since the dispersion of all other layers ε_k^{α} depend on

5. Theory

ν indirectly over the inverse mapping $k(\nu)$. The bare density of states in the first layer is given by

$$\begin{aligned} N_{\parallel}^{\beta}(\varepsilon) &= \frac{\mathcal{V}_{2D}}{(2\pi)^2} \int d\mathbf{S}_{\parallel} \frac{d\mathbf{k}_{\parallel}}{d\nu} \\ &= \frac{\mathcal{V}_{2D} k}{(2\pi)} \frac{dk}{d\nu}. \end{aligned}$$

Hence the dispersion reads

$$\frac{d\nu}{dk} = \frac{\mathcal{V}_{2D} k}{2\pi N_{\parallel}^{\beta}(\nu)}. \quad (5.27)$$

Similar to the bulk case, we separate the variables and integrate both sides of (5.27) from the lower band edge to an energy inside the band

$$\int_{\Delta_0^{\beta} - D_{\parallel}^{\beta}}^{\nu'} d\nu N_{\parallel}^1(\nu) = \frac{\mathcal{V}_{2D} k^2}{4\pi}.$$

By inserting (4.14) we obtain

$$\nu(k) = \varepsilon_k^{\beta} = \frac{\mathcal{V}_{2D} D_{\parallel}^{\beta}}{2\pi} k^2 + \Delta_0^{\beta} - D_{\parallel}^{\beta}, \quad (5.28)$$

and the inverse mapping reads

$$k(\nu) = \underbrace{\sqrt{\frac{4\pi}{D_{\parallel}^{\beta}}(\nu - \Delta_0^{\beta} + D_{\parallel}^{\beta})}}_{=: \tilde{k}(\nu)} \frac{1}{a}. \quad (5.29)$$

Here, we have introduced the dimensionless wavenumber $\tilde{k}(\nu)$. In addition, we have used that the unit cell volume of a (100) monolayer of Europium monoxide is given by $\mathcal{V}_{2D} = a^2/2$, where a is the lattice parameter of the bulk FCC lattice. Note, that by combining (5.28) and (5.29) the parallel dispersions in all layers can now be written as functions of ν by

$$\varepsilon^{\alpha}(\nu) = \varepsilon^{\alpha}(k(\nu)) = \frac{D_{\parallel}^{\alpha}}{D_{\parallel}^{\beta}} \nu - \Delta_0^{\beta} + \Delta_0^{\alpha} + D_{\parallel}^{\beta} - D_{\parallel}^{\alpha}. \quad (5.30)$$

Now we can substitute the wavenumber integral in (5.25) and (5.26) by

$$\int dk = \int d\nu \frac{2\pi N_{\parallel}^{\beta}(\nu)}{\mathcal{V}_{2D} k(\nu)}$$

and obtain for the parallel Green's function

$$G_{c\sigma}^{\alpha\beta}(\mathbf{r}_{\parallel}, z) = \int d\nu N_{\parallel}^{\beta}(\nu) J_0(\tilde{k}(\nu)\tilde{r}) G_{c\sigma}^{\alpha\beta}(\varepsilon^1(\nu), \varepsilon^2(\nu), \dots; z), \quad (5.31)$$

and for the perpendicular Green's function

$$G_{c\sigma}^{\alpha\beta}(z) = \int d\nu N_{\parallel}^{\beta}(\nu) G_{c\sigma}^{\alpha\beta}(\varepsilon^1(\nu), \varepsilon^2(\nu), \dots; z). \quad (5.32)$$

Again, we made use of the dimensionless position $\tilde{r} = ra$ here.

Numerical evaluation

In comparison to the bulk case, the numerical evaluation of (5.31) and (5.32) turns out to be much more difficult. It is advantageous to use the following shorthand notation for the momentum dependent Green's function:

$$G_{c\sigma}^{\alpha\beta}(\nu, z) \equiv G_{c\sigma}^{\alpha\beta}(\varepsilon^1(\nu), \varepsilon^2(\nu), \dots; z). \quad (5.33)$$

Moreover, we choose $\nu = \varepsilon_{\mathbf{k}\parallel}^1$ as an integration variable to obtain for the parallel conduction band spectral density

$$A_{c\sigma}^{\alpha\beta}(\mathbf{r}_{\parallel}, \omega) = \int d\nu N_{\parallel}(\nu) J_0(\tilde{k}(\nu)\tilde{r}) A_{c\sigma}^{\alpha\beta}(\nu, \omega), \quad (5.34)$$

and for the perpendicular conduction band spectral density

$$A_{c\sigma}^{\alpha\beta}(\omega) = \int d\nu N_{\parallel}(\nu) A_{c\sigma}^{\alpha\beta}(\nu, \omega). \quad (5.35)$$

where we have used the shorthand notation $N_{\parallel}(\nu) = N_{\parallel}^1(\nu)$ and due to equations (5.19) and (5.20) the momentum dependent spectral density is given by

$$\begin{aligned} A_{c\sigma}^{\alpha\beta}(\nu, \omega) &= \frac{1}{\pi} \text{Im} G_{c\sigma}^{\alpha\beta}(\nu, \omega - i0^+) \\ &= \frac{1}{\pi} \begin{cases} (-1)^{\alpha+\beta} t_{\beta+1} t_{\beta+2} \cdots t_{\alpha} \text{Im} \frac{\Theta_{\beta-1}(\nu, \omega - i0^+) \Phi_{\alpha+1}(\nu, \omega - i0^+)}{\Theta_N(\nu, \omega - i0^+)} & \text{for } \alpha > \beta \\ \text{Im} \frac{\Theta_{\alpha-1}(\nu, \omega - i0^+) \Phi_{\alpha+1}(\nu, \omega - i0^+)}{\Theta_N(\nu, \omega - i0^+)} & \text{for } \alpha = \beta \end{cases}. \end{aligned}$$

In order to evaluate the integrals in (5.34) and (5.35), it is necessary to investigate the poles in the ν dependence of the spectral density $A_{c\sigma}^{\alpha\beta}(\nu, \omega)$. In the following, we will skip the ω dependence of the minors for better readability and introduce the *polefunction* P as

$$P_{\alpha\beta}(\nu) := \frac{\Theta_N(\nu)}{\Theta_{\beta-1}(\nu) \Phi_{\alpha+1}(\nu)}.$$

The spectral density can then be written as

$$A_{c\sigma}^{\alpha\beta}(\nu, \omega) \propto \text{Im} \frac{1}{P_{\alpha\beta}(\nu)} = \frac{-\text{Im} P_{\alpha\beta}(\nu)}{[\text{Re} P_{\alpha\beta}(\nu)]^2 + [\text{Im} P_{\alpha\beta}(\nu)]^2}. \quad (5.36)$$

In general, $A_{c\sigma}^{\alpha\beta}(\nu, \omega)$ will be comprised of N Lorentz peaks at the positions of the poles (see figure 5.1). Their width is determined by the imaginary parts of the self-energies $\Sigma_{c\sigma}^{\alpha}(\omega - i0^+)$. In contrast to the bulk case, there is no analytical formula connecting the $\Sigma_{c\sigma}^{\alpha}(\omega - i0^+)$ and the width of the individual peaks. In order to ensure a minimum width of the peaks one has to introduce a very small additional artificial imaginary part η in the self-energy,

$$\Sigma_{c\sigma}^{\alpha}(\omega - i0^+) \rightarrow \Sigma_{c\sigma}^{\alpha}(\omega - i0^+) + \eta. \quad (5.37)$$

5. Theory

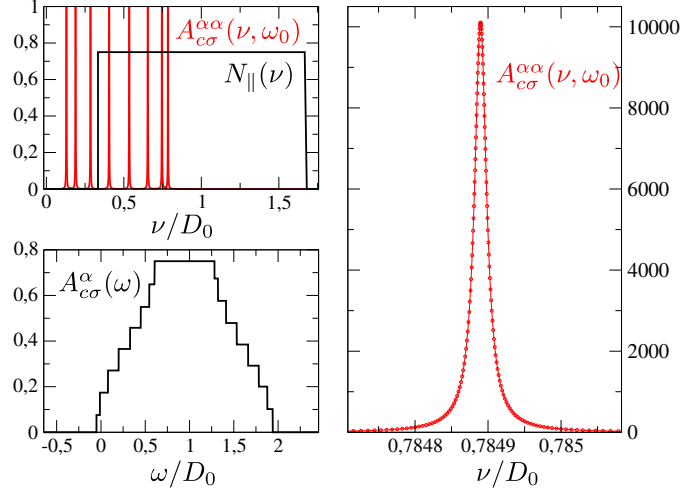


Figure 5.1.: Calculation of the local conduction band spectral density in the case of 15 mirror symmetric non-interacting layers with $\eta = 10^{-5}$, a temperature of $T = 20K$ and a band filling of $x = 0.01$. $A_{c\sigma}^{\alpha\alpha}(\nu, \omega)$ is evaluated at a fixed $\omega_0 = 0.4D_0$ and we chose the middle layer $\alpha = 7$. Due to the mirror symmetry, there are 8 distinct resonances of width η which are properly resolved by our integration grid. The steps in the resulting local spectral density (bottom left) originate in the “sudden” overlap of the peaks with the bare density of states $N_{\parallel}(\nu)$ when ω changes.

To resolve all peaks in the integrand of (5.34) and (5.35), we use our integration grid library [43] which allows for an arbitrary number of logarithmically dense grid regions that can even intersect each other (see appendix E). With this, it is possible to calculate with an accuracy that is limited only by the size of η and the machine precision, respectively.

Due to equation (5.36) the position of the poles are given by the roots of the real part of the polefunction. If the imaginary parts of the self-energies are small, the real part of the polefunction is approximately given by

$$\text{Re}P_{\alpha\beta}(\nu) = \text{Re} \frac{\Theta_N(\nu)}{\Theta_{\beta-1}(\nu)\Phi_{\alpha+1}(\nu)} \stackrel{\text{Im}\Sigma \ll 1}{\approx} \frac{\text{Re}\Theta_N(\nu)}{\text{Re}\Theta_{\beta-1}(\nu)\text{Re}\Phi_{\alpha+1}(\nu)}. \quad (5.38)$$

Therefore, the necessary condition for the roots of the polefunction reads

$$\text{Re}\Theta_N(\nu) \stackrel{!}{=} 0. \quad (5.39)$$

and a sufficient condition is given by

$$\text{Re}P_{\alpha\beta}(\nu) \stackrel{!}{=} 0. \quad (5.40)$$

Note that since $\Theta_N(\nu)$ does not depend on the layer indices, the necessary condition applies for the roots of all polefunctions, $P_{\alpha\beta}(\nu)$, $\forall \alpha, \beta$. Therefore one has to solve (5.39)

only once and check if equation (5.40) holds afterwards only at the position where (5.39) is fulfilled. If the imaginary part is not small, we can still use (5.39) to find the position of the poles. Due to the increased width of the peaks, a small translation of the center of the logarithmically dense integration grid region will not affect the resolution of the peaks.

In the non-interacting limit,

$$\Sigma_{c\sigma}^{\alpha}(\omega - i0^+) = i0^+, \quad \forall \alpha,$$

the imaginary part of the polefunction will also vanish, $\text{Im}P_{\alpha\beta}(\nu) = 0^+$ and the approximation in equation (5.38) becomes exact. In this limit, the spectral density (5.36) reduces to a sum of delta functions

$$A_{c\sigma}^{\alpha\beta}(\nu, \omega) \propto \text{Im} \frac{1}{P_{\alpha\beta}(\nu)} = \pi \sum_i \delta(\nu - \nu_i) \frac{1}{\left| \frac{\partial}{\partial \nu} \text{Re}P_{\alpha\beta}(\nu) \right|_{\nu=\nu_i}}, \quad (5.41)$$

where the $\{\nu_i\}$ are the roots of $\text{Re}P_{\alpha\beta}(\nu)$ which are determined by the equations (5.38), (5.39) and (5.40).

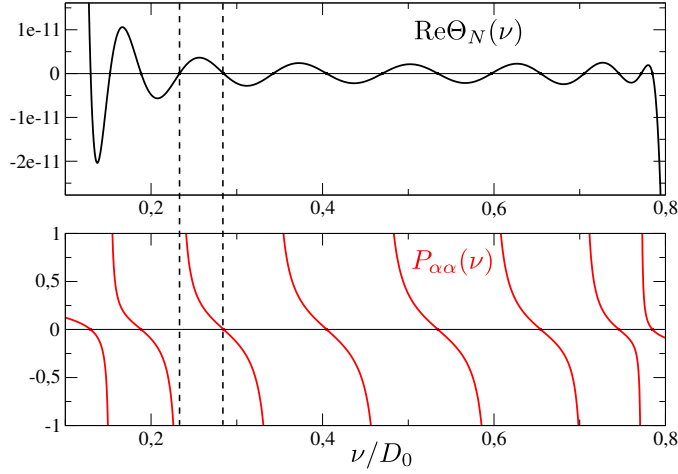


Figure 5.2.: Necessary and sufficient condition for the roots of the polefunction for a system of 15 mirror symmetric non-interacting layers with $\eta = 10^{-5}$, a temperature of $T = 20K$ and a band filling of $x = 0.01$. The functions are evaluated at a fixed $\omega = 0.4D_0$ and we chose the middle layer $\alpha = 7$.

In the following we will discuss the details of the root-finding algorithm. The minor $\Theta_N(\nu)$ is the determinant of the $N \times N$ inverse Green's function matrix (5.19). Therefore it is a polynomial of N th order and therewith it possesses N roots. The polefunction itself is a rational function (see figure 5.2). We found that both, the minimal distance between local maxima and local minima scales with $\Delta\Theta_{\min}$ as well as the minimal distance between two neighboring poles $\Delta\nu_{\min}$ scale with

$$\Delta\Theta_{\min} \sim \Delta\nu_{\min} \sim \prod_{\alpha=2}^N t_{\alpha}.$$

5. Theory

With $t = 0.01D_0$, $\Delta\nu_{\min}$ can fall below machine precision at system sizes around $N = 17$. Beyond this threshold, we use the multiple precision library MPFR [54] to compute with arbitrary precision floating point numbers. The price one has to pay for this is a significant increase in the computation time.

The root-finding algorithm starts at some position far below the first root. Then the algorithm scans the functions for sign changes in the function itself or its derivative while increasing ν stepwise. Once a sign change in the function occurs, the intermediate root is found by the bisection method. If a sign change in the derivative is detected, the intermediate extremum is determined by the golden section method. Afterwards the algorithm checks if the extremum has crossed the ν -axis. If this is the case, there must be two additional roots in between, which are found via the bisection method. If not, the algorithm proceeds by searching for sign changes in the function. This is repeated until the whole region is scanned and all N roots are found. The success of the procedure is ensured by our method even in case of extremely small distances between neighboring roots. With this, we achieve high precision and reliability. In the non-interacting case the method is extremely fast due to the absence of numerical integration.

5.2. Impurities

In this section we will discuss the interaction of conduction and impurity electrons described by the Hamiltonians (4.4) and (4.13), respectively. In particular, we will derive their contribution to the conduction electron self-energy in (5.1) and (5.19). The first part will treat the problem of randomly distributed impurities. Here, we will find that the contribution to the conduction electron self-energy is given by the impurity Green's function. Afterwards, we will show how to calculate the impurity Green's function in the case of Oxygen vacancies as well as for Gadolinium impurities.

5.2.1. Dilute impurities

In the following, we will solve the problem of dilute impurities in an Europium monoxide crystal. We follow [55] and [25] for the bulk case and extend these results to the multilayer case in the second part of this section. We begin by considering a system with a fixed but random distribution of N_i impurities throughout the crystal. In this case the translational symmetry is broken, and according to (4.3) and (4.12) the full conduction electron Green's function reads

$$\begin{aligned}
 G_{c\sigma}(\mathbf{r}_b, \mathbf{r}_a, z) &= \overleftarrow{\overleftarrow{\mathbf{r}_b}}^{\overleftarrow{\mathbf{r}_a}} \overleftarrow{\overleftarrow{\mathbf{r}_a}}^{\overleftarrow{\mathbf{r}_b}} \overleftarrow{\overleftarrow{\mathbf{r}_a}}^{\overleftarrow{\mathbf{r}_b}} \\
 &= \overleftarrow{\overleftarrow{\mathbf{r}_b}}^{\overleftarrow{\mathbf{r}_a}} + \overleftarrow{\overleftarrow{\mathbf{r}_b}}^{\overleftarrow{\mathbf{r}_a}} \overleftarrow{\overleftarrow{\mathbf{r}_a}}^{\overleftarrow{\mathbf{r}_b}} \overleftarrow{\overleftarrow{\mathbf{r}_a}}^{\overleftarrow{\mathbf{r}_b}} \overleftarrow{\overleftarrow{\mathbf{r}_a}}^{\overleftarrow{\mathbf{r}_b}} \overleftarrow{\overleftarrow{\mathbf{r}_a}}^{\overleftarrow{\mathbf{r}_b}} + \dots \\
 &= G_{c\sigma}^0(\mathbf{r}_b, \mathbf{r}_a, z) + \sum_{n=1}^{\infty} G_{c\sigma}^{(n)}(\mathbf{r}_b, \mathbf{r}_a, z). \tag{5.42}
 \end{aligned}$$

Here, a dashed impurity line correspond to a dressed propagator which incorporates the on-site Coulomb interaction U but not the hybridization V (cf. (4.3) and (4.12)). Throughout this section however, we will denote them as bare propagators $G_{c\sigma}^0$ and postpone the treatment of the Coulomb interaction to section 5.2.2.

Bulk case

In contrast to the bare conduction electron Green's function, (5.42) does not depend on the position difference due to the absence of isotropy in the system. The n -th term of the perturbative series is given by

$$\begin{aligned}
 G_{c\sigma}^{(n)}(\mathbf{r}_b, \mathbf{r}_a, z) &= \sum_{j_1, \dots, j_n}^{N_i} G_{c\sigma}^0(\mathbf{r}_b - \mathbf{r}_{j_n}, z) V^2 G_{d\sigma}^{j_n, 0}(z) G_{c\sigma}^0(\mathbf{r}_{j_n} - \mathbf{r}_{j_{n-1}}, z) \cdot \dots \\
 &\quad \dots V^2 G_{d\sigma}^{j_1, 0}(z) G_{c\sigma}^0(\mathbf{r}_{j_1} - \mathbf{r}_a, z) \\
 &= \frac{1}{N^2} \sum_{\mathbf{k}_b \mathbf{k}_a} e^{i\mathbf{k}_b \mathbf{r}_b - i\mathbf{k}_a \mathbf{r}_a} \left\{ \sum_{j_1, \dots, j_n}^{N_i} \frac{1}{N^{n-1}} \sum_{\mathbf{k}_1 \dots \mathbf{k}_{n-1}} G_{c\sigma}^0(\mathbf{k}_b, z) V^2 G_{d\sigma}^{j_n, 0}(z) \right. \\
 &\quad \cdot G_{c\sigma}^0(\mathbf{k}_{n-1}, z) \cdot \dots \cdot G_{c\sigma}^0(\mathbf{k}_1, z) \\
 &\quad \cdot \underbrace{V^2 G_{d\sigma}^{j_1, 0}(z) G_{c\sigma}^0(\mathbf{k}_a, z) e^{-i[(\mathbf{k}_b - \mathbf{k}_{n-1})\mathbf{r}_{j_n} + \dots + (\mathbf{k}_1 - \mathbf{k}_a)\mathbf{r}_{j_1}]} }_{G_{c\sigma}^{(n)}(\mathbf{k}_b, \mathbf{k}_a, z)} \left. \right\}, \tag{5.43}
 \end{aligned}$$

where we have denoted the impurity Green's function at site \mathbf{r}_{j_l} by $G_{d\sigma}^{j_l, 0}(z)$ and inserted the Fourier transforms $G_{c\sigma}^0(\mathbf{r}, z) = \frac{1}{N} \sum_{\mathbf{k}} e^{i\mathbf{k}\mathbf{r}} G_{c\sigma}^0(\mathbf{k}, z)$ for the bare conduction electron Green's functions. Since it is neither desirable nor feasible to determine the position of all impurities we will consider the average over all possible distributions of impurity positions over the lattice sites, the so called *configurational average* [55]. In this process, the impurity concentration $n_i = N_i/N$, with N being the number of lattice sites, is held constant. The n -th term of the full conduction electron Green's function then becomes

$$G_{c\sigma}^{(n)}(\mathbf{r}_b, \mathbf{r}_a, z) \rightarrow \langle G_{c\sigma}^{(n)}(\mathbf{r}_b, \mathbf{r}_a, z) \rangle_{\text{imp}} = \frac{1}{N^n} \sum_{j_1=1}^N \dots \sum_{j_n=1}^N G_{c\sigma}^{(n)}(\mathbf{r}_b, \mathbf{r}_a, z).$$

By the averaging over all possible configurations, translational symmetry is restored and the impurity Green's function becomes position independent:

$$G_{d\sigma}^{j_l, 0}(z) = G_{d\sigma}^0(z).$$

In addition, we have

$$\langle G_{c\sigma}(\mathbf{r}_b, \mathbf{r}_a, z) \rangle_{\text{imp}} = G_{c\sigma}(\mathbf{r}_b - \mathbf{r}_a, z) = \frac{1}{N} \sum_{\mathbf{k}} e^{i\mathbf{k}(\mathbf{r}_b - \mathbf{r}_a)} G_{c\sigma}(\mathbf{k}, z), \tag{5.44}$$

5. Theory

where we have identified the configuration-averaged conduction electron Green's function with the translationally invariant Green's function (5.3) of section 5.1.1. The n -th order term of this Green's function is given by

$$\begin{aligned}
G_{c\sigma}^{(n)}(\mathbf{r}_b - \mathbf{r}_a, z) &= \langle G_{c\sigma}^{(n)}(\mathbf{r}_b, \mathbf{r}_a, z) \rangle_{\text{imp}} \\
&= \frac{1}{N^n} \sum_{j_1=1}^N \cdots \sum_{j_n=1}^N \sum_{j_1, \dots, j_n}^{N_i} G_{c\sigma}^0(\mathbf{r}_b - \mathbf{r}_a - \mathbf{r}_{j_n}, z) V^2 G_{d\sigma}^0(z) \\
&\quad \cdot G_{c\sigma}^0(\mathbf{r}_{j_n} - \mathbf{r}_{j_{n-1}}, z) \cdot \dots \cdot V^2 G_{d\sigma}^0(z) G_{c\sigma}^0(\mathbf{r}_{j_1} - 0, z) \\
&= \frac{1}{N} \sum_{\mathbf{k}} e^{i\mathbf{k}(\mathbf{r}_b - \mathbf{r}_a)} \left\{ \sum_{j_1=1}^N \cdots \sum_{j_n=1}^N \sum_{j_1, \dots, j_n}^{N_i} \frac{1}{N^{2n}} \sum_{\mathbf{k}_1 \cdots \mathbf{k}_n} G_{c\sigma}^0(\mathbf{k}, z) \right. \\
&\quad \cdot V^2 G_{d\sigma}^0(z) G_{c\sigma}^0(\mathbf{k}_n, z) \cdot \dots \cdot V^2 G_{d\sigma}^0(z) \\
&\quad \cdot G_{c\sigma}^0(\mathbf{k}_1, z) e^{-i[(\mathbf{k} - \mathbf{k}_n)\mathbf{r}_{j_n} + \dots + (\mathbf{k}_2 - \mathbf{k}_1)\mathbf{r}_{j_1}]} \left. \right\}. \quad (5.45)
\end{aligned}$$

$\underbrace{\hspace{15em}}_{G_{c\sigma}^{(n)}(\mathbf{k}, z)}$

For further investigation of the momentum dependent conduction electron Green's function, we pull all Green's functions out of the summation over lattice sites and introduce the momentum differences $\mathbf{q}_i := \mathbf{k}_{i+1} - \mathbf{k}_i$ with $\mathbf{q}_n := \mathbf{k} - \mathbf{k}_n$. This yields

$$\begin{aligned}
G_{c\sigma}^{(n)}(\mathbf{k}, z) &= \frac{1}{N^n} \sum_{\mathbf{k}_1 \cdots \mathbf{k}_n} G_{c\sigma}^0(\mathbf{k}, z) V^2 G_{d\sigma}^0(z) G_{c\sigma}^0(\mathbf{k}_n, z) \cdot \dots \cdot V^2 G_{d\sigma}^0(z) G_{c\sigma}^0(\mathbf{k}_1, z) \\
&\quad \cdot \underbrace{\frac{1}{N^n} \sum_{j_1=1}^N \cdots \sum_{j_n=1}^N \sum_{j_1, \dots, j_n}^{N_i} e^{-i[\mathbf{q}_n \mathbf{r}_{j_n} + \dots + \mathbf{q}_1 \mathbf{r}_{j_1}]} }_{=: X(\mathbf{q}_1, \dots, \mathbf{q}_n)}. \quad (5.46)
\end{aligned}$$

Here, we have defined the function $X(\mathbf{q}_1, \dots, \mathbf{q}_n)$, which contains all the spatial information about the random scattering. We proceed by ordering this quantity by the number of impurities which are involved. The first term corresponds to a process where an electron is scattered n times at the same impurity, i.e. $j_1 = j_2 = \dots = j_n = h_1$. The second

term describes the scattering at two different impurities, and so on.

$$\begin{aligned}
X(\mathbf{q}_1, \dots, \mathbf{q}_n) &= \frac{1}{N} \sum_{h_1=1}^N \sum_{h_1}^{N_i} e^{-i(\sum_{j_1 \in Q} \mathbf{q}_{j_1}) \mathbf{r}_{h_1}} \\
&\quad + \sum_{Q_1 \cup Q_2} \left(\frac{1}{N} \sum_{h_1=1}^N \sum_{h_1}^{N_i} e^{-i(\sum_{j_1 \in Q_1} \mathbf{q}_{j_1}) \mathbf{r}_{h_1}} \right) \left(\frac{1}{N} \sum_{h_2=1}^N \sum_{h_2}^{N_i} e^{-i(\sum_{j_2 \in Q_2} \mathbf{q}_{j_2}) \mathbf{r}_{h_2}} \right) \\
&\quad + \dots \\
&= N_i \delta_{\mathbf{0}, \sum_{j_1 \in Q} \mathbf{q}_{j_1}} + \sum_{Q_1 \cup Q_2} N_i \delta_{\mathbf{0}, \sum_{j_1 \in Q_1} \mathbf{q}_{j_1}} N_i \delta_{\mathbf{0}, \sum_{j_2 \in Q_2} \mathbf{q}_{j_2}} + \dots \\
&= \sum_{p=1}^n \left(\sum_{Q_1 \cup Q_2 \cup \dots \cup Q_p = Q} \prod_{h=1}^p \delta_{\mathbf{0}, \sum_{j_h \in Q_h} \mathbf{q}_{j_h}} N_i \right).
\end{aligned}$$

Here, we have introduced $Q = (\mathbf{q}_1, \dots, \mathbf{q}_n)$, which is the set of all momentum vectors and $Q_1 \cup Q_2 \cup \dots \cup Q_p = Q$ denotes the union of all possible p disjoint and non-empty subsets of Q . By inserting this into (5.46) we obtain for the $n = 1$ contribution to the momentum dependent conduction electron Green's function

$$\begin{aligned}
G_{c\sigma}^{(1)}(\mathbf{k}, z) &= \frac{1}{N} \sum_{\mathbf{k}_1} G_{c\sigma}^0(\mathbf{k}, z) V^2 G_{d\sigma}^0(z) G_{c\sigma}^0(\mathbf{k}_1, z) \delta_{\mathbf{0}, \mathbf{k} - \mathbf{k}_1} N_i \\
&= n_i G_{c\sigma}^0(\mathbf{k}, z) V^2 G_{d\sigma}^0(z) G_{c\sigma}^0(\mathbf{k}, z) \\
&= \begin{array}{c} \times \\ | \\ \text{---} \bullet \text{---} \\ | \\ \mathbf{k} \quad \mathbf{k} \end{array},
\end{aligned}$$

and for the $n = 2$ contribution

$$\begin{aligned}
G_{c\sigma}^{(2)}(\mathbf{k}, z) &= \frac{1}{N^2} \sum_{\mathbf{k}_1 \mathbf{k}_2} G_{c\sigma}^0(\mathbf{k}, z) V^2 G_{d\sigma}^0(z) G_{c\sigma}^0(\mathbf{k}_2, z) V^2 G_{d\sigma}^0(z) G_{c\sigma}^0(\mathbf{k}_1, z) \\
&\quad \cdot \left(\delta_{\mathbf{0}, \mathbf{k} - \mathbf{k}_2 + \mathbf{k}_2 - \mathbf{k}_1} N_i + \delta_{\mathbf{0}, \mathbf{k} - \mathbf{k}_2} N_i \delta_{\mathbf{0}, \mathbf{k}_2 - \mathbf{k}_1} N_i \right) \\
&= n_i G_{c\sigma}^0(\mathbf{k}, z) V^2 G_{d\sigma}^0(z) \left(\frac{1}{N} \sum_{\mathbf{k}_2} G_{c\sigma}^0(\mathbf{k}_2, z) \right) V^2 G_{d\sigma}^0(z) G_{c\sigma}^0(\mathbf{k}, z) \\
&\quad + n_i^2 G_{c\sigma}^0(\mathbf{k}, z) V^2 G_{d\sigma}^0(z) G_{c\sigma}^0(\mathbf{k}, z) V^2 G_{d\sigma}^0(z) G_{c\sigma}^0(\mathbf{k}, z) \\
&= \begin{array}{c} \times \\ \diagup \quad \diagdown \\ \text{---} \bullet \text{---} \bullet \text{---} \\ | \quad | \\ \mathbf{k} \quad \mathbf{k}_2 \quad \mathbf{k} \end{array} + \begin{array}{c} \times \quad \times \\ | \quad | \\ \text{---} \bullet \text{---} \bullet \text{---} \\ | \quad | \\ \mathbf{k} \quad \mathbf{k} \quad \mathbf{k} \end{array}.
\end{aligned}$$

With this, we can identify the following Feynman rules:

5. Theory

1. The fermion lines $\overleftarrow{\text{---}}$ denote the bare conduction electron Green's function $G_{c\sigma}^0(\mathbf{k}, z)$.
2. The impurity lines $-\cdot-\cdot-\cdot$ denote the bare impurity scattering $V^2 G_{d\sigma}^0(z)$.
3. The scattering vertices are given by \times and correspond to $n_i \delta_{\mathbf{0}, \sum_{j_h \in Q_h} \mathbf{q}_{j_h}}$, where momentum conservation at each vertex is imposed.
4. All internal momenta are summed over: $\frac{1}{N} \sum_{\mathbf{k}}$.

Since the impurity concentration is assumed to be small, it is reasonable to order the diagrams in powers of n_i . Hence, the full conduction electron Green's function reads

$$\begin{aligned}
 G_{c\sigma}(\mathbf{k}, z) &= \overleftarrow{\text{---}}_{\mathbf{k}} \\
 &= \overleftarrow{\text{---}}_{\mathbf{k}} + \overleftarrow{\text{---}}_{\mathbf{k}} \cdot \overleftarrow{\text{---}}_{\mathbf{k}} + \dots \\
 &+ \overleftarrow{\text{---}}_{\mathbf{k}} \cdot \overleftarrow{\text{---}}_{\mathbf{k}_1} \cdot \overleftarrow{\text{---}}_{\mathbf{k}} \cdot \overleftarrow{\text{---}}_{\mathbf{k}_2} \cdot \overleftarrow{\text{---}}_{\mathbf{k}} + \dots \quad (5.47)
 \end{aligned}$$

The last two diagrams in (5.47) are both of second order in the impurity concentration n_i . Due to the single internal sum in the crossed diagram, the phase space is reduced in comparison with the non-crossed diagram. Therefore, we will neglect such diagrams. This approximation is called the single-site-T-matrix approximation [55] and is justified as long as n_i is small. With this, the conduction electron self energy reads

$$\begin{aligned}
 \Sigma_{c\sigma}(z) &= \begin{array}{c} \times \\ | \\ \bullet \end{array} + \begin{array}{c} \times \\ / \quad \backslash \\ \bullet \quad \bullet \\ | \quad | \\ \mathbf{k}_1 \end{array} + \begin{array}{c} \times \\ / \quad \backslash \\ \bullet \quad \bullet \\ | \quad | \\ \mathbf{k}_1 \quad \mathbf{k}_2 \end{array} + \dots \\
 &= n_i V^2 (G_{d\sigma}^0(z) + G_{d\sigma}^0(z) V^2 G_{c\sigma}^0(z) G_{d\sigma}^0(z) + \dots) \\
 &= n_i V^2 \left(\underbrace{\overleftarrow{\text{---}}_{\mathbf{d}} + \overleftarrow{\text{---}}_{\mathbf{d}} \cdot \overleftarrow{\text{---}}_{\mathbf{c}} \cdot \overleftarrow{\text{---}}_{\mathbf{d}} + \dots}_{= \overleftarrow{\text{---}}_{\mathbf{d}} =} \right) \\
 &= n_i V^2 G_{d\sigma}(z), \quad (5.48)
 \end{aligned}$$

Note that within the single-site-T-matrix approximation the conduction electron self energy becomes momentum independent and therefore local (cf. equation (5.1)).

Multilayer case

The starting point for the derivation of the dilute impurity contribution to the conduction electron self-energy in the multilayer case is again the system with a fixed, random

distribution of impurities in the crystal. We Fourier transform the corresponding conduction electron Green's function (5.42) only in the parallel direction. The n -th term of the perturbative series (5.43) then reads

$$\begin{aligned}
G_{c\sigma}^{(n)}(\mathbf{r}_b, \mathbf{r}_a, z) &= G_{c\sigma}^{\beta\alpha, (n)}(\mathbf{r}_{\parallel b}, \mathbf{r}_{\parallel a}, z) \\
&= \sum_{j_1, \dots, j_n}^{N_i} G_{c\sigma}^{\beta\alpha_{j_n}, 0}(\mathbf{r}_{\parallel b} - \mathbf{r}_{\parallel j_n}, z) V^2 G_{d\sigma}^{\alpha_{j_n}, 0}(\mathbf{r}_{\parallel j_n}, z) \cdot \dots \\
&\quad \cdot G_{c\sigma}^{\alpha_{j_2} \alpha_{j_1}, 0}(\mathbf{r}_{\parallel j_2} - \mathbf{r}_{\parallel j_1}, z) V^2 G_{d\sigma}^{\alpha_{j_1}, 0}(\mathbf{r}_{\parallel j_1}, z) G_{c\sigma}^{\alpha_{j_1} \alpha, 0}(\mathbf{r}_{\parallel j_1} - \mathbf{r}_{\parallel a}, z) \\
&= \frac{1}{N_{\parallel}^2} \sum_{\mathbf{k}_{\parallel b} \mathbf{k}_{\parallel a}} e^{i\mathbf{k}_{\parallel b} \mathbf{r}_{\parallel b} - i\mathbf{k}_{\parallel a} \mathbf{r}_{\parallel a}} \\
&\quad \cdot \left\{ \sum_{j_1, \dots, j_n}^{N_i} \frac{1}{N_{\parallel}^{n-1}} \sum_{\mathbf{k}_{\parallel 1} \dots \mathbf{k}_{\parallel n-1}} G_{c\sigma}^{\beta\alpha_{j_n}, 0}(\mathbf{k}_{\parallel b}, z) V^2 G_{d\sigma}^{\alpha_{j_n}, 0}(\mathbf{r}_{\parallel j_n}, z) \right. \\
&\quad \cdot G_{c\sigma}^{\alpha_{j_n} \alpha_{j_{n-1}}, 0}(\mathbf{k}_{\parallel n-1}, z) \cdot \dots \cdot G_{c\sigma}^{\alpha_2 \alpha_1, 0}(\mathbf{k}_{\parallel 1}, z) V^2 G_{d\sigma}^{\alpha_{j_1}, 0}(\mathbf{r}_{\parallel j_1}, z) \\
&\quad \cdot G_{c\sigma}^{\alpha_{j_1} \alpha, 0}(\mathbf{k}_{\parallel a}, z) e^{-i[(\mathbf{k}_{\parallel b} - \mathbf{k}_{\parallel n-1})\mathbf{r}_{\parallel j_n} + \dots + (\mathbf{k}_{\parallel 1} - \mathbf{k}_{\parallel a})\mathbf{r}_{\parallel j_1}]} \left. \right\}, \\
&\quad \underbrace{\hspace{15em}}_{G_{c\sigma}^{\beta, \alpha, (n)}(\mathbf{k}_{\parallel b}, \mathbf{k}_{\parallel a}, z)}
\end{aligned} \tag{5.49}$$

where we have denoted the impurity Green's function at site $\mathbf{r}_{j_l} = (\mathbf{r}_{\parallel j_l}, \alpha_{j_l})$ by $G_{d\sigma}^{\alpha_{j_l}, 0}(\mathbf{r}_{\parallel j_l}, z)$ and inserted the Fourier transform $G_{c\sigma}^{\alpha\beta, 0}(\mathbf{r}_{\parallel}, z) = \frac{1}{N_{\parallel}} \sum_{\mathbf{k}_{\parallel}} e^{i\mathbf{k}_{\parallel} \mathbf{r}_{\parallel}} G_{c\sigma}^{\alpha\beta, 0}(\mathbf{k}_{\parallel}, z)$ for the bare conduction electron Green's functions.

Again, we define the configurational average by summing over all possible realizations of impurity positions. However, in contrast to the bulk case, the impurity Green's function should differ from layer to layer. Hence, the translational symmetry is restored in the parallel direction only. We write for the n -th term of the full conduction electron Green's function

$$G_{c\sigma}^{\beta\alpha, (n)}(\mathbf{r}_{\parallel b}, \mathbf{r}_{\parallel a}, z) \rightarrow \langle G_{c\sigma}^{\beta\alpha, (n)}(\mathbf{r}_{\parallel b}, \mathbf{r}_{\parallel a}, z) \rangle_{\text{imp}} = \frac{1}{N_n} \sum_{j_1}^N \dots \sum_{j_n}^N G_{c\sigma}^{\beta\alpha, (n)}(\mathbf{r}_{\parallel b}, \mathbf{r}_{\parallel a}, z).$$

At the same time, we require that the impurity Green's function is still layer dependent after the configurational average

$$G_{d\sigma}^{\alpha_{j_l}, 0}(\mathbf{r}_{\parallel j_l}, z) = G_{d\sigma}^{\alpha_{j_l}, 0}(z),$$

and the full conduction electron Green's function becomes translationally invariant in the parallel direction

$$\langle G_{c\sigma}^{\beta\alpha}(\mathbf{r}_{\parallel b}, \mathbf{r}_{\parallel a}, z) \rangle_{\text{imp}} = G_{c\sigma}^{\beta\alpha}(\mathbf{r}_{\parallel b} - \mathbf{r}_{\parallel a}, z) = \frac{1}{N_{\parallel}} \sum_{\mathbf{k}_{\parallel}} e^{i\mathbf{k}_{\parallel}(\mathbf{r}_{\parallel b} - \mathbf{r}_{\parallel a})} G_{c\sigma}^{\beta\alpha}(\mathbf{k}_{\parallel}, z). \tag{5.50}$$

5. Theory

Now we can identify the Green's function of (5.50) with the multilayer Green's function of equation (5.23) and (5.24), respectively. We utilize the translational invariance to obtain the Fourier transform of the n -th order term of the conduction electron Green's function

$$\begin{aligned}
G_{c\sigma}^{\beta\alpha,(n)}(\mathbf{r}_{\parallel b} - \mathbf{r}_{\parallel a}, z) &= \langle G_{c\sigma}^{\beta\alpha,(n)}(\mathbf{r}_{\parallel b}, \mathbf{r}_{\parallel a}, z) \rangle_{\text{imp}} \\
&= \frac{1}{N^n} \sum_{j_1}^N \cdots \sum_{j_n}^N \sum_{j_1 \cdots j_n}^{N_i} \\
&\quad \cdot \left\{ G_{c\sigma}^{\beta\alpha_{j_n},0}(\mathbf{r}_{\parallel b} - \mathbf{r}_{\parallel a} - \mathbf{r}_{\parallel j_n}, z) V^2 G_{d\sigma}^{\alpha_{j_n},0}(z) \cdots \right. \\
&\quad \cdot G_{c\sigma}^{\alpha_{j_2}\alpha_{j_1},0}(\mathbf{r}_{\parallel j_2} - \mathbf{r}_{\parallel j_1}, z) V^2 G_{d\sigma}^{\alpha_{j_1},0}(z) G_{c\sigma}^{\alpha_{j_1},\alpha,0}(\mathbf{r}_{\parallel j_1} - \mathbf{0}_{\parallel}, z) \left. \right\} \\
&= \frac{1}{N_{\parallel}} \sum_{\mathbf{k}_{\parallel}} e^{i\mathbf{k}_{\parallel}(\mathbf{r}_{\parallel b} - \mathbf{r}_{\parallel a})} \\
&\quad \cdot \left\{ \frac{1}{N^n} \sum_{j_1}^N \cdots \sum_{j_n}^N \sum_{j_1 \cdots j_n}^{N_i} \frac{1}{N_{\parallel}^n} \sum_{\mathbf{k}_{\parallel 1} \cdots \mathbf{k}_{\parallel n}} \right. \\
&\quad \cdot G_{c\sigma}^{\beta\alpha_{j_n},0}(\mathbf{k}_{\parallel}, z) V^2 G_{d\sigma}^{\alpha_{j_n},0}(z) \cdots \\
&\quad \cdot G_{c\sigma}^{\alpha_{j_2}\alpha_{j_1},0}(\mathbf{k}_{\parallel 2}, z) V^2 G_{d\sigma}^{\alpha_{j_1},0}(z) G_{c\sigma}^{\alpha_{j_1},\alpha,0}(\mathbf{k}_{\parallel 1}, z) \\
&\quad \cdot \underbrace{e^{-i[(\mathbf{k}_{\parallel} - \mathbf{k}_{\parallel n})\mathbf{r}_{\parallel j_n} + \cdots + (\mathbf{k}_{\parallel 2} - \mathbf{k}_{\parallel 1})\mathbf{r}_{\parallel j_1}]}]}_{G_{c\sigma}^{\beta,\alpha,(n)}(\mathbf{k}_{\parallel}, z)} \left. \right\}. \quad (5.51)
\end{aligned}$$

Before we proceed with the investigation of the momentum dependent Green's function, we split up the sum over the fixed, random configurations into a parallel and perpendicular contribution as follows:

$$\begin{aligned}
\sum_{j_l}^{N_i} f(\mathbf{r}_{j_l}) &= \sum'_{\mathbf{r}_{\parallel j_l}} \sum'_{\alpha_{j_l}} f(\mathbf{r}_{\parallel j_l}, \alpha_{j_l}) \\
&= \sum'_{\mathbf{r}_{\parallel j_l}} \sum'_{\alpha_{j_l}} g(\mathbf{r}_{\parallel j_l}) h(\alpha_{j_l}) \\
&= \sum_{\gamma} h(\gamma) \sum'_{\mathbf{r}_{\parallel j_l}} \sum'_{\alpha_{j_l}} g(\mathbf{r}_{\parallel j_l}) \delta_{\gamma\alpha_{j_l}} \\
&= \sum_{\gamma} h(\gamma) \sum_{j_l}^{N_i} g(\mathbf{r}_{\parallel j_l}) \delta_{\gamma\alpha_{j_l}}, \quad (5.52)
\end{aligned}$$

where we have introduced the primed sum to indicate the summation of the fixed configuration of N_i impurities and assumed that the function f can be factorized as $f(\mathbf{r}_{\parallel j_l}, \alpha_{j_l}) = g(\mathbf{r}_{\parallel j_l}) h(\alpha_{j_l})$.

Similar to the bulk case, we introduce the momentum differences $\mathbf{q}_{\parallel i} := \mathbf{k}_{\parallel i+1} - \mathbf{k}_{\parallel i}$ with $\mathbf{q}_{\parallel n} := \mathbf{k}_{\parallel} - \mathbf{k}_{\parallel n}$ and separate the summation over parallel positions from the one over perpendicular positions with the help of (5.52). With this, the parallel momentum dependent conduction electron Green's function (5.51) reads

$$\begin{aligned}
G_{c\sigma}^{\beta,\alpha,(n)}(\mathbf{k}_{\parallel}, z) = & \frac{1}{N_{\parallel}^n} \sum_{\mathbf{k}_{\parallel 1} \dots \mathbf{k}_{\parallel n}} \sum_{\gamma_1 \dots \gamma_n} \left\{ G_{c\sigma}^{\beta\gamma_n,0}(\mathbf{k}_{\parallel}, z) V^2 G_{d\sigma}^{\gamma_n,0}(z) \dots \right. \\
& \cdot G_{c\sigma}^{\gamma_2\gamma_1,0}(\mathbf{k}_{\parallel 2}, z) V^2 G_{d\sigma}^{\gamma_1,0}(z) G_{c\sigma}^{\gamma_1,\alpha,0}(\mathbf{k}_{\parallel 1}, z) \\
& \cdot \underbrace{\left[\frac{1}{N^n} \sum_{\alpha_{j_1} \dots \alpha_{j_n}} \sum_{\mathbf{r}_{\parallel j_1} \dots \mathbf{r}_{\parallel j_n}} \sum_{j_1, \dots, j_n}^{N_i} e^{-i \sum_{l=1}^n \mathbf{q}_{\parallel l} \mathbf{r}_{\parallel j_l}} \prod_{l=1}^n \delta_{\gamma_l \alpha_{j_l}} \right]}_{=: Y_{\mathbf{q}_{\parallel 1}, \dots, \mathbf{q}_{\parallel n}}^{\gamma_1, \dots, \gamma_n}} \left. \right\} \quad (5.53)
\end{aligned}$$

Here, we have defined the function $Y_{\mathbf{q}_{\parallel 1}, \dots, \mathbf{q}_{\parallel n}}^{\gamma_1, \dots, \gamma_n}$, which contains all spatial information about the random scattering. Analogously to the bulk case, we want to order this quantity by the number of impurities involved. To this end, we introduce the tuple of parallel momentum vector and perpendicular position $(\mathbf{q}_{\parallel}, \alpha)$. We collect several of these tuples in the set $Q = ((\mathbf{q}_{\parallel 1}, \alpha_1), \dots, (\mathbf{q}_{\parallel n}, \alpha_n))$ and the corresponding union of all possible p disjoint non-empty subsets of Q is given by $Q_1 \cup Q_2 \cup \dots \cup Q_p = Q$. We write

5. Theory

$$\begin{aligned}
Y_{\mathbf{q}_{\parallel 1}, \dots, \mathbf{q}_{\parallel n}}^{\gamma_1, \dots, \gamma_n} &= \frac{1}{N} \sum_{\alpha_{h_1}} \sum_{\mathbf{r}_{\parallel h_1}} \sum_{h_1}^{N_i} e^{-i(\sum_{j_1 \in Q} \mathbf{q}_{\parallel j_1}) \mathbf{r}_{\parallel h_1}} \prod_{i=1}^n \delta_{\gamma_i \alpha_{h_1}} \\
&+ \sum_{Q_1 \cup Q_2} \left(\sum_{h_1}^{N_i} \left[\frac{1}{N_{\parallel}} \sum_{\mathbf{r}_{\parallel h_1}} e^{-i(\sum_{j_1 \in Q_1} \mathbf{q}_{\parallel j_1}) \mathbf{r}_{\parallel h_1}} \right] \left[\frac{1}{N_{\perp}} \sum_{\alpha_{h_1}} \prod_{i_1 \in Q_1} \delta_{\gamma_{i_1} \alpha_{h_1}} \right] \right) \\
&\quad \cdot \left(\sum_{h_2}^{N_i} \left[\frac{1}{N_{\parallel}} \sum_{\mathbf{r}_{\parallel h_2}} e^{-i(\sum_{j_2 \in Q_2} \mathbf{q}_{\parallel j_2}) \mathbf{r}_{\parallel h_2}} \right] \left[\frac{1}{N_{\perp}} \sum_{\alpha_{h_2}} \prod_{i_2 \in Q_2} \delta_{\gamma_{i_2} \alpha_{h_2}} \right] \right) \\
&+ \dots \\
&= \frac{N_i}{N_{\perp}} \delta_{\mathbf{0}_{\parallel}, \sum_{j_1 \in Q_1} \mathbf{q}_{\parallel j_1}} \sum_{\alpha_{h_1}} \prod_{i=1}^n \delta_{\gamma_i \alpha_{h_1}} \\
&+ \sum_{Q_1 \cup Q_2} \left(\frac{N_i}{N_{\perp}} \delta_{\mathbf{0}_{\parallel}, \sum_{j_1 \in Q_1} \mathbf{q}_{\parallel j_1}} \sum_{\alpha_{h_1}} \prod_{i_1 \in Q_1} \delta_{\gamma_{i_1} \alpha_{h_1}} \right) \\
&\quad \cdot \left(\frac{N_i}{N_{\perp}} \delta_{\mathbf{0}_{\parallel}, \sum_{j_2 \in Q_2} \mathbf{q}_{\parallel j_2}} \sum_{\alpha_{h_2}} \prod_{i_2 \in Q_2} \delta_{\gamma_{i_2} \alpha_{h_2}} \right) \\
&+ \dots \\
&= \sum_{p=1}^n \left\{ \sum_{Q_1 \cup Q_2 \cup \dots \cup Q_p} \prod_{h=1}^p \left(\frac{N_i^p}{N_{\perp}^p} \delta_{\mathbf{0}_{\parallel}, \sum_{j_h \in Q_h} \mathbf{q}_{\parallel j_h}} \sum_{\alpha_{l_h}} \prod_{i_h} \delta_{\gamma_{i_h} \alpha_{l_h}} \right) \right\}, \quad (5.54)
\end{aligned}$$

where we have introduced the number of layers N_{\perp} , so that the total number of lattice sites is given by $N = N_{\perp} N_{\parallel}$. By inserting (5.54) into (5.51), we obtain for the $n = 1$ contribution to the parallel momentum dependent conduction electron Green's function

$$\begin{aligned}
G_{c\sigma}^{\beta\alpha, (1)}(\mathbf{k}_{\parallel}, z) &= \frac{N_i}{N_{\parallel} N_{\perp}} \sum_{\gamma} \sum_{\mathbf{k}_{\parallel 1}} G_{c\sigma}^{\beta\gamma, 0}(\mathbf{k}_{\parallel}, z) V^2 G_{d\sigma}^{\gamma, 0}(z) G_{c\sigma}^{\gamma, \alpha, 0}(\mathbf{k}_{\parallel 1}, z) \sum_{\alpha_{h_1}} \delta_{\mathbf{0}_{\parallel}, \mathbf{k}_{\parallel} - \mathbf{k}_{\parallel 1}} \delta_{\gamma \alpha_{h_1}} \\
&= n_i \sum_{\gamma} G_{c\sigma}^{\beta\gamma, 0}(\mathbf{k}_{\parallel}, z) V^2 G_{d\sigma}^{\gamma, 0}(z) G_{c\sigma}^{\gamma, \alpha, 0}(\mathbf{k}_{\parallel}, z) \\
&= \begin{array}{c} \gamma \\ \times \\ | \\ \beta \longleftarrow \bullet \longrightarrow \alpha \\ \mathbf{k}_{\parallel} \qquad \mathbf{k}_{\parallel} \end{array},
\end{aligned}$$

and the $n = 2$ contribution reads

$$\begin{aligned}
G_{c\sigma}^{\beta\alpha,(2)}(\mathbf{k}_{\parallel}, z) &= \frac{1}{N_{\parallel}^2} \sum_{\mathbf{k}_{\parallel 1} \mathbf{k}_{\parallel 2}} \sum_{\gamma \delta} G_{c\sigma}^{\beta\delta,0}(\mathbf{k}_{\parallel}, z) V^2 G_{d\sigma}^{\delta,0}(z) G_{c\sigma}^{\delta,\gamma,0}(\mathbf{k}_{\parallel 2}, z) V^2 G_{d\sigma}^{\gamma,0}(z) G_{c\sigma}^{\gamma,\alpha,0}(\mathbf{k}_{\parallel 1}, z) \\
&\quad \cdot \left\{ \frac{N_i}{N_{\perp}} \delta_{\mathbf{0}_{\parallel}, \mathbf{k}_{\parallel} - \mathbf{k}_{\parallel 2} + \mathbf{k}_{\parallel 2} - \mathbf{k}_{\parallel 1}} \sum_{\alpha_{h_1}} \delta_{\gamma \alpha_{h_1}} \delta_{\delta \alpha_{h_1}} \right. \\
&\quad \left. + \frac{N_i^2}{N_{\perp}^2} \delta_{\mathbf{0}_{\parallel}, \mathbf{k}_{\parallel} - \mathbf{k}_{\parallel 2}} \delta_{\mathbf{0}_{\parallel}, \mathbf{k}_{\parallel 2} - \mathbf{k}_{\parallel 1}} \sum_{\alpha_{h_1}} \delta_{\gamma \alpha_{h_1}} \sum_{\alpha_{h_2}} \delta_{\delta \alpha_{h_2}} \right\} \\
&= n_i \sum_{\gamma} G_{c\sigma}^{\beta\gamma,0}(\mathbf{k}_{\parallel}, z) V^2 G_{d\sigma}^{\gamma,0}(z) \left(\frac{1}{N_{\parallel}} \sum_{\mathbf{k}_{\parallel 2}} G_{c\sigma}^{\gamma\gamma,0}(\mathbf{k}_{\parallel}, z) \right) V^2 G_{d\sigma}^{\gamma,0}(z) G_{c\sigma}^{\gamma,\alpha,0}(\mathbf{k}_{\parallel}) \\
&\quad + n_i^2 \sum_{\gamma \delta} G_{c\sigma}^{\beta\delta,0}(\mathbf{k}_{\parallel}, z) V^2 G_{d\sigma}^{\delta,0}(z) G_{c\sigma}^{\delta,\gamma,0}(\mathbf{k}_{\parallel}, z) V^2 G_{d\sigma}^{\gamma,0}(z) G_{c\sigma}^{\gamma,\alpha,0}(\mathbf{k}_{\parallel}, z) \\
&= \text{Diagram 1} + \text{Diagram 2} .
\end{aligned}$$

The diagrams are Feynman diagrams representing the two terms in the final line. Diagram 1 shows a horizontal line with three vertices. The leftmost vertex is labeled β and the rightmost is labeled α . The middle vertex is connected to the leftmost by a solid line labeled \mathbf{k}_{\parallel} and to the rightmost by a solid line labeled \mathbf{k}_{\parallel} . A dashed line labeled γ connects the leftmost and middle vertices. Diagram 2 shows a horizontal line with three vertices. The leftmost vertex is labeled β and the rightmost is labeled α . The middle vertex is connected to the leftmost by a solid line labeled \mathbf{k}_{\parallel} and to the rightmost by a solid line labeled \mathbf{k}_{\parallel} . Two dashed lines, labeled δ and γ , connect the middle vertex to the leftmost and rightmost vertices respectively.

With this, we can identify the following Feynman rules:

1. The fermion lines $\beta \xleftarrow{\mathbf{k}_{\parallel}} \alpha$ denote the bare conduction electron Green's function from layer α to layer β , $G_{c\sigma}^{\beta\alpha,0}(\mathbf{k}_{\parallel}, z)$.
2. The impurity lines $\text{---} \alpha \text{---}$ denote the bare impurity scattering at layer α , $V^2 G_{d\sigma}^{\alpha,0}(z)$.
3. The scattering vertices are given by $\alpha \times$ and correspond to $n_i \delta_{\mathbf{0}_{\parallel}, \sum_{j_h \in Q_h} \mathbf{q}_{\parallel j_h}}$, where parallel momentum conservation at each vertex is imposed.
4. All internal parallel momenta are summed over: $\frac{1}{N_{\parallel}} \sum_{\mathbf{k}_{\parallel}}$.

Since the impurity concentration is again assumed to be small, we order the diagrams in

5. Theory

powers of n_i . Hence, the full conduction electron Green's function reads

$$\begin{aligned}
 G_{c\sigma}^{\beta\alpha}(\mathbf{k}_{\parallel}, z) &= \frac{\beta \xleftarrow{\alpha}}{\mathbf{k}_{\parallel}} \\
 &= \frac{\beta \xleftarrow{\alpha}}{\mathbf{k}_{\parallel}} + \frac{\beta \xleftarrow{\alpha}}{\mathbf{k}_{\parallel}} \frac{\gamma \times}{\bullet} \frac{\alpha \xleftarrow{\alpha}}{\mathbf{k}_{\parallel}} + \dots \\
 &+ \frac{\beta \xleftarrow{\alpha}}{\mathbf{k}_{\parallel}} \frac{\delta \times}{\bullet} \frac{\gamma \times}{\bullet} \frac{\alpha \xleftarrow{\alpha}}{\mathbf{k}_{\parallel}} + \frac{\beta \xleftarrow{\alpha}}{\mathbf{k}_{\parallel}} \frac{\delta \times}{\bullet} \frac{\gamma \times}{\bullet} \frac{\delta \times}{\bullet} \frac{\gamma \times}{\bullet} \frac{\alpha \xleftarrow{\alpha}}{\mathbf{k}_{\parallel}} + \dots, \quad (5.55)
 \end{aligned}$$

Similar to the bulk case, we apply the single-site-T-matrix approximation [55] and neglect crossed diagrams like the last one in (5.55) due to the reduced phase space in comparison to the non-crossed diagrams. In this approximation, the conduction electron self energy becomes independent of the parallel momentum and reads

$$\begin{aligned}
 \Sigma_{c\sigma}^{\alpha}(z) &= \frac{\alpha \times}{\bullet} + \frac{\alpha \times}{\bullet} \frac{\alpha \xleftarrow{\alpha}}{\mathbf{k}_{\parallel 1}} + \frac{\alpha \times}{\bullet} \frac{\alpha \xleftarrow{\alpha}}{\mathbf{k}_{\parallel 1}} \frac{\alpha \xleftarrow{\alpha}}{\mathbf{k}_{\parallel 2}} + \dots \\
 &= n_i V^2 (G_{d\sigma}^{\alpha,0}(z) + G_{d\sigma}^{\alpha,0}(z) V^2 G_{c\sigma}^{\alpha,0}(z) G_{d\sigma}^{\alpha,0}(z) + \dots) \\
 &= n_i V^2 \left(- \frac{\alpha \xleftarrow{\alpha}}{d} - + - \frac{\alpha \xleftarrow{\alpha}}{d} \frac{V}{c} \frac{\alpha \xleftarrow{\alpha}}{d} \frac{V}{c} \frac{\alpha \xleftarrow{\alpha}}{d} - + \dots \right) \\
 &\quad \underbrace{\hspace{10em}}_{= \frac{\alpha \xleftarrow{\alpha}}{d} =} \\
 &= n_i V^2 G_{d\sigma}^{\alpha}(z). \quad (5.56)
 \end{aligned}$$

5.2.2. Dynamical impurities

Up to now, we have circumvented the problem of on-site Coulomb interaction by pulling the interaction into the definition of the bare propagator in (5.42). In the following, we will solve the impurity problem and show how to calculate the impurity Green's function for two different types of parameters in the Anderson Hamiltonian, representing Gadolinium impurities and Oxygen vacancies, respectively.

According to (4.3) and (4.12), the local impurity Green's function of an impurity located at $\mathbf{r} = (\mathbf{r}_{\parallel}, \alpha)$ is calculated from the local conduction electron Green's function at that particular position. Due to the configurational average and the corresponding translational symmetry, the problem reduces to the calculation of the local impurity Green's function $G_{d\sigma}(z)$ from the bare local conduction electron Green's function $G_{c\sigma}^0(z)$

in the bulk case, and the calculation of the local impurity Green's function in layer α , $G_{d\sigma}^\alpha(z)$, from the bare local conduction electron Green's function in layer α , $G_{c\sigma}^{\alpha,0}(z)$, in the multilayer case. Since the full conduction electron Green's function in turn depends on the impurity Green's function, we can make the equations self-consistent replacing the bare Conduction electron Green's function with the full ones. Due to the local nature of the impurity scattering, it is sufficient to formulate the impurity problem for the bulk case. The multilayer case is obtained by assigning a layer index to the all occurring Green's functions and self-energies.

Gadolinium impurities

As mentioned before, Gadolinium impurities have a strong on-site Coulomb repulsion and one excess electron per impurity. Therefore, we set $U \rightarrow \infty$ in the Anderson Hamiltonian ((4.3) and (4.12)). Since double occupancy can now only be realized by virtual excitations, this essentially leads to a magnetic impurity. The corresponding low lying spin fluctuations at the impurity sites will lead to the formation of a Kondo resonance at the Fermi edge. This scenario was already discussed in section 3.1. We use the pseudo-particle representation (section 3.2) and apply the non-crossing approximation (section 3.3) to calculate the full local impurity Green's function from the local conduction electron Green's function by means of the self-consistent NCA equations (3.15), (3.16) and (3.17).

$$\text{Im}\tilde{\Sigma}_b(\omega - i0^+) = \Gamma \sum_{\sigma} \int d\varepsilon \frac{f(\varepsilon)(1 - f(\omega + \varepsilon))}{f(-\omega)} A_{c\sigma}(\varepsilon) \tilde{A}_{f\sigma}(\omega + \varepsilon), \quad (5.57)$$

$$\text{Im}\tilde{\Sigma}_{f\sigma}(\omega - i0^+) = \Gamma \int d\varepsilon \frac{f(-\varepsilon)(1 - f(\omega - \varepsilon))}{f(-\omega)} A_{c\sigma}(\varepsilon) \tilde{A}_b(\omega - \varepsilon), \quad (5.58)$$

$$A_{d\sigma}(\omega) = \int d\varepsilon [f(\omega + \varepsilon)f(-\varepsilon) + f(-\varepsilon - \omega)f(\varepsilon)] \tilde{A}_{f\sigma}(\omega + \varepsilon) \tilde{A}_b(\varepsilon), \quad (5.59)$$

Note that we have replaced the bare conduction electron spectral density $A_{c\sigma}^0(\varepsilon)$ by the full one $A_{c\sigma}(\varepsilon)$ here. In contrast to the original equations in chapter 3 we do not set the chemical potential μ to zero at this point of our derivation. With this, the pseudo-particle spectral densities read

$$\tilde{A}_b(\omega) = \frac{1}{\pi} \frac{\text{Im}\tilde{\Sigma}_b(\omega)}{[\omega + \lambda_0 - \text{Re}\Sigma_b(\omega)]^2 + [\text{Im}\Sigma_b(\omega)]^2}, \quad (5.60)$$

$$\tilde{A}_{f\sigma}(\omega) = \frac{1}{\pi} \frac{\text{Im}\tilde{\Sigma}_{f\sigma}(\omega)}{[\omega + \lambda_0 + \mu - E_d - \text{Re}\Sigma_{f\sigma}(\omega)]^2 + [\text{Im}\Sigma_{f\sigma}(\omega)]^2}, \quad (5.61)$$

and the corresponding condition for λ_0 is given by

$$F(\lambda_0) = \int d\omega f(\omega) \left[\sum_{\sigma} \tilde{A}_{f\sigma}(\omega) + \tilde{A}_b(\omega) \right] - 1 \stackrel{!}{=} 0. \quad (5.62)$$

5. Theory

Oxygen vacancies

Since Oxygen vacancies provide two excess electrons per vacancy and are assumed to have a weak on-site Coulomb interaction we will apply perturbation theory in U . The vertices stemming from the second and third part of the Anderson Hamiltonian (4.3) and (4.12) are shown in figure 5.3.

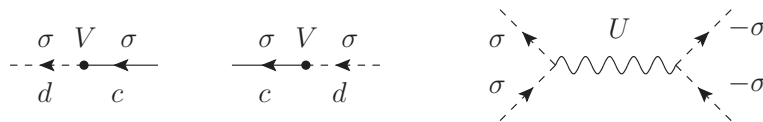




Figure 5.3.: Vertices of the Anderson Hamiltonian

If we expand the impurity Green's function up to second order in the Coulomb interaction U , we obtain

$$\begin{aligned}
G_{d\sigma}(z) &= \text{diagram with a horizontal line of length } d \text{ and } \sigma \text{ labels at both ends} \\
&= \text{diagram with a horizontal line of length } d \text{ and } \sigma \text{ labels at both ends} \\
&\quad + \text{diagram with a horizontal line of length } d \text{ and } \sigma \text{ labels at both ends, with a vertex } V \text{ in the middle} \\
&\quad + \text{diagram with a horizontal line of length } d \text{ and } \sigma \text{ labels at both ends, with a vertex } U \text{ in the middle} \\
&\quad + \text{diagram with a horizontal line of length } d \text{ and } \sigma \text{ labels at both ends, with a vertex } U \text{ in the middle}
\end{aligned}$$

Note that due to the Pauli principle the diagrams like  and  do not occur. In the following, we will evaluate the different contributions to the impurity self-energy. We begin with the contribution stemming from the hybridization of impurity and conduction band

$$\begin{aligned}\Sigma_{d\sigma}^{(c)}(i\omega_n) &= \text{---} \bullet \xleftarrow{c} \bullet \text{---} \\ &= V^2 G_{c\sigma}(i\omega_n).\end{aligned}\quad (5.63)$$

Similar to the Gadolinium case, we have replaced the bare conduction electron Green's function by the full one in order to achieve self-consistency. The contribution of leading

order in U is given by

$$\begin{aligned}
\Sigma_{d\sigma}^{(1)}(i\omega_n) &= \text{diagram: a dashed circle with an arrow pointing clockwise, labeled } \omega_l, -\sigma \text{ above it, and a wavy line labeled } U \text{ below it.} \\
&= (-1)^2 U \frac{1}{\beta} \sum_l [-G_{d-\sigma}(i\omega_l)] \\
&= -U \oint_C \frac{dz}{2\pi i} f(z) G_{d-\sigma}(z) \\
&= -U \int \frac{d\varepsilon}{2\pi i} f(\varepsilon) \underbrace{[G_{d-\sigma}(\varepsilon + i0^+) - G_{d-\sigma}(\varepsilon - i0^+)]}_{2i\text{Im}G_{d-\sigma}^R(\varepsilon) = -2\pi i A_{d-\sigma}(\varepsilon)} \\
&= U \int d\varepsilon f(\varepsilon) A_{d-\sigma}(\varepsilon). \tag{5.64}
\end{aligned}$$

The integration in the third step is performed over a contour shown in figure 5.4. Note that the first order contribution is frequency independent and purely real. Finally, the

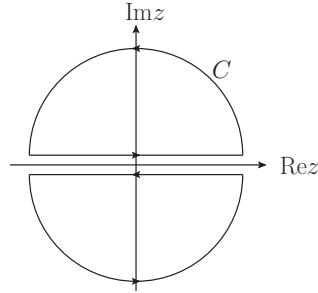


Figure 5.4.: Contour integration in the calculation of the first order contribution to the impurity self-energy

5. Theory

second order contribution reads

$$\begin{aligned}
\Sigma_{d\sigma}^{(2)}(i\omega_n) &= \text{Diagram: A loop with two wavy lines labeled U and two dashed lines. The top dashed line is labeled $\omega_k + \omega_l, -\sigma$ with an arrow pointing right. The bottom dashed line is labeled $\omega_n + \omega_l, \sigma$ with an arrow pointing left. The left wavy line is labeled $\omega_k, -\sigma$ with an arrow pointing down. The right wavy line is labeled ω_l, σ with an arrow pointing up.} \\
&= (-1)^2 U^2 \frac{1}{\beta^2} \sum_{lk} [-G_{d\sigma}(i\omega_n + i\omega_l)] [-G_{d-\sigma}(i\omega_k)] [-G_{d-\sigma}(i\omega_k + i\omega_l)] \\
&\quad \int d\zeta \frac{A_{d\sigma}(\zeta)}{i\omega_n + i\omega_l - \zeta} \int d\alpha \frac{A_{d-\sigma}(\alpha)}{i\omega_k - \alpha} \int d\varepsilon \frac{A_{d-\sigma}(\varepsilon)}{i\omega_k + i\omega_l - \varepsilon} \\
&= \frac{-U^2}{\beta} \sum_l \int d\zeta \int d\alpha \int d\varepsilon \frac{A_{d\sigma}(\zeta) A_{d-\sigma}(\alpha) A_{d-\sigma}(\varepsilon)}{i\omega_n + i\omega_l - \zeta} \underbrace{\frac{1}{\beta} \sum_k \frac{1}{i\omega_k - \alpha} \frac{1}{i\omega_k + i\omega_l - \varepsilon}}_{\oint \frac{dz}{2\pi i} f(z) \frac{1}{z-\alpha} \frac{1}{z+i\omega_l-\varepsilon} = \frac{f(\alpha)-f(\varepsilon)}{i\omega_l+\alpha-\varepsilon}} \\
&= -U^2 \int d\zeta \int d\alpha \int d\varepsilon A_{d\sigma}(\zeta) A_{d-\sigma}(\alpha) A_{d-\sigma}(\varepsilon) [f(\alpha) - f(\varepsilon)] \\
&\quad \cdot \underbrace{\frac{1}{\beta} \sum_l \frac{1}{i\omega_n + i\omega_l - \zeta} \frac{1}{i\omega_l + \alpha - \varepsilon}}_{-\oint \frac{dz}{2\pi i} \frac{b(z)}{(z+i\omega_n-\zeta)(z+\alpha-\varepsilon)} = \frac{-f(\zeta)-b(\varepsilon-\alpha)}{i\omega_n+\varepsilon-\zeta-\alpha}} \\
&= U^2 \int d\zeta \int d\alpha \int d\varepsilon A_{d\sigma}(\zeta) A_{d-\sigma}(\alpha) A_{d-\sigma}(\varepsilon) \frac{[f(\alpha) - f(\varepsilon)] [f(\zeta) + b(\varepsilon - \alpha)]}{i\omega_n + \varepsilon - \zeta - \alpha}. \tag{5.65}
\end{aligned}$$

We further evaluate the imaginary part of the advanced self-energy. The corresponding real part can be calculated by the Kramers-Kronig relation.

$$\begin{aligned}
\text{Im}\Sigma_{d\sigma}^{(2)}(\omega - i0^+) &= U^2 \int d\zeta \int d\alpha \int d\varepsilon A_{d\sigma}(\zeta) A_{d-\sigma}(\alpha) A_{d-\sigma}(\varepsilon) \\
&\quad \cdot [f(\alpha) - f(\varepsilon)] [f(\zeta) + b(\varepsilon - \alpha)] \underbrace{\text{Im} \frac{1}{\omega + \varepsilon - \zeta - \alpha - i0^+}}_{\pi \delta(\zeta - \omega - \varepsilon + \alpha)} \\
&= \pi U^2 \int d\alpha \int d\varepsilon A_{d\sigma}(\omega + \varepsilon - \alpha) A_{d-\sigma}(\alpha) A_{d-\sigma}(\varepsilon) \\
&\quad \cdot [f(\alpha) - f(\varepsilon)] [f(\omega + \varepsilon - \alpha) + b(\varepsilon - \alpha)]. \tag{5.66}
\end{aligned}$$

With this, we can calculate the impurity spectral density from the impurity self-energy $\Sigma_{d\sigma} = \Sigma_{d\sigma}^{(c)} + \Sigma_{d\sigma}^{(1)} + \Sigma_{d\sigma}^{(2)}$ by

$$A_{d\sigma}(\omega) = \frac{1}{\pi} \frac{\text{Im}\Sigma_{d\sigma}(\omega - i0^+)}{[\omega - E_d + \mu - \text{Re}\Sigma_{d\sigma}(\omega - i0^+)]^2 + [\text{Im}\Sigma_{d\sigma}(\omega - i0^+)]^2}. \tag{5.67}$$

5.3. Heisenberg lattice

In this section, we will discuss the approximations use for the magnetic subsystem which consists of the localized $4f$ spins and the spins of the itinerant conduction electrons. We will begin with the mean-field approximation for the bulk and the multilayer case. Afterwards, we will extend the mean-field equations by including long range RKKY coupling.

5.3.1. Mean field approximation in the bulk case

The magnetic part of the bulk Hamiltonian is given by equation (4.4). In order to apply a mean-field approximation [55], we assume the fluctuations of the $4f$ spins and the conduction electrons spins to be small, i.e.

$$\begin{aligned}\Delta \mathbf{S}_i &= \mathbf{S}_i - \langle \mathbf{S}_i \rangle \ll 1 \\ \Delta \boldsymbol{\sigma}_i &= \boldsymbol{\sigma}_i - \langle \boldsymbol{\sigma}_i \rangle \ll 1.\end{aligned}$$

By expressing all spin operators in (4.4) in terms of fluctuations and expectation values, neglecting all higher order terms in the former, and afterwards expressing the fluctuations in terms of spin operators and expectation values, one obtains

$$\begin{aligned}H_{cf} &= - \sum_{ij} J_{ij} (\langle \mathbf{S}_j \rangle \mathbf{S}_i + \mathbf{S}_j \langle \mathbf{S}_i \rangle - \langle \mathbf{S}_j \rangle \langle \mathbf{S}_i \rangle) \\ &\quad - \sum_i J_{cf} (\langle \boldsymbol{\sigma}_i \rangle \mathbf{S}_i + \mathbf{S}_i \langle \boldsymbol{\sigma}_i \rangle - \langle \boldsymbol{\sigma}_i \rangle \langle \mathbf{S}_i \rangle).\end{aligned}\quad (5.68)$$

Due to translational invariance, the mean-field expectation value cannot depend on the position. Moreover, if we assume that the conduction electron spin and the $4f$ spin are parallel, and pointing into the z -direction, we can write

$$\langle \mathbf{S}_i \rangle = \langle \mathbf{S} \rangle = \langle S \rangle \mathbf{e}_z \quad \text{and} \quad \langle \boldsymbol{\sigma}_i \rangle = \langle \boldsymbol{\sigma} \rangle = \langle \sigma \rangle \mathbf{e}_z.$$

For symmetry reasons, $J_{ij} = J_{ji}$ holds and the magnetic Hamiltonian can be written in terms of the z components of the $4f$ spin, S_i , and the conduction electron spin, σ_i , as

$$H_{cf} = H_{cf}^S + H_{cf}^\sigma + H_{cf}^0 \quad (5.69)$$

with

$$H_{cf}^S = - \sum_i \left(\sum_j J_{ij} 2 \langle S \rangle + J_{cf} \langle \sigma \rangle \right) S_i \quad (5.70)$$

$$H_{cf}^\sigma = - J_{cf} \sum_i \langle S \rangle \sigma_i \quad (5.71)$$

$$H_{cf}^0 = \sum_{ij} J_{ij} \langle S \rangle^2 + J_{cf} \sum_i \langle \sigma \rangle \langle S \rangle.$$

5. Theory

Because of the isotropy of the bulk system, we can introduce the integrated $4f$ coupling

$$J_{4f} := \sum_j J_{ij}, \quad (5.72)$$

which is position independent. This coupling is chosen such that the experimentally observed Curie temperature of around 69 K in stoichiometric EuO is reproduced [18, 56–58]. To be consistent with the work of Arnold and Kroha [18, 25], we choose $J_{4f} = 7 \times 10^{-5} D_0 = 5.6 \times 10^{-4} \text{eV}$, which leads to a Curie temperature of $68.3\text{K} + 0.01\text{K}$ (see figure 5.5). With this, we can write the $4f$ spin dependent part of the Hamiltonian as

$$H_{cf}^S = - \sum_i \left(2J_{4f} \langle S \rangle + J_{cf} \langle \sigma \rangle \right) S_i. \quad (5.73)$$

The $4f$ spin expectation value can then be calculated by

$$\begin{aligned} \langle S \rangle &= \frac{\text{tr} \{ S e^{-\beta H} \}}{\text{tr} \{ e^{-\beta H} \}} \\ &= \frac{\sum_{S=-\frac{7}{2}}^{\frac{7}{2}} S e^{\beta(2J_{4f} \langle S \rangle + J_{cf} \langle \sigma \rangle) S}}{\sum_{S=-\frac{7}{2}}^{\frac{7}{2}} e^{\beta(2J_{4f} \langle S \rangle + J_{cf} \langle \sigma \rangle) S}}, \end{aligned} \quad (5.74)$$

where we have used that the only $4f$ spin dependent contribution to the full Hamiltonian is given by equation (5.73). All other terms lead to non spin dependent factors which can be pulled out of the sum in both the numerator and the denominator of (5.74) and hereby cancel each other out. The above equation is self-consistent and can be solved numerically. The only external parameter is the conduction electron spin expectation value $\langle \sigma \rangle$. In order to calculate it, we consider the conduction electron spin expectation value at position \mathbf{r} , which reads

$$\begin{aligned} \langle \sigma(\mathbf{r}) \rangle &= \left\langle \frac{1}{2} \sum_{\sigma\sigma'} c_{\mathbf{r}\sigma}^\dagger \tau_{\sigma\sigma'}^z c_{\mathbf{r}\sigma'} \right\rangle \\ &= \sum_{\sigma} \sigma \langle c_{\mathbf{r}\sigma}^\dagger c_{\mathbf{r}\sigma} \rangle \\ &= - \sum_{\sigma} \sigma \langle c_{\mathbf{r}\sigma}(0) c_{\mathbf{r}\sigma}^\dagger(0) \rangle \\ &= - \sum_{\sigma} \sigma \lim_{t' \rightarrow t+0+} \underbrace{\langle c_{\mathbf{r}\sigma}(t') c_{\mathbf{r}\sigma}^\dagger(t) \rangle}_{iG_{c\sigma}^>(\mathbf{r}, \mathbf{r}, t'-t)=i \int \frac{d\omega}{2\pi} e^{i(\omega-i0^+)(t'-t)} \underbrace{G_{c\sigma}^>(\mathbf{r}, \mathbf{r}, \omega)}_{2\pi i f(\omega) A_{c\sigma}(\mathbf{r}, \mathbf{r}, \omega)}} \Big|_{t=0} \\ &= \sum_{\sigma} \sigma \int d\omega f(\omega) A_{c\sigma}(\mathbf{r}, \mathbf{r}, \omega). \end{aligned} \quad (5.75)$$

Since the mean-field expectation value cannot depend on the position, we choose the origin $\langle \sigma \rangle = \langle \sigma(\mathbf{0}) \rangle$ and obtain

$$\langle \sigma \rangle = \frac{1}{2} \int d\omega f(\omega) [A_{c\uparrow}(\omega) - A_{c\downarrow}(\omega)], \quad (5.76)$$

which is the difference of spin-up and spin-down occupation of the conduction band.

Now we are able to calculate the spin expectation value for a given conduction band Green's function. In order to close the self-consistent logic, we need to calculate the contribution of the magnetic subsystem to the conduction electron self-energy. According to the mean-field approximation, the only term which involves conduction electron operators is (5.71)

$$H_{cf}^\sigma = -J_{cf} \sum_i \langle S \rangle \sigma_i = -J_{cf} \langle S \rangle \sum_{\mathbf{R}\sigma} \sigma c_{\mathbf{R}\sigma}^\dagger c_{\mathbf{R}\sigma},$$

where \mathbf{R} are the lattice vectors on the position of the Eu atoms in the FCC lattice. If we restrict ourselves to this interaction for a moment, the real space conduction band Green's function reads

$$\overleftrightarrow{G}_{\mathbf{r}\mathbf{r}'}^{z,\sigma} = \overleftrightarrow{G}_{\mathbf{r}\mathbf{r}'}^{z,\sigma} + \overleftrightarrow{G}_{\mathbf{r}\mathbf{r}''}^{z,\sigma} \overleftrightarrow{G}_{\mathbf{r}''\mathbf{r}'}^{z,\sigma} \frac{-J_{cf} \langle S \rangle \sigma}{\phantom{\overleftrightarrow{G}_{\mathbf{r}\mathbf{r}''}^{z,\sigma} \overleftrightarrow{G}_{\mathbf{r}''\mathbf{r}'}^{z,\sigma}}}$$

Since the real space self-energy is local and position independent, the contribution to the momentum dependent self-energy in (5.1) can be read off directly (see (B.1)). It is given by

$$\Sigma_\sigma(z) = -J_{cf} \langle S \rangle \sigma. \quad (5.77)$$

5.3.2. Mean field approximation in the multilayer case

In order to apply a mean-field approximation on the multilayer magnetic Hamiltonian (4.13), we begin with the same assumption of small spin fluctuations as in the bulk case,

$$\begin{aligned} \Delta \mathbf{S}_{i\alpha} &= \mathbf{S}_{i\alpha} - \langle \mathbf{S}_{i\alpha} \rangle \ll 1 \\ \Delta \boldsymbol{\sigma}_{i\alpha} &= \boldsymbol{\sigma}_{i\alpha} - \langle \boldsymbol{\sigma}_{i\alpha} \rangle \ll 1. \end{aligned}$$

Following the procedure that led to (5.68) one can derive the mean-field version of (4.13). It reads

$$\begin{aligned} H_{cf} &= - \sum_{\substack{ij \\ \alpha\beta}} J_{ij}^{\alpha\beta} (\langle \mathbf{S}_{j\beta} \rangle \mathbf{S}_{i\alpha} + \mathbf{S}_{j\beta} \langle \mathbf{S}_{i\alpha} \rangle - \langle \mathbf{S}_{j\beta} \rangle \langle \mathbf{S}_{i\alpha} \rangle) \\ &\quad - \sum_{i\alpha} J_{cf} (\langle \boldsymbol{\sigma}_{i\alpha} \rangle \mathbf{S}_{i\alpha} + \mathbf{S}_{i\alpha} \langle \boldsymbol{\sigma}_{i\alpha} \rangle - \langle \boldsymbol{\sigma}_{i\alpha} \rangle \langle \mathbf{S}_{i\alpha} \rangle). \end{aligned}$$

Since we have translation symmetry in the parallel direction, we assume all spin expectation values within a given plane to be equal. Moreover, due to the coupling, it is reasonable to presume that the spin directions are equal in all layers, and we choose the z -direction as the magnetic axis. With this, we can write

$$\langle \mathbf{S}_{i\alpha} \rangle = \langle \mathbf{S}_\alpha \rangle = \langle S_\alpha \rangle \mathbf{e}_z \quad \text{and} \quad \langle \boldsymbol{\sigma}_{i\alpha} \rangle = \langle \boldsymbol{\sigma}_\alpha \rangle = \langle \sigma_\alpha \rangle \mathbf{e}_z.$$

5. Theory

Again, $J_{ij}^{\alpha\beta} = J_{ji}^{\beta\alpha}$ holds and therefore the magnetic Hamiltonian can be written in terms of the z components of the $4f$ spin, $S_{i\alpha}$, and the conduction electron spin, $\sigma_{i\alpha}$. It reads

$$H_{cf} = H_{cf}^S + H_{cf}^\sigma + H_{cf}^0 \quad (5.78)$$

with

$$H_{cf}^S = - \sum_{i\alpha} \left(\sum_{j\beta} J_{ij}^{\alpha\beta} 2\langle S_\beta \rangle + J_{cf} \langle \sigma_\alpha \rangle \right) S_{i\alpha} \quad (5.79)$$

$$H_{cf}^\sigma = -J_{cf} \sum_{i\alpha} \langle S_\alpha \rangle \sigma_{i\alpha} \quad (5.80)$$

$$H_{cf}^0 = \sum_{\substack{ij \\ \alpha\beta}} J_{ij}^{\alpha\beta} \langle S_\alpha \rangle \langle S_\beta \rangle + J_{cf} \sum_{i\alpha} \langle \sigma_\alpha \rangle \langle S_\alpha \rangle.$$

Due to the isotropy in the parallel direction we can introduce the parallel coupling

$$J_{4f}^{\parallel\alpha} := \sum_j J_{ij}^{\alpha\alpha}, \quad (5.81)$$

and the perpendicular coupling

$$J_{4f}^{\alpha\beta} := \sum_j J_{ij}^{\alpha\beta} \quad \text{for } \alpha \neq \beta, \quad (5.82)$$

which are both independent of the parallel position i . Now, the $4f$ spin dependent part of the Hamiltonian can be written as

$$H_{cf}^S = - \sum_{i\alpha} \left(2J_{4f}^{\parallel\alpha} \langle S_\alpha \rangle + 2 \sum_{\beta \neq \alpha} J_{4f}^{\alpha\beta} \langle S_\beta \rangle + J_{cf} \langle \sigma_\alpha \rangle \right) S_{i\alpha}. \quad (5.83)$$

With this, the spin expectation values in the different layers can be determined self-consistently through the calculation of the trace

$$\begin{aligned} \langle S_\alpha \rangle &= \frac{\text{tr} \{ S_\alpha e^{-\beta H} \}}{\text{tr} \{ e^{-\beta H} \}} \\ &= \frac{\sum_{S=-\frac{7}{2}}^{\frac{7}{2}} S e^{\beta(2J_{4f}^{\parallel\alpha} \langle S_\alpha \rangle + 2 \sum_{\beta \neq \alpha} J_{4f}^{\alpha\beta} \langle S_\beta \rangle + J_{cf} \langle \sigma_\alpha \rangle) S}}{\sum_{S=-\frac{7}{2}}^{\frac{7}{2}} e^{\beta(2J_{4f}^{\parallel\alpha} \langle S_\alpha \rangle + 2 \sum_{\beta \neq \alpha} J_{4f}^{\alpha\beta} \langle S_\beta \rangle + J_{cf} \langle \sigma_\alpha \rangle) S}}. \end{aligned} \quad (5.84)$$

Similar to the bulk case, we have used that the only $4f$ spin dependent contribution to the full Hamiltonian is given by equation (5.83). Again, all other terms lead to non spin dependent factors which can be pulled out of the sum in both the numerator and the denominator of (5.84) and therefore cancel each other out.

Since the coupling $J_{ij}^{\alpha\beta}$ originates in virtual transitions from the $4f$ to the $5d$ shell in the same or on of the neighboring EuO ions [3], it is reasonable to restrict the perpendicular

coupling to the nearest neighboring layers (NN). Therefore the simplest approximation is to set

$$J_{4f}^{\alpha\beta} = \begin{cases} J_{4f}^{\perp} & \text{for } \alpha = \beta \pm 1 \\ 0 & \text{else} \end{cases}. \quad (5.85)$$

As 4 of the 12 nearest neighbors in an FCC lattice are in the same (100) monolayer and 4 nearest neighbors are in each neighboring monolayers, we set

$$J_{4f}^{\parallel\alpha} = J_{4f}^{\perp} = \frac{1}{3}J_{4f} \quad (5.86)$$

for all α in order to get a resulting Curie temperature of 69 Kelvin for stoichiometric EuO. On the other hand, one can go one step further and assume an inverse cubic behavior (IC) according to the RKKY coupling in a free band [59] and write

$$J_{4f}^{\alpha\beta} = \frac{J_{4f}^{0\perp}}{|\alpha - \beta|^3}, \quad (5.87)$$

where the constant is chosen such that the bulk limit of the Curie temperature is the same as in the nearest neighbor case. This holds if

$$\sum_{\beta=\alpha}^{\infty} J_{4f}^{\alpha\beta} \stackrel{!}{=} J_{4f}^{\perp}.$$

Therefore, we set

$$\frac{J_{4f}^{0\perp}}{J_{4f}^{\perp}} = \sum_{\alpha=1}^{\infty} \frac{1}{\alpha^3} = \zeta(3) \approx 1.202,$$

where $\zeta(x)$ is the Riemann zeta function. The difference of the nearest neighbor approach and the inverse cubic ansatz can be seen in the solutions to the self-consistent equation (5.84) without coupling to the conduction band ($J_{cf} = 0$), which are depicted in figure 5.5. The missing coupling partners at the surfaces of the system leads to a decrease of the Curie temperature with respect to the thickness and to a decrease of the spin expectation value at the outer monolayers. Moreover, as expected, the presence of a surface has a greater impact in the case of the inverse cubic approach due to its long range character. However, the difference is not too profound due to the fast (cubic) decrease of the long range coupling with the distance. For the same reason the dependence of the mean-field spin on the layer index and the temperature in the inverse cubic case (not shown) does not differ significantly from the nearest neighbor case.

For the self-consistent theory including the conduction band, we need to calculate the conduction electron spin expectation value $\langle \sigma_{\alpha}(\mathbf{r}_{\parallel}) \rangle$ at site $\mathbf{r} = (\mathbf{r}_{\parallel}, \alpha)$. The calculation is the same as in (5.75) and yields

$$\langle \sigma_{\alpha}(\mathbf{r}_{\parallel}) \rangle = \sum_{\sigma} \sigma \int d\omega f(\omega) A_{c\sigma}^{\alpha}(\mathbf{r}_{\parallel}, \mathbf{r}_{\parallel}, \omega). \quad (5.88)$$

5. Theory

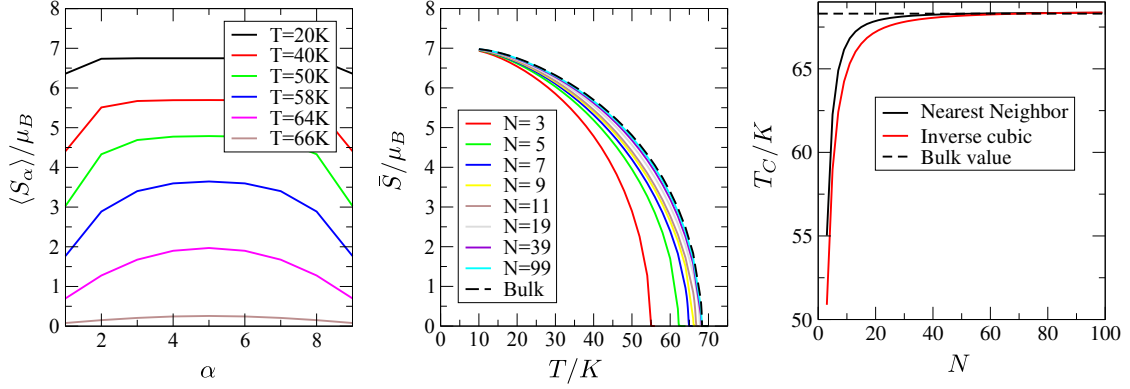


Figure 5.5.: Left: Mean-field spin against the monolayer index α for various temperatures (NN) in a system of 9 monolayers. Center: The spin averaged over all monolayers \bar{S} versus the temperature for various numbers of monolayers N in comparison to the bulk curve (NN). Right: Increasing Curie temperature T_C with the number of monolayers N for the nearest neighbor coupling (NN) and long range inverse cubic coupling (IC).

Due to the mean-field assumption, we can choose $\langle \sigma_\alpha \rangle = \langle \sigma_\alpha(\mathbf{0}_\parallel) \rangle$ and obtain

$$\langle \sigma_\alpha \rangle = \frac{1}{2} \int d\omega f(\omega) [A_{c\uparrow}^\alpha(\omega) - A_{c\downarrow}^\alpha(\omega)], \quad (5.89)$$

which is the difference in the spin-up and spin-down conduction band occupation number in layer α . Similar to the bulk case, the contribution to the conduction electron self-energy originates in (5.80), which can be written as

$$H_{cf}^\sigma = -J_{cf} \sum_{i\alpha} \langle S_\alpha \rangle \sigma_{i\alpha} = -J_{cf} \sum_{\mathbf{R}_\parallel \alpha \sigma} \sigma \langle S_\alpha \rangle c_{\mathbf{R}_\parallel \alpha}^\dagger c_{\mathbf{R}_\parallel \alpha},$$

where the sum runs over all lattice vectors \mathbf{R}_\parallel in the (100) monolayer of an FCC lattice. The corresponding contribution to the conduction electron Green's function reads

$$\overleftrightarrow{g}_{\mathbf{r}_\parallel, \alpha}^{z, \sigma}(\mathbf{r}'_\parallel, \beta) = \overleftrightarrow{g}_{\mathbf{r}_\parallel, \alpha}^{z, \sigma}(\mathbf{r}'_\parallel, \beta) + \overleftrightarrow{g}_{\mathbf{r}_\parallel, \alpha}^{z, \sigma}(\mathbf{R}_\parallel, \gamma) \overleftrightarrow{g}_{\mathbf{R}_\parallel, \gamma}^{z, \sigma}(\mathbf{r}'_\parallel, \beta),$$

Since the real space self-energy is local and independent of the parallel position, the contribution to the momentum dependent self-energy in (5.22) can be read off directly (see (B.2)). It is given by

$$\Sigma_{c\sigma}^\alpha(z) = -J_{cf} \langle S_\alpha \rangle \sigma. \quad (5.90)$$

The multilayer system of conduction band and localized $4f$ moments can now be solved self-consistently. The mean-field $4f$ spins determine the conduction electron Green's function via equation (5.90). Using this, one can calculate the conduction electron spin by applying equation (5.89), which is the only external parameter in the formula for the mean-field $4f$ spins (5.84). The special case of mirror symmetric systems is described in appendix C.

5.3.3. Long range RKKY interaction

Up to now, the conduction band induced coupling between two spatially separated $4f$ spins is mediated by the self-consistency described at the end of the last section. For a more precise treatment of the long range RKKY coupling, one has to go one step further. In the following we will derive the RKKY coupling between spatially separated $4f$ spins and integrate it into the self-consistent theory. In the course of this, we extend the work of Mauger et. al. [3] and Burg et. al. [60] to multilayer systems. Moreover, our theory is applicable to an arbitrary conduction band.

We begin by considering the conduction electron spin expectation value in z -direction at a position \mathbf{r} (see (5.75)), which is given by

$$\langle \sigma(\mathbf{r}) \rangle = \sum_{\sigma} \sigma \int d\omega f(\omega) A_{c\sigma}(\mathbf{r}, \mathbf{r}, \omega),$$

in the presence of a lattice of localized spins. The interaction stems from the second term of (4.4), which reads

$$H' = -J_{cf} \sum_i \boldsymbol{\sigma}_i \mathbf{S}_i,$$

with $\sigma_i^j = \frac{1}{2} \sum_{\sigma\sigma'} c_{\mathbf{R}_i\sigma}^\dagger \tau_{\sigma\sigma'}^j c_{\mathbf{R}_i\sigma'}$. The perturbative expansion of the local Green's function then reads

$$\begin{aligned} \overleftrightarrow{\mathbf{r}}_{\mathbf{r}}^{z,\sigma} &= \overleftrightarrow{\mathbf{r}}_{\mathbf{r}}^{z,\sigma} + \overleftrightarrow{\mathbf{r}}_{\mathbf{r}}^{z,\sigma} \xrightarrow{\mathbf{R}_i} \overleftrightarrow{\mathbf{r}}_{\mathbf{r}}^{z,\sigma} + \overleftrightarrow{\mathbf{r}}_{\mathbf{r}}^{z,\sigma} \xrightarrow{\mathbf{R}_i} \overleftrightarrow{\mathbf{r}}_{\mathbf{r}}^{z,\sigma'} \xrightarrow{\mathbf{R}_j} \overleftrightarrow{\mathbf{r}}_{\mathbf{r}}^{z,\sigma} + \dots \\ &= \overleftrightarrow{\mathbf{r}}_{\mathbf{r}}^{z,\sigma} + \overleftrightarrow{\mathbf{r}}_{\mathbf{r}}^{z,\sigma} \xrightarrow{\mathbf{R}_i} \overleftrightarrow{\mathbf{r}}_{\mathbf{r}}^{z,\sigma} + \mathcal{O}(J_{cf}^2). \end{aligned}$$

From now on, we will restrict ourselves to the lowest order in the coupling J_{cf} . The evaluation of the corresponding diagrams yield for the local spectral density

$$\begin{aligned} A_{c\sigma}(\mathbf{r}, \mathbf{r}, \omega) &= A_{c\sigma}^0(\mathbf{r}, \mathbf{r}, \omega) - J_{cf} \sum_i S_i^z \sigma \frac{1}{\pi} \text{Im} \{ [G_{c\sigma}^0(\mathbf{R}_i, \mathbf{r}, \omega - i0^+)]^2 \} \\ &= A_{c\sigma}^0(\mathbf{r}, \mathbf{r}, \omega) - 2J_{cf} \sum_i S_i^z \sigma A_{c\sigma}^0(\mathbf{R}_i, \mathbf{r}, \omega) \text{Re} G_{c\sigma}^0(\mathbf{R}_i, \mathbf{r}, \omega - i0^+). \end{aligned}$$

With this, the conduction electron spin expectation value at lattice site \mathbf{R}_j reads

$$\langle \sigma(\mathbf{R}_j) \rangle = \langle \sigma(\mathbf{R}_j) \rangle_0 - \frac{J_{cf}}{2} \sum_i S_i^z \sum_{\sigma} \int d\omega f(\omega) A_{c\sigma}^0(\mathbf{R}_i, \mathbf{R}_j, \omega) \text{Re} G_{c\sigma}^0(\mathbf{R}_i, \mathbf{R}_j, \omega - i0^+). \quad (5.91)$$

Next, we replace the bare Green's function in the above equation by the full Green's function and insert (5.91) into the mean-field Hamiltonian (5.70). Due to the bulk mean-field approximation, we can use the $\langle \sigma(\mathbf{R}_i) \rangle = \langle \sigma \rangle$ in that particular step. With this, we can identify an additional term in the bulk mean-field Hamiltonian. It reads

$$H_{\text{RKKY}} = - \sum_{ij} J_{ij}^{\text{RKKY}} S_i^z S_j^z, \quad (5.92)$$

5. Theory

where the RKKY coupling is given by

$$J_{ij}^{\text{RKKY}} = -\frac{J_{cf}^2}{2} \sum_{\sigma} \int d\omega f(\omega) A_{c\sigma}(\mathbf{R}_i, \mathbf{R}_j, \omega) \text{Re} G_{c\sigma}(\mathbf{R}_i, \mathbf{R}_j, \omega - i0^+). \quad (5.93)$$

In the following, we will discuss the implications of the additional RKKY coupling for the mean-field theory from section 5.3.1. The additional Hamiltonian (5.92) corresponds to the replacement of the coupling J_{ij} in (5.70) by

$$J_{ij} \rightarrow J_{ij} + J_{ij}^{\text{RKKY}}.$$

With this, the integrated coupling in equation (5.72) becomes

$$J_{4f} = \sum_j J_{ij} - \frac{J_{cf}^2}{2} \sum_{\substack{\mathbf{R} \\ |\mathbf{R}| < R_{\text{max}}}} \sum_{\sigma} \int d\omega f(\omega) A_{c\sigma}(\mathbf{R}, \omega) \text{Re} G_{c\sigma}(\mathbf{R}, \omega - i0^+), \quad (5.94)$$

where the first term is constant and the sum in the second term is restricted to the nearest neighbors in an FCC lattice at a maximal distance R_{max} (see figure 5.6). This is reasonable, as the RKKY coupling is expected to fall off with the third power in the distance. With this, not only the conduction electron spin expectation value, but also the $4f$ coupling enters the trace formula (5.74) as an external parameter which depends on the conduction electron Green's function.

In the multilayer case, we insert (5.91) into (5.79) under use of the mean-field relation $\langle \sigma(\mathbf{R}) \rangle = \langle \sigma(\mathbf{R}_{\parallel i}, \alpha) \rangle = \langle \sigma_{\alpha} \rangle$. Thus, we obtain an additional term in the multilayer mean-field Hamiltonian (5.83), which reads

$$H_{\text{RKKY}} = - \sum_{\substack{ij \\ \alpha\beta}} J_{ij}^{\alpha\beta, \text{RKKY}} S_{i\alpha}^z S_{j\beta}^z. \quad (5.95)$$

The RKKY coupling is given by

$$J_{ij}^{\alpha\beta, \text{RKKY}} = -\frac{J_{cf}^2}{2} \sum_{\sigma} \int d\omega f(\omega) A_{c\sigma}^{\alpha\beta}(\mathbf{R}_{\parallel i}, \mathbf{R}_{\parallel j}, \omega) \text{Re} G_{c\sigma}^{\alpha\beta}(\mathbf{R}_{\parallel i}, \mathbf{R}_{\parallel j}, \omega - i0^+).$$

The consequences to the multilayer mean-field theory are the following. The parallel coupling (5.81) becomes

$$J_{4f}^{\parallel\alpha} = \sum_j J_{ij}^{\alpha\alpha} - \frac{J_{cf}^2}{2} \sum_{\substack{\mathbf{R}_{\parallel} \\ |\mathbf{R}_{\parallel}| < R_{\text{max}}}} \sum_{\sigma} \int d\omega f(\omega) A_{c\sigma}^{\alpha}(\mathbf{R}_{\parallel}, \omega) \text{Re} G_{c\sigma}^{\alpha}(\mathbf{R}_{\parallel}, \omega - i0^+). \quad (5.96)$$

Similar to the bulk case, the first term is constant and the sum in the second term is restricted to the nearest neighbors in an (100) monolayer of an FCC lattice at a maximal

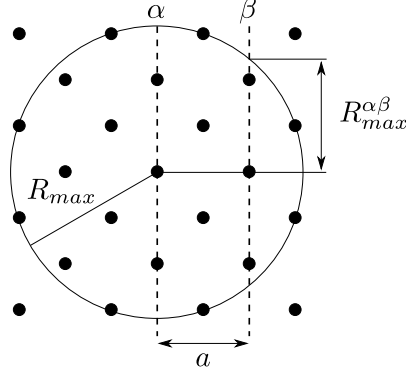


Figure 5.6.: Summation of over the nearest neighbors in an (100) monolayer of an FCC lattice. Due to the cubic decrease of the coupling one can restrict the summation to an area within a circle of radius R_{\max} . The generalization to the bulk case is obvious.

distance R_{\max} (see figure 5.6). The perpendicular coupling (5.82) becomes

$$J_{4f}^{\alpha\beta} = \sum_j J_{ij}^{\alpha\beta} - \frac{J_{cf}^2}{2} \sum_{\mathbf{R}_{\parallel}} \sum_{\sigma} \int d\omega f(\omega) A_{c\sigma}^{\alpha\beta}(\mathbf{R}_{\parallel}, \omega) \text{Re} G_{c\sigma}^{\alpha\beta}(\mathbf{R}_{\parallel}, \omega - i0^+) \quad \text{for } \alpha \neq \beta, \quad (5.97)$$

$|\mathbf{R}_{\parallel}| < R_{\max}^{\alpha\beta}$

where the maximum parallel distance $R_{\max}^{\alpha\beta}$ decreases with the interlayer distance $|\alpha - \beta|$ according to (see figure 5.6)

$$R_{\max}^{\alpha\beta} = R_{\max}^{|\alpha-\beta|} = \sqrt{R_{\max}^2 - \left(\frac{a}{2}|\alpha - \beta|\right)^2}.$$

As in the bulk case, the introduction of the RKKY couplings (5.96) and (5.97) represents additional external parameters for the $4f$ spin expectation value formula (5.84), which depends on the conduction electron Green's function.

For the numerical calculation of the RKKY coupling it turns out to be advantageous to make use of

$$J_{ij}^{\text{RKKY}} = J^{\text{RKKY}}(|\mathbf{R}_i - \mathbf{R}_j|), \quad (5.98)$$

which is a consequence of the isotropy in the bulk systems. With this, we can write the integrated coupling J_{4f}^{RKKY} , which is the second term of (5.94), as

$$J_{4f}^{\text{RKKY}}(R_{\max}) = \sum_j J_{ij}^{\text{RKKY}} = \sum_{\substack{\mathbf{R} \\ |\mathbf{R}| < R_{\max}}} J^{\text{RKKY}}(|\mathbf{R}|) = \sum_{R_n < R_{\max}} J^{\text{RKKY}}(R_n) W(R_n). \quad (5.99)$$

Here, R_n are the radii of spheres intersecting neighboring points of equal distance to the origin (see figure 5.6). The number of these points define the weights $W(R_n)$. For instance

5. Theory

for the nearest neighbors in the FCC lattice, we have $R_1 = a/\sqrt{2}$ and $W(R_1) = 12$. In the multilayer case, we have

$$J_{ij}^{\alpha\alpha, \text{RKKY}} = J^{\alpha\alpha, \text{RKKY}}(|\mathbf{R}_{\parallel i} - \mathbf{R}_{\parallel j}|) =: J^{\alpha, \text{RKKY}}(|\mathbf{R}_{\parallel i} - \mathbf{R}_{\parallel j}|), \quad (5.100)$$

due to the isotropy in the parallel direction. Analogously to the bulk case, we can simplify the summation over the parallel positions in (5.96). The second term of (5.96) defines the integrated parallel coupling in layer α , $J_{4f}^{\parallel\alpha, \text{RKKY}}$. It can be written as

$$\begin{aligned} J_{4f}^{\parallel\alpha, \text{RKKY}}(R_{\max}^\alpha) &= \sum_j J_{ij}^{\alpha\alpha, \text{RKKY}} \\ &= \sum_{\substack{\mathbf{R}_{\parallel} \\ |\mathbf{R}_{\parallel}| < R_{\max}^\alpha}} J^{\alpha, \text{RKKY}}(|\mathbf{R}_{\parallel}|) \\ &= \sum_{R_n < R_{\max}^\alpha} J^{\alpha, \text{RKKY}}(R_n) W(R_n). \end{aligned} \quad (5.101)$$

Similar to the bulk case, the R_n are the radii of circles intersecting neighboring points of equal distance to the origin (see figure 5.6). Again, the number of these points define the weights $W(R_n)$. As an example, we consider the nearest neighbors in the (100) monolayer of an FCC lattice. Here, we have $R_1 = a/\sqrt{2}$ and $W(R_1) = 4$. For later use, we define the perpendicular RKKY coupling between the layers α and β as the second term of (5.97). It reads

$$J_{\text{RKKY}}^{\alpha\beta} = -\frac{J_{cf}^2}{2} \sum_{\substack{\mathbf{R}_{\parallel} \\ |\mathbf{R}_{\parallel}| < R_{\max}^{\alpha\beta}}} \sum_{\sigma} \int d\omega f(\omega) A_{c\sigma}^{\alpha\beta}(\mathbf{R}_{\parallel}, \omega) \text{Re} G_{c\sigma}^{\alpha\beta}(\mathbf{R}_{\parallel}, \omega - i0^+) \quad \text{for } \alpha \neq \beta. \quad (5.102)$$

5.4. Electrostatics

5.4.1. Thomas-Fermi-approximation

In this section we will derive the electrostatic part of our theory under use of the Thomas-Fermi-approximation [61]. In the bulk case, the system is assumed to be charge neutral. This means that the excess charge density introduced by the doping has to match the ionic background in the whole system. Therefore, the following charge neutrality condition must hold:

$$n_c + n_i n_d = n_{cc}, \quad (5.103)$$

where the conduction band occupation number is given by

$$n_c = \sum_{\sigma} \int d\omega f(\omega) A_{c\sigma}(\omega), \quad (5.104)$$

and the impurity occupation number reads

$$n_d = \sum_{\sigma} \int d\omega f(\omega) A_{d\sigma}(\omega). \quad (5.105)$$

The number of excess charge carriers in the system depends on the type of the impurity (cf. chapter 4),

$$n_{cc} = \begin{cases} n_i & \text{for } \text{Eu}_{1-x}\text{Gd}_x\text{O} \\ 2n_i & \text{for } \text{EuO}_{1-x} \end{cases}. \quad (5.106)$$

In order to fulfill the charge neutrality condition (5.103), we introduce an energy shift μ_0 which is added to the chemical potential in (5.1), (5.61) and (5.67):

$$\mu \rightarrow \mu + \mu_0. \quad (5.107)$$

With this, the conduction electron and impurity occupation numbers (5.104) and (5.105) become functions of μ_0 , and in order to fulfill the charge neutrality condition one needs to find the roots of

$$n_c(\mu_0) + n_i n_d(\mu_0) - n_{cc}.$$

In the multilayer case the situation is more complicated. As we allow for broken translational symmetry in the perpendicular direction, we can have a finite charge carrier density in each layer. Similar to (5.103) it reads

$$\Delta n_{\alpha} = n_c^{\alpha} + n_i n_d^{\alpha} - n_{cc}, \quad (5.108)$$

where the conduction band occupation number in layer α is given by

$$n_c^{\alpha} = \sum_{\sigma} \int d\omega f(\omega) A_{c\sigma}^{\alpha}(\omega), \quad (5.109)$$

and the impurity occupation number in layer α reads

$$n_d^{\alpha} = \sum_{\sigma} \int d\omega f(\omega) A_{d\sigma}^{\alpha}(\omega). \quad (5.110)$$

In order to ensure overall charge neutrality,

$$\sum_{\alpha} \Delta n_{\alpha} \stackrel{!}{=} 0 \quad (5.111)$$

has to be fulfilled. Similar to the bulk case, we add an energy shift μ_0 to the chemical potential in (5.19), (5.61) and (5.67):

$$\mu \rightarrow \mu + \mu_0. \quad (5.112)$$

With this, the left-hand side of (5.111) becomes a function of μ_0 and the task of ensuring overall charge neutrality reduces to a root finding problem.

5. Theory

The charge carrier density Δn_α generates an electrostatic potential ϕ_α which is determined by the Poisson equation (4.10)

$$\frac{\partial^2}{\partial \alpha^2} \phi_\alpha = -\kappa \Delta n_\alpha,$$

with $\kappa = \frac{e^2}{\varepsilon_0 a}$. For a given charge carrier density Δn_α , the resulting electrostatic potential can be calculated by discretizing the derivative in the Poisson equation in the following way:

$$\frac{\partial^2}{\partial \alpha^2} \phi_\alpha = \phi_{\alpha+1} + \phi_{\alpha-1} - 2\phi_\alpha.$$

Together with the boundary conditions for the electrostatic potential at the positions outside of the system, ϕ_0 and ϕ_{N+1} , we can write the Poisson equation as a system of linear equations

$$\begin{pmatrix} -\kappa \Delta n_1 - \phi_0 \\ -\kappa \Delta n_1 \\ \vdots \\ -\kappa \Delta n_{N-1} \\ -\kappa \Delta n_N - \phi_{N+1} \end{pmatrix} = \begin{pmatrix} -2 & 1 & & \\ 1 & -2 & 1 & \\ & \ddots & \ddots & \\ & & 1 & -2 & 1 \\ & & & 1 & -2 \end{pmatrix} \begin{pmatrix} \phi_1 \\ \phi_2 \\ \vdots \\ \phi_{N-1} \\ \phi_N \end{pmatrix}. \quad (5.113)$$

Since we want to simulate vacuum outside of our system, the electrostatic boundary conditions are given by

$$\phi_0 = \phi_{N+1} = 0. \quad (5.114)$$

The mirror symmetric case is discussed in appendix C. We solve the Poisson equation (5.113) for the electrostatic potential by using Gaussian elimination [62].

The contribution from the electrostatic potential to the conduction electron self energy originates in the first term of the Hamiltonian (4.11) and is calculated similar to the magnetic interaction in (5.90) by using (B.2). It reads

$$\Sigma_{c\sigma}^\alpha(z) = \phi_\alpha. \quad (5.115)$$

Analogously, the second term of the Hamiltonian (4.11) leads to an additional term in the impurity self-energy, which is given by

$$\Sigma_{d\sigma}^\alpha(z) = \phi_\alpha. \quad (5.116)$$

In the Gadolinium case, the energy shift enters the calculation of the impurity Green's function as an additional term in the pseudo-fermion self-energy:

$$\Sigma_{f\sigma}^\alpha(z) = \phi_\alpha. \quad (5.117)$$

5.4.2. Interfaces

If a multilayer system is comprised of more than one type of material, there is an additional subtlety in the self-consistent theory that has to be taken into account, the matching of energy scales. In this work we restrict ourselves to systems with two components in the non-mirror-symmetric case and three components in the mirror symmetric case, respectively. We will mostly consider interfaces of Europium monoxide films and some metallic substrate. The latter is characterized by omitting the impurity and Heisenberg lattice contributions to the self-energy in the substrate layers. The energy scheme for the isolated components of such a heterostructure is depicted in figure 5.7.

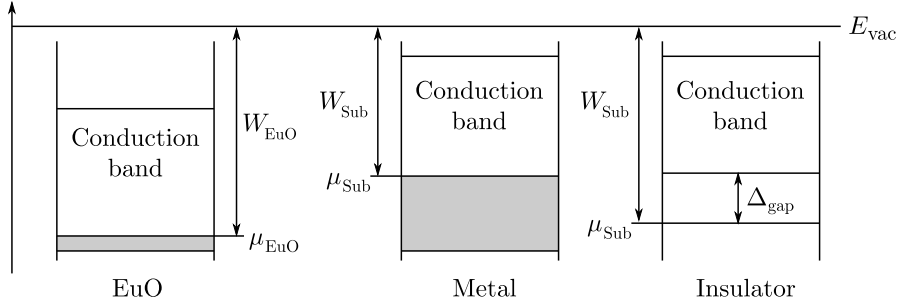


Figure 5.7.: Energy scheme for the isolated components of an EuO-substrate heterostructure. The work function $W = E_{\text{vac}} - \mu$ differs for various types of components. We consider metallic and insulating substrates. For the latter, the half insulating gap is given by Δ_{gap} .

The work function is the energy one has to pay in order to remove an electron from the Fermi edge and bring it to the vacuum $W = E_{\text{vac}} - \mu$. We define the work function difference as

$$\Delta W := W_{\text{EuO}} - W_{\text{Sub}}.$$

In order to match the energy scales of two components, the chemical potentials of the isolated systems must obey the following relation:

$$\mu_{\text{Sub}} = \mu_{\text{EuO}} + \Delta W.$$

For a moment we will assume that the work function difference is vanishing, $\mu_{\text{Sub}} = \mu_{\text{EuO}}$. In this case, we can match the chemical potentials in both isolated systems by shifting the energy of the electrons in both isolated systems according to

$$\begin{aligned} \varepsilon_{\mathbf{k}_{\parallel}}^{\alpha} &\rightarrow \varepsilon_{\mathbf{k}_{\parallel}}^{\alpha} + \tilde{\Delta}_0 \\ E_d &\rightarrow E_d + \tilde{\Delta}_0 \end{aligned} \quad \text{with} \quad \tilde{\Delta}_0 = \begin{cases} \Delta_{0l} & \text{for EuO layers} \\ \Delta_{0r} & \text{for Substrate layers} \end{cases}. \quad (5.118)$$

Here, the energy shifts Δ_{0l} and Δ_{0r} are chosen such that the charge neutrality condition (5.111) is fulfilled in both isolated systems. Since the energy of the electrons enters the conduction electron and impurity Green's functions ((5.19), (5.61) and (5.67)) with

5. Theory

opposite sign compared to the chemical potential, this is the case if

$$\begin{aligned}\Delta_{0l} &= -\mu_{0l} \\ \Delta_{0r} &= -\mu_{0r}\end{aligned}$$

holds. Here, μ_{0l} and μ_{0r} denote the energy shift in the isolated systems of Europium monoxide and substrate, respectively. Therewith, the chemical potential is equal in both parts of the composite heterostructure. If the work function difference is non-vanishing, we have

$$\begin{aligned}\Delta_{0l} &= -\mu_{0l} \\ \Delta_{0r} &= -\mu_{0r} + \Delta W.\end{aligned}\tag{5.119}$$

To obtain the energy shifts, one has to calculate the solution to both isolated systems. Afterwards one can shift the energies in (5.19), (5.67) and (5.61) according to (5.118) and (5.119) in order obtain the correct work function difference to enter a heterostructure calculation.

5.5. Self consistent theory

5.5.1. Self consistent formulation

In this section, we recall the most important formulas from the previous sections and combine them to a self-consistent theory. We will formulate the self-consistent theory in terms of the most general case, the multilayer system with long range RKKY coupling, and point out the simplifications of special cases during the discussion only if they are not obvious. The equations for the bulk case are always obtained by dropping the layer indices in the multilayer equations. Moreover, we set the chemical potential to zero in all remaining sections of this work. Due to the charge neutrality conditions ((5.103) and (5.111)) and the corresponding energy shift μ_0 (cf. section 5.4), this essentially results in a replacement of μ by μ_0 in all equations.

The central quantity is the local conduction electron self-energy ((5.1) and (5.19)). It reads

$$\Sigma_{c\sigma}^\alpha(z) = n_i V^2 G_{d\sigma}^\alpha(z) - J_{cf} \langle S_\alpha \rangle \sigma + \phi_\alpha$$

The first contribution stems from the hybridization with the randomly distributed impurities (5.48) and (5.56). The second and third contributions come from the ferromagnetic interaction with the localized $4f$ spins and the electrostatic energy shift due to charge variation along the perpendicular direction, respectively ((5.77), (5.90) and (5.115)). Note that the latter is not present in the bulk case due to the full translational invariance and the corresponding charge neutrality throughout the system. Together with the bare density of states ((4.5) and (4.14)), the knowledge of the local self-energy enables us to calculate the local as well as the non-local conduction electrons Green's function

from the momentum dependent conduction electron Green's function (cf. section 5.1).

$$\hat{G}_{c\sigma}^{-1}(\mathbf{k}_{\parallel}, z) = \begin{pmatrix} z - \varepsilon_{\mathbf{k}_{\parallel}}^1 + \mu_0 - \Sigma_{c\sigma}^1(z) & -t_2 & 0 & \cdots \\ -t_2 & z - \varepsilon_{\mathbf{k}_{\parallel}}^2 + \mu_0 - \Sigma_{c\sigma}^2(z) & -t_3 & \cdots \\ 0 & -t_3 & z - \varepsilon_{\mathbf{k}_{\parallel}}^3 + \mu_0 - \Sigma_{c\sigma}^3(z) & \cdots \\ \vdots & \vdots & \ddots & \ddots \end{pmatrix} \quad (5.19)$$

Note that according to the above discussion, we have replaced the chemical potential μ by the energy shift μ_0 here. The energy shift μ_0 has to be chosen such that the charge neutrality conditions are fulfilled. We will discuss the corresponding procedure below.

Besides the conduction electron self-energy and the corresponding Green's functions, the impurity Green's function plays a central role in the self-consistent theory. Most of the observables can be calculated solely from these two quantities. In the Gadolinium case, the pseudo-particle self-energies are calculated directly from the conduction electron spectral density via (5.57) and (5.58)

$$\begin{aligned} \text{Im}\tilde{\Sigma}_b^{\alpha}(\omega - i0^+) &= \Gamma \sum_{\sigma} \int d\varepsilon \frac{f(\varepsilon)(1 - f(\omega + \varepsilon))}{f(-\omega)} A_{c\sigma}^{\alpha}(\varepsilon) \tilde{A}_{f\sigma}^{\alpha}(\omega + \varepsilon), \\ \text{Im}\tilde{\Sigma}_{f\sigma}^{\alpha}(\omega - i0^+) &= \Gamma \int d\varepsilon \frac{f(-\varepsilon)(1 - f(\omega - \varepsilon))}{f(-\omega)} A_{c\sigma}^{\alpha}(\varepsilon) \tilde{A}_b^{\alpha}(\omega - \varepsilon). \end{aligned}$$

By considering the electrostatic energy shift (5.117) and the energy shift μ_0 connected to the charge neutrality, the pseudo-particle spectral densities are given by

$$\begin{aligned} \tilde{A}_b^{\alpha}(\omega) &= \frac{1}{\pi} \frac{\text{Im}\tilde{\Sigma}_b^{\alpha}(\omega)}{[\omega + \lambda_0 - \text{Re}\Sigma_b^{\alpha}(\omega)]^2 + [\text{Im}\Sigma_b^{\alpha}(\omega)]^2}, \\ \tilde{A}_{f\sigma}^{\alpha}(\omega) &= \frac{1}{\pi} \frac{\text{Im}\tilde{\Sigma}_{f\sigma}^{\alpha}(\omega)}{[\omega + \lambda_0 + \mu_0 - E_d - \phi_{\alpha} - \text{Re}\Sigma_{f\sigma}^{\alpha}(\omega)]^2 + [\text{Im}\Sigma_{f\sigma}^{\alpha}(\omega)]^2}, \end{aligned}$$

where λ_0 has to be determined such that

$$F^{\alpha}(\lambda_0) = \int d\omega f(\omega) \left[\sum_{\sigma} \tilde{A}_{f\sigma}^{\alpha}(\omega) + \tilde{A}_b^{\alpha}(\omega) \right] - 1 \stackrel{!}{=} 0 \quad (5.120)$$

holds. Finally, the impurity spectral density can be calculated by

$$A_{d\sigma}^{\alpha}(\omega) = \int d\varepsilon [f(\omega + \varepsilon)f(-\varepsilon) + f(-\varepsilon - \omega)f(\varepsilon)] \tilde{A}_{f\sigma}^{\alpha}(\omega + \varepsilon) \tilde{A}_b^{\alpha}(\varepsilon).$$

In contrast, in the Oxygen case, the impurity spectral density can be calculated directly from the corresponding self-energy under use of (5.67). It reads

$$A_{d\sigma}^{\alpha}(\omega) = \frac{1}{\pi} \frac{\text{Im}\Sigma_{d\sigma}^{\alpha}(\omega - i0^+)}{[\omega - E_d + \mu_0 - \text{Re}\Sigma_{d\sigma}^{\alpha}(\omega - i0^+)]^2 + [\text{Im}\Sigma_{d\sigma}^{\alpha}(\omega - i0^+)]^2}.$$

5. Theory

Considering the electrostatic contribution (5.117) and the impurity contributions (5.63), (5.64) and (5.66), the impurity self-energy is in total given by

$$\Sigma_{d\sigma}^{\alpha}(\omega - i0^+) = \phi_{\alpha} + V^2 G_{c\sigma}^{\alpha}(\omega - i0^+) + U \int d\varepsilon f(\varepsilon) A_{d-\sigma}^{\alpha}(\varepsilon) + \Sigma_{d\sigma}^{\alpha,(2)}(\omega - i0^+),$$

where the imaginary part of the second order term reads

$$\begin{aligned} \text{Im}\Sigma_{d\sigma}^{\alpha,(2)}(\omega - i0^+) = \pi U^2 \int d\alpha \int d\varepsilon A_{d\sigma}^{\alpha}(\omega + \varepsilon - \alpha) A_{d-\sigma}^{\alpha}(\alpha) A_{d-\sigma}^{\alpha}(\varepsilon) \\ \cdot [f(\alpha) - f(\varepsilon)] [f(\omega + \varepsilon - \alpha) + b(\varepsilon - \alpha)] . \end{aligned}$$

The real part is calculated using the Kramers-Kronig relation (see appendix D).

Both the conduction electron and the impurity Green's function have to be calculated with such a μ_0 that the charge neutrality condition ((5.103) and (5.111)) is obeyed. Moreover, in the Gadolinium case, a λ_0 has to be found so that the pseudo-particle number constraint (5.120) is fulfilled. In order to comply the charge neutrality condition a root finding algorithm is applied. For given self-energies, the spectral densities are calculated for several values of μ_0 during the procedure. In each iteration, which corresponds to a fixed value of μ_0 , another root finding algorithm for finding the correct λ_0 is applied. Both root finding algorithms are combined methods, which rely on the monotonic behavior of the function whose root needs to be found (cf. section 3.4). After scanning the region with increasing step width for two points with opposite signs, a bisection or secant method is applied. In the Gadolinium case, the multiple calculation of the impurity spectral density for various values of μ_0 would have a profound impact on the calculation time. Therefore, we use the pseudo-particle spectral density to calculate the impurity occupation number

$$n_d^{\alpha} = \sum_{\sigma} \int d\omega f(\omega) A_{d\sigma}^{\alpha}(\omega) = \sum_{\sigma} \int d\omega f(\omega) \tilde{A}_{f\sigma}^{\alpha}(\omega),$$

and calculate the impurity spectral density only after the root-finding procedure, i.e. when the right μ_0 is found.

In the following we discuss the spin expectation value $\langle S_{\alpha} \rangle$ and its dependence on the conduction electron Green's function (cf. section 5.3). The mean-field formula for the spin expectation values in layer α is given by

$$\langle S_{\alpha} \rangle = \frac{\sum_{S=-\frac{7}{2}}^{\frac{7}{2}} S e^{\beta(2J_{4f}^{\parallel} \langle S_{\alpha} \rangle + 2 \sum_{\beta \neq \alpha} J_{4f}^{\alpha\beta} \langle S_{\beta} \rangle + J_{cf} \langle \sigma_{\alpha} \rangle) S}}{\sum_{S=-\frac{7}{2}}^{\frac{7}{2}} e^{\beta(2J_{4f}^{\parallel} \langle S_{\alpha} \rangle + 2 \sum_{\beta \neq \alpha} J_{4f}^{\alpha\beta} \langle S_{\beta} \rangle + J_{cf} \langle \sigma_{\alpha} \rangle) S}}. \quad (5.84)$$

Here, the external parameters are the conduction electron spin

$$\langle \sigma_{\alpha} \rangle = \frac{1}{2} \int d\omega f(\omega) [A_{c\uparrow}^{\alpha}(\omega) - A_{c\downarrow}^{\alpha}(\omega)], \quad (5.89)$$

and, in the case of long range RKKY coupling, the parallel coupling

$$J_{4f}^{\parallel\alpha} = \sum_j J_{ij}^{\alpha\alpha} - \frac{J_{cf}^2}{2} \sum_{\substack{\mathbf{R}_{\parallel} \\ |\mathbf{R}_{\parallel}| < R_{\max}}} \sum_{\sigma} \int d\omega f(\omega) A_{c\sigma}^{\alpha}(\mathbf{R}_{\parallel}, \omega) \text{Re} G_{c\sigma}^{\alpha}(\mathbf{R}_{\parallel}, \omega - i0^+), \quad (5.96)$$

as well as the perpendicular coupling

$$J_{4f}^{\alpha\beta} = \sum_j J_{ij}^{\alpha\beta} - \frac{J_{cf}^2}{2} \sum_{\sigma} \int d\omega f(\omega) A_{c\sigma}^{\alpha\beta}(\omega) \text{Re} G_{c\sigma}^{\alpha\beta}(\omega - i0^+) \quad \text{for } \alpha \neq \beta. \quad (5.97)$$

Here, similar to (5.85), the constant perpendicular coupling is restricted to the nearest neighbors by

$$\sum_j J_{4f}^{\alpha\beta} = \begin{cases} J_{4f}^{\perp} & \text{for } \alpha = \beta \pm 1 \\ 0 & \text{else} \end{cases}.$$

In the bulk case, the perpendicular coupling is not present and the parallel coupling is replaced by the three dimensional coupling from equation (5.94).

Finally, we summarize the calculation of the electrostatic potential from the conduction electron and impurity spectral density discussed in section 5.4. According to equations (5.108), (5.109) and (5.110), the charge carrier density at layer α reads

$$\Delta n_{\alpha} = n_c^{\alpha} + n_i n_d^{\alpha} - n_{cc} = \sum_{\sigma} \int d\omega f(\omega) (A_{c\sigma}^{\alpha}(\omega) + n_i A_{d\sigma}^{\alpha}(\omega)) - n_{cc}.$$

The corresponding electrostatic potential is determined by solving the Poisson equation

$$\begin{pmatrix} -\kappa \Delta n_1 - \phi_0 \\ -\kappa \Delta n_1 \\ \vdots \\ -\kappa \Delta n_{N-1} \\ -\kappa \Delta n_N - \phi_{N+1} \end{pmatrix} = \begin{pmatrix} -2 & 1 & & \\ 1 & -2 & 1 & \\ & \ddots & \ddots & \\ & & 1 & -2 & 1 \\ & & & 1 & -2 \end{pmatrix} \begin{pmatrix} \phi_1 \\ \phi_2 \\ \vdots \\ \phi_{N-1} \\ \phi_N \end{pmatrix}, \quad (5.113)$$

via Gaussian elimination.

In summary, the main quantities of the self-consistent theory are the conduction electron Green's function, G_c^{α} , the impurity Green's function G_d^{α} , the mean-field spin expectation value $\langle S_{\alpha} \rangle$, and the electrostatic potential ϕ_{α} . Their dependencies are listed in table 5.1.

5.5.2. Numerical solution of the self-consistent theory

In the following, we will explain the details of the numerical solution of the self-consistent theory. Roughly speaking, a solution is obtained by inserting the quantities of table 5.1 into each other over and over again until these quantities reach a stable point. In this process, we use the imaginary part of the conduction electron and impurity spectral

5. Theory

Quantity	Dependence
G_c^α	$G_d^\alpha, \langle S_\alpha \rangle, \phi_\alpha$
G_d^α	$G_c^\alpha, G_d^\alpha, \phi_\alpha$
$\langle S_\alpha \rangle$	G_c^α
ϕ_α	G_c^α, G_d^α

Table 5.1.: Quantities of the self-consistent theory and their dependencies.

Green's function, i.e. the spectral densities. The real part is calculated via the Kramers-Kronig relation if needed.

We begin with a discussion about the proper resolution of the spectral densities involved. Both, $A_{c\sigma}^\alpha(\omega)$ and $A_{d\sigma}^\alpha(\omega)$ are defined on the same integration grid, which possesses several logarithmic cluster points to resolve the features occurring in both functions (see appendix E). The minimal resolution of the logarithmic grid regions is equal in order to ensure a smooth overlap. The first two regions are placed at the two impurity peaks in $A_{d\uparrow}^\alpha(\omega)$ and $A_{d\downarrow}^\alpha(\omega)$, which are tracked during the iteration procedure and the integration grid is adapted if necessary. In order to resolve the Fermi function properly, two logarithmic cluster points are placed at the two inflection points of the Fermi function $\log(2 \pm \sqrt{3})/\beta$. Their maximal resolution is chosen to be $0.04/\beta$. While ω changes, each time a peak in the momentum dependent conduction electron spectral density in the integral (5.35) overlaps with the bare density of states, a step in the local conduction electron spectral density occurs (see figure 5.1). The position of the peaks in ν space are found during the calculation of the conduction electron spectral density (cf. section 5.1.2). Therefore, we can identify the position of the steps in ω space by detecting a change in the number of peaks in ν space, which overlap with the bare density of states. Afterwards, each step is resolved by a logarithmic grid region. Obviously, the step positions will change during the iteration process and the corresponding grid regions must be adapted accordingly.

In the Gadolinium case, the modified pseudo-particle spectral densities $\tilde{A}_{f\sigma}^\alpha$ and \tilde{A}_b^α are used. As discussed in chapter 3, these functions possess two pronounced features at the position of the respective resonances. Therefore, we calculate the pseudo-particle spectral densities on a grid which features two logarithmic grid regions for the pseudo-particle resonances, and two grid regions to resolve the Fermi function similar to the above grid for the conduction electron and impurity spectral densities. The pseudo-particle peaks are also tracked during the iteration and the grid is adapted if necessary.

Besides the proper resolution of the spectral densities, the order in which the self-consistent equations are evaluated is of great importance. For instance, it may be necessary to iterate the conduction band and impurity spectral density for fixed spin and electrostatic potential value in a sub-loop. In doing so, G_c^α is always calculated from the G_d^α of the previous iteration and vice versa. The iteration procedure is sketched in figure 5.8. Moreover, a careful course of action during the iteration procedure is mandatory. This is achieved by mixing only a small fraction of the new solution to the old one in each iteration step. It is necessary to apply this relaxation on all four quantities of table

5.1.

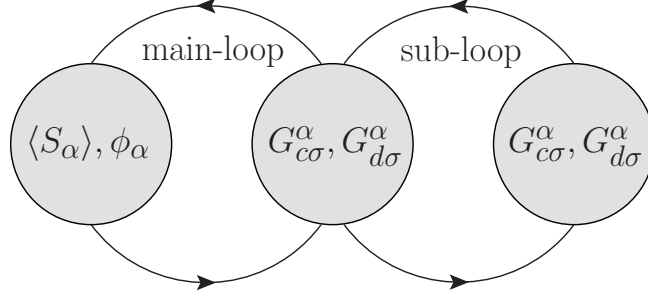


Figure 5.8.: Sketch of the iteration procedure for the solution of the self-consistent theory.

The numerical accuracy $\Delta(\Delta n_\alpha)$ with which the charge neutrality condition is fulfilled directly affects how well the doping in the system is realized. Moreover, since the accuracy of charge carrier density and conduction electron spin are comparable, $\Delta(\Delta n_\alpha) \approx \Delta\sigma$, the former has a huge impact on the magnetic properties of the system and therefore on the exact position of the Curie temperature. In order to increase the accuracy, one has to either increase the number of integration grid points or introduce an artificial imaginary part in the conduction electron and impurity self-energy:

$$\begin{aligned} \text{Im}\Sigma_{c\sigma}(\omega) &\rightarrow \text{Im}\Sigma_{c\sigma}(\omega) + \eta, \\ \text{Im}\Sigma_{d\sigma/f\sigma}(\omega) &\rightarrow \text{Im}\Sigma_{d\sigma/f\sigma}(\omega) + \zeta. \end{aligned}$$

This effectively broadens the resonances in the conduction band and impurity spectral densities. In particular, the spectral weight inside the high temperature gap in the conduction band spectral density is increased. Therefore, one has to decrease the number of excess charge carriers per Europium site by a small amount,

$$n_{cc} \rightarrow x_{cc}n_{cc}.$$

Here, $x_{cc} \lesssim 1$ and it is chosen such that the Fermi energy lies exactly in the middle of the gap in the high temperature phase conduction electron spectral density. Thus, we ensure that the high temperature phase is indeed insulating.

In view of the similarities in the bulk and multilayer theory, a single program which incorporates all special cases was created. It can be found in [63]. Especially the calculation of heterogeneous multilayer systems is extremely demanding with respect to computational resources, due to the multiple calculation of the conduction electron spectral density. Therefore, we implemented parallelizations at multiple points in the calculation. In most cases the frequency grid in ω space was split up among the subprocesses in an alternating fashion. In the case of two subprocesses for instance, the first one would calculate all even points and the second one all odd points. By this means, we ensure that the workload is evenly distributed among the subprocesses. This is necessary since the number of integration grid points strongly depends on the value of ω . As an example, we consider the calculation of the conduction band spectral density via (5.35). Here, the

5. Theory

number of resonances in $A_{c\sigma}^{\alpha\beta}(\nu, \omega)$ which overlaps with the bare density of states $N_{\parallel}(\nu)$ varies with the value of ω (cf. figure 5.1). Therefore, the number of integration grid points in ν space strongly depends on the value of ω and so does the calculation time.

5.6. Conductivity

After the solution of the self-consistent theory is found, one can calculate the transport properties solely from the converged solution for the conduction electron Green's function. This is the topic of the present section. We begin with a brief review of linear response theory and proceed to the calculation of the conductivity in the bulk case. Afterwards, the transport properties in multilayer systems are derived. The section concludes with details of the numerical calculation of the conductivity in both cases.

The conductivity is defined as the response function of the electric current $\mathbf{J}^e = (J_x^e, J_y^e, J_z^e)$ if one applies an external electric field $\mathbf{E} = (E_x, E_y, E_z)$:

$$J_i^e(\mathbf{r}, t) = \sum_j \int d^3r' \int dt \sigma_{ij}(\mathbf{r}, \mathbf{r}', t, t') E_j(\mathbf{r}', t').$$

Here, $\sigma_{ij}(\mathbf{r}, \mathbf{r}', t, t')$ are the conductivity tensor components. In the following, we will use the shorthand notation

$$\mathbf{J}^e(\mathbf{r}, t) = \int d^3r' \int dt \bar{\sigma}(\mathbf{r}, \mathbf{r}', t, t') \mathbf{E}(\mathbf{r}', t'). \quad (5.121)$$

For systems which are not explicitly time dependent, the conductivity depends only on the time difference,

$$\bar{\sigma}(\mathbf{r}, \mathbf{r}', t, t') = \bar{\sigma}(\mathbf{r}, \mathbf{r}', t - t').$$

Furthermore, it turns out to be beneficial to use the Fourier transform

$$\begin{aligned} \mathbf{J}^e(\mathbf{r}, t) &= \int d^3r' \int dt' \underbrace{\bar{\sigma}(\mathbf{r}, \mathbf{r}', t - t')}_{\int \frac{d\omega}{2\pi} e^{i\omega(t-t')} \bar{\sigma}(\mathbf{r}, \mathbf{r}', \omega)} \underbrace{\mathbf{E}(\mathbf{r}', t')}_{\int \frac{d\omega'}{2\pi} e^{i\omega' t'} \mathbf{E}(\mathbf{r}', \omega')} \\ &= \int d^3r' \int \frac{d\omega}{2\pi} e^{i\omega t} \bar{\sigma}(\mathbf{r}, \mathbf{r}', \omega) \mathbf{E}(\mathbf{r}', \omega). \end{aligned} \quad (5.122)$$

5.6.1. Linear response theory

In the following, we derive a general expression for the conductivity in linear response theory. In the course of this, we follow [55, 61]. We consider a system described by the Hamiltonian H_0 , which is perturbed by an external electric field. In the gauge where the external potential vanishes, $\phi = 0$, the perturbing Hamiltonian reads

$$H'_t = e \int d^3r \mathbf{J}(\mathbf{r}) \mathbf{A}_t(\mathbf{r}),$$

where \mathbf{J} is the particle current ($\mathbf{J}^e = -e\mathbf{J}$) and the subscript t indicates the explicit time dependence due to the external field $\mathbf{E}_t(\mathbf{r})$ with vector potential $\mathbf{A}_t(\mathbf{r})$. If we switch to the Heisenberg picture, an additional, implicit time dependence will occur:

$$H'_t(t) = e \int d^3r \mathbf{J}(\mathbf{r}, t) \mathbf{A}_t(\mathbf{r}). \quad (5.123)$$

According to [55], the current is given by a paramagnetic and a diamagnetic contribution

$$\mathbf{J}(\mathbf{r}) = \mathbf{J}_0(\mathbf{r}) + \frac{e}{m} (\mathbf{A}_0(\mathbf{r}) + \mathbf{A}(\mathbf{r})) \rho(\mathbf{r}), \quad (5.124)$$

where

$$\mathbf{J}_0(\mathbf{r}) = \frac{\hbar}{2mi} (\psi^\dagger(\mathbf{r}) \nabla_{\mathbf{r}} \psi(\mathbf{r}) - [\nabla_{\mathbf{r}} \psi^\dagger(\mathbf{r})] \psi(\mathbf{r})),$$

and $\mathbf{A}_0(\mathbf{r})$ is the vector potential in the system before the perturbation is applied. In our case, for vanishing magnetic field, we can set $\mathbf{A}_0(\mathbf{r})$ to zero. The expectation value of the current in linear response theory is given by [55, 61]

$$\langle \mathbf{J}(\mathbf{r}) \rangle_t = \langle \mathbf{J}(\mathbf{r}) \rangle_0 - \frac{i}{\hbar} \int_{-\infty}^t dt' \langle [\mathbf{J}(\mathbf{r}, t), H'_{t'}(t')] \rangle_0. \quad (5.125)$$

By inserting (5.124) into (5.123), and (5.125) and restricting ourselves to contributions linear in $\mathbf{A}_t(\mathbf{r})$, we obtain

$$\langle \mathbf{J}(\mathbf{r}) \rangle_t = \langle \mathbf{J}(\mathbf{r}) \rangle_0 - \frac{i}{\hbar} \int_{-\infty}^t dt' \langle [\mathbf{J}_0(\mathbf{r}, t), e \int d^3r' \mathbf{J}_0(\mathbf{r}', t') \mathbf{A}_{t'}(\mathbf{r}')] \rangle_0. \quad (5.126)$$

Using that the paramagnetic current vanishes in the unperturbed system $\langle \mathbf{J}_0(\mathbf{r}) \rangle_0 = 0$, the first term of equation (5.126) becomes

$$\begin{aligned} \langle \mathbf{J}(\mathbf{r}) \rangle_0 &= \frac{e}{m} \langle \rho(\mathbf{r}) \rangle_0 \underbrace{\mathbf{A}_t(\mathbf{r})}_{\int \frac{d\omega}{2\pi} e^{i\omega t} \mathbf{A}_\omega(\mathbf{r})} \\ &= \int d^3r' \int \frac{d\omega}{2\pi} e^{i\omega t} \left(\frac{e}{i\omega m} \delta(\mathbf{r} - \mathbf{r}') \langle \rho(\mathbf{r}) \rangle_0 \right) \mathbf{E}_\omega(\mathbf{r}), \end{aligned} \quad (5.127)$$

where we have used that $\mathbf{A}_\omega(\mathbf{r}) = \frac{1}{i\omega} \mathbf{E}_\omega(\mathbf{r})$. By introducing the current-current correlation function

$$\bar{\Pi}^R(\mathbf{r}, \mathbf{r}', t, t') = \bar{\Pi}^R(\mathbf{r}, \mathbf{r}', t - t') = -i\Theta(t - t') \langle [\mathbf{J}_0(\mathbf{r}, t), \mathbf{J}_0(\mathbf{r}', t')] \rangle_0,$$

the second term of equation (5.126) becomes

$$\begin{aligned} \langle \mathbf{J}(\mathbf{r}) \rangle_t - \langle \mathbf{J}(\mathbf{r}) \rangle_0 &= \frac{e}{\hbar} \int_{-\infty}^t dt' e \int d^3r' \underbrace{\bar{\Pi}^R(\mathbf{r}, \mathbf{r}', t - t')}_{\int \frac{d\omega}{2\pi} e^{i\omega(t-t')} \bar{\Pi}^R(\mathbf{r}, \mathbf{r}', \omega)} \underbrace{\mathbf{A}_{t'}(\mathbf{r}')}_{\int \frac{d\omega'}{2\pi} e^{i\omega' t'} \mathbf{A}_{\omega'}(\mathbf{r}')} \\ &= \int d^3r' \int \frac{d\omega}{2\pi} e^{i\omega t} \left(\frac{e}{i\hbar\omega} \bar{\Pi}^R(\mathbf{r}, \mathbf{r}', \omega) \right) \mathbf{E}_\omega(\mathbf{r}'). \end{aligned} \quad (5.128)$$

5. Theory

Finally, we compare equations (5.127) and (5.128) with (5.122) to read off the conductivity

$$\sigma_{ij}(\mathbf{r}, \mathbf{r}', \omega) = \frac{ie^2}{\hbar\omega} \Pi_{ij}^R(\mathbf{r}, \mathbf{r}', \omega) - \frac{e^2}{i\omega m} \delta(\mathbf{r} - \mathbf{r}') \delta_{ij} \langle \rho(\mathbf{r}) \rangle_0. \quad (5.129)$$

From now on, we will restrict ourselves to the dissipative part of the conductivity. Therefore, we take the real part of (5.129),

$$\sigma_{ij}(\mathbf{r}, \mathbf{r}', \omega) = -\frac{e^2}{\hbar\omega} \text{Im} \Pi_{ij}^R(\mathbf{r}, \mathbf{r}', \omega). \quad (5.130)$$

Thus, we have reduced the problem of calculating the conductivity to the calculation of the current-current correlation function. From now on, we will skip the subscript in the paramagnetic current, so that the tensor components of the current-current correlation function read

$$\Pi_{ij}^R(\mathbf{r}, \mathbf{r}', t, t') = \Pi_{ij}^R(\mathbf{r}, \mathbf{r}', t - t') = -i\Theta(t - t') \langle [J_i(\mathbf{r}, t), J_j(\mathbf{r}', t')] \rangle_0.$$

5.6.2. Conductivity in the bulk system

In the following section, we will show how to calculate the conductivity (5.130) in the bulk case. This was done in [25], but will be performed here in greater detail for the sake of completeness. In this work, we mainly follow [55]. Since the system is translationally invariant in all directions, the conductivity tensor becomes diagonal and independent of the direction,

$$\sigma_{ij}(\mathbf{r}, \mathbf{r}', \omega) = \delta_{ij} \sigma(\mathbf{r}, \mathbf{r}', \omega).$$

Moreover, it depends only on the spatial difference:

$$\sigma(\mathbf{r}, \mathbf{r}', \omega) = \sigma(\mathbf{r} - \mathbf{r}', \omega). \quad (5.131)$$

By using (5.131) in equation (5.122) and Fourier transforming, one obtains

$$\begin{aligned} J_i^e(\mathbf{r}, t) &= \int d^3 r' \int \frac{d\omega}{2\pi} e^{i\omega t} \underbrace{\sigma(\mathbf{r} - \mathbf{r}', \omega)}_{\int \frac{d^3 k}{(2\pi)^3} e^{i\mathbf{k}(\mathbf{r}-\mathbf{r}')} \sigma(\mathbf{k}, \omega)} \underbrace{E_i(\mathbf{r}', \omega)}_{\int \frac{d^3 k'}{(2\pi)^3} e^{i\mathbf{k}'\mathbf{r}'} E_i(\mathbf{k}', \omega)} \\ &= \int \frac{d^3 k}{(2\pi)^3} \int \frac{d\omega}{2\pi} e^{i(\mathbf{k}\mathbf{r} + \omega t)} \underbrace{\sigma(\mathbf{k}, \omega) E_i(\mathbf{k}, \omega)}_{J_i^e(\mathbf{k}, \omega)}, \end{aligned}$$

and therefore

$$J_i^e(\mathbf{k}, \omega) = \sigma(\mathbf{k}, \omega) E_i(\mathbf{k}, \omega). \quad (5.132)$$

We are interested in the response of the system to a spatially homogeneous and time independent electric field

$$E_i(\mathbf{r}, t) = \int \frac{d^3 k}{(2\pi)^3} \int \frac{d\omega}{2\pi} e^{i(\mathbf{k}\mathbf{r} + \omega t)} E_i(\mathbf{k}, \omega) = \text{const.},$$

and we obtain

$$E_i(\mathbf{k}, \omega) \propto \delta(\mathbf{k})\delta(\omega).$$

The same holds for the current and the conductivity in (5.132). The quantity of interest is the DC-conductivity defined by

$$\sigma = \lim_{\omega \rightarrow 0} \lim_{\mathbf{k} \rightarrow 0} \sigma(\mathbf{k}, \omega). \quad (5.133)$$

The resistivity ρ is then given by the inverse of the conductivity. It reads

$$\rho = \frac{1}{\sigma}. \quad (5.134)$$

Current-current correlation function

Based on (5.133) and (5.130), we aim to calculate the current-current correlation function in wavenumber and frequency space for finite temperatures. For this purpose, we begin by considering the Matsubara current-current correlation function. Since the conductivity is diagonal and isotropic we will restrict our discussion to the Matsubara current-current correlation function in x -direction:

$$\begin{aligned} \Pi_{xx}(\mathbf{r}, \mathbf{r}', \tau, \tau') &= \Pi_{xx}(\mathbf{r} - \mathbf{r}', \tau - \tau') \\ &= \int \frac{d^3k}{(2\pi)^3} e^{i\mathbf{k}(\mathbf{r}-\mathbf{r}')} \frac{1}{\hbar\beta} \sum_n e^{i\omega_n(\tau-\tau')} \tilde{\Pi}_{xx}(\mathbf{k}, i\omega_n) \\ &= \frac{1}{\mathcal{V}N} \sum_{\mathbf{k}} e^{i\mathbf{k}(\mathbf{r}-\mathbf{r}')} \frac{1}{\hbar\beta} \sum_n e^{i\omega_n(\tau-\tau')} \tilde{\Pi}_{xx}(\mathbf{k}, i\omega_n) \end{aligned} \quad (5.135)$$

$$= \frac{1}{N} \sum_{\mathbf{k}} e^{i\mathbf{k}(\mathbf{r}-\mathbf{r}')} \frac{1}{\hbar\beta} \sum_n e^{i\omega_n(\tau-\tau')} \Pi_{xx}(\mathbf{k}, i\omega_n). \quad (5.136)$$

Here, we have performed the transformation from continuous to discrete momentum vectors to account for the finite system size (cf. section 5.1.1). Concomitantly, we have incorporated the factor $\frac{1}{\mathcal{V}}$ in the definition $\Pi_{xx}(\mathbf{k}, i\omega_n)$ in the last step. On the other hand, if we insert the Fourier transform of the current operators directly, we have

$$\begin{aligned} \Pi_{xx}(\mathbf{r} - \mathbf{r}', \tau - \tau') &= -\langle T_\tau J_x(\mathbf{r}, \tau) J_x(\mathbf{r}', \tau') \rangle \\ &= -\langle T_\tau \frac{1}{N} \sum_{\mathbf{k}} \frac{1}{N} \sum_{\mathbf{k}'} e^{i(\mathbf{k}\mathbf{r} + \mathbf{k}'\mathbf{r}')} \\ &\quad \cdot \frac{1}{(\hbar\beta)^2} \sum_{nm} e^{i(\omega_n\tau + \omega_m\tau')} J_x(\mathbf{k}, i\omega_n) J_x(\mathbf{k}', i\omega_m) \rangle \\ &= -\frac{1}{N} \sum_{\mathbf{k}} e^{i\mathbf{k}(\mathbf{r}-\mathbf{r}')} \frac{1}{\hbar\beta} \sum_n e^{i\omega_n(\tau-\tau')} \\ &\quad \cdot \underbrace{\frac{1}{N} \sum_{\mathbf{k}'} e^{i(\mathbf{k}+\mathbf{k}')\mathbf{r}'} \frac{1}{\hbar\beta} \sum_m e^{i(\omega_n+\omega_m)\tau'} \langle J_x(\mathbf{k}, i\omega_n) J_x(\mathbf{k}', i\omega_m) \rangle}_{\Pi_{xx}(\mathbf{k}, i\omega_n)}. \end{aligned}$$

5. Theory

In the last step we used that $\tau - \tau' \in [0, \hbar\beta]$ is already time ordered. Since $\Pi_{xx}(\mathbf{k}, i\omega_n)$ can not depend on \mathbf{r}' or τ' we have $\mathbf{k}' = -\mathbf{k}$ and $\omega_m = -\omega_n$, and hence

$$\Pi_{xx}(\mathbf{k}, i\omega_n) = -\frac{1}{\tilde{\mathcal{V}}\hbar\beta} \langle T_\tau J_x(\mathbf{k}, i\omega_n) J_x(-\mathbf{k}, -i\omega_n) \rangle. \quad (5.137)$$

For better readability, we introduced the factor $\tilde{\mathcal{V}} = \mathcal{V}N$.

Current operator

In order to calculate (5.137), we need the current operator in wavenumber and frequency space. We start with the continuity equation for the particle density

$$\nabla_{\mathbf{r}} \cdot \mathbf{J}(\mathbf{r}, t) = -\frac{\partial}{\partial t} \rho(\mathbf{r}, t), \quad (5.138)$$

and its Fourier transform

$$i\mathbf{q} \cdot \mathbf{J}(\mathbf{q}, t) = -\frac{\partial}{\partial t} \rho(\mathbf{q}, t).$$

If we assume that the external electric field is directed in x -direction, we have $J_y = J_z = 0$ and hence

$$\begin{aligned} J_x(\mathbf{q}, t) &= -\frac{1}{iq_x} \frac{\partial}{\partial t} \rho(\mathbf{q}, t) \\ &= -\frac{1}{\hbar q_x} [\rho(\mathbf{q}, t), H] \\ &= -\frac{1}{\hbar q_x} \sum_{\mathbf{k}, \sigma} (\varepsilon_{\mathbf{k}} - \varepsilon_{\mathbf{k}-\mathbf{q}}) c_{\mathbf{k}-\mathbf{q}\sigma}^\dagger(t) c_{\mathbf{k}\sigma}(t), \end{aligned} \quad (5.139)$$

where the calculation of the commutator in the second step is shown in appendix A.1. Note that hereby the current operator is restricted to discrete momentum values inside the Brillouin zone and the transformation in (5.136) is justified. After performing the analytic continuation to imaginary time, the current operator reads

$$\begin{aligned} J_x(\mathbf{q}, \tau) &= -\frac{1}{\hbar q_x} \sum_{\mathbf{k}, \sigma} (\varepsilon_{\mathbf{k}} - \varepsilon_{\mathbf{k}-\mathbf{q}}) c_{\mathbf{k}-\mathbf{q}\sigma}^\dagger(\tau) c_{\mathbf{k}\sigma}(\tau) \\ &= -\frac{1}{\hbar q_x} \sum_{\mathbf{k}, \sigma} (\varepsilon_{\mathbf{k}} - \varepsilon_{\mathbf{k}-\mathbf{q}}) \frac{1}{(\hbar\beta)^2} \sum_{ml} e^{i(\omega_l - \omega_m)\tau} c_{\mathbf{k}-\mathbf{q}\sigma}^\dagger(i\omega_m) c_{\mathbf{k}\sigma}(i\omega_l). \end{aligned} \quad (5.140)$$

Inserting (5.140) into the Fourier transform yields

$$\begin{aligned} J_x(\mathbf{q}, i\omega_n) &= \int d\tau e^{-i\omega_n\tau} J_x(\mathbf{q}, \tau) \\ &= -\frac{1}{\hbar q_x} \sum_{\mathbf{k}, \sigma} (\varepsilon_{\mathbf{k}} - \varepsilon_{\mathbf{k}-\mathbf{q}}) \frac{1}{(\hbar\beta)^2} \sum_{ml} \underbrace{\int_0^{\hbar\beta} d\tau e^{i(\omega_l - \omega_m - \omega_n)\tau}}_{\hbar\beta\delta(\omega_l - \omega_n - \omega_m)} c_{\mathbf{k}-\mathbf{q}\sigma}^\dagger(i\omega_m) c_{\mathbf{k}\sigma}(i\omega_l) \\ &= -\frac{1}{\hbar q_x} \sum_{\mathbf{k}, \sigma} (\varepsilon_{\mathbf{k}} - \varepsilon_{\mathbf{k}-\mathbf{q}}) \frac{1}{\hbar\beta} \sum_l c_{\mathbf{k}-\mathbf{q}\sigma}^\dagger(i\omega_l - i\omega_n) c_{\mathbf{k}\sigma}(i\omega_l). \end{aligned} \quad (5.141)$$

According to (5.133), we are interested in the limit $\mathbf{q} \rightarrow 0$. The energy difference becomes a derivative and we have

$$\lim_{\mathbf{q} \rightarrow 0} J_x(\pm \mathbf{q}, \pm i\omega_n) = -\frac{1}{\hbar} \sum_{\mathbf{k}, \sigma} \frac{\partial \varepsilon_{\mathbf{k}}}{\partial k_x} \frac{1}{\hbar \beta} \sum_l c_{\mathbf{k}\sigma}^\dagger(i\omega_l \mp i\omega_n) c_{\mathbf{k}\sigma}(i\omega_l). \quad (5.142)$$

Diagrammatic evaluation

We proceed by inserting (5.142) into (5.137) and taking the limit $\mathbf{q} \rightarrow 0$,

$$\lim_{\mathbf{q} \rightarrow 0} \Pi_{xx}(\mathbf{q}, i\omega_n) = \frac{-1}{\tilde{\mathcal{V}} \hbar^5 \beta^3} \sum_{\substack{\mathbf{k} \mathbf{p} \\ \sigma \sigma'}} \frac{\partial \varepsilon_{\mathbf{k}}}{\partial k_x} \frac{\partial \varepsilon_{\mathbf{p}}}{\partial p_x} \sum_{lm} \langle c_{\mathbf{k}\sigma}^\dagger(i\omega_l - i\omega_n) c_{\mathbf{k}\sigma}(i\omega_l) c_{\mathbf{p}\sigma'}^\dagger(i\omega_m + i\omega_n) c_{\mathbf{p}\sigma'}(i\omega_m) \rangle. \quad (5.143)$$

In order to evaluate the expectation value in (5.143) we will use Feynman diagrams. The task at hand is now to connect the two vertices shown in figure 5.9, i.e. to find all possible

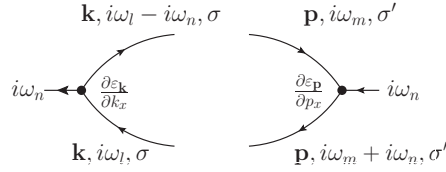


Figure 5.9.: Vertices for the current-current correlation function

contractions of the expectation value in (5.143) according to the bulk model Hamiltonian (4.1). Since all interactions preserve spin, momentum and energy, we have $\sigma = \sigma'$, $\mathbf{k} = \mathbf{p}$ and $\omega_l = \omega_m + \omega_n$. Moreover, the only interaction which can connect the upper and lower fermion lines in figure 5.9 is the impurity scattering. Therefore, we can write (5.143) in terms of dressed Green's functions

$$\lim_{\mathbf{q} \rightarrow 0} \Pi_{xx}(\mathbf{q}, i\omega_n) = \text{Diagram 1} + \text{Diagram 2} + \text{Diagram 3} + \dots \quad (5.144)$$

The double lines denotes the full propagator (see equation (5.2)). In the following, we will neglect the vertex corrections and restrict ourselves to the first contribution in (5.144). We begin with the calculation of the undressed version of this particular diagram.

5. Theory

Afterwards, we will replace the bare propagators by the full ones.

$$\begin{aligned}
\lim_{\mathbf{q} \rightarrow 0} \Pi_{xx}^0(\mathbf{q}, i\omega_n) &= \text{Diagram: A bubble with two vertices. The left vertex is labeled with momentum $\mathbf{k}, i\omega_l - i\omega_n, \sigma$ and the right vertex with $\mathbf{p}, i\omega_m, \sigma'$. The left vertex also has $\mathbf{k}, i\omega_l, \sigma$ below it. The right vertex also has $\mathbf{p}, i\omega_m + i\omega_n, \sigma'$ below it. The bubble contains two internal lines: one labeled $\frac{\partial \varepsilon_{\mathbf{k}}}{\partial k_x}$ and the other $\frac{\partial \varepsilon_{\mathbf{p}}}{\partial p_x}$} \\
&= \frac{-1}{\tilde{\mathcal{V}} \hbar^5 \beta^3} \sum_{\mathbf{k}\mathbf{p}} \frac{\partial \varepsilon_{\mathbf{k}}}{\partial k_x} \frac{\partial \varepsilon_{\mathbf{p}}}{\partial p_x} \sum_{lm} \overbrace{c_{\mathbf{k}\sigma}^\dagger(i\omega_l - i\omega_n) c_{\mathbf{k}\sigma}(i\omega_l) c_{\mathbf{p}\sigma'}^\dagger(i\omega_m + i\omega_n) c_{\mathbf{p}\sigma'}(i\omega_m)}^{c_{\mathbf{p}\sigma'}(i\omega_m) c_{\mathbf{k}\sigma}^\dagger(i\omega_l - i\omega_n) c_{\mathbf{k}\sigma}(i\omega_l) c_{\mathbf{p}\sigma'}^\dagger(i\omega_m + i\omega_n) (-1)^3} \\
&= \frac{1}{\tilde{\mathcal{V}} \hbar^2} \sum_{\mathbf{k}\sigma} \left(\frac{\partial \varepsilon_{\mathbf{k}}}{\partial k_x} \right)^2 \frac{1}{\hbar \beta} \sum_m G_{\mathbf{c}\mathbf{k}\sigma}^0(i\omega_m) G_{\mathbf{c}\mathbf{k}\sigma}^0(i\omega_m + i\omega_n),
\end{aligned}$$

where we have used $\overbrace{c_{\mathbf{k}\sigma}(i\omega_l) c_{\mathbf{p}\sigma'}^\dagger(i\omega_m)}^{\delta_{\mathbf{k}\parallel\mathbf{p}} \delta_{\sigma\sigma'}}$ and

$$\begin{aligned}
\overbrace{c_{\mathbf{k}\sigma}(i\omega_l) c_{\mathbf{k}\sigma}^\dagger(i\omega_m)} &= \int d\tau \int d\tau' e^{-i(\omega_n \tau - \omega_l \tau')} \overbrace{c_{\mathbf{k}\sigma}(\tau) c_{\mathbf{k}\sigma}^\dagger(\tau')}^{c_{\mathbf{k}\sigma}(\tau) c_{\mathbf{k}\sigma}^\dagger(\tau')} \\
&\quad - G_{\mathbf{c}\mathbf{k}\sigma}^0(\tau - \tau') = -\frac{1}{\hbar \beta} \sum_m e^{i\omega_m(\tau - \tau')} G_{\mathbf{c}\mathbf{k}\sigma}^0(i\omega_m) \\
&= -\frac{1}{\hbar \beta} \sum_m G_{\mathbf{c}\mathbf{k}\sigma}^0(i\omega_m) \underbrace{\int d\tau e^{i(\omega_m - \omega_n)\tau}}_{\hbar \beta \delta_{mn}} \underbrace{\int d\tau' e^{i(\omega_l - \omega_m)\tau'}}_{\hbar \beta \delta_{lm}} \\
&= -\hbar \beta \delta_{ln} G_{\mathbf{c}\mathbf{k}\sigma}^0(i\omega_n).
\end{aligned}$$

By replacing the bare propagators by the full propagators, we obtain

$$\begin{aligned}
\lim_{\mathbf{q} \rightarrow 0} \Pi_{xx}(\mathbf{q}, i\omega_n) &= \text{Diagram: A bubble with two vertices. The left vertex is labeled with momentum $\mathbf{k}, i\omega_m$ and the right vertex with $\mathbf{k}, i\omega_m + i\omega_n$. Both vertices also have $\frac{\partial \varepsilon_{\mathbf{k}}}{\partial k_x}$ next to them. The bubble contains two internal lines, both labeled $\frac{\partial \varepsilon_{\mathbf{k}}}{\partial k_x}$} \\
&= \frac{1}{\tilde{\mathcal{V}} \hbar^2} \sum_{\mathbf{k}\sigma} \left(\frac{\partial \varepsilon_{\mathbf{k}}}{\partial k_x} \right)^2 \frac{1}{\hbar \beta} \sum_m G_{\mathbf{c}\mathbf{k}\sigma}(i\omega_m) G_{\mathbf{c}\mathbf{k}\sigma}(i\omega_m + i\omega_n) \\
&= \frac{1}{\tilde{\mathcal{V}} \hbar^2} \sum_{\mathbf{k}\sigma} \left(\frac{\partial \varepsilon_{\mathbf{k}}}{\partial k_x} \right)^2 \int_{-\infty}^{\infty} d\varepsilon f(\varepsilon) A_{\mathbf{c}\mathbf{k}\sigma}(\varepsilon) [G_{\mathbf{c}\mathbf{k}\sigma}(\varepsilon + i\omega_n) + G_{\mathbf{c}\mathbf{k}\sigma}(\varepsilon - i\omega_n)].
\end{aligned} \tag{5.145}$$

The evaluation of the Matsubara sum in the second step is shown in appendix A.3. After analytic continuation back to real frequencies we can calculate the imaginary part of the

retarded current-current correlation function. This is also shown in A.3 and yields

$$\lim_{\mathbf{q} \rightarrow 0} \text{Im} \Pi_{xx}^R(\mathbf{q}, \omega) = \frac{\pi}{\tilde{\mathcal{V}} \hbar^2} \sum_{\mathbf{k}\sigma} \left(\frac{\partial \varepsilon_{\mathbf{k}}}{\partial k_x} \right)^2 \int d\varepsilon [f(\varepsilon) - f(\varepsilon - \omega)] A_{c\mathbf{k}\sigma}(\varepsilon) A_{c\mathbf{k}\sigma}(\varepsilon - \omega). \quad (5.146)$$

Finally, we are able to calculate the DC-conductivity according to (5.133), (5.130) and (5.146):

$$\begin{aligned} \sigma &= \lim_{\mathbf{q} \rightarrow 0} \lim_{\omega \rightarrow 0} \sigma(\mathbf{q}, \omega) \\ &= -\frac{e^2}{\hbar} \lim_{\omega \rightarrow 0} \lim_{\mathbf{q} \rightarrow 0} \frac{\text{Im} \Pi_{xx}(\mathbf{q}, \omega + i0^+)}{\omega} \\ &= -\frac{e^2 \pi}{\tilde{\mathcal{V}} \hbar^3} \sum_{\mathbf{k}\sigma} \left(\frac{\partial \varepsilon_{\mathbf{k}}}{\partial k_x} \right)^2 \int d\varepsilon \lim_{\omega \rightarrow 0} \frac{f(\varepsilon) - f(\varepsilon - \omega)}{\omega} A_{c\mathbf{k}\sigma}(\varepsilon) A_{c\mathbf{k}\sigma}(\varepsilon - \omega) \\ &= \frac{e^2 \pi}{\tilde{\mathcal{V}} \hbar^3} \sum_{\mathbf{k}\sigma} \left(\frac{\partial \varepsilon_{\mathbf{k}}}{\partial k_x} \right)^2 \int d\varepsilon \left(-\frac{\partial f(\varepsilon)}{\partial \varepsilon} \right) [A_{c\mathbf{k}\sigma}(\varepsilon)]^2. \end{aligned} \quad (5.147)$$

5.6.3. Parallel and perpendicular conductivity in the multilayer system

In the multilayer system, translational symmetry is broken in the z -direction. Therefore, we write $\mathbf{r} = (\mathbf{r}_{\parallel}, \alpha)$ and the spatial integration becomes $\int d^3r = \int d\alpha \int d^2r$. The calculation will be analogous to the one for the bulk model, except that we will Fourier transform only in the parallel direction. The conductivity tensor is still diagonal but differs for directions parallel and perpendicular to the $x - y$ plane.

$$\sigma_{ij}(\mathbf{r}, \mathbf{r}', \omega) = \delta_{ij} \sigma_i(\mathbf{r}, \mathbf{r}', \omega),$$

with

$$\sigma_x(\mathbf{r}, \mathbf{r}', \omega) = \sigma_y(\mathbf{r}, \mathbf{r}', \omega). \quad (5.148)$$

Moreover, it depends only on the spatial difference in the $x - y$ plane,

$$\sigma_i(\alpha, \mathbf{r}_{\parallel}, \beta, \mathbf{r}'_{\parallel}, \omega) = \sigma_i(\alpha, \beta, \mathbf{r}_{\parallel} - \mathbf{r}'_{\parallel}, \omega). \quad (5.149)$$

By using (5.149) in equation (5.122) and Fourier transforming, one obtains

$$\begin{aligned} J_i^e(\alpha, \mathbf{r}_{\parallel}, t) &= \int d\beta \int d^2r' \int \frac{d\omega}{2\pi} e^{i\omega t} \underbrace{\sigma_i(\alpha, \beta, \mathbf{r}_{\parallel} - \mathbf{r}'_{\parallel}, \omega)}_{\int \frac{d^2k}{(2\pi)^2} e^{i\mathbf{k}_{\parallel}(\mathbf{r}_{\parallel} - \mathbf{r}'_{\parallel})} \sigma_i(\alpha, \beta, \mathbf{k}_{\parallel}, \omega)} \underbrace{E_i(\beta, \mathbf{r}'_{\parallel}, \omega)}_{\int \frac{d^2k'}{(2\pi)^2} e^{i\mathbf{k}'_{\parallel} \mathbf{r}'_{\parallel}} E_i(\beta, \mathbf{k}'_{\parallel}, \omega)} \\ &= \int \frac{d^2k}{(2\pi)^2} \int \frac{d\omega}{2\pi} e^{i(\mathbf{k}_{\parallel} \mathbf{r}_{\parallel} + \omega t)} \underbrace{\int d\beta \sigma_i(\alpha, \beta, \mathbf{k}_{\parallel}, \omega) E_i(\beta, \mathbf{k}_{\parallel}, \omega)}_{J_i^e(\alpha, \mathbf{k}_{\parallel}, \omega)}, \end{aligned}$$

5. Theory

and therefore

$$J_i^e(\alpha, \mathbf{k}_\parallel, \omega) = \int d\beta \sigma_i(\alpha, \beta, \mathbf{k}_\parallel, \omega) E_i(\beta, \mathbf{k}_\parallel, \omega). \quad (5.150)$$

Since the external electric field is assumed to be time independent and spatially homogeneous in the $x - y$ plane, we have

$$E_i(\alpha, \mathbf{k}_\parallel, \omega) \propto \delta(\mathbf{k}_\parallel) \delta(\omega).$$

By inserting this into (5.150), we see that the quantity of interest is

$$\sigma_i(\alpha, \beta) = \lim_{\omega \rightarrow 0} \lim_{\mathbf{k}_\parallel \rightarrow 0} \sigma_i(\alpha, \beta, \mathbf{k}_\parallel, \omega), \quad (5.151)$$

which is the DC-conductivity between the layers α and β . We define the parallel conductivity in layer α as

$$\sigma_\parallel(\alpha) := \sigma_x(\alpha, \alpha) = \sigma_y(\alpha, \alpha), \quad (5.152)$$

and the perpendicular conductivity between the layers α and β as

$$\sigma_\perp(\alpha, \beta) := \sigma_z(\alpha, \beta). \quad (5.153)$$

In order to assess the transport properties along the parallel direction, we define the parallel resistivity as

$$\rho_\parallel(\alpha) = \frac{1}{\sigma_\parallel(\alpha)}. \quad (5.154)$$

In an experiment, the perpendicular transport through a multilayer system would be probed by applying a voltage U_\perp between the outer layers. Moreover, the current density along the perpendicular direction has to be constant $J_\perp^e(\alpha) = J_\perp^e$ [49]. In this case, (5.150) becomes

$$\begin{aligned} J_\perp^e &:= \lim_{\omega \rightarrow 0} \lim_{\mathbf{k}_\parallel \rightarrow 0} J_z^e(\alpha, \mathbf{k}_\parallel, \omega) \\ &= \int d\beta \sigma_\perp(\alpha, \beta) \underbrace{\lim_{\omega \rightarrow 0} \lim_{\mathbf{k}_\parallel \rightarrow 0} E_z(\beta, \mathbf{k}_\parallel, \omega)}_{=: E_\perp(\beta)} \\ &= \tilde{a} \sum_\beta \sigma_\perp(\alpha, \beta) E_\perp(\beta) \end{aligned}$$

where the β integral was replaced by the sum over discrete perpendicular positions. The factor $\tilde{a} = a/2$ is the interlayer distance. This is a matrix equation in the layer indices, which can be solved for the electric field by inverting the conductivity matrix $\sigma_\perp(\alpha, \beta)$:

$$E(\alpha) = \frac{1}{\tilde{a}} \sum_\beta \sigma_\perp^{-1}(\alpha, \beta) J_\perp^e,$$

where $\sigma_{\perp}^{-1}(\alpha, \beta)$ is the α, β element of the inverse of the conductivity matrix. With this, we can derive the voltage-current relation

$$U_{\perp} = \tilde{a} \sum_{\alpha} E_{\alpha} = J_{\perp}^e \underbrace{\sum_{\alpha\beta} (\sigma_{\perp})_{\alpha\beta}^{-1}}_{=:\rho_{\perp}},$$

where we have introduced the perpendicular resistivity

$$\rho_{\perp} = \sum_{\alpha\beta} (\sigma_{\perp})_{\alpha\beta}^{-1}, \quad (5.155)$$

as the quantity which is relevant for experiments. In a multilayer system with a surface area A , the resistance R would be

$$R = \frac{\rho_{\perp}}{A},$$

and Ohm's law $U_{\perp} = RI$ would hold with a current $I = J_{\perp}^e A$.

Current-current correlation function

Analogously to the bulk model calculation and based on (5.133) and (5.130), we will proceed by writing down the Matsubara current-current correlation function and Fourier transforming in the parallel direction.

$$\begin{aligned} \Pi_{ii}(\mathbf{r}, \mathbf{r}', \tau, \tau') &= \Pi_{ii}(\alpha, \beta, \mathbf{r}_{\parallel} - \mathbf{r}'_{\parallel}, \tau - \tau') \\ &= \int \frac{d^2 k}{(2\pi)^2} e^{i\mathbf{k}_{\parallel}(\mathbf{r}_{\parallel} - \mathbf{r}'_{\parallel})} \frac{1}{\hbar\beta} \sum_n e^{i\omega_n(\tau - \tau')} \tilde{\Pi}_{ii}(\alpha, \beta, \mathbf{k}_{\parallel}, i\omega_n) \\ &= \frac{1}{\mathcal{V}_{2D} N_{\parallel}} \sum_{\mathbf{k}_{\parallel}} e^{i\mathbf{k}_{\parallel}(\mathbf{r}_{\parallel} - \mathbf{r}'_{\parallel})} \frac{1}{\hbar\beta} \sum_n e^{i\omega_n(\tau - \tau')} \tilde{\Pi}_{ii}(\alpha, \beta, \mathbf{k}_{\parallel}, i\omega_n) \end{aligned} \quad (5.156)$$

$$= \frac{1}{N_{\parallel}} \sum_{\mathbf{k}_{\parallel}} e^{i\mathbf{k}_{\parallel}(\mathbf{r}_{\parallel} - \mathbf{r}'_{\parallel})} \frac{1}{\hbar\beta} \sum_n e^{i\omega_n(\tau - \tau')} \Pi_{ii}(\alpha, \beta, \mathbf{k}_{\parallel}, i\omega_n). \quad (5.157)$$

Similar to the bulk case, we have performed the transformation to a discrete momentum sum (cf. section 5.1.2) and incorporated the factor $\frac{1}{\mathcal{V}_{2D}}$ into the definition of $\Pi_{ii}(\alpha, \beta, \mathbf{k}_{\parallel}, i\omega_n)$ in the last step. On the other hand, if we insert the Fourier transform of the current

5. Theory

operators directly, we have

$$\begin{aligned}
\Pi_{ii}(\alpha, \beta, \mathbf{r}_{\parallel} - \mathbf{r}'_{\parallel}, \tau - \tau') &= -\langle T_{\tau} J_i(\alpha, \mathbf{r}_{\parallel}, \tau) J_i(\beta, \mathbf{r}'_{\parallel}, \tau') \rangle \\
&= -\langle T_{\tau} \frac{1}{N_{\parallel}} \sum_{\mathbf{k}_{\parallel}} \frac{1}{N_{\parallel}} \sum_{\mathbf{k}'_{\parallel}} e^{i(\mathbf{k}_{\parallel} \mathbf{r}_{\parallel} + \mathbf{k}'_{\parallel} \mathbf{r}'_{\parallel})} \\
&\quad \cdot \frac{1}{(\hbar\beta)^2} \sum_{nm} e^{i(\omega_n \tau + \omega_m \tau')} J_i(\alpha, \mathbf{k}_{\parallel}, i\omega_n) J_i(\beta, \mathbf{k}'_{\parallel}, i\omega_m) \rangle . \\
&= -\frac{1}{N_{\parallel}} \sum_{\mathbf{k}_{\parallel}} e^{i\mathbf{k}_{\parallel}(\mathbf{r}_{\parallel} - \mathbf{r}'_{\parallel})} \frac{1}{\hbar\beta} \sum_n e^{i\omega_n(\tau - \tau')} \\
&\quad \cdot \underbrace{\frac{1}{N_{\parallel}} \sum_{\mathbf{k}'_{\parallel}} e^{i(\mathbf{k}_{\parallel} + \mathbf{k}'_{\parallel})\mathbf{r}'_{\parallel}} \frac{1}{\hbar\beta} \sum_m e^{i(\omega_n + \omega_m)\tau'} \langle J_i(\alpha, \mathbf{k}_{\parallel}, i\omega_n) J_i(\beta, \mathbf{k}'_{\parallel}, i\omega_m) \rangle}_{\Pi_{ii}(\alpha, \beta, \mathbf{k}_{\parallel}, i\omega_n)} .
\end{aligned}$$

Again, we have used that $\tau - \tau' \in [0, \hbar\beta]$ is already time ordered in the last step. Moreover, since $\Pi_{ii}(\alpha, \beta, \mathbf{k}_{\parallel}, i\omega_n)$ can not depend on \mathbf{r}'_{\parallel} or τ' we have $\mathbf{k}'_{\parallel} = -\mathbf{k}_{\parallel}$ and $\omega_m = -\omega_n$, and hence

$$\Pi_{ii}(\alpha, \beta, \mathbf{k}_{\parallel}, i\omega_n) = -\frac{1}{\tilde{\mathcal{V}}_{2D} \hbar\beta} \langle T_{\tau} J_i(\alpha, \mathbf{k}_{\parallel}, i\omega_n) J_i(\beta, -\mathbf{k}_{\parallel}, -i\omega_n) \rangle . \quad (5.158)$$

Here, we have introduced the factor $\tilde{\mathcal{V}}_{2D} = \mathcal{V}_{2D} N_{\parallel}$ for notational convenience.

Current operator

In order to calculate the current operators in (5.137), we begin with the Fourier transform of the continuity equation (5.138) in the parallel direction. In doing so, we introduce the parallel current $\mathbf{J}_{\parallel} = (J_x, J_y)$ and obtain

$$\begin{aligned}
i\mathbf{q}_{\parallel} \cdot \mathbf{J}_{\parallel}(\alpha, \mathbf{q}_{\parallel}, t) + \frac{1}{a} \frac{\partial}{\partial \alpha} J_z(\alpha, \mathbf{q}_{\parallel}, t) &= -\frac{\partial}{\partial t} \rho(\alpha, \mathbf{q}_{\parallel}, t) \\
&= -\frac{i}{\hbar} [\rho(\alpha, \mathbf{q}_{\parallel}, t), H] \quad (5.159)
\end{aligned}$$

In appendix A.2 the calculation of the commutator for the multilayer Hamiltonian (4.6) is performed. It reads

$$\begin{aligned}
[\rho(\alpha, \mathbf{q}_{\parallel}), H] &= \frac{1}{a} \sum_{\mathbf{k}_{\parallel} \sigma} \left(\varepsilon_{\mathbf{k}_{\parallel}}^{\alpha} - \varepsilon_{\mathbf{k}_{\parallel} - \mathbf{q}_{\parallel}}^{\alpha} \right) c_{\mathbf{k}_{\parallel} - \mathbf{q}_{\parallel} \alpha \sigma}^{\dagger} c_{\mathbf{k}_{\parallel} \alpha \sigma} \\
&\quad + \frac{1}{a} \sum_{\mathbf{k}_{\parallel} \sigma} \left(t_{\alpha} c_{\mathbf{k}_{\parallel} - \mathbf{q}_{\parallel} \alpha \sigma}^{\dagger} c_{\mathbf{k}_{\parallel} \alpha - 1 \sigma} + t_{\alpha+1} c_{\mathbf{k}_{\parallel} - \mathbf{q}_{\parallel} \alpha \sigma}^{\dagger} c_{\mathbf{k}_{\parallel} \alpha + 1 \sigma} \right. \\
&\quad \left. - t_{\alpha} c_{\mathbf{k}_{\parallel} - \mathbf{q}_{\parallel} \alpha - 1 \sigma}^{\dagger} c_{\mathbf{k}_{\parallel} \alpha \sigma} - t_{\alpha+1} c_{\mathbf{k}_{\parallel} - \mathbf{q}_{\parallel} \alpha + 1 \sigma}^{\dagger} c_{\mathbf{k}_{\parallel} \alpha \sigma} \right) , \quad (5.160)
\end{aligned}$$

where we have dropped the time dependence for convenience. Again, the current operator is restricted to discrete momentum values inside the Brillouin zone and the transformation in (5.157) is justified. By comparing (5.159) and (5.160) we can identify the parallel contribution to the current as

$$\mathbf{q}_{\parallel} \cdot \mathbf{J}_{\parallel}(\alpha, \mathbf{q}_{\parallel}, t) = \frac{1}{a} \sum_{\mathbf{k}_{\parallel}\sigma} \left(\varepsilon_{\mathbf{k}_{\parallel}}^{\alpha} - \varepsilon_{\mathbf{k}_{\parallel}-\mathbf{q}_{\parallel}}^{\alpha} \right) c_{\mathbf{k}_{\parallel}-\mathbf{q}_{\parallel}\alpha\sigma}^{\dagger}(t) c_{\mathbf{k}_{\parallel}\alpha\sigma}(t).$$

Due to (5.148) and without loss of generality, we restrict ourselves to σ_x and assume that the electric field is vanishing in the y direction. Then, we have $J_y = 0$ and hence

$$J_x(\alpha, \mathbf{q}_{\parallel}, t) = -\frac{1}{\hbar q_x a} \sum_{\mathbf{k}_{\parallel}\sigma} \left(\varepsilon_{\mathbf{k}_{\parallel}}^{\alpha} - \varepsilon_{\mathbf{k}_{\parallel}-\mathbf{q}_{\parallel}}^{\alpha} \right) c_{\mathbf{k}_{\parallel}-\mathbf{q}_{\parallel}\alpha\sigma}^{\dagger}(t) c_{\mathbf{k}_{\parallel}\alpha\sigma}(t). \quad (5.161)$$

A calculation similar to the one performed in (5.140) and (5.141) leads to

$$\begin{aligned} J_x(\alpha, \mathbf{q}_{\parallel}, i\omega_n) &= \int d\tau e^{-i\omega_n \tau} J_x(\alpha, \mathbf{q}_{\parallel}, \tau) \\ &= -\frac{1}{\hbar q_x a} \sum_{\mathbf{k}_{\parallel}, \sigma} \left(\varepsilon_{\mathbf{k}_{\parallel}}^{\alpha} - \varepsilon_{\mathbf{k}_{\parallel}-\mathbf{q}_{\parallel}}^{\alpha} \right) \frac{1}{\hbar \beta} \sum_l c_{\mathbf{k}_{\parallel}-\mathbf{q}_{\parallel}\alpha\sigma}^{\dagger}(i\omega_l - i\omega_n) c_{\mathbf{k}_{\parallel}\alpha\sigma}(i\omega_l), \end{aligned}$$

and in the limit $\mathbf{q}_{\parallel} \rightarrow 0$ we finally get the following expression for the parallel current component:

$$\lim_{\mathbf{q}_{\parallel} \rightarrow 0} J_x(\alpha, \pm \mathbf{q}_{\parallel}, \pm i\omega_n) = -\frac{1}{\hbar a} \sum_{\mathbf{k}_{\parallel}, \sigma} \frac{\partial \varepsilon_{\mathbf{k}_{\parallel}}^{\alpha}}{\partial k_x} \frac{1}{\hbar \beta} \sum_l c_{\mathbf{k}_{\parallel}\alpha\sigma}^{\dagger}(i\omega_l - i\omega_n) c_{\mathbf{k}_{\parallel}\alpha\sigma}(i\omega_l). \quad (5.162)$$

The perpendicular component of the current operator can be obtained in the same manner by comparing (5.159) and (5.160). We drop the time dependence for a moment and use the discrete representation of the derivative:

$$\begin{aligned} \frac{\partial}{\partial \alpha} J_z(\alpha, \mathbf{q}_{\parallel}) &= J_z\left(\alpha + \frac{1}{2}, \mathbf{q}_{\parallel}\right) - J_z\left(\alpha - \frac{1}{2}, \mathbf{q}_{\parallel}\right) \\ &= \frac{i}{\hbar} \sum_{\mathbf{k}_{\parallel}\sigma} t_{\alpha+1} \left(c_{\mathbf{k}_{\parallel}-\mathbf{q}_{\parallel}\alpha+1\sigma}^{\dagger} c_{\mathbf{k}_{\parallel}\alpha\sigma} - c_{\mathbf{k}_{\parallel}-\mathbf{q}_{\parallel}\alpha\sigma}^{\dagger} c_{\mathbf{k}_{\parallel}\alpha+1\sigma} \right) \\ &\quad - \frac{i}{\hbar} \sum_{\mathbf{k}_{\parallel}\sigma} t_{\alpha} \left(c_{\mathbf{k}_{\parallel}-\mathbf{q}_{\parallel}\alpha\sigma}^{\dagger} c_{\mathbf{k}_{\parallel}\alpha-1\sigma} - c_{\mathbf{k}_{\parallel}-\mathbf{q}_{\parallel}\alpha-1\sigma}^{\dagger} c_{\mathbf{k}_{\parallel}\alpha\sigma} \right). \end{aligned}$$

Now we can identify the current operators for positions in between the layers as

$$J_z\left(\alpha + \frac{1}{2}, \mathbf{q}_{\parallel}\right) = \frac{i}{\hbar} \sum_{\mathbf{k}_{\parallel}\sigma} t_{\alpha+1} \left(c_{\mathbf{k}_{\parallel}-\mathbf{q}_{\parallel}\alpha+1\sigma}^{\dagger} c_{\mathbf{k}_{\parallel}\alpha\sigma} - c_{\mathbf{k}_{\parallel}-\mathbf{q}_{\parallel}\alpha\sigma}^{\dagger} c_{\mathbf{k}_{\parallel}\alpha+1\sigma} \right),$$

5. Theory

and

$$J_z(\alpha - \frac{1}{2}, \mathbf{q}_{\parallel}) = \frac{i}{\hbar} \sum_{\mathbf{k}_{\parallel}\sigma} t_{\alpha} \left(c_{\mathbf{k}_{\parallel}-\mathbf{q}_{\parallel}\alpha\sigma}^{\dagger} c_{\mathbf{k}_{\parallel}\alpha-1\sigma} - c_{\mathbf{k}_{\parallel}-\mathbf{q}_{\parallel}\alpha-1\sigma}^{\dagger} c_{\mathbf{k}_{\parallel}\alpha\sigma} \right).$$

The current operator at the position of a specific layer could be calculated as the average $J_z(\alpha, \mathbf{q}_{\parallel}, t) = \frac{1}{2}(J_z(\alpha + \frac{1}{2}, \mathbf{q}_{\parallel}, t) + J_z(\alpha - \frac{1}{2}, \mathbf{q}_{\parallel}, t))$. Nevertheless, it turns out to be more convenient to proceed with the current at an interstitial position and calculate the conductivity between interstitial positions. Therefore, we introduce a shorthand notation for the interlayer positions,

$$\alpha^+ = \alpha + \frac{1}{2}.$$

Note that in the end we are interested only in the conductivity between the outer layers. Taking the limit $\mathbf{q}_{\parallel} \rightarrow 0$ yields

$$\lim_{\mathbf{q}_{\parallel} \rightarrow 0} J_z(\alpha^+, \pm \mathbf{q}_{\parallel}, t) = \frac{i}{\hbar} t_{\alpha+1} \sum_{\mathbf{k}_{\parallel}\sigma} \left(c_{\mathbf{k}_{\parallel}\alpha+1\sigma}^{\dagger} c_{\mathbf{k}_{\parallel}\alpha\sigma} - c_{\mathbf{k}_{\parallel}\alpha\sigma}^{\dagger} c_{\mathbf{k}_{\parallel}\alpha+1\sigma} \right).$$

By going to imaginary times and Fourier transforming similar to (5.140) and (5.141), we finally obtain

$$\lim_{\mathbf{q}_{\parallel} \rightarrow 0} J_z(\alpha^+, \pm \mathbf{q}_{\parallel}, \pm i\omega_n) = \frac{i}{\hbar} t_{\alpha+1} \sum_{\mathbf{k}_{\parallel}\sigma} \frac{1}{\hbar\beta} \sum_l \left(c_{\mathbf{k}_{\parallel}\alpha+1\sigma}^{\dagger}(i\omega_l \mp i\omega_n) c_{\mathbf{k}_{\parallel}\alpha\sigma}(i\omega_l) - c_{\mathbf{k}_{\parallel}\alpha\sigma}^{\dagger}(i\omega_l \mp i\omega_n) c_{\mathbf{k}_{\parallel}\alpha+1\sigma}(i\omega_l) \right). \quad (5.163)$$

Diagrammatic evaluation for the parallel conductivity

The calculation of the parallel conductivity (5.152) is very similar to the bulk case. We proceed by inserting (5.162) into (5.158) and take the limit $\mathbf{q}_{\parallel} \rightarrow 0$,

$$\begin{aligned} \lim_{\mathbf{q}_{\parallel} \rightarrow 0} \Pi_{xx}(\alpha, \alpha, \mathbf{q}_{\parallel}, i\omega_n) &= \frac{-1}{a^2 \tilde{\mathcal{V}}_{2D} \hbar^5 \beta^3} \sum_{\substack{\mathbf{k}_{\parallel} \mathbf{p}_{\parallel} \\ \sigma \sigma'}} \frac{\partial \varepsilon_{\mathbf{k}_{\parallel}}^{\alpha}}{\partial k_x} \frac{\partial \varepsilon_{\mathbf{p}_{\parallel}}^{\alpha}}{\partial p_x} \\ &\cdot \sum_{lm} \langle c_{\mathbf{k}_{\parallel}\alpha\sigma}^{\dagger}(i\omega_l - i\omega_n) c_{\mathbf{k}_{\parallel}\alpha\sigma}(i\omega_l) c_{\mathbf{p}_{\parallel}\alpha\sigma'}^{\dagger}(i\omega_m + i\omega_n) c_{\mathbf{p}_{\parallel}\alpha\sigma'}(i\omega_m) \rangle. \end{aligned} \quad (5.164)$$

In order to compute the expectation value, we need to find all possible contractions, i.e. find all diagrams which connect the two vertices shown in figure 5.10.

Similar to the bulk case, we have $\sigma = \sigma'$ and $\omega_l = \omega_m + \omega_n$. However, in the multilayer case only the parallel momentum is conserved and $\mathbf{k}_{\parallel} = \mathbf{p}_{\parallel}$ holds. If we express (5.164) in terms of dressed Green's functions, we can expand it in orders of impurity scattering since this is the only interaction which can connect the upper and lower fermion lines:

$$\lim_{\mathbf{q}_{\parallel} \rightarrow 0} \Pi_{xx}(\alpha, \alpha, \mathbf{q}_{\parallel}, i\omega_n) = \text{Diagram 1} + \text{Diagram 2} + \text{Diagram 3} + \dots \quad (5.165)$$

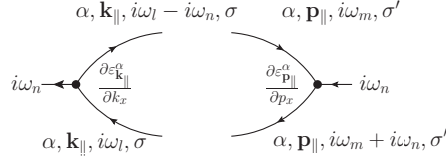


Figure 5.10.: Vertices for the parallel current-current correlation function

Here, the double lines denotes the full propagator (see equation (5.22)). In the following, we will neglect the vertex corrections and restrict ourselves to the first contribution in (5.165). After calculating the undressed version of this particular diagram, we will replace the bare propagators by the full ones.

$$\begin{aligned}
\lim_{\mathbf{q}_{\parallel} \rightarrow 0} \Pi_{xx}^0(\alpha, \alpha, \mathbf{q}_{\parallel}, i\omega_n) &= \text{Diagram} \\
&= \frac{-1}{a^2 \tilde{\mathcal{V}}_{2D} \hbar^5 \beta^3} \sum_{\substack{\mathbf{k}_{\parallel} \mathbf{p}_{\parallel} \\ \sigma \sigma'}} \frac{\partial \varepsilon_{\mathbf{k}_{\parallel}}^{\alpha}}{\partial k_x} \frac{\partial \varepsilon_{\mathbf{p}_{\parallel}}^{\alpha}}{\partial p_x} \\
&\quad \cdot \sum_{lm} \overbrace{c_{\mathbf{k}_{\parallel} \alpha \sigma}^{\dagger}(i\omega_l - i\omega_n) c_{\mathbf{k}_{\parallel} \alpha \sigma}(i\omega_l) c_{\mathbf{p}_{\parallel} \alpha \sigma'}^{\dagger}(i\omega_m + i\omega_n) c_{\mathbf{p}_{\parallel} \alpha \sigma'}(i\omega_m)}^{c_{\mathbf{p}_{\parallel} \alpha \sigma'}(i\omega_m) c_{\mathbf{k}_{\parallel} \alpha \sigma}^{\dagger}(i\omega_l - i\omega_n) c_{\mathbf{k}_{\parallel} \alpha \sigma}(i\omega_l) c_{\mathbf{p}_{\parallel} \alpha \sigma'}^{\dagger}(i\omega_m + i\omega_n) (-1)^3} \\
&= \frac{1}{a^2 \tilde{\mathcal{V}}_{2D} \hbar^2} \sum_{\mathbf{k}_{\parallel} \sigma} \left(\frac{\partial \varepsilon_{\mathbf{k}_{\parallel}}^{\alpha}}{\partial k_x} \right)^2 \frac{1}{\hbar \beta} \sum_m G_{c\mathbf{k}_{\parallel} \sigma}^{\alpha, 0}(i\omega_m) G_{c\mathbf{k}_{\parallel} \sigma}^{\alpha, 0}(i\omega_m + i\omega_n),
\end{aligned}$$

where we have used

$$c_{\mathbf{k}_{\parallel} \alpha \sigma}(i\omega_l) c_{\mathbf{p}_{\parallel} \beta \sigma'}^{\dagger}(i\omega_m) = -\hbar \beta \delta_{ln} \delta_{\mathbf{k}_{\parallel} \mathbf{p}_{\parallel}} \delta_{\sigma \sigma'} G_{c\mathbf{k}_{\parallel} \sigma}^{\alpha \beta, 0}(i\omega_n) \quad (5.166)$$

and applied the shorthand notation $G_{c\mathbf{k}_{\parallel} \sigma}^{\alpha \alpha, 0}(i\omega_n) = G_{c\mathbf{k}_{\parallel} \sigma}^{\alpha, 0}(i\omega_n)$ for the diagonal elements of the Green's function matrix. We insert the full propagators and evaluate the Matsubara sum (see A.3) and obtain

5. Theory

$$\begin{aligned}
\lim_{\mathbf{q}_{\parallel} \rightarrow 0} \Pi_{xx}(\alpha, \alpha, \mathbf{q}_{\parallel}, i\omega_n) &= \text{Diagram} \\
&= \frac{1}{a^2 \tilde{\mathcal{V}}_{2D} \hbar^2} \sum_{\mathbf{k}_{\parallel} \sigma} \left(\frac{\partial \varepsilon_{\mathbf{k}_{\parallel}}^{\alpha}}{\partial k_x} \right)^2 \\
&\quad \cdot \int_{-\infty}^{\infty} d\varepsilon f(\varepsilon) A_{c\mathbf{k}_{\parallel}\sigma}^{\alpha}(\varepsilon) [G_{c\mathbf{k}_{\parallel}\sigma}^{\alpha}(\varepsilon + i\omega_n) + G_{c\mathbf{k}_{\parallel}\sigma}^{\alpha}(\varepsilon - i\omega_n)].
\end{aligned} \tag{5.167}$$

The imaginary part of the retarded current-current correlation function reads (see A.3)

$$\begin{aligned}
\lim_{\mathbf{q}_{\parallel} \rightarrow 0} \text{Im} \Pi_{xx}^R(\alpha, \alpha, \mathbf{q}_{\parallel}, \omega) &= \frac{\pi}{a^2 \tilde{\mathcal{V}}_{2D} \hbar^2} \sum_{\mathbf{k}_{\parallel} \sigma} \left(\frac{\partial \varepsilon_{\mathbf{k}_{\parallel}}^{\alpha}}{\partial k_x} \right)^2 \\
&\quad \cdot \int d\varepsilon [f(\varepsilon) - f(\varepsilon - \omega)] A_{c\mathbf{k}_{\parallel}\sigma}^{\alpha}(\varepsilon) A_{c\mathbf{k}_{\parallel}\sigma}^{\alpha}(\varepsilon - \omega).
\end{aligned} \tag{5.168}$$

Combining equations (5.152), (5.130) and (5.168), the resulting parallel conductivity reads

$$\begin{aligned}
\sigma_{\parallel}(\alpha) &= \lim_{\mathbf{q}_{\parallel} \rightarrow 0} \lim_{\omega \rightarrow 0} \sigma(\alpha, \alpha, \mathbf{q}_{\parallel}, \omega) \\
&= -\frac{e^2}{\hbar} \lim_{\omega \rightarrow 0} \lim_{\mathbf{q}_{\parallel} \rightarrow 0} \frac{\text{Im} \Pi_{xx}(\alpha, \alpha, \mathbf{q}_{\parallel}, \omega + i0^+)}{\omega} \\
&= \frac{e^2 \pi}{a^2 \tilde{\mathcal{V}}_{2D} \hbar^3} \sum_{\mathbf{k}_{\parallel} \sigma} \left(\frac{\partial \varepsilon_{\mathbf{k}_{\parallel}}^{\alpha}}{\partial k_x} \right)^2 \int d\varepsilon \left(-\frac{\partial f(\varepsilon)}{\partial \varepsilon} \right) [A_{c\mathbf{k}_{\parallel}\sigma}^{\alpha}(\varepsilon)]^2.
\end{aligned} \tag{5.169}$$

Diagrammatic evaluation for the perpendicular conductivity

In order to compute the perpendicular conductivity (5.153), we plug (5.163) into (5.158) and take the limit $\mathbf{q}_{\parallel} \rightarrow 0$:

$$\begin{aligned}
\lim_{\mathbf{q}_{\parallel} \rightarrow 0} \Pi_{zz}(\alpha^+, \beta^+, \mathbf{q}_{\parallel}, i\omega_n) &= \frac{t_{\alpha+1} t_{\beta+1}}{\tilde{\mathcal{V}}_{2D} \hbar^5 \beta^3} \sum_{\mathbf{k}_{\parallel} \mathbf{p}_{\parallel}} \sum_{lm} \\
&\cdot \langle c_{\mathbf{k}_{\parallel} \alpha+1 \sigma}^{\dagger} (i\omega_l - i\omega_n) c_{\mathbf{k}_{\parallel} \alpha \sigma} (i\omega_l) c_{\mathbf{p}_{\parallel} \beta+1 \sigma'}^{\dagger} (i\omega_m + i\omega_n) c_{\mathbf{p}_{\parallel} \beta \sigma'} (i\omega_m) \\
&- c_{\mathbf{k}_{\parallel} \alpha \sigma}^{\dagger} (i\omega_l - i\omega_n) c_{\mathbf{k}_{\parallel} \alpha+1 \sigma} (i\omega_l) c_{\mathbf{p}_{\parallel} \beta+1 \sigma'}^{\dagger} (i\omega_m + i\omega_n) c_{\mathbf{p}_{\parallel} \beta \sigma'} (i\omega_m) \\
&- c_{\mathbf{k}_{\parallel} \alpha+1 \sigma}^{\dagger} (i\omega_l - i\omega_n) c_{\mathbf{k}_{\parallel} \alpha \sigma} (i\omega_l) c_{\mathbf{p}_{\parallel} \beta \sigma'}^{\dagger} (i\omega_m + i\omega_n) c_{\mathbf{p}_{\parallel} \beta+1 \sigma'} (i\omega_m) \\
&+ c_{\mathbf{k}_{\parallel} \alpha \sigma}^{\dagger} (i\omega_l - i\omega_n) c_{\mathbf{k}_{\parallel} \alpha+1 \sigma} (i\omega_l) c_{\mathbf{p}_{\parallel} \beta \sigma'}^{\dagger} (i\omega_m + i\omega_n) c_{\mathbf{p}_{\parallel} \beta+1 \sigma'} (i\omega_m) \rangle.
\end{aligned} \tag{5.170}$$

We proceed by calculating the contribution from the first term. The calculation of the other three terms is analogue as they differ from the first contribution only by interchanging the layer indices. First, we need to find all possible contractions in the expectation value of the first term. This corresponds to finding all possible Feynman diagrams which connect the two vertices shown in figure 5.11.

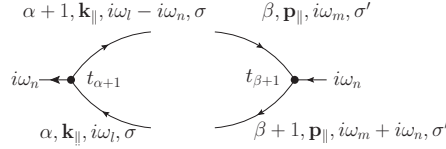


Figure 5.11.: Vertices for the first contribution to the perpendicular current-current correlation function

As in the parallel case, we have $\sigma = \sigma'$, $\mathbf{k}_{\parallel} = \mathbf{p}_{\parallel}$ and $\omega_l = \omega_m + \omega_n$. Similar to (5.165), we can express (5.170) in terms of dressed Green's functions,

$$\lim_{\mathbf{q}_{\parallel} \rightarrow 0} \Pi_{zz}^1(\alpha^+, \beta^+, \mathbf{q}_{\parallel}, i\omega_n) = \text{Diagram 1} + \text{Diagram 2} + \text{Diagram 3} + \dots, \tag{5.171}$$

and neglect all terms following the first one. We calculate the bare diagram and insert

5. Theory

the dressed propagators in the end:

$$\begin{aligned}
\lim_{\mathbf{q}_{\parallel} \rightarrow 0} \Pi_{zz}^{1,0}(\alpha^+, \beta^+, \mathbf{q}_{\parallel}, i\omega_n) &= \text{Diagram: A bubble diagram with two vertices. The top vertex is labeled } \alpha+1, \mathbf{k}_{\parallel}, i\omega_l \text{ and the bottom vertex is labeled } \beta, \mathbf{p}_{\parallel}, i\omega_m, \sigma'. \text{ The left arc is labeled } \alpha, \mathbf{k}_{\parallel}, i\omega_l, \sigma \text{ and the right arc is labeled } \beta+1, \mathbf{p}_{\parallel}, i\omega_m + i\omega_n, \sigma'. \text{ The vertices are labeled } t_{\alpha+1} \text{ and } t_{\beta+1}. \\
&= \frac{t_{\alpha+1} t_{\beta+1}}{\tilde{\mathcal{V}}_{2D} \hbar^5 \beta^3} \sum_{\substack{\mathbf{k}_{\parallel} \mathbf{p}_{\parallel} \\ \sigma \sigma'}} \sum_{lm} \\
&\quad \cdot \underbrace{c_{\mathbf{k}_{\parallel} \alpha+1 \sigma}^{\dagger}(i\omega_l - i\omega_n) c_{\mathbf{k}_{\parallel} \alpha \sigma}(i\omega_l) c_{\mathbf{p}_{\parallel} \beta+1 \sigma'}^{\dagger}(i\omega_m + i\omega_n) c_{\mathbf{p}_{\parallel} \beta \sigma'}(i\omega_m)}_{c_{\mathbf{p}_{\parallel} \beta \sigma'}(i\omega_m) c_{\mathbf{k}_{\parallel} \alpha+1 \sigma}^{\dagger}(i\omega_l - i\omega_n) c_{\mathbf{k}_{\parallel} \alpha \sigma}(i\omega_l) c_{\mathbf{p}_{\parallel} \beta+1 \sigma'}^{\dagger}(i\omega_m + i\omega_n) (-1)^3} \\
&= \frac{-t_{\alpha+1} t_{\beta+1}}{\tilde{\mathcal{V}}_{2D} \hbar^2} \sum_{\mathbf{k}_{\parallel} \sigma} \frac{1}{\hbar \beta} \sum_m G_{c\mathbf{k}_{\parallel} \sigma}^{\beta\alpha+1,0}(i\omega_m) G_{c\mathbf{k}_{\parallel} \sigma}^{\alpha\beta+1,0}(i\omega_m + i\omega_n),
\end{aligned}$$

where we have used (5.166). We replace the bare propagators by the full ones and evaluate the Matsubara sum according to appendix A.3:

$$\begin{aligned}
\lim_{\mathbf{q}_{\parallel} \rightarrow 0} \Pi_{zz}^1(\alpha^+, \beta^+, \mathbf{q}_{\parallel}, i\omega_n) &= \text{Diagram: A bubble diagram with two vertices. The top vertex is labeled } \alpha+1 \text{ and the bottom vertex is labeled } \beta. \text{ The left arc is labeled } \alpha \text{ and the right arc is labeled } \beta+1. \text{ The vertices are labeled } t_{\alpha+1} \text{ and } t_{\beta+1}. \text{ The top arc is labeled } \mathbf{k}_{\parallel}, i\omega_m \text{ and the bottom arc is labeled } \mathbf{k}_{\parallel}, i\omega_m + i\omega_n. \\
&= \frac{-t_{\alpha+1} t_{\beta+1}}{\tilde{\mathcal{V}}_{2D} \hbar^2} \sum_{\mathbf{k}_{\parallel} \sigma} \int_{-\infty}^{\infty} d\varepsilon f(\varepsilon) \\
&\quad \cdot \left(A_{c\mathbf{k}_{\parallel} \sigma}^{\beta\alpha+1}(\varepsilon) G_{c\mathbf{k}_{\parallel} \sigma}^{\alpha\beta+1}(\varepsilon + i\omega_n) + G_{c\mathbf{k}_{\parallel} \sigma}^{\beta\alpha+1}(\varepsilon - i\omega_n) A_{c\mathbf{k}_{\parallel} \sigma}^{\alpha\beta+1}(\varepsilon) \right). \tag{5.172}
\end{aligned}$$

With this, we obtain for imaginary part of the retarded current-current correlation function (see A.3)

$$\begin{aligned}
\lim_{\mathbf{q}_{\parallel} \rightarrow 0} \text{Im} \Pi_{zz}^{1,R}(\alpha^+, \beta^+, \mathbf{q}_{\parallel}, \omega) &= \frac{-t_{\alpha+1} t_{\beta+1}}{\tilde{\mathcal{V}}_{2D} \hbar^2} \sum_{\mathbf{k}_{\parallel} \sigma} \\
&\quad \cdot \int d\varepsilon [f(\varepsilon) - f(\varepsilon - \omega)] A_{c\mathbf{k}_{\parallel} \sigma}^{\alpha\beta+1}(\varepsilon) A_{c\mathbf{k}_{\parallel} \sigma}^{\beta,\alpha+1}(\varepsilon - \omega). \tag{5.173}
\end{aligned}$$

If we combine (5.153), (5.130) and (5.173), the contribution to the perpendicular con-

ductivity due to the first term in (5.170) reads

$$\begin{aligned}
\sigma_{\perp}^1(\alpha^+, \beta^+) &= \lim_{\mathbf{q}_{\parallel} \rightarrow 0} \lim_{\omega \rightarrow 0} \sigma^1(\alpha^+, \beta^+, \mathbf{q}_{\parallel}, \omega) \\
&= -\frac{e^2}{\hbar} \lim_{\omega \rightarrow 0} \lim_{\mathbf{q}_{\parallel} \rightarrow 0} \frac{\text{Im} \Pi_{zz}(\alpha^+, \beta^+, \mathbf{q}_{\parallel}, \omega + i0^+)}{\omega} \\
&= \frac{-e^2 \pi t_{\alpha+1} t_{\beta+1}}{\tilde{\mathcal{V}}_{2D} \hbar^3} \sum_{\mathbf{k}_{\parallel} \sigma} \int d\varepsilon \left(-\frac{\partial f(\varepsilon)}{\partial \varepsilon} \right) A_{c\mathbf{k}_{\parallel}\sigma}^{\beta\alpha+1}(\varepsilon) A_{c\mathbf{k}_{\parallel}\sigma}^{\alpha\beta+1}(\varepsilon).
\end{aligned}$$

The second, third, and fourth contribution of the current-current correlation functions in (5.170) yield

$$\begin{aligned}
\lim_{\mathbf{q}_{\parallel} \rightarrow 0} \Pi_{zz}(\alpha^+, \beta^+, \mathbf{q}_{\parallel}, i\omega_n) &= \begin{array}{c} \begin{array}{cc} \begin{array}{c} \text{Diagram 1: Loop with } \mathbf{k}_{\parallel}, i\omega_m \text{ and } \mathbf{k}_{\parallel}, i\omega_m + i\omega_n. \end{array} & \begin{array}{c} \text{Diagram 2: Loop with } \mathbf{k}_{\parallel}, i\omega_m \text{ and } \mathbf{k}_{\parallel}, i\omega_m + i\omega_n. \end{array} \\ \hline \begin{array}{cc} \begin{array}{c} \text{Diagram 3: Loop with } \mathbf{k}_{\parallel}, i\omega_m \text{ and } \mathbf{k}_{\parallel}, i\omega_m + i\omega_n. \end{array} & \begin{array}{c} \text{Diagram 4: Loop with } \mathbf{k}_{\parallel}, i\omega_m \text{ and } \mathbf{k}_{\parallel}, i\omega_m + i\omega_n. \end{array} \end{array} \end{array} \\
&= \begin{array}{c} \begin{array}{cc} \begin{array}{c} \text{Diagram 1: Loop with } \mathbf{k}_{\parallel}, i\omega_m \text{ and } \mathbf{k}_{\parallel}, i\omega_m + i\omega_n. \end{array} & \begin{array}{c} \text{Diagram 2: Loop with } \mathbf{k}_{\parallel}, i\omega_m \text{ and } \mathbf{k}_{\parallel}, i\omega_m + i\omega_n. \end{array} \\ \hline \begin{array}{cc} \begin{array}{c} \text{Diagram 3: Loop with } \mathbf{k}_{\parallel}, i\omega_m \text{ and } \mathbf{k}_{\parallel}, i\omega_m + i\omega_n. \end{array} & \begin{array}{c} \text{Diagram 4: Loop with } \mathbf{k}_{\parallel}, i\omega_m \text{ and } \mathbf{k}_{\parallel}, i\omega_m + i\omega_n. \end{array} \end{array} \end{array}
\end{aligned}$$

Hence, the total perpendicular conductivity reads

$$\begin{aligned}
\sigma_{\perp}(\alpha^+, \beta^+) &= \frac{-e^2 \pi t_{\alpha+1} t_{\beta+1}}{\tilde{\mathcal{V}}_{2D} \hbar^3} \sum_{\mathbf{k}_{\parallel} \sigma} \int d\varepsilon \left(-\frac{\partial f(\varepsilon)}{\partial \varepsilon} \right) \\
&\quad \cdot \left(A_{c\mathbf{k}_{\parallel}\sigma}^{\beta\alpha+1}(\varepsilon) A_{c\mathbf{k}_{\parallel}\sigma}^{\alpha\beta+1}(\varepsilon) - A_{c\mathbf{k}_{\parallel}\sigma}^{\beta\alpha}(\varepsilon) A_{c\mathbf{k}_{\parallel}\sigma}^{\alpha+1\beta+1}(\varepsilon) \right. \\
&\quad \left. - A_{c\mathbf{k}_{\parallel}\sigma}^{\beta+1\alpha+1}(\varepsilon) A_{c\mathbf{k}_{\parallel}\sigma}^{\alpha\beta}(\varepsilon) + A_{c\mathbf{k}_{\parallel}\sigma}^{\beta+1\alpha}(\varepsilon) A_{c\mathbf{k}_{\parallel}\sigma}^{\alpha+1\beta}(\varepsilon) \right)
\end{aligned}$$

Due to equation (5.21) the symmetry relation $A_{c\mathbf{k}_{\parallel}\sigma}^{\alpha\beta}(\varepsilon) = A_{c\mathbf{k}_{\parallel}\sigma}^{\beta\alpha}(\varepsilon)$ holds, and the total perpendicular conductivity reduces to

$$\begin{aligned}
\sigma_{\perp}(\alpha^+, \beta^+) &= \frac{2\pi e^2 t_{\alpha+1} t_{\beta+1}}{\tilde{\mathcal{V}}_{2D} \hbar^3} \sum_{\mathbf{k}_{\parallel} \sigma} \int d\varepsilon \left(-\frac{\partial f(\varepsilon)}{\partial \varepsilon} \right) \\
&\quad \cdot \left(A_{c\mathbf{k}_{\parallel}\sigma}^{\alpha\beta}(\varepsilon) A_{c\mathbf{k}_{\parallel}\sigma}^{\alpha+1\beta+1}(\varepsilon) - A_{c\mathbf{k}_{\parallel}\sigma}^{\alpha+1\beta}(\varepsilon) A_{c\mathbf{k}_{\parallel}\sigma}^{\alpha\beta+1}(\varepsilon) \right). \quad (5.174)
\end{aligned}$$

5.6.4. Numerical calculation

In this section we will explain the details of the numerical calculation of the bulk conductivity (5.147), the parallel conductivity (5.174), and the perpendicular conductivity (5.169). In particular, the evaluation of the various wavenumber summations will be explained. We will proceed in exactly the same way as it was done in the calculation of the real space conduction band Green's functions in section 5.1.1 and 5.1.2.

5. Theory

Bulk conductivity

We begin with the calculation of the bulk conductivity (5.147),

$$\sigma = \frac{e^2 \pi}{\mathcal{V} \hbar^3} \int d\omega \left(-\frac{\partial f(\omega)}{\partial \omega} \right) \underbrace{\frac{1}{N} \sum_{\mathbf{k}\sigma} \left(\frac{\partial \varepsilon_{\mathbf{k}}}{\partial k_x} \right)^2}_{=:X} [A_{c\sigma}(\mathbf{k}, \omega)]^2.$$

As the wavenumber enters in X only via the dispersion $\varepsilon_{\mathbf{k}}$, the calculation is similar to the one for the local Green's function (5.4) in the bulk case. If one performs the continuum limit and assumes an isotropic dispersion, one obtains

$$\begin{aligned} X &= \frac{\mathcal{V}}{2\pi^2} \int_0^{k_{max}} dk k^2 \left(\frac{\partial \varepsilon_k}{\partial k} \right)^2 \sum_{\sigma} [A_{c\sigma}(\epsilon_k, \omega)]^2 \\ &= \frac{\mathcal{V}}{2\pi^2} \int d\varepsilon k(\varepsilon)^2 \underbrace{\frac{\partial \varepsilon_k}{\partial k}}_{\stackrel{(5.7)}{=} \frac{\mathcal{V} k(\varepsilon)^2}{2\pi^2 N(\varepsilon)}} \sum_{\sigma} [A_{c\sigma}(\epsilon, \omega)]^2 \\ &= \frac{\mathcal{V}^2}{4\pi^4} \int d\varepsilon \frac{k(\varepsilon)^4}{N(\varepsilon)} \sum_{\sigma} [A_{c\sigma}(\epsilon, \omega)]^2 \\ &= \frac{\mathcal{V}}{16\pi^4 a} \int d\varepsilon \frac{\tilde{k}(\varepsilon)^4}{N(\varepsilon)} \sum_{\sigma} [A_{c\sigma}(\epsilon, \omega)]^2 \end{aligned}$$

analogously to (5.6), where $k(\varepsilon) = \tilde{k}(\varepsilon)/a$ is the radius of the spherical Brillouin zone (5.8). The volume of the spherical unit cell was set equal to the volume of the realistic FCC unit cell $\mathcal{V} = a^3/4$. With this, we finally obtain for the conductivity

$$\sigma = \frac{e^2}{16\pi^3 a \hbar^3} \int d\omega \left(-\frac{\partial f(\omega)}{\partial \omega} \right) \int d\varepsilon \frac{\tilde{k}(\varepsilon)^4}{N(\varepsilon)} \sum_{\sigma} [A_{c\sigma}(\epsilon, \omega)]^2. \quad (5.175)$$

The numerical evaluation of the ε integral is similar to the calculation of the local conduction band Green's function in section 5.1.1. Nevertheless, due to the square of the spectral density in the integrand it is not possible to perform the limit of vanishing imaginary parts of the self-energy (cf. (5.15)). Therefore a small constant imaginary part $\tilde{\eta} = 10^{-10}$ is added to the self-energy (cf. (5.14)) during the calculation of the conductivity.

Parallel conductivity

In the multilayer case, the calculation will be analogously to the calculation of the local Green's function in (5.24). The parallel conductivity (5.169) reads

$$\sigma_{\parallel}(\alpha) = \frac{e^2 \pi}{a^2 \mathcal{V}_{2D} \hbar^3} \int d\omega \left(-\frac{\partial f(\omega)}{\partial \omega} \right) \underbrace{\frac{1}{N_{\parallel}} \sum_{\mathbf{k}_{\parallel}\sigma} \left(\frac{\partial \varepsilon_{\mathbf{k}_{\parallel}}^{\alpha}}{\partial k_x} \right)^2}_{=:Y} [A_{c\sigma}^{\alpha}(\mathbf{k}_{\parallel}, \omega)]^2.$$

By taking the continuum limit and assuming that the dispersion is isotropic in the plane parallel to the layers, similar to (5.26) one obtains

$$Y = \frac{\mathcal{V}_{2D}}{2\pi} \int_0^{k_{max}} dk k \left(\frac{\partial \varepsilon_k^\alpha}{\partial k} \right)^2 \sum_\sigma [A_{c\sigma}^\alpha(\varepsilon_k^1, \varepsilon_k^2, \dots; \omega)]^2.$$

Without loss of generality, we choose $\nu = \varepsilon_k^1$ as an integration variable. According to (5.30),

$$\frac{\partial \varepsilon_k^\alpha}{\partial k} = \frac{D_\parallel^\alpha}{D_\parallel^1} \frac{\partial \nu}{\partial k} \quad \forall \alpha$$

holds and hence

$$\begin{aligned} Y &= \frac{\mathcal{V}_{2D}}{2\pi} \left(\frac{D_\parallel^\alpha}{D_\parallel^1} \right)^2 \int d\nu k(\nu) \underbrace{\frac{\partial \nu}{\partial k}}_{\stackrel{(5.27)}{=} \frac{\mathcal{V}_{2D} k(\nu)}{2\pi N_\parallel^1(\nu)}} \sum_\sigma [A_{c\sigma}^\alpha(\varepsilon^1(\nu), \varepsilon^2(\nu), \dots; \omega)]^2 \\ &= \frac{\mathcal{V}_{2D}^2}{4\pi^2} \left(\frac{D_\parallel^\alpha}{D_\parallel^1} \right)^2 \int d\nu \frac{k(\nu)^2}{N_\parallel^1(\nu)} \sum_\sigma [A_{c\sigma}^\alpha(\varepsilon^1(\nu), \varepsilon^2(\nu), \dots; \omega)]^2. \end{aligned}$$

Using the dimensionless wavenumber $\tilde{k} = ka$, and identifying the volume of the circular unit cell with the volume of the unit cell in a (100) monolayer of Europium monoxide (FCC), $\mathcal{V}_{2D} = a^2/2$, one obtains

$$Y = \frac{\mathcal{V}_{2D}}{8\pi^2} \left(\frac{D_\parallel^\alpha}{D_\parallel^1} \right)^2 \int d\nu \frac{\tilde{k}(\nu)^2}{N_\parallel^1(\nu)} \sum_\sigma [A_{c\sigma}^\alpha(\varepsilon^1(\nu), \varepsilon^2(\nu), \dots; \omega)]^2.$$

The parallel conductivity in layer α now reads

$$\sigma_\parallel(\alpha) = \frac{e^2}{8\pi a^2 \hbar^3} \left(\frac{D_\parallel^\alpha}{D_\parallel^1} \right)^2 \int d\omega \left(-\frac{\partial f(\omega)}{\partial \omega} \right) \int d\nu \frac{\tilde{k}(\nu)^2}{N_\parallel^1(\nu)} \sum_\sigma [A_{c\sigma}^\alpha(\varepsilon^1(\nu), \varepsilon^2(\nu), \dots; \omega)]^2. \quad (5.176)$$

Perpendicular conductivity

Due to the absence of a dispersion in the formula for the perpendicular conductivity (5.174),

$$\begin{aligned} \sigma_\perp(\alpha^+, \beta^+) &= \frac{2\pi e^2 t_{\alpha+1} t_{\beta+1}}{\mathcal{V}_{2D} \hbar^3} \int d\omega \left(-\frac{\partial f(\omega)}{\partial \omega} \right) \\ &\quad \cdot \frac{1}{N_\parallel} \sum_{\mathbf{k}_\parallel \sigma} \left(A_{c\sigma}^{\alpha\beta}(\mathbf{k}_\parallel, \omega) A_{c\sigma}^{\alpha+1\beta+1}(\mathbf{k}_\parallel, \omega) - A_{c\sigma}^{\alpha+1\beta}(\mathbf{k}_\parallel, \omega) A_{c\sigma}^{\alpha\beta+1}(\mathbf{k}_\parallel, \omega) \right), \end{aligned}$$

5. Theory

the calculation can be done in direct analogy to the calculation of the local Green's function in 5.1.2. Again, we assume isotropic dispersions, use $\mathcal{V}_{2D} = a^2/2$ and choose $\nu = \varepsilon_k^1$ as a integration variable. Similar to (5.32) one obtains

$$\begin{aligned} \sigma_{\perp}(\alpha^+, \beta^+) &= \frac{4\pi e^2 t_{\alpha+1} t_{\beta+1}}{a^2 \hbar^3} \int d\omega \left(-\frac{\partial f(\omega)}{\partial \omega} \right) \\ &\cdot \int d\nu N_{\parallel}^1(\nu) \sum_{\sigma} \left(A_{c\sigma}^{\alpha\beta}(\nu, \omega) A_{c\mathbf{k}_{\parallel}\sigma}^{\alpha+1\beta+1}(\nu, \omega) - A_{c\mathbf{k}_{\parallel}\sigma}^{\alpha+1\beta}(\nu, \omega) A_{c\mathbf{k}_{\parallel}\sigma}^{\alpha\beta+1}(\nu, \omega) \right). \end{aligned} \quad (5.177)$$

Here, we used the following shorthand notation for the ν dependence of the spectral densities:

$$A_{c\sigma}^{\alpha\beta}(\nu, \omega) = A_{c\sigma}^{\alpha\beta}(\varepsilon^1(\nu), \varepsilon^2(\nu), \dots; \omega).$$

See section 5.1.2 for further details.

The numerical calculation of the ν integrals in (5.176) and (5.177) is performed analogously to the calculation of the parallel and perpendicular conduction electron Green's function in the multilayer case (cf. section 5.1.2). Similar to the numerical evaluation of the bulk conductivity, the introduction of a small constant imaginary part in the self-energy is mandatory due to the square of the spectral density in the integrand.

6. Bulk systems of electron doped Europium monoxide

In this chapter, we present our results for bulk systems of electron doped Europium monoxide. We begin with a discussion of the ferromagnetic semiconductor-metal transition in bulk $\text{Eu}_{1-x}\text{Gd}_x\text{O}$ as well as in EuO_{1-x} with nearest neighbor interaction. In the course of this, we inspect the differences between the two types of electron doping in detail. Afterwards, we investigate the influence of long range RKKY coupling on the bulk $\text{Eu}_{1-x}\text{Gd}_x\text{O}$ model (cf. section 5.3.3). Here, we fix the coupling parameter J_{cf} for the long range RKKY coupling in multilayer systems of $\text{Eu}_{1-x}\text{Gd}_x\text{O}$.

6.1. Bulk $\text{Eu}_{1-x}\text{Gd}_x\text{O}$

In the following, we discuss the results of the self-consistent theory for bulk $\text{Eu}_{1-x}\text{Gd}_x\text{O}$ systems with nearest neighbor interaction as it was presented in chapters 4 and 5. In accordance with [18], we choose the model parameters as $D_0 = 8\text{eV}$, $\Delta_0 = 1.0D_0$, $E_d = 0.0D_0$, $\Gamma = 0.05D_0$, $J_{cf} = 0.05D_0$, which puts the bare impurity level and the lower edge of the bare conduction band to the same energy. Moreover, we set the direct ferromagnetic coupling to $J_{4f} = 7 \times 10^{-5}D_0$ in order to obtain a Curie temperature of $T_C = 68.3\text{K} + 0.01\text{K}$ in the case of vanishing doping concentration (cf. section 5.3.1).

The theory correctly predicts the simultaneous second order phase transition between a half metallic and ferromagnetic phase at low temperatures and a semiconducting and paramagnetic phase at high temperatures. Figure 6.1 shows the total magnetization $M = \langle S \rangle + \langle \sigma \rangle$ (cf. section 5.3.1) as well as the bulk resistivity $\rho = 1/\sigma$ (cf. equation 5.147) against the temperature for various doping concentrations.

Numerically, the Curie temperature is defined as the maximal temperature with a total magnetization M greater than $0.005\mu_B$. The accuracy of the Curie temperature is determined by the minimal temperature step across the phase boundary. If not otherwise stated, this accuracy is set to 0.1 K in all remaining chapters. Apart from numerical errors, we were able to reproduce the results of Arnold and Kroha [18] who investigated the model for doping concentrations from $n_i = 0.003$ to $n_i = 0.018$. The numerical noise on top of the resistivity curves is a result of the strong dependence of the conductivity on the amount of spectral weight around the Fermi edge. If the conduction band spectral density is very small in the Fermi region, as it is the case in the high temperature phase, the numerical error of the integral in the charge neutrality condition (5.103) strongly increases the inaccuracy in the determination of μ_0 (cf. section 5.4). This could result in a slightly misplaced position of the chemical potential inside the high temperature gap of the conduction band spectral density (see figure 6.2). Since the resistivity is strongly

6. Bulk systems of electron doped Europium monoxide

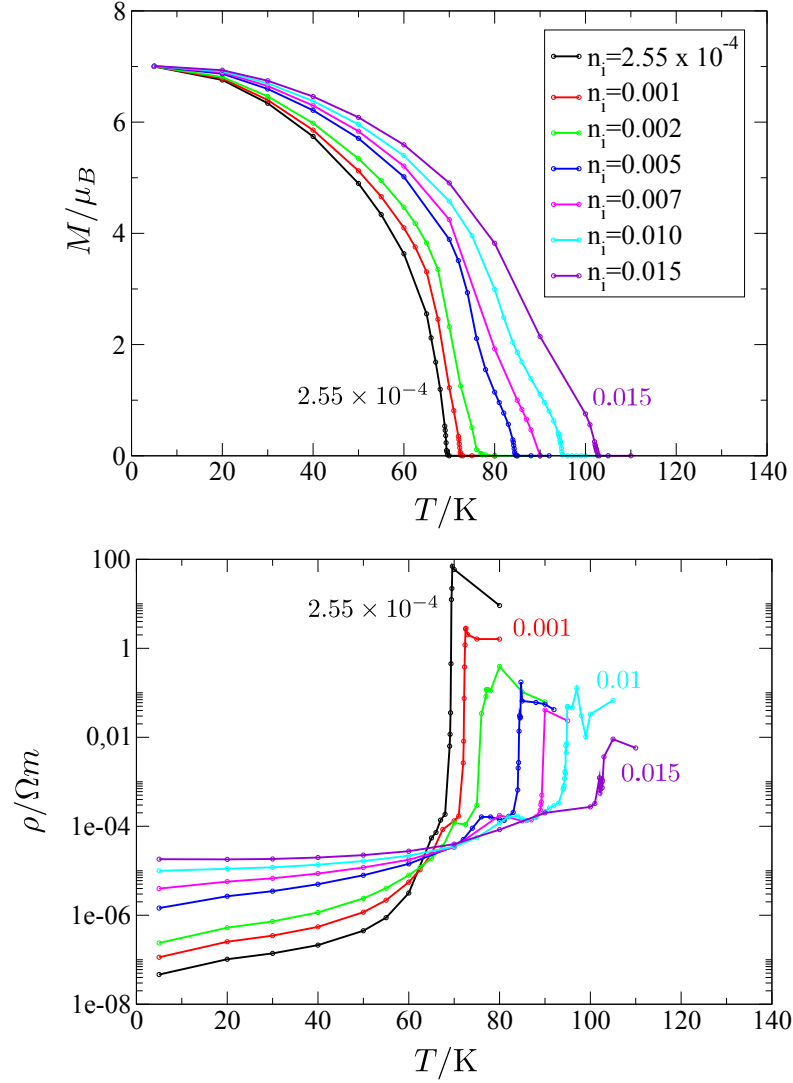


Figure 6.1.: Simultaneous ferromagnetic semiconductor-metal transition in bulk $\text{Eu}_{1-x}\text{Gd}_x\text{O}$ as seen in the total magnetization $M = \langle S \rangle + \langle \sigma \rangle$ (top) and the bulk resistivity $\rho = 1/\sigma$ (bottom) against the temperature for various doping concentrations.

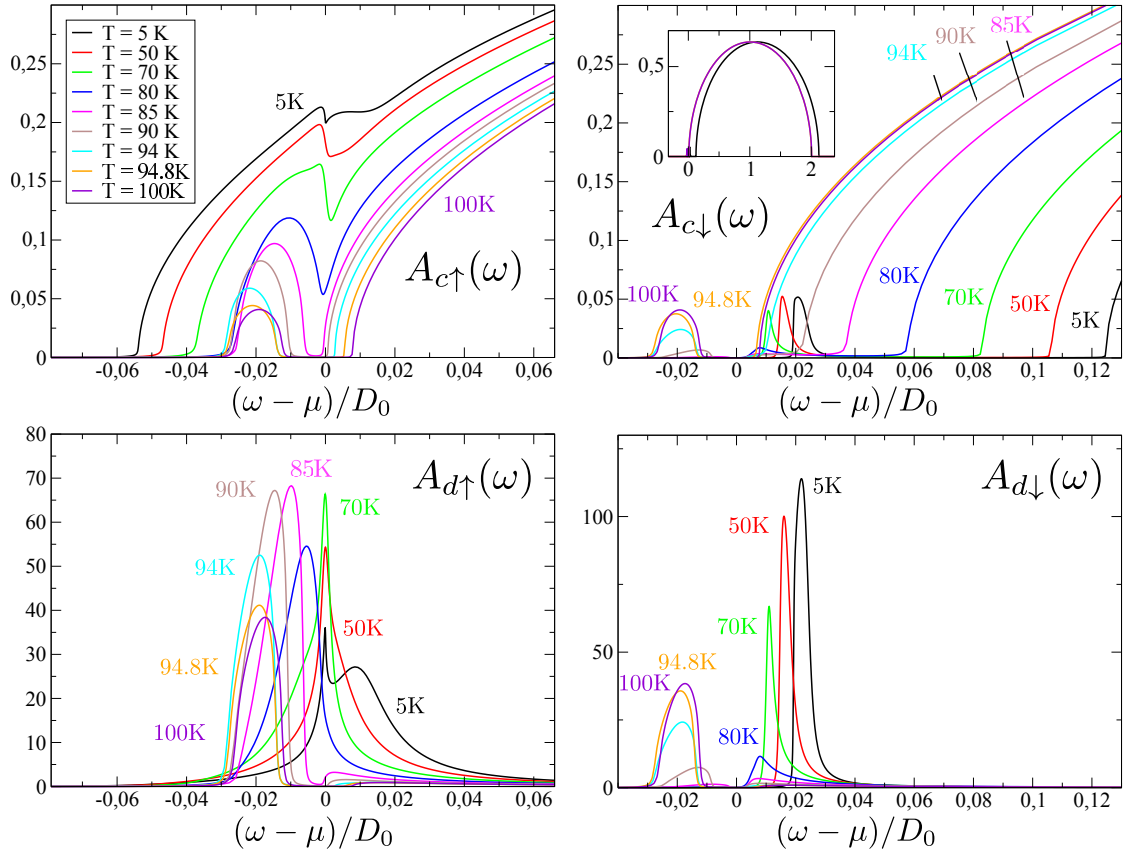


Figure 6.2.: Conduction electron and impurity spectral densities for various temperatures across the phase transition in bulk $\text{Eu}_{1-x}\text{Gd}_x\text{O}$. The doping concentration is $x = n_i = 0.01$

6. Bulk systems of electron doped Europium monoxide

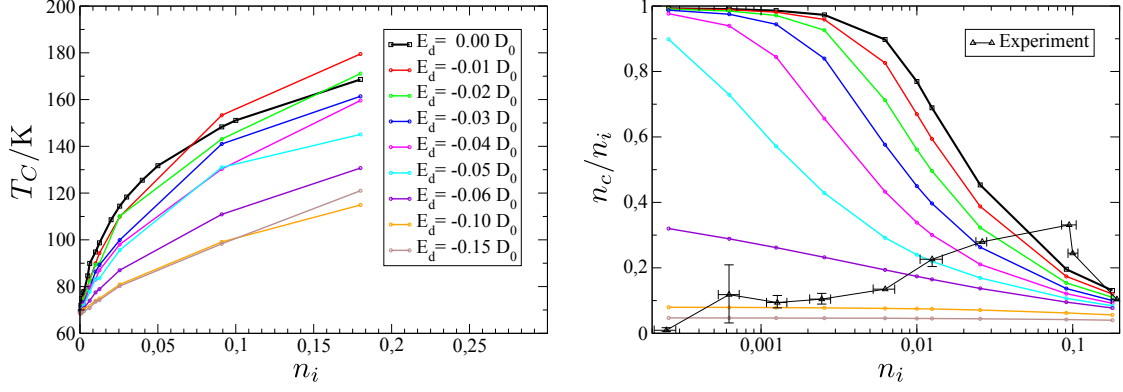


Figure 6.3.: Curie temperature T_C (left) and dopant activation n_c/n_i at $T = 5\text{K}$ (right) plotted against the doping concentration n_i for different impurity level energies E_d in bulk $\text{Eu}_{1-x}\text{Gd}_x\text{O}$. The experimental data is taken from Mairoser et. al. [15].

influenced by the overlap of the derivative of the Fermi function $\left(-\frac{\partial f(\omega)}{\partial \omega}\right)$ with the spectral density, such a misplacement has in turn a huge impact on the value of the resistivity. Above the Curie temperature, all resistivity curves exhibit a slight decrease of the resistivity with the temperature. This behavior is related to the broadening of the Fermi function with increasing temperature. Once the Curie temperature is reached, the high temperature spectral function will not change significantly with increasing temperature anymore. In contrast, the Fermi region $k_B T$ will grow and intersect more and more with the slopes on both side of the gap.

The simultaneity of the phase transition can be understood by investigating the change in the impurity and conduction band spectral densities, $A_{d\sigma}(\omega)$ and $A_{c\sigma}(\omega)$, across the phase transition in figure 6.2. Above the Curie temperature T_C , the spectral densities are spin degenerate. Moreover, there is an interaction induced level repulsion between the impurity level and the conduction band, which leads to the opening of a gap between a broad band stemming from the bare density of states and an impurity induced side band below the Fermi energy. Due to the absence of spectral weight at the Fermi edge, this gap is responsible for the large resistivity in the high temperature phase. As the temperature is lowered, the ordering of the magnetic moments sets in. Concomitantly, the spin degeneracy is lifted and the gap is closed, leaving the system in a half metallic state. This is the reason for the simultaneity of the phase transition. As the doping concentration increased, the impurity induced side band gets broader, which effectively reduces the gap width. Therefore the resistivity in the high temperature phase is decreased with increasing doping concentration. This is in agreement with experiments [15, 16] (cf. figures 2.4 and 2.5).

In order to gain more insight into the mechanisms responsible for the doping induced T_C enhancement, we investigate various values of the impurity level E_d . Figure 6.3 shows the Curie temperature and the dopant activation n_c/n_i against the doping concentration n_i

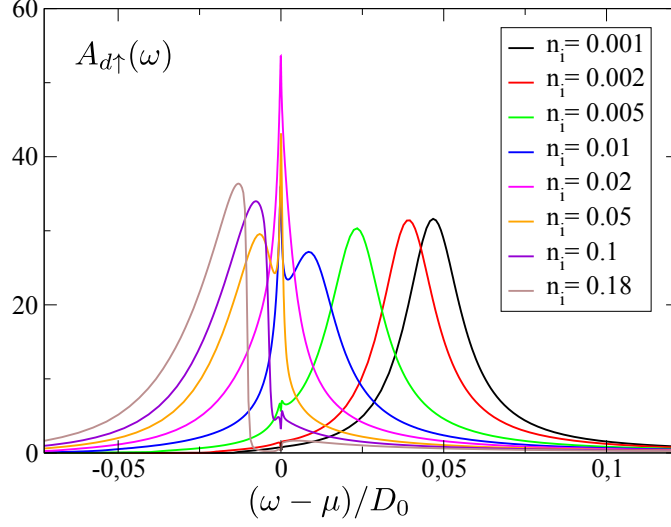


Figure 6.4.: Majority impurity spectral density at $T = 5\text{K}$ for various doping concentrations n_i in bulk $\text{Eu}_{1-x}\text{Gd}_x\text{O}$.

for various impurity level energies E_d . Here, n_c is the occupation of the conduction band (cf. section 5.4). The increase of the Curie temperature with the doping concentration is in qualitative agreement with experiments [15, 16]. As shown by Mairosier et. al. [15], this behavior is associated with the population of the conduction band. Moreover, these authors found that the saturation of the Curie temperature for high doping concentrations is a result of the lack of conduction electrons in this regime. It is reasonable to assume that these electrons are bound in the localized impurity states. Indeed, our results support this hypothesis. The experimental data in figure 6.3 exhibits a reduced dopant activation for low as well as high doping concentrations. For the former, the effect can not be explained by our theory and the responsible mechanism remains unknown. However, the decrease of the dopant activation for high concentrations is qualitatively predicted by our theory.

According to the charge carrier constraint (5.103), the population of the impurity leads to a depopulation of the conduction band. Figure 6.4 shows the majority impurity spectral density $A_{d\uparrow}(\omega)$ at $T = 5\text{K}$ for various doping concentrations. At low doping concentration, the impurity is effectively unoccupied. As the doping concentration is increased, the impurity peak gets shifted across the Fermi energy and the impurity becomes more and more populated. Concomitant with this, the conduction band is depopulated. Obviously, this process occurs at even lower concentrations as the impurity level is reduced (see figure 6.3). This explains the reduction of the Curie temperature with the impurity level energy E_d .

Besides the population of the conduction band, there is an additional mechanism connected to the magnetic nature of the impurities, which drives the phase transition. From figure 6.2, one can deduce that there is a strong influence of the impurity spectral density onto the conduction electron spectral density and vice versa. Due to the magnetic

6. Bulk systems of electron doped Europium monoxide

nature of the impurity, there is a tendency towards the formation of a Kondo resonance in $A_{d\sigma}(\omega)$ at the Fermi energy, even for temperatures well above the Kondo temperature. As the temperature is lowered, the majority impurity spectral density $A_{d\uparrow}(\omega)$ crosses the Fermi edge. Here, a resonance at $\omega = \mu$ appears which is associated with the Kondo resonance. We conjecture that, due to the hybridization, this mechanism is responsible for the closing of the gap in the conduction electron density of states at elevated temperatures and therefore causes the increased transition temperature. This matter is further investigated in the subsequent section on Oxygen deficient EuO.

6.2. Bulk EuO_{1-x}

As mentioned before, Oxygen vacancies enter our theory as Anderson impurities with weak on-site Coulomb repulsion (cf. section 5.2.2). However, due to the lack of consistent experimental data for this material (cf. chapter 2), it is not possible to determine the impurity parameters on this foundation. Therefore, we investigate the model for EuO_{1-x} for various values of the impurity level E_d and the on-site Coulomb repulsion U . The hybridization is held constant at the same value as in the Gadolinium case, $\Gamma = 0.05D_0$. Since the perturbation theory in U is valid as long as $U \ll \Gamma$ holds (cf. section 5.2.2), the parameter range for U is restricted by this upper boundary.

Figure 6.5 shows the conduction band and impurity spectral density for various temperatures across the phase transition. Similar to the Gadolinium case, the closing of the gap triggers the phase transition. However, there is no Kondo resonance at the Fermi edge in the impurity spectral density. Due to the weak on-site Coulomb repulsion, the two excess electrons are believed to occupy a non-magnetic singlet state at the position of the Oxygen vacancies. Therefore there will be no low lying spin fluctuations which could result in the formation of a Kondo resonance. With this, the tendency for closing the gap should be weaker than in the Gadolinium case. As the on-site Coulomb repulsion U is increased, the formation of a singlet becomes less likely and even impossible in the limit of $U \rightarrow \infty$, which corresponds to the Gadolinium theory. Following this line of thought, the increase of U should result in an enhancement of the Curie temperature. Indeed, we observe an increase in T_C with the Coulomb repulsion U (see figure 6.6).

On the other hand, the Curie temperature is reduced by lowering the impurity level energy E_d , which effectively reduces the conduction band occupation similarly to the Gadolinium case. It is reasonable to assume that one could completely suppress the doping induced T_C enhancement in the $U = 0$ case, if the impurity level was sufficiently far below the Fermi energy and therefore all electrons were bound in localized states [17].

Figure 6.7 compares the dopant activation for the Oxygen and the Gadolinium case. It is remarkable that despite the fact that the dopant activation is nearly twice as large in the Oxygen case as in the Gadolinium case, the T_C enhancement is relatively weak. This demonstrates how important the spin fluctuations and the associated Kondo resonance are for the enhancement of the Curie temperature in electron doped EuO.

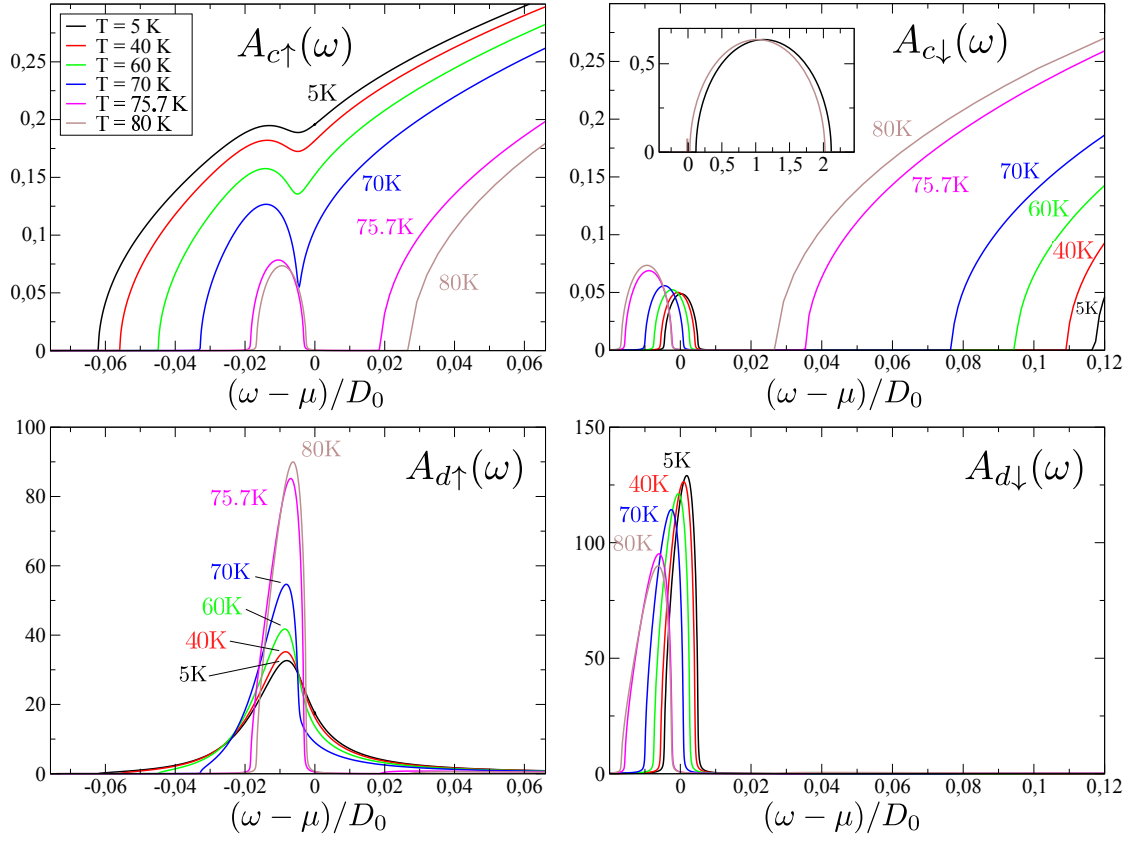


Figure 6.5.: Conduction electron and impurity spectral densities for various temperatures across the phase transition in bulk EuO_{1-x} with $U = 0.002D_0$, $E_d = -0.01D_0$ and $x = n_i = 0.01$. The Curie temperature is $T_C = 75.6\text{K}$.

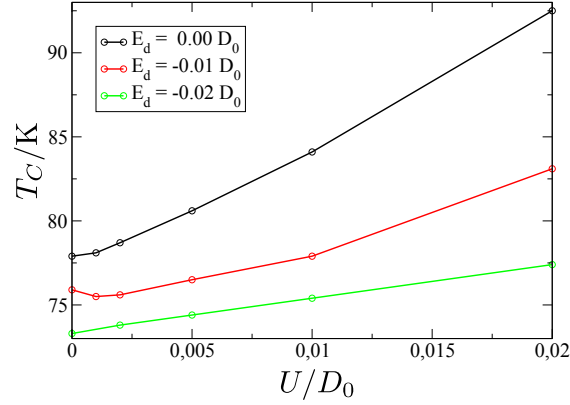


Figure 6.6.: Curie temperature T_C of a bulk EuO_{1-x} system with $x = n_i = 0.01$ in dependence of the impurity on-site Coulomb repulsion U and the bare impurity level E_d .

6. Bulk systems of electron doped Europium monoxide

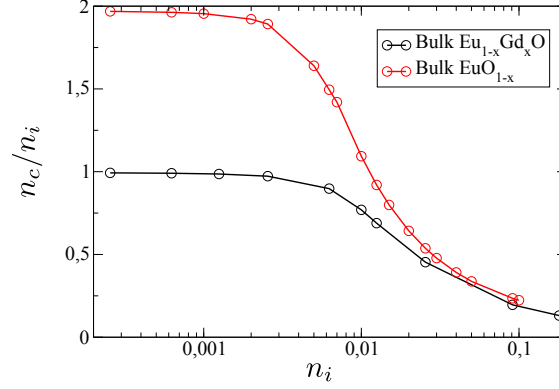


Figure 6.7.: Dopant activation n_c/n_i for bulk EuO_{1-x} with $U = 0.000D_0$, $E_d = 0.0D_0$ as well as for bulk $\text{Eu}_{1-x}\text{Gd}_x\text{O}$.

6.3. Bulk $\text{Eu}_{1-x}\text{Gd}_x\text{O}$ with long range RKKY coupling

In this section, we discuss the results of the theory for bulk $\text{Eu}_{1-x}\text{Gd}_x\text{O}$ with the long range RKKY interaction of section 5.3.3. We use the same parameters as in the nearest neighbor case of section 6.1, except for the coupling J_{cf} . The latter is chosen such that the Curie temperature in the long range case T_C^{RKKY} is comparable to the one in the nearest neighbor case T_C^{NN} . The left hand side of figure 6.8 shows the ratio $T_C^{\text{RKKY}}/T_C^{\text{NN}}$ against the doping concentration for different values of J_{cf} . We set $J_{cf} = 0.0405D_0$ in all remaining long range RKKY calculations, both for bulk and multilayer systems of electrons doped Europium monoxide.

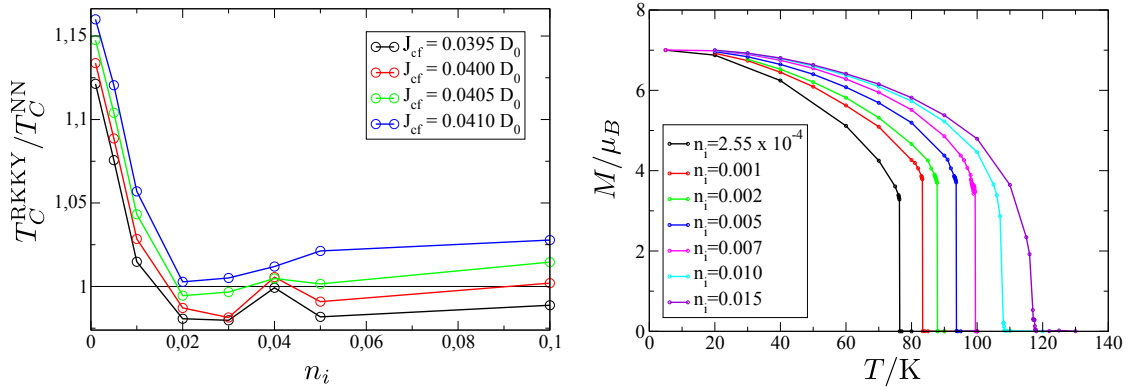


Figure 6.8.: Curie temperature ratio $T_C^{\text{RKKY}}/T_C^{\text{NN}}$ plotted against the doping concentration n_i for different values of the coupling J_{cf} (left) and total magnetization $M = \langle S \rangle + \langle \sigma \rangle$ against the temperature for various doping concentrations in bulk $\text{Eu}_{1-x}\text{Gd}_x\text{O}$ with long range RKKY coupling (right).

Since the coupling J_{cf} is reduced, the conduction band occupation has an even greater impact on the indirect interaction between the $4f$ moments in the long range case than

in the nearest neighbor case. Therefore it is plausible that the magnetization remains high for elevated temperatures and falls off more abruptly than in the nearest neighbor case, as it can be seen on the right hand side of figure 6.8. This also explains the relative increase in the Curie temperatures T_C^{RKKY} for low doping concentrations.

In the case of free electrons at zero temperature, the RKKY coupling is proportional to $[\cos(k_F R) - k_F R \sin(k_F R)]/(k_F R)^4$, where k_F is the Fermi momentum and R is the distance between the magnetic moments [60]. In particular, the coupling falls off with the third power in $k_F R$. We expect a similar behavior in the interacting case at finite temperatures. The top of figure 6.9 shows the RKKY coupling $J^{\text{RKKY}}(R)$ (cf. equation (5.98)) for different temperatures in the case of $n_i = 0.04$. As expected, the magnitude of the oscillations in $J^{\text{RKKY}}(R)$ is reduced together with the population of the conduction band for elevated temperatures, while the oscillation wavelength remains constant.

In all calculations, the cutoff R_{max} has to be chosen sufficiently large, such that J_{4f} and therefore T_C^{RKKY} does not change significantly. For this purpose, we show the normalized integrated coupling

$$\bar{J}_{4f}^{\text{RKKY}}(R) = \frac{J_{4f}^{\text{RKKY}}(R)}{J^{\text{RKKY}}(R_{\text{max}})},$$

at $T = 20\text{K}$, for various doping concentrations at the bottom of figure 6.9. Here, $J_{4f}^{\text{RKKY}}(R)$ is the integrated coupling up to the maximal distance R as it is given in (5.99). Together with the doping concentration, the Fermi momentum is increased. Thus, the range of the interaction should be reduced, which is supported by our findings. For the above calculations, the cutoff distance was set to $R_{\text{max}} = 20a$. In the multilayer calculations, the choice of R_{max} has a huge influence on the calculation time, since the number of non-local Green's functions grows with the third power of R_{max} . In order to keep these calculations feasible, we set

$$R_{\text{max}} = \begin{cases} 5a & \text{if } n_i \geq 0.01 \\ 10a & \text{if } n_i < 0.01 \end{cases}$$

in all multilayer calculations. In doing so, we accept errors in J_{4f}^{RKKY} up to a few percent (see figure 6.9).

6.4. Conclusion

We have shown that the simultaneous phase transition in electron doped Europium monoxide is qualitatively well described by our theory. Moreover, we identified two mechanisms which are responsible for the increase of the Curie temperature with the doping concentration. On the one hand, we could support the findings of Mairoser et. al. that the population of the conduction band is strongly related to the increase in the transition temperature. In particular, we found that the saturation effect at high doping concentrations can be attributed to increasingly occupied impurity states. On the other hand, we demonstrated that the low lying spin fluctuation on magnetic impurities and the corresponding transfer of spectral weight towards the Fermi edge has an even greater

6. Bulk systems of electron doped Europium monoxide

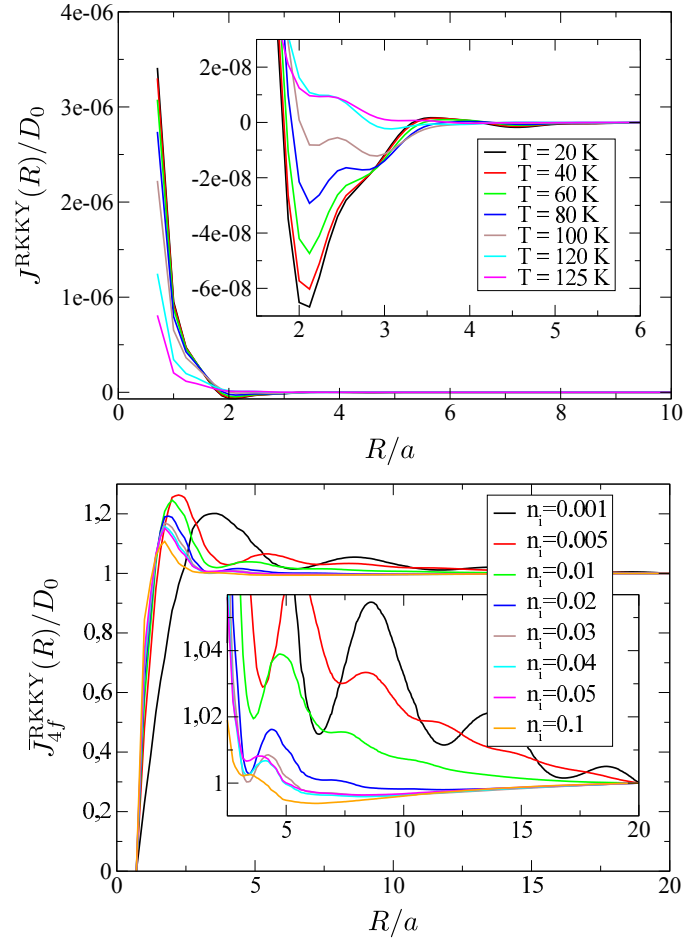


Figure 6.9.: Long range RKKY coupling $J^{\text{RKKY}}(R)$ for $x = n_i = 0.04$ and various temperatures in bulk $\text{Eu}_{1-x}\text{Gd}_x\text{O}$ (top) and the corresponding normalized integrated coupling $\bar{J}_{4f}^{\text{RKKY}}(R)$ at $T = 20\text{K}$ for different doping concentrations n_i (bottom).

impact on the doping induced T_C enhancement. This provides a possible explanation for the absence of doping induced T_C enhancement in oxygen deficient Europium monoxide, as it reported by several authors [6–11]. With the prospect of describing multilayer systems beyond the nearest neighbor approximation, we investigated the theory including long range RKKY interaction and fixed the free parameter J_{cf} such that the results are compatible to the nearest neighbor case.

7. Thin films of Gadolinium doped Europium monoxide

In this chapter, we investigate the influence of finite size effects onto the phase transition in thin films of $\text{Eu}_{1-x}\text{Gd}_x\text{O}$. To ensure comparability, we make use of the same model parameters as in the bulk case. However, the film thickness, which is determined by the number of layers N , and the doping concentration n_i remain as variable parameters. In a systematic investigation, we explore this two dimensional parameter space around a central point at $N = 9$ and $n_i = 0.01$. Throughout this chapter, we consider mirror symmetric systems of $N = 2\tilde{N} - 1$ monolayers (cf. appendix C). In contrast to the nomenclature in the appendix, we use α as the layer index with $\alpha = 0$ denoting the symmetry plane.

In addition, we investigate thin films of a simple metal for comparison. For this purpose, we restrict ourselves to the conduction band parts of the Hamiltonian (4.8) and (4.9), which substantially simplifies the theory of chapter 5 due to the absence of impurity and $4f$ moment contributions. The filling of the metal conduction band is then determined by the parameter n_{cc} (cf. section 5.4).

The chapter is divided into two parts. In the first section, we work out the mechanisms which influence the simultaneous phase transition in thin films by means of the multilayer theory with nearest neighbor interaction. Afterwards, in the second part, we compare the results to the ones for the theory with long range RKKY coupling.

7.1. Nearest neighbor case

In the following we discuss the solution of the multilayer theory with nearest neighbor magnetic interaction applied to the case of isolated thin films of $\text{Eu}_{1-x}\text{Gd}_x\text{O}$. We expose the most characteristic features by analyzing the prototype system with $N = 9$ and $n_i = 0.01$. Afterwards, we investigate the influence of varying film thicknesses and doping concentrations.

The most important difference to the bulk system is the variation of charge carrier density along the perpendicular direction Δn_α . It is depicted in figure 7.1 for the prototype system for various temperatures across the phase transition. There is an electron depletion at the surface and the onset of Friedel oscillations towards the inner layers. This can be seen by comparison with the results for a thicker metal film, which are depicted in the inset of figure 7.1. The magnitude of these oscillations decreases with the temperature since the electrons depopulate the conduction band in favor of the impurity states with increasing temperature (see bottom left of figure 6.2). This is in contrast to the behavior in the metal film, where the charge carrier density does not change significantly with

7. Thin films of Gadolinium doped Europium monoxide

the temperature due to the absence of impurities (not shown). The wavelength of these oscillations decreases with rising doping concentration, since the Fermi wavenumber is increased together with the conduction band occupation (cf. figure 8.1). Due to the small doping concentrations n_i , the contribution of the impurity occupation number n_d^α to the charge carrier density $\Delta n_\alpha = n_c^\alpha + n_i n_d^\alpha - n_{cc}$ is small. Hence, the behavior of the latter is mainly governed by the conduction band occupation number n_c^α . By comparing figures 7.1 and 7.2, we see that electron depletion and accumulation in Δn_α is indeed related to conduction band occupation reduction and increase, respectively. Concomitantly, the impurity occupation is enhanced if the conduction band occupation is lowered.

The impact of charge carrier density variations onto the spectral densities can be observed in figure 7.3, where we depict the conduction electron spectral density at different perpendicular positions in the low temperature phase $T = 20\text{K}$. Due to the finite system size, the curves acquire a step-like structure (cf. section 5.1.2). The varying occupation of majority conduction band states in the different layers is mainly responsible for charge carrier density variations. In other respects, the behavior is quite similar to the bulk case including the impurity induced side band and the appearance of a gap in the high temperature phase (cf. figure 6.2).

This can be seen in figure 7.4, where we depict the conduction band spectral density in the high temperature phase.

We now inspect the ferromagnetic phase transition. To gain insight into the spatial distribution of the magnetic moments across the perpendicular direction, we depict the total magnetization in layer α , which is given by $M_\alpha = \langle S_\alpha \rangle + \langle \sigma_\alpha \rangle$, for various temperatures in the left hand side of figure 7.5. For the definition of the Curie temperature T_C we use the average magnetization $\bar{M} = \frac{1}{N} \sum_{\alpha=1}^N M_\alpha$. Similar to the bulk case, T_C is defined as the maximal temperature with $\bar{M} > 0.005\mu_B$. In comparison to the bulk value of $T_C = 94.8\text{K}$, the thin film exhibits a substantially decreased transition temperature of 83K in the thin film system of 9 layers ($n_i = 0.01$). The reason for this is twofold. First of all, the missing coupling partners at the surface lead to a reduction of the magnetization in the outmost layers. This is similar to the effect in an isolated film of a Heisenberg lattice (cf. figure 5.5). In addition, the depletion of surface conduction band electrons leads to a reduction of the indirect coupling between $4f$ moments, both inside the surface layer as well as in between different layers near the surface.

The semiconductor-metal transition also occurs in the thin film system, as one can see in figure 7.6. Here, we depict the parallel resistivity $\rho_{\parallel}(\alpha)$ (5.154) for various layer indices α as well as the perpendicular resistivity ρ_{\perp} (5.155). For low temperatures, the parallel resistivity is increased at the surface due to the depletion of electrons in the outer layers. For the same reason, the high temperature gap is shifted more and more while going from the center to the surface (see figure 7.4). This leads to a decrease of the parallel resistivity with increasing layer index for high temperatures. The perpendicular resistivity is sensitive to the strongest resistivity contribution along the perpendicular direction. This means that whenever there is a gap in the spectral density along the layers, the overall perpendicular resistivity is high and the system is semiconducting with respect to the perpendicular direction. As a result, the perpendicular resistivity roughly follows the maximal values of the parallel resistivities in the different layers.

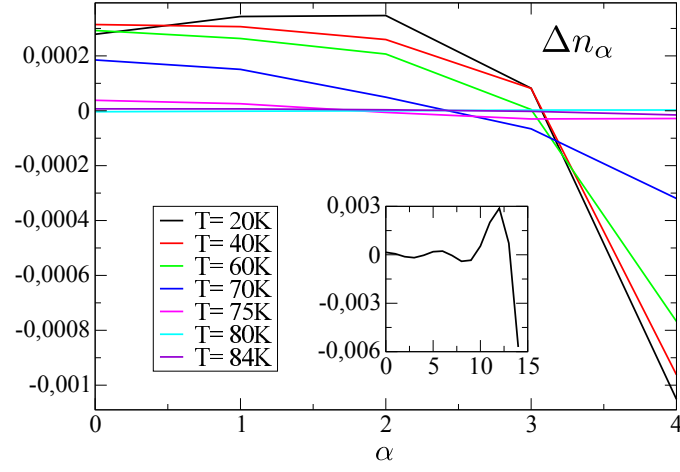


Figure 7.1.: Charge carrier density against the layer index for various temperatures in an isolated mirror symmetric film of $\text{Eu}_{1-x}\text{Gd}_x\text{O}$ with $N = 9$ ($\tilde{N} = 5$) and $n_i = 0.01$. The insets show the charge carrier density for a metal system with $N = 29$ ($\tilde{N} = 15$) and $n_{cc} = 0.01$ at $T = 20\text{K}$.

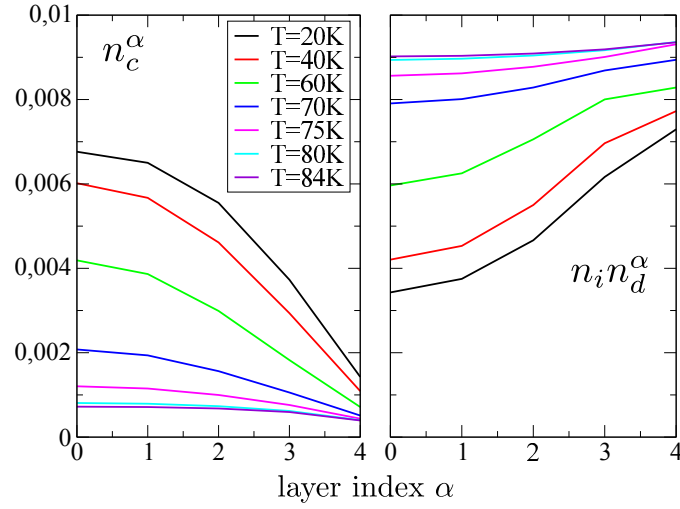


Figure 7.2.: Conduction band occupation number n_c^α (left) and impurity occupation number n_d^α (right) against the layer index for various temperatures in an isolated mirror symmetric film of $\text{Eu}_{1-x}\text{Gd}_x\text{O}$ with $N = 9$ ($\tilde{N} = 5$) and $n_i = 0.01$.

7. Thin films of Gadolinium doped Europium monoxide

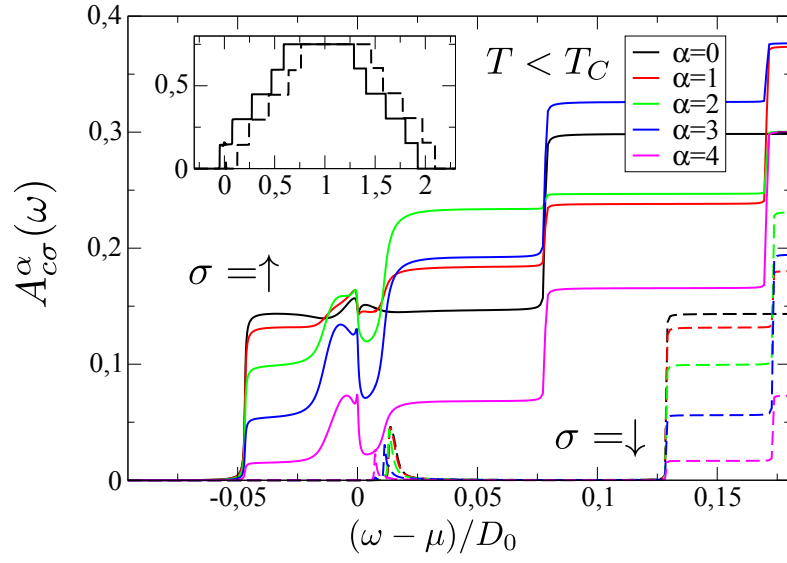


Figure 7.3.: Majority (solid lines) and minority (dashed lines) conduction band spectral density for different layers at $T = 20\text{K}$ in an isolated mirror symmetric film of $\text{Eu}_{1-x}\text{Gd}_x\text{O}$ with $N = 9$ and $n_i = 0.01$.

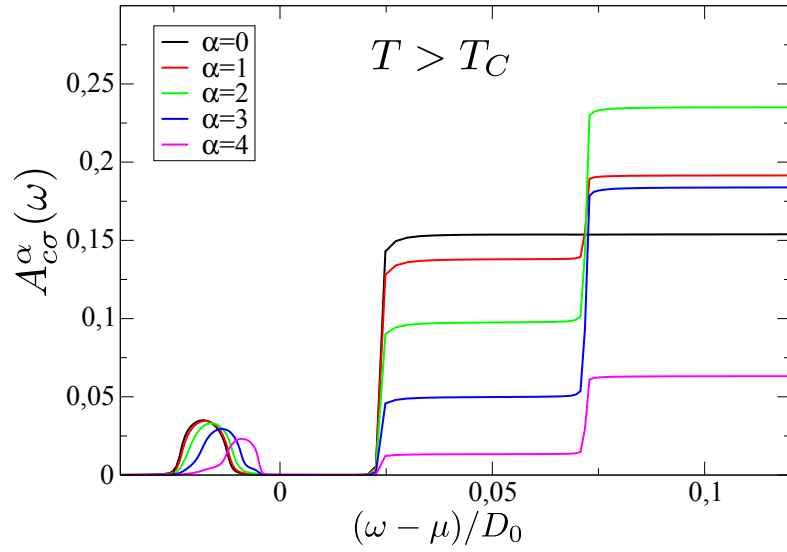


Figure 7.4.: Spin degenerate conduction band spectral density for different layers at $T = 100\text{K}$ in an isolated mirror symmetric film of $\text{Eu}_{1-x}\text{Gd}_x\text{O}$ with $N = 9$ and $n_i = 0.01$.

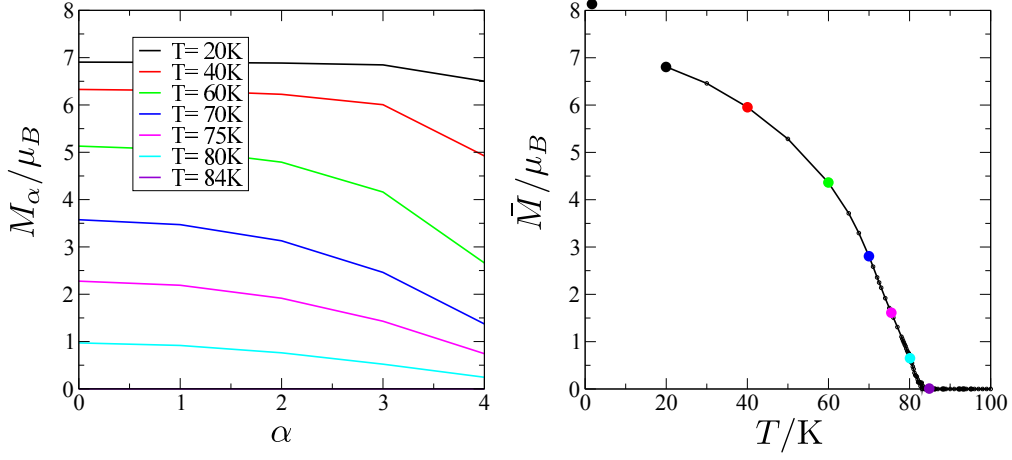


Figure 7.5.: Ferromagnetic phase transition in an isolated mirror symmetric film of $\text{Eu}_{1-x}\text{Gd}_x\text{O}$ with $N = 9$ and $n_i = 0.01$ as seen in the layer dependent magnetization M_α for various temperatures (left) as well as the average magnetization \bar{M} against the temperature (right).

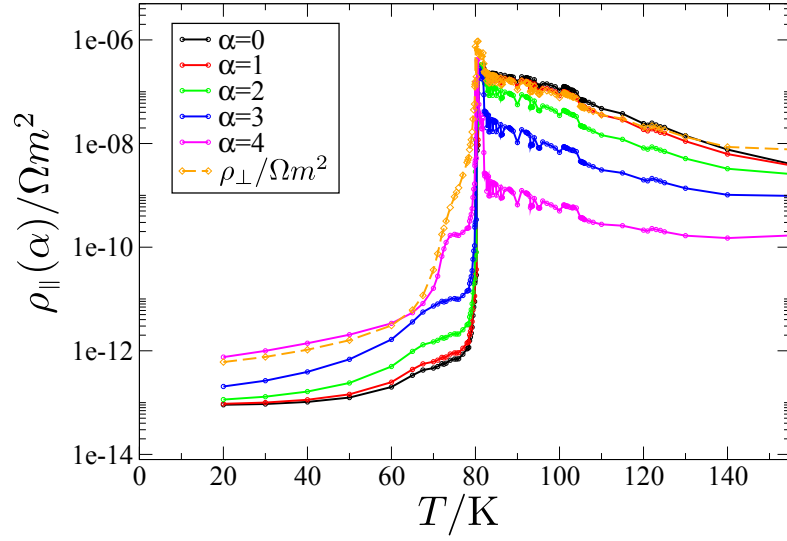


Figure 7.6.: Parallel resistivity $\rho_\parallel(\alpha)$ for various layer indices α and perpendicular resistivity ρ_\perp for an isolated mirror symmetric film of $\text{Eu}_{1-x}\text{Gd}_x\text{O}$ with $N = 9$ and $n_i = 0.01$.

7. Thin films of Gadolinium doped Europium monoxide

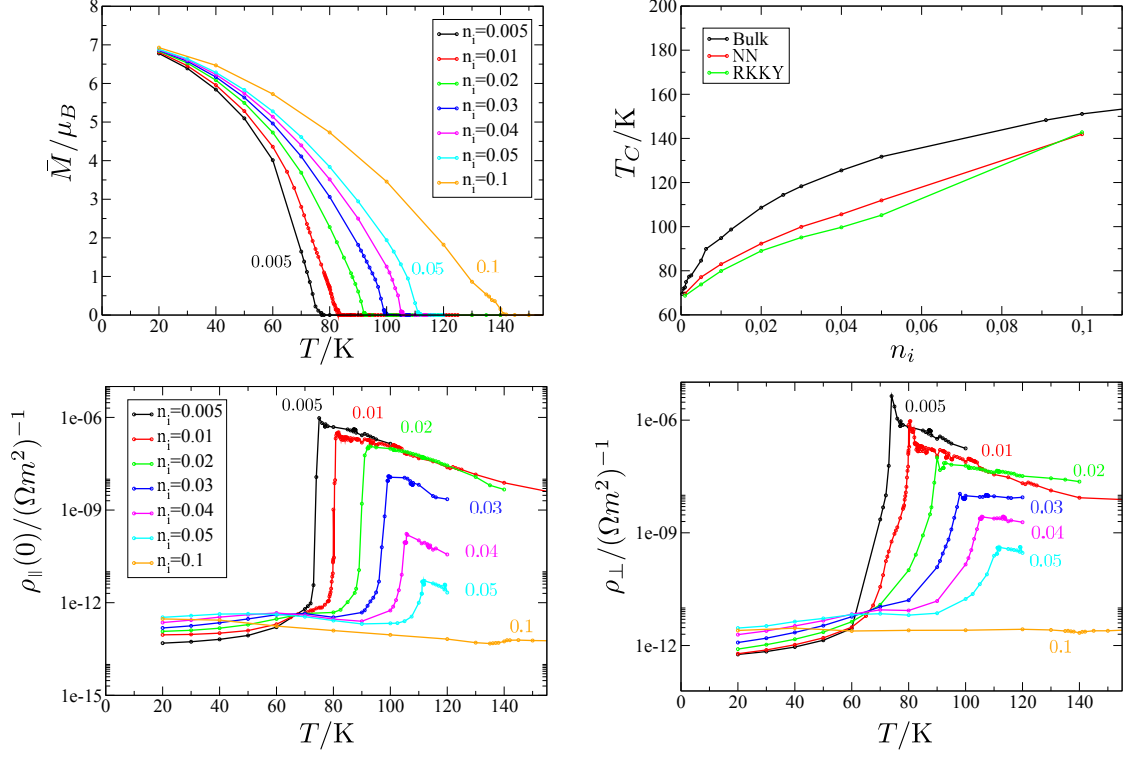


Figure 7.7.: Influence of the doping concentration n_i on the phase transition in an isolated mirror symmetric film of $\text{Eu}_{1-x}\text{Gd}_x\text{O}$ with $N = 15$ ($\tilde{N} = 9$) as seen in the average magnetization \bar{M} (top left), the parallel resistivity $\rho_{\parallel}(\alpha) = 1/\sigma_{\parallel}(\alpha)$ at $\alpha = 0$ (bottom left) and the perpendicular resistivity ρ_{\perp} (bottom right) against the temperature for various doping concentrations n_i . The Curie temperature T_C against the doping concentration n_i is shown in the top right figure. For comparison, we show the corresponding curves for the bulk and long range RKKY system.

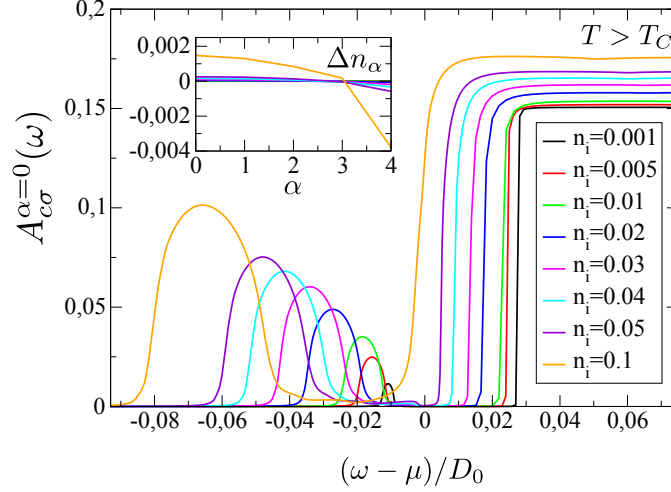


Figure 7.8.: Spin degenerate conduction band spectral density $A_{c\sigma}^{\alpha}(\omega)$ in the middle layer $\alpha = 0$ of an $\text{Eu}_{1-x}\text{Gd}_x\text{O}$ film with $N = 9$ for various doping concentrations n_i . The temperatures $T(n_i) = T_C(n_i) + 0.1\text{K}$ are taken slightly above the Curie temperatures, which are given by $T_C(0.001) = 69.7\text{K}$, $T_C(0.002) = 77.1\text{K}$, $T_C(0.01) = 83.0\text{K}$, $T_C(0.02) = 92.3\text{K}$, $T_C(0.03) = 99.9\text{K}$, $T_C(0.04) = 105.6\text{K}$, $T_C(0.05) = 111.9\text{K}$ and $T_C(0.1) = 141.9\text{K}$.

To investigate the influence of the doping concentration on the phase transition, we keep the film thickness constant to $N = 9$ and examine the results for various doping concentrations in figure 7.7. Similar to the bulk case, the Curie temperature increases with the doping concentration. On the other hand, there is an overall reduction in T_C around 10%, which can be attributed to the finite size effects. Concomitant with the ferromagnetic phase transition, there is a semiconductor metal transition in the parallel resistivity as well as the perpendicular resistivity. However, by increasing the doping concentration, the resistivity step at the Curie temperature gets weaker and weaker until, at $n_i = 0.1$, there is no semiconductor-metal transition at all. The reason for this can be seen in figure 7.8. Since the overall scale of the charge carrier density variations along the perpendicular direction is increased together with the doping concentration, the gap in the conduction band spectral density of the middle layer is shifted downwards more and more while the doping concentration rises. At $n_i = 0.1$, this shift is so strong that the gap is below the Fermi edge and the system is conducting even in the high temperature phase.

To further examine the finite size effects, we hold the doping concentration constant to $n_i = 0.01$ and inspect the results for different film thicknesses N in figure 7.9. We already saw a T_C reduction of around 10% due to the presence of the surface in films with $N = 9$. From experiments [19, 21, 23, 24, 29] we know that the impact of the surface should get stronger the thinner the film is. Indeed, we observe a decrease of the transition temperature with the film thickness up to $T_C = 69.9\text{K}$ for a film with $N = 3$. However, these results are not directly comparable to the experimental data since the

7. Thin films of Gadolinium doped Europium monoxide

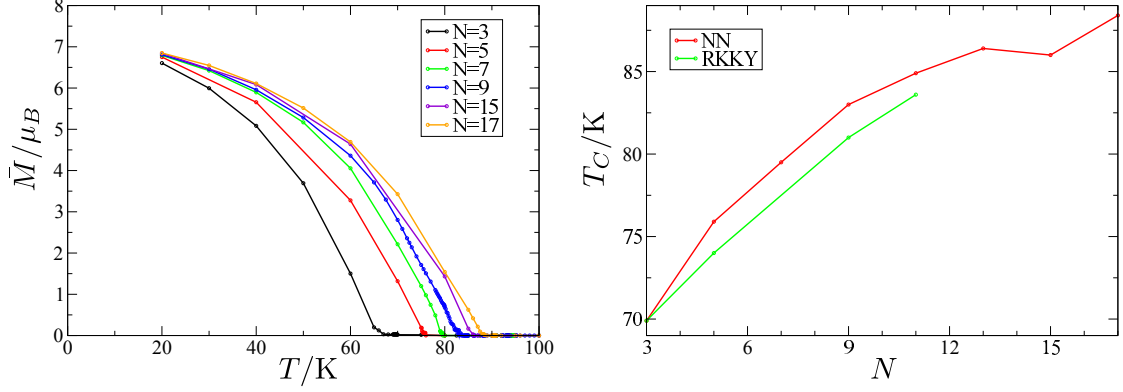


Figure 7.9.: Influence of the film thickness N on the Curie temperature in an isolated mirror symmetric film of $\text{Eu}_{1-x}\text{Gd}_x\text{O}$ with $n_i = 0.01$ as seen in the average magnetization \bar{M} against the temperature for various film thicknesses N (left) as well as the Curie temperature T_C against the film thickness (right). For comparison, we show the corresponding curve for the long range RKKY case in the right figure.

measurements were either performed for stoichiometric EuO [19, 21, 24, 29] or a highly influential substrate was used [23].

7.2. Long range RKKY coupling case

In the bulk case, the effect of including long range RKKY interactions were small, since we chose J_{cf} such that the Curie temperatures were approximately equal in the nearest neighbor and in the long range RKKY case. However, in the multilayer case we expect a greater impact on the ferromagnetic phase transition. As we have seen in section 6.3, the range of the RKKY coupling of the size of a few lattice constants, which should make the physical behavior more sensitive to finite size effects than in the nearest neighbor case. We conduct the same systematic analysis as in the nearest neighbor case and change the variables N and n_i around the prototype system with $N = 9$ and $n_i = 0.01$. The increase of T_C with the doping concentration is shown on the right hand side of figure 7.9. The effect of missing coupling partners and electron depletion at the surface leads to a more pronounced T_C reduction in the RKKY case, due to the longer range of the interaction (cf. figure 5.5). The general behavior is similar to the nearest neighbor case except for sharper magnetization curves as they were also observed in the bulk long range RKKY case (not shown).

The position dependence of the RKKY coupling in a multilayer system can be seen in figures 7.10 and 7.11, where we depict the parallel coupling (5.100) and the perpendicular coupling (5.102) in an $\text{Eu}_{1-x}\text{Gd}_x\text{O}$ film with $N = 9$ and $n_i = 0.01$. There is a reduction in the overall strength of the coupling at the surface, which is connected to the electron depletion at the surface and the increase of the conduction band occupation

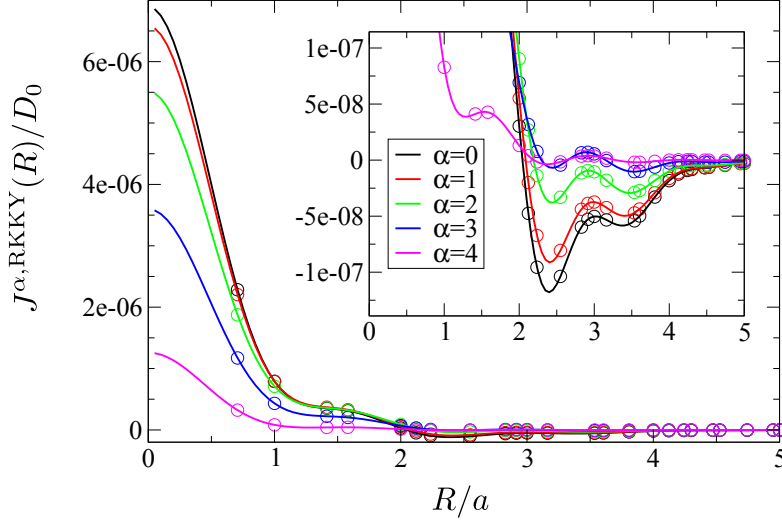


Figure 7.10.: Parallel RKKY coupling in the different layers of a system an $N = 9$ $\text{Eu}_{1-x}\text{Gd}_x\text{O}$ film with $n_i = 0.01$ at $T = 20\text{K}$. The circles indicate the positions of the nearest neighbors in an (100) monolayer of an FCC lattice.

towards the inner layers. The charge carrier density shows a similar behavior as in the nearest neighbor case (not shown). In the region between 2 and 4 lattice constants, the perpendicular coupling becomes anti-ferromagnetic. However, since the intralayer coupling and the coupling between neighboring layers is ferromagnetic, the overall behavior remains ferromagnetic and the total magnetization M_α shows the same behavior as in the nearest neighbor case (see figure 7.5).

7.3. Conclusion

We have shown that the Curie temperature for the simultaneous ferromagnetic semiconductor to metal transition in $\text{Eu}_{1-x}\text{Gd}_x\text{O}$ is reduced by finite size effects in thin films. This effect is even more pronounced in the more realistic case of including long range RKKY interaction in the theory. In all cases, the charge carrier density shows an electron depletion at the surface and Friedel oscillations inside the system. Towards the surface layers, the mean field magnetization decreases due to the absence of magnetic moments in the vacuum and the reduced conduction band occupation at the surface. On the other hand, all the general characteristics of the phase transition, like the doping induced T_C enhancement and the simultaneity with respect to the semiconductor-metal transition, are preserved. However, in the case of $N = 9$ and $n_i = 0.1$, the surface induced charge carrier variation is so strong, that the system becomes metallic even in the high temperature phase due to the shift of the gap. The band bending effects in a heterostructure are expected to have a comparable or even stronger impact on the charge carrier density and therefore on the fragile occurrence of a semiconducting high temperature phase. This matter is further investigated in the subsequent chapter.

7. Thin films of Gadolinium doped Europium monoxide

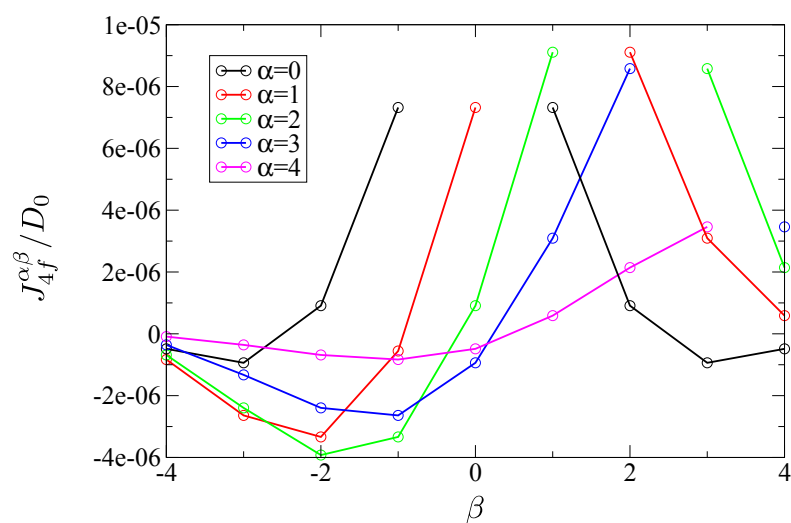


Figure 7.11.: Perpendicular RKKY coupling for the different layers of an $N = 9$ $\text{Eu}_{1-x}\text{Gd}_x\text{O}$ film with $n_i = 0.01$ at $T = 20\text{K}$. Note that the distance between to neighboring layers is $a/2$.

8. Metal-Eu_{1-x}Gd_xO-metal heterostructures

In a metal-metal interface, band bending effects can lead to diffusion of charge carriers from one material to the other and the formation of a space charge region [64]. In the simplest approximation, the direction of the charge flow is determined by the work functions of the two materials. The electrons gain energy by diffusing from the material with smaller work function to the other one (cf. figure 5.7). We expect similar effects to occur in an interface of electron doped EuO and an ordinary metal. Moreover, the electron accumulation or depletion near the surface should have a large effect on the transition temperature, since we saw that the conduction band occupation is responsible for the enhancement of the Curie temperature (cf. figures 6.1 and 7.7). Although the theory neglects effects like surface reconstruction, we expect it to describe the qualitative features, especially with respect to the phase transition.

In this chapter, we consider mirror symmetric three component heterostructures consisting of an Eu_{1-x}Gd_xO film with a metal film on top and below. For the Eu_{1-x}Gd_xO film, we use the same parameters as in the bulk case of chapter 6 and the case of isolated films of chapter 7. However, as variable parameters, we use the doping concentration n_i and the number of Eu_{1-x}Gd_xO layers, which we again denote by N . As mentioned before, we model a metal by omitting the impurity and magnetic parts of the theory, which leaves us with a non-interacting conduction band. The filling of the latter is denoted by n_m and the number of metal layers by M . In the metal layers, we use the same value for the half band width as in the Eu_{1-x}Gd_xO layers. As a result, the interlayer hopping t_α does not depend on the layer index (cf. chapter 4). In order to apply the multilayer theory of chapter 5 to such a heterostructure, one has to consider a mirror symmetric two component system. The self-energy in the first N layers is characterized by the contributions from the impurity (5.56), the $4f$ moments (5.90) and the electrostatic potential (5.115). In the following M layers, only the electrostatic contribution (5.115) remains. Since the self-energy is purely real in the metal layers, we expect extremely narrow peaks in the momentum dependent conduction electron Green's function (5.19). Therefore, the usage of several logarithmically dense regions in the integration grid as well as an extremely accurate localization of the poles in (5.19) is imperative (cf. section 5.1.2).

The remaining parameter for the heterostructures is the work function difference $\Delta W = W_{\text{EuO}} - W_{\text{Metal}}$. As it was explained in section 5.4.2, one needs to solve the theory for the isolated subsystems first, in order to match the energy scales and obtain the input parameters for the heterostructure theory which correspond to the correct value of ΔW . Thus, we need to solve the theory for the isolated Eu_{1-x}Gd_xO film with thickness N and the doping concentration n_i as well as the isolated metal film with thickness

8. Metal-Eu_{1-x}Gd_xO-metal heterostructures

M and band filling n_m , both for the temperature at hand. This procedure is automated by a set of programs, which store the energy shifts μ_0 for the isolated systems in a database [65]. Whenever a heterostructure calculation is started within this framework, the database is checked for the corresponding values of the isolated constituent systems. If the results for one of the subsystems are not present, the corresponding calculation is initiated. Afterwards, the heterostructure calculation is resumed automatically with the correct input parameters.

In the first section of this chapter, we perform a thorough investigation on the influence of the various material parameters on the phase transition in the Eu_{1-x}Gd_xO film. For this purpose, we use the nearest neighbor approximation in the magnetic coupling. In the second part, we include long range RKKY interactions and compare the results to the nearest neighbor case.

8.1. Nearest neighbor case

In order to assess the variety of phenomena which can occur in such heterostructures, we conduct a systematic analysis in the parameters N , M , n_i , n_m and ΔW . Due to the increased demands of the heterostructure calculation concerning computer resources, we start with a certain point in parameter space and investigate the behavior along the five different parameter axes separately. As the central point, which we call the prototype system, we choose $N = 9$, $M = 9$, $n_i = 0.01$, $n_m = 0.01$ and $\Delta W = 0.125D_0 = 1\text{eV}$.

8.1.1. Influence of the metal band filling

The investigation of different metal band fillings n_m provides us with an overview of the most important mechanisms in a metal-Eu_{1-x}Gd_xO-metal heterostructure. As one can see in the top of figure 8.1, the electron depletion at the vacuum-metal interface strongly depends on the metal band filling, and so does the Friedel oscillation wavelength.

In the case of $n_m = 1.0$, the nodes of the oscillations coincide with the layer position, so that no oscillation can be observed. Moreover, there is an accumulation of charge carriers in the outmost layers of the Eu_{1-x}Gd_xO film and a depletion in the inner metal layers. This is the result of the positive work function difference $\Delta W = 0.125D_0 = 1\text{eV}$, which leads to an upwards band bending in the inner metal layers and a downwards band bending at the surfaces of the Europium monoxide film.

In order to minimize their energy, electrons pass over from the metal to the Eu_{1-x}Gd_xO. This process is more effective the more electrons are available in the metal. Therefore the charge carrier accumulation increases with the metal band filling n_m . On the other hand, the decrease in Δn_α towards the inner layers is more abrupt for high metal band fillings than for low ones. It turns out that this behavior is not advantageous for the T_C enhancement. The magnetization M_α follows the behavior of the conduction band occupation n_c^α for most of the layer indices, which can be observed in figure 8.2. At the outmost Eu_{1-x}Gd_xO layer, the magnetization is reduced due to the missing coupling partners. However, as a result of the conduction electron accumulation, the reduction is not as pronounced as in the isolated case. As the metal band filling decreases, the

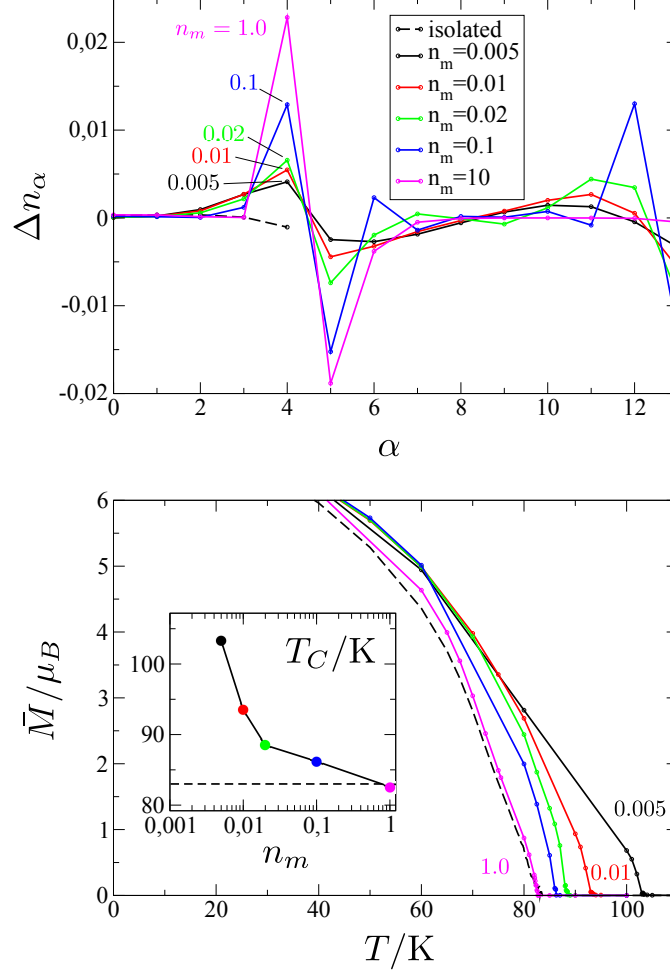


Figure 8.1.: Influence of the metal band filling n_m on the ferromagnetic phase transition in a metal-Eu_{1-x}Gd_xO-metal heterostructure with $N = 9$, $M = 9$, $n_i = 0.01$ and $\Delta W = 1\text{eV}$ as seen in the charge carrier density Δn_α against the layer index α (top) as well as the average magnetization \bar{M} against the temperature (bottom). The inset in the bottom figure depicts the Curie temperature versus n_m . For comparison, we show the results for the corresponding isolated Eu_{1-x}Gd_xO film (dashed lines).

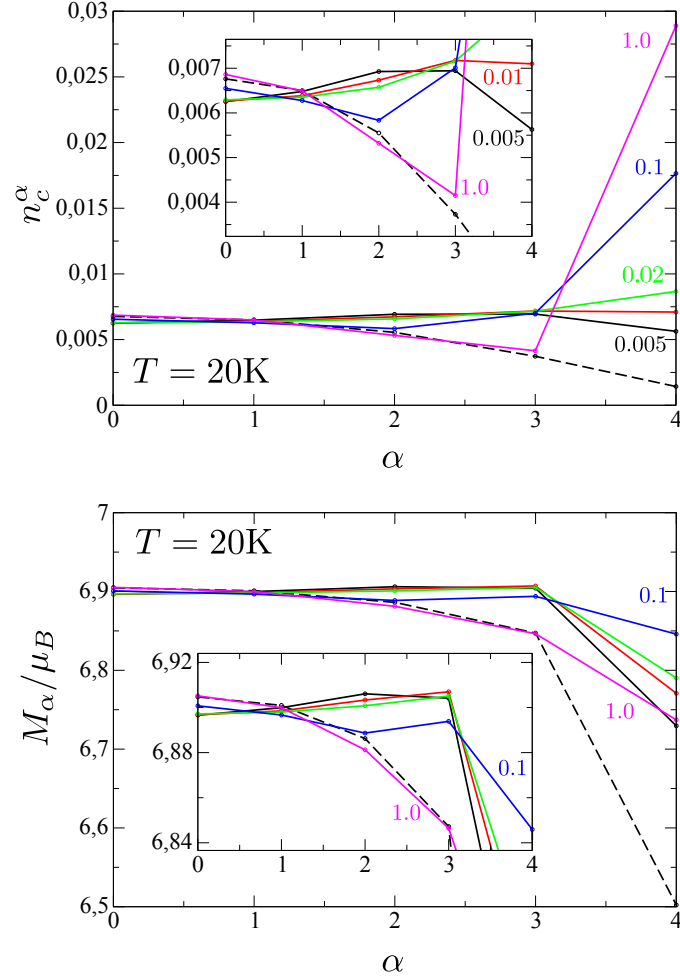


Figure 8.2.: Influence of the metal band filling n_m on the ferromagnetic phase transition in a metal-Eu_{1-x}Gd_xO-metal heterostructure with $N = 9$, $M = 9$, $n_i = 0.01$ and $\Delta W = 1\text{eV}$ as seen in the conduction band occupation n_c^α (top) and the magnetization M_α (bottom) against the layer index, respectively. For comparison, we show the results for the corresponding isolated Eu_{1-x}Gd_xO film (dashed lines).

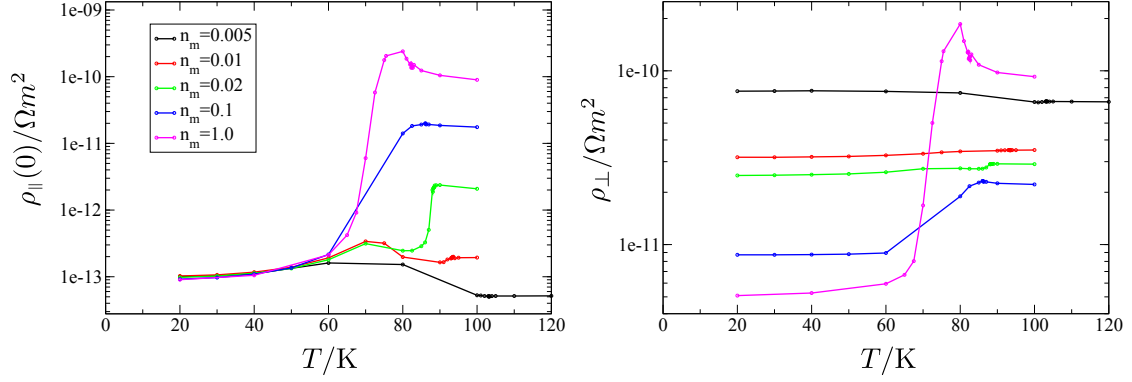


Figure 8.3.: Influence of the metal band filling n_m on the semiconductor-metal transition in a metal-Eu_{1-x}Gd_xO-metal heterostructure with $N = 9$, $M = 9$, $n_i = 0.01$ and $\Delta W = 1\text{eV}$ as seen in the parallel resistivity in the middle layer $\rho_{\parallel}(0)$ (left) and the perpendicular resistivity ρ_{\perp} (right).

strength of the charge carrier accumulation decreases. At the same time however, an increase in the conduction band occupation over a wider range of layers can be observed. This leads to an increase of the perpendicular coupling between the inner layers and therefore to a strong T_C enhancement up to $T_C = 103.3\text{K}$ in the case of $n_m = 0.005$ (see bottom of figure 8.1). Despite the fact that the conduction band accumulation is maximal for $n_m = 1.0$, there is no T_C enhancement in this case. In comparison to the isolated case, the magnetic interaction is only increased significantly in the outer layer $\alpha = 4$. The resulting increase in the magnetic coupling cannot outweigh the missing coupling partners in the metal layers. Moreover, the slight reduction of n_c^α at $\alpha = 3$ seems to have a greater impact on the ferromagnetic transition since the Curie temperature of $T_C = 82.6\text{K}$ is even smaller than in the isolated case, where we have $T_C = 83\text{K}$.

The price one has to pay for the T_C enhancement is the disappearance of the semiconductor metal transition as one can see in figure 8.3. Here, we show the parallel resistivity in the middle layer and the perpendicular resistivity for the various metal band fillings n_m . While the resistivity step is still present for $n_m = 1.0$, $n_m = 0.1$ and $n_m = 0.02$, it disappears for lower metal band fillings. In figure 8.4 one can see the origin of this behavior. We show the spin degenerate conduction band spectral density in the middle layer slightly above the Curie temperature for the different metal band fillings n_m . Due to charge carrier variations, the gap is shifted such that the system is metallic even in the high temperature phase for $n_m = 0.005$, $n_m = 0.01$. For the same reason, the resistivity step is substantially reduced with respect to the isolated system for $n_m = 0.02$, $n_m = 0.1$ and $n_m = 1.0$ (cf. figure 7.6).

8.1.2. Influence of the Eu_{1-x}Gd_xO film thickness

Since the magnitude of the charge carrier variations falls off towards the inner layers, one might conjecture that the high temperature gap remains undisturbed far away from the

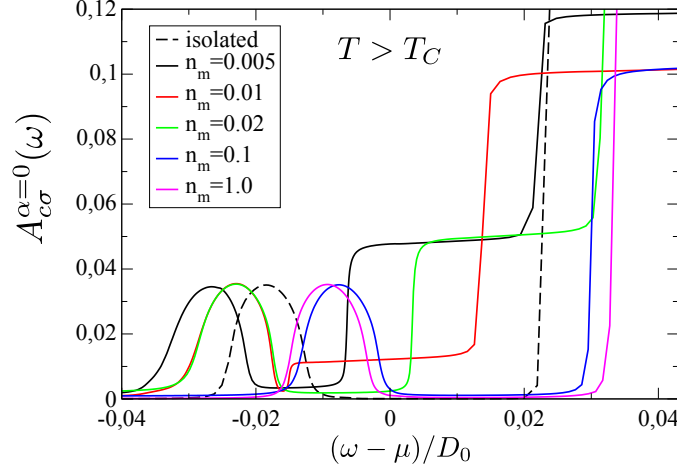


Figure 8.4.: Spin degenerate conduction band spectral density in the middle layer $A_{c\sigma}^{\alpha=0}(\omega)$ of a metal-Eu_{1-x}Gd_xO-metal heterostructure with $N = 9$, $M = 9$, $n_i = 0.01$ and $\Delta W = 1\text{eV}$ for various metal band fillings n_m . The temperatures $T(n_m) = T_C(n_m) + 0.1\text{K}$ are taken slightly above the Curie temperatures, which are given by $T_C(0.005) = 103.4\text{K}$, $T_C(0.01) = 93.6\text{K}$, $T_C(0.02) = 88.6\text{K}$, $T_C(0.1) = 86.3\text{K}$, $T_C(1.0) = 82.7\text{K}$ and $T_C(1.99) = 105.3\text{K}$. For comparison, we show the corresponding curve for the isolated system with $T_C = 83\text{K}$ (dashed line).

interfaces in a very thick sample. On the other hand, the interface induced T_C enhancement should be weakened as the Eu_{1-x}Gd_xO film thickness is increased. In figure 8.5, we show the impact of varying Eu_{1-x}Gd_xO film thicknesses on the ferromagnetic phase transition. With respect to the other parameters, the investigated heterostructures are equal to the prototype system. In particular, there is a positive work function difference which yields a charge carrier accumulation in the outer Eu_{1-x}Gd_xO layers. Together with the charge carrier density, the conduction band occupation is decreased towards the inner layers. As a result, the ferromagnetic interaction is not enhanced in the inner layers of a thick Eu_{1-x}Gd_xO film. This leads to a decrease of the Curie temperature with the Eu_{1-x}Gd_xO film thickness. Moreover, the semiconductor metal transition is restored for large N , since the perturbation of the gap position in the middle layer is reduced by increasing the distance to the interface (see figure 8.6). However, the step in the resistivity remains relatively weak. Note that the scale on the right hand side of figure 8.6 is linear. Obviously, there is still a small charge carrier density variation in the middle layer, which strongly affects the transport properties even in the $N = 17$ case. This leads us to the conclusion that the T_C enhancement via band bending is inevitably connected to the reduction of the semiconductor metal transition.

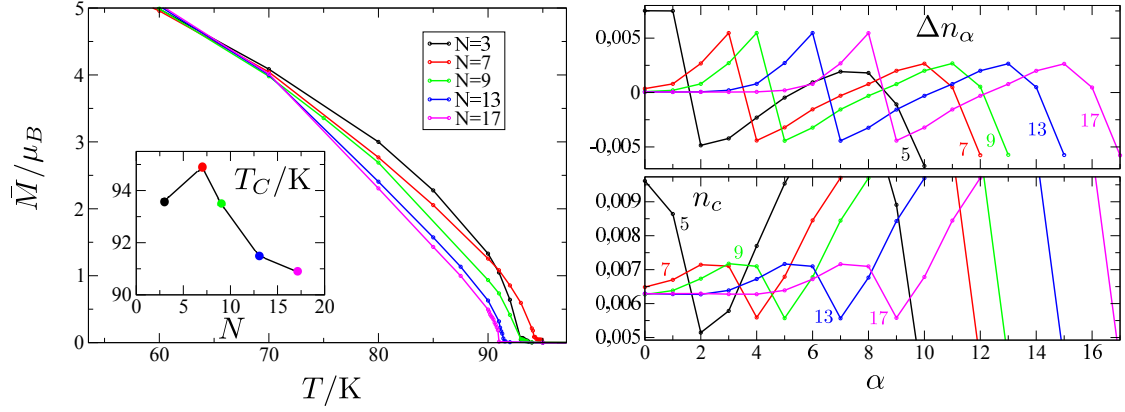


Figure 8.5.: Influence of the $\text{Eu}_{1-x}\text{Gd}_x\text{O}$ film thickness N on the ferromagnetic phase transition in a metal- $\text{Eu}_{1-x}\text{Gd}_x\text{O}$ -metal heterostructure with $M = 9$, $n_i = 0.01$, $n_m = 0.01$ and $\Delta W = 1\text{eV}$ as seen in the average magnetization \bar{M} against the temperature (left), as well as the charge carrier density Δn_α and the conduction band occupation n_c^α against the layer index (right), respectively. The inset in the left figure depicts the Curie temperature versus N .

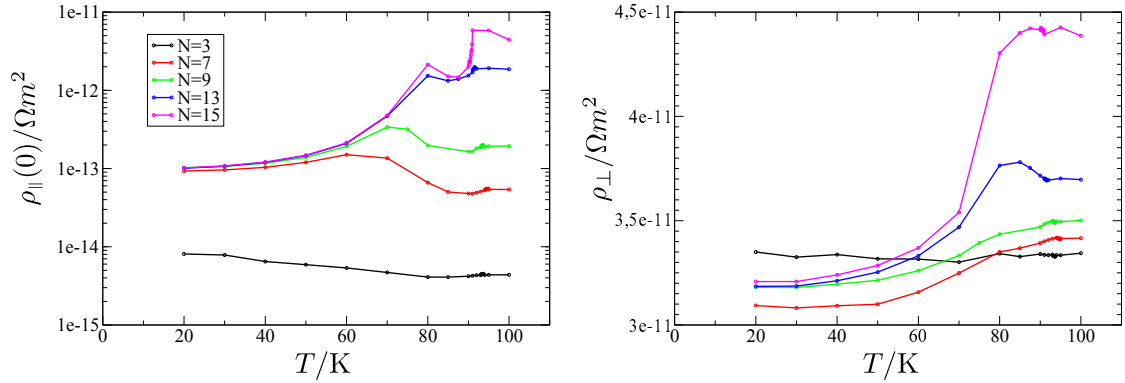


Figure 8.6.: Influence of the $\text{Eu}_{1-x}\text{Gd}_x\text{O}$ film thickness N on the semiconductor-metal transition in a metal- $\text{Eu}_{1-x}\text{Gd}_x\text{O}$ -metal heterostructure with $M = 9$, $n_i = 0.01$, $n_m = 0.01$ and $\Delta W = 1\text{eV}$ as seen in the parallel resistivity in the middle layer $\rho_{||}(0)$ (left) and the perpendicular resistivity ρ_{\perp} (right).

8. Metal-Eu_{1-x}Gd_xO-metal heterostructures

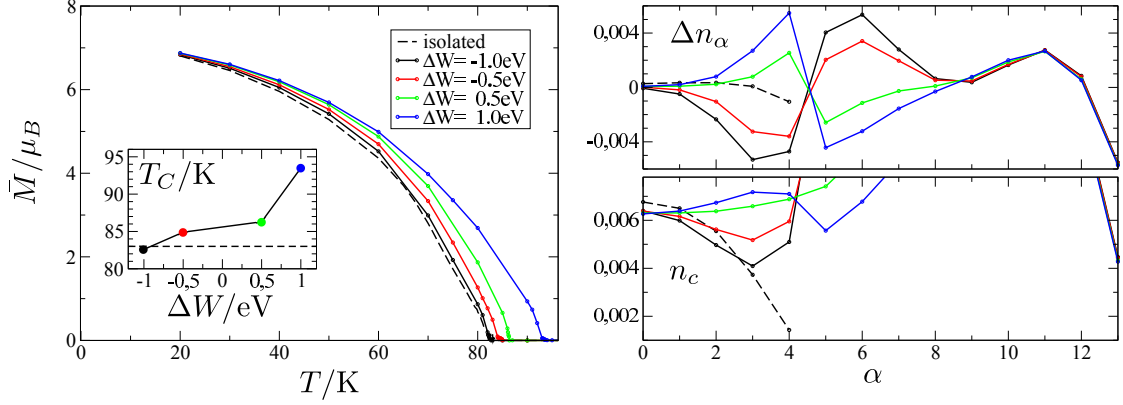


Figure 8.7.: Influence of the work function difference $\Delta W = W_{\text{EuO}} - W_{\text{Metal}}$ on the ferromagnetic phase transition in a metal-Eu_{1-x}Gd_xO-metal heterostructure with $N = 9$, $M = 9$, $n_i = 0.01$ and $n_m = 0.01$ as seen in the average magnetization \bar{M} against the temperature (left), as well as the charge carrier density Δn_α and the conduction band occupation n_c^α against the layer index (right), respectively. The inset in the left figure depicts the Curie temperature versus ΔW . For comparison, we show the results for the corresponding isolated Eu_{1-x}Gd_xO film (dashed lines).

8.1.3. Further exploration of the parameter space

So far, we have exposed the most influential mechanisms for the phase transition in metal-Eu_{1-x}Gd_xO-metal heterostructures. Here, we continue to explore the parameter space by variation of the work function difference ΔW , the doping concentration n_i and the metal film thickness M . Selecting $n_m = 0.01$, we have a relatively large penetration depth of the interface induced disturbance in the charge carrier density. As a result, the conduction band occupation is shifted to such an extent that the semiconductor-metal transition is suppressed. Since we would not gain any additional insight from it, we refrain from showing the transport properties in these system and rather focus on the ferromagnetic phase transition.

We begin with the variation of the work function difference. In figure 8.7, we see that there is an electron accumulation or depletion in the outmost Eu_{1-x}Gd_xO layers depending on the sign of ΔW . Despite the fact that there is a substantial depletion of electrons in the case of negative work function differences, the conduction band occupation is still enhanced in comparison to the isolated case. This is a consequence of the presence of the metal in comparison to the vacuum. Consequently, we see a reduction in the Curie temperature only for the strong negative work function difference of $\Delta W = -1\text{eV}$. In all other cases, we have a T_C enhancement. Due to the increased amount of conduction electrons in the Eu_{1-x}Gd_xO film, the Curie temperature increases with the work function difference.

In figure 8.8, we see that the doping concentration has a similar effect on the Curie temperature as in bulk Eu_{1-x}Gd_xO and isolated films of Eu_{1-x}Gd_xO (cf. figure 6.1

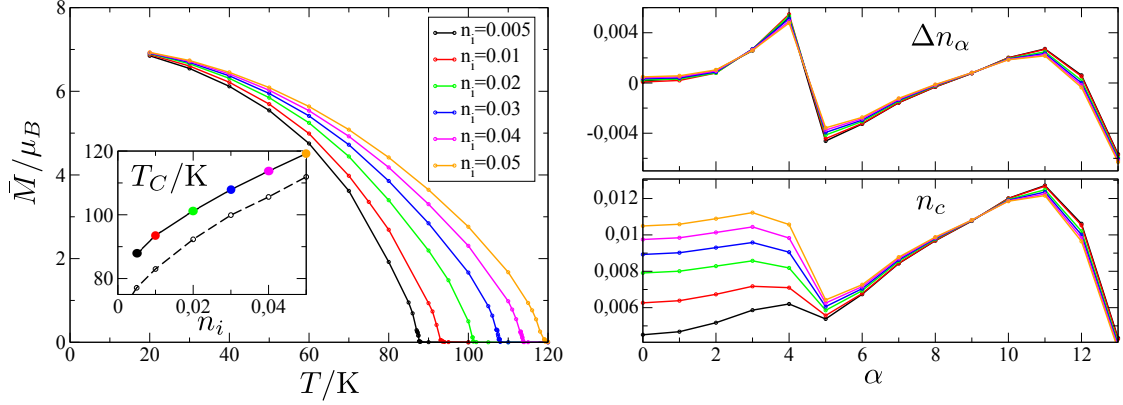


Figure 8.8.: Influence of the doping concentration n_i on the ferromagnetic phase transition in a metal-Eu_{1-x}Gd_xO-metal heterostructure with $N = 9$, $M = 9$, $n_m = 0.01$ and $\Delta W = 1\text{eV}$ as seen in the average magnetization \bar{M} against the temperature (left), as well as the charge carrier density Δn_α and the conduction band occupation n_c^α against the layer index (right), respectively. The inset in the left figure shows the Curie temperature versus n_i and the curve for the corresponding isolated Eu_{1-x}Gd_xO systems for comparison (dashed line).

and figure 7.7). Similarly, the Curie temperature is increased together with the doping concentration.

Finally, we inspect the effect of various metal film thicknesses M in figure 8.9. The Friedel oscillations in the metal are interrupted by the interface at different distances from the metal-vacuum interface. This leads to a diverse behavior with respect to the charge carrier accumulation in the Eu_{1-x}Gd_xO film. While the T_C enhancement is relatively weak for $M = 5$, $M = 9$ and $M = 11$, there is a strongly increased Curie temperature $T_C = 101.8\text{K}$ in the case of $M = 7$. Here, the metal-Eu_{1-x}Gd_xO interface coincides with a valley in the Friedel oscillation. Hence, the decrease of the metal charge carrier density at the interface, which already appears as a result of the positive work function difference, is intensified.

8.2. Long range RKKY coupling case

In this section, we compare the results of the heterostructure theory with and without the inclusion of long range RKKY interactions. For this purpose, we inspect the results for the prototype system as well as for a system which differs from the prototype system by a metal band filling of $n_m = 1.0$. As we saw in the previous section, the latter is characterized by a short penetration depth of the electron accumulation in the Eu_{1-x}Gd_xO film, and as a result, the conservation of the semiconductor-metal transition despite the presence of the metal interface. The results are depicted in figure 8.10. For both metal band fillings, the conduction band occupation is reduced in the RKKY case. However,

8. Metal-Eu_{1-x}Gd_xO-metal heterostructures

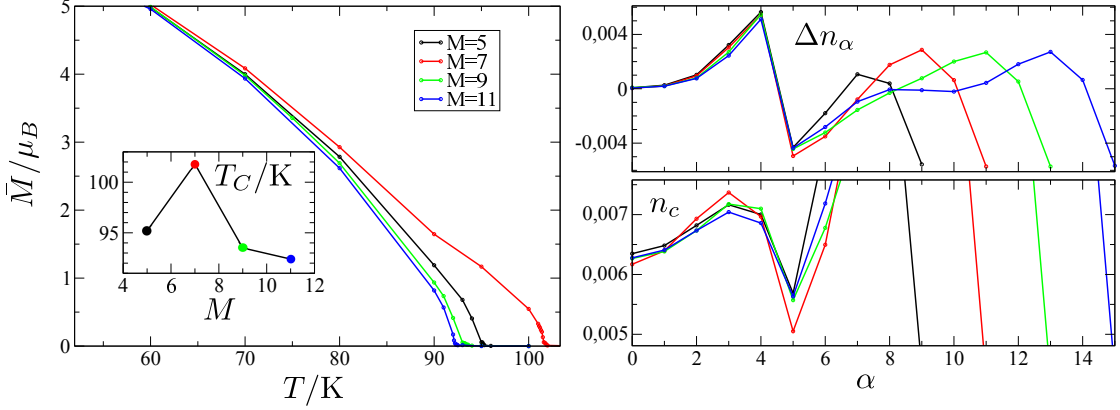


Figure 8.9.: Influence of the metal film thickness M on the ferromagnetic phase transition in a metal-Eu_{1-x}Gd_xO-metal heterostructure with $N = 9$, $n_i = 0.01$, $n_m = 0.01$ and $\Delta W = 1\text{eV}$ as seen in the average magnetization \bar{M} against the temperature (left), as well as the charge carrier density Δn_α and the conduction band occupation n_c^α against the layer index (right), respectively. The inset in the left figure depicts the Curie temperature versus M .

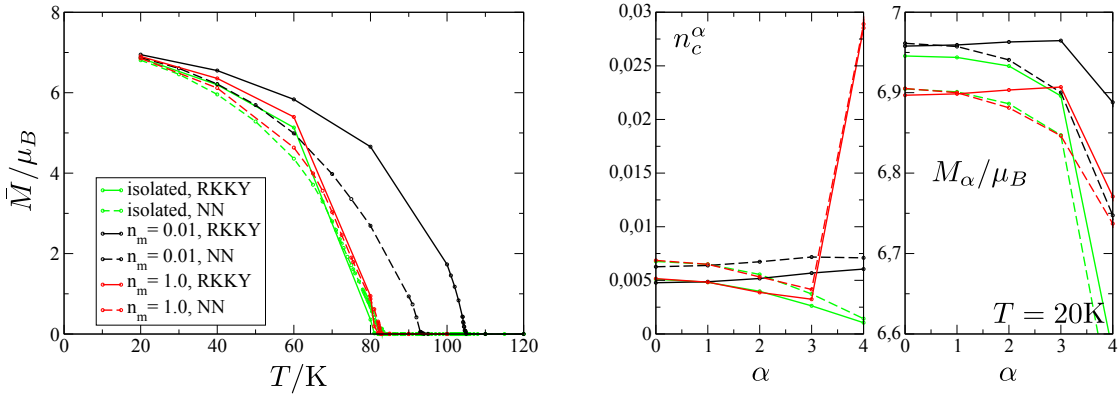


Figure 8.10.: Difference of the nearest neighbor (dashed lines) and long range RKKY coupling case (solid lines), as seen in the average magnetization \bar{M} against the temperature (left) as well as in the conduction band occupation n_c^α (center) and the magnetization M_α (right) against the layer index for a metal-Eu_{1-x}Gd_xO-metal heterostructure with $N = 9$, $M = 9$, $n_i = 0.01$ and $\Delta W = 1\text{eV}$.

the magnetization exhibits an enhancement for most of the perpendicular positions. This is in agreement with the results for the bulk and isolated systems with long range RKKY coupling. Including the latter, we observed a stronger magnitude of the magnetization at low temperatures. Due to the strong localization of the electron accumulation at $\alpha = 4$, there is no significant T_C enhancement with respect to the isolated system for $n_m = 1.0$. This statement holds for the nearest neighbor case as well as for the long range RKKY case. In contrast, there is a substantial T_C enhancement for $n_m = 0.01$, where we have $T_C = 93.5\text{K}$ for the nearest neighbor case and $T_C = 104.9\text{K}$ for the RKKY case. It is remarkable that the T_C enhancement in the RKKY case is twice as large as in the nearest neighbor case. From this, we can deduce that the multilayer theory with nearest neighbor coupling underestimates the conduction band induced T_C enhancement, at least in the case where the conduction band occupation is increased in multiple neighboring layers.

8.3. Conclusion

We performed a systematic analysis on the simultaneous ferromagnetic semiconductor-metal transition in metal-Eu_{1-x}Gd_xO-metal heterostructures. In the course of this, we investigated the influence of the metal band filling and thickness, the doping concentration and thickness in the Eu_{1-x}Gd_xO film and the work function difference. With respect to the increase of the simultaneous phase transition temperature, we found two counteracting mechanisms. On the one hand, the Curie temperature can be substantially increased up to 20% if the work function difference is positive and the metal band filling is small. On the other hand, the large penetration depth of the charge carrier accumulation, which is responsible for the T_C enhancement, suppresses the semiconductor-metal transition since the fragile position of the gap is disturbed. Investigating the same heterostructures with inclusion of long range RKKY coupling, we found that the nearest neighbor approximation underestimates the effect of electron accumulation induced T_C enhancement under certain circumstances.

9. Ferromagnet-Eu_{1-x}Gd_xO-ferromagnet heterostructures

In the previous section, we saw that the coupling to a metal film can increase the Curie temperature up to around 20%. However, this approach of T_C enhancement is inextricably linked to a suppression of the semiconductor metal transition. In the present chapter, we investigate the approach of increasing the Curie temperature in an Eu_{1-x}Gd_xO film by the coupling to a ferromagnet. In contrast to prototype ferromagnets like iron, where the magnetization is provided by itinerant electrons, we investigate ferromagnets which are characterized by spatially localized magnetic moments and the indirect exchange interaction between these moments. An example for such a ferromagnet is Gadolinium. It crystallizes in a hexagonal closed packing with lattice parameters $a = 3.636 \text{ \AA}$ and $c = 5.783 \text{ \AA}$, and has an electronic configuration of $4f^7 5d^1 6s^2$. The $4f$ electrons build a lattice of localized spin $7/2$ moments interacting via the conduction band, which consists of the $5d$ and $6s$ states [66–68]. Due to the substantial occupation of the conduction band, Gadolinium has a Curie temperature around room temperature, $T_C = 293\text{K}$ [67].

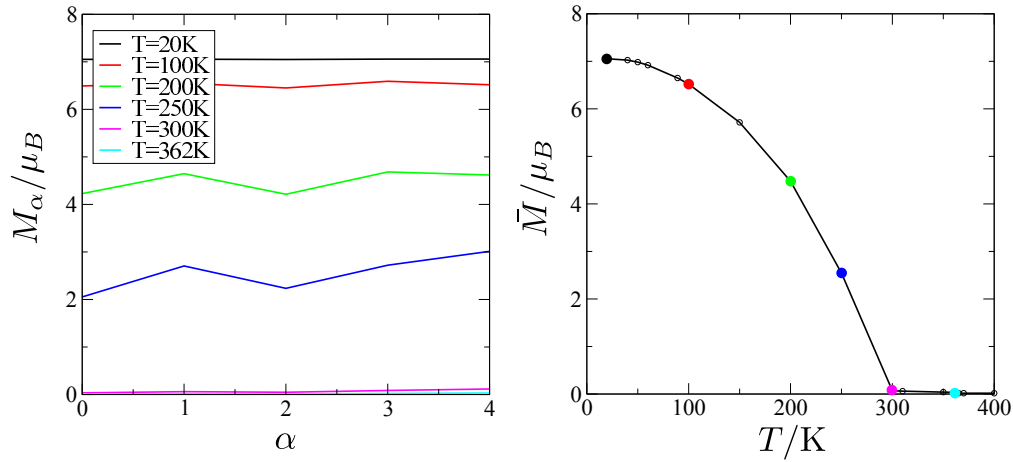


Figure 9.1.: Ferromagnetic phase transition in a ferromagnetic film of $M = 9$ layers and a conduction band occupation of $n_m = 0.1$ as seen in the magnetization against the layer index M_α for various temperatures (left) and the average magnetization \bar{M} against the temperature (right).

In order to assess the qualitative influence of such a ferromagnet onto the phase transition in Eu_{1-x}Gd_xO, we consider a heterostructure which consists of an Eu_{1-x}Gd_xO film with a ferromagnetic film on top and below. For the ferromagnet, we use the theory

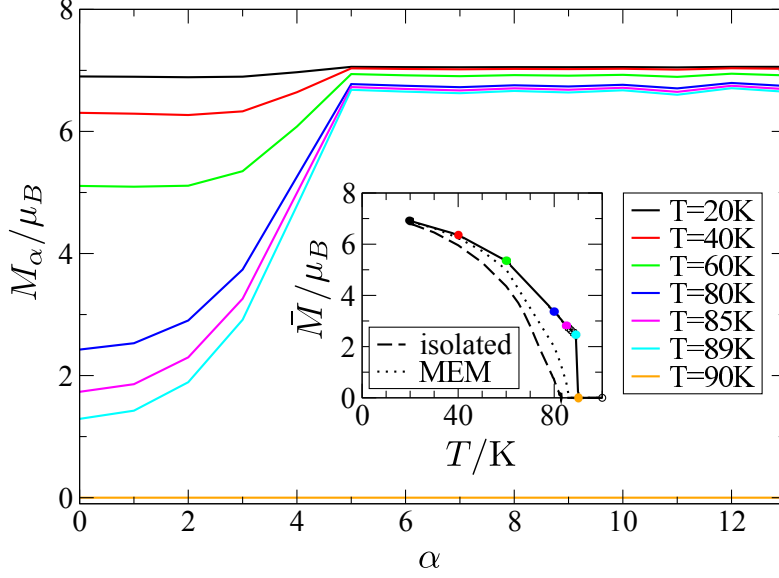


Figure 9.2.: Magnetization against the layer index for various temperatures in a ferromagnet-Eu_{1-x}Gd_xO-ferromagnet heterostructure with $N = 9$, $M = 9$, $n_i = 0.01$, $n_m = 0.1$ and $\Delta W = 1\text{eV}$. The inset shows the average magnetization versus the temperatures. For comparison, we depict the corresponding curve for the isolated Eu_{1-x}Gd_xO film and the metal-Eu_{1-x}Gd_xO-metal heterostructure (MEM).

for electron doped EuO, where we omit the impurity contribution given by (4.3) and (4.12), respectively. Similar to the metal case, the parameter n_{cc} determines the conduction band filling. For simplicity, we choose all other parameters to be the same as in the Eu_{1-x}Gd_xO film. This includes the arrangement of the localized moments on an FCC lattice. We do not expect the model to accurately describe the physics of Gadolinium. However, it should provide us with a qualitative description of the influence onto the phase transition in electron doped Europium monoxide. Analogously to the previous chapter, the heterostructure parameters are the Eu_{1-x}Gd_xO film thickness N , the doping concentration n_i , the thickness of the ferromagnet M , the conduction band occupation in the ferromagnet n_m , and the work function difference $\Delta W = W_{\text{EuO}} - W_{\text{FM}}$. In order to estimate the influence of a ferromagnet with a much greater transition temperature, we choose $n_m = 0.1$ which yields a Curie temperature of around $T_C \approx 300\text{K}$ in an isolated ferromagnetic film of $M = 9$ layers (see figure 9.1). Note that the magnetization falls below $0.02\mu_B$ already at around $T = 300\text{K}$ but crosses the $0.005\mu_B$ threshold not until $T = 362\text{K}$. For the Eu_{1-x}Gd_xO film, we choose a doping concentration of $n_i = 0.01$ and a film thickness of $N = 9$. The results for the corresponding heterostructure with a work function difference of $\Delta W = 0.125D_0 = 1\text{eV}$ are depicted in figure 9.2. Since the charge carrier distribution does not differ significantly from the one of the corresponding metal-Eu_{1-x}Gd_xO-metal heterostructure (see figure 8.1), we refrain from showing it. One might naively expect the Curie temperature of the Eu_{1-x}Gd_xO film to be substantially

increased due to the presence of the high T_C ferromagnet. However, in fact, it is the other way around. Due to the coupling to the reduced magnetic moments in the $\text{Eu}_{1-x}\text{Gd}_x\text{O}$ film, the magnetization in the ferromagnet is pulled down so that the magnetization of the whole heterostructure vanishes at $T_C = 89\text{K} + 1\text{K}$. This is only a slight increase with respect to the corresponding metal- $\text{Eu}_{1-x}\text{Gd}_x\text{O}$ -metal heterostructure, where the Curie temperature is $T_C = 86.2\text{K} + 0.1\text{K}$. Despite the fact that we have not investigated a variety of heterostructure parameters, we can already conclude from this example that the coupling to the magnetic moments of a high T_C ferromagnet of this kind does not significantly increase the transition temperature in $\text{Eu}_{1-x}\text{Gd}_x\text{O}$.

10. Prediction of STS spectra

The content of this chapter is the prediction of scanning tunneling spectroscopy (STS) spectra in systems of electron doped Europium monoxide. In an STS experiment, the electrons tunnel from the tip into the probe material or vice versa. Assuming a constant density of states in the tip, the measured spectra are proportional to the density of states of the probe $\rho(\omega)$. In the case of Europium monoxide with a dilute concentration of impurities, the density of states is given by the spin integrated full conduction band spectral density:

$$\rho(\omega) = \sum_{\sigma} A_{c\sigma}(\omega).$$

However, in the vicinity of an impurity one expects corrections to the spectra which should increase with decreasing distance to the impurity. According to Újsághy et. al. [69], the correction to the local density of states at distance R to the impurity is given by

$$\delta\rho(R, \omega) = \sum_{\sigma} \frac{1}{\pi} \text{Im} \{ G_{c\sigma}(R, \omega - i0^+) V^2 G_{d\sigma}(\omega - i0^+) G_{c\sigma}(R, \omega - i0^+) \}.$$

Here, $G_{d\sigma}(\omega)$ is the local impurity Green's function and $G_{c\sigma}(R, \omega) = G_{c\sigma}(|\mathbf{R}|, \omega)$ is the non-local conduction electron Green's function (cf. section 5.1). It was assumed that the spatial dependence of the conduction electron Green's function is isotropic, which is conform with our theory. With this, the total density of states at distance R to the impurity is given by $\rho(R, \omega) = \rho(\omega) + \delta\rho(R, \omega)$.

In the multilayer case, we consider the density of states in layer α , $\rho_{\alpha}(R, \omega) = \sum_{\sigma} A_{c\sigma}^{\alpha}(\omega) + \delta\rho_{\alpha}(R, \omega)$. Here, R is the distance between two points in layer α . We obtain for the correction to the density of states:

$$\delta\rho_{\alpha}(R, \omega) = \sum_{\sigma} \frac{1}{\pi} \text{Im} \{ G_{c\sigma}^{\alpha}(R, \omega - i0^+) V^2 G_{d\sigma}^{\alpha}(\omega - i0^+) G_{c\sigma}^{\alpha}(R, \omega - i0^+) \}.$$

At first, we compare the predicted spectra for the two types of impurities, Gadolinium and Oxygen, by examination of $\delta\rho$ for increasing distances to the impurity in the low temperature phase. Figures 10.1 and 10.2 show the corresponding results. In both cases, there are two peaks stemming from the spin split majority and minority resonances in the impurity spectral density. Moreover, there is a Fano dip which becomes visible for distances beyond one lattice constant from the impurity. However, due to the magnetic nature of the Gadolinium impurities, the peaks in $\delta\rho$ are sharper than in the Oxygen case. This may be used to distinguish between a Gadolinium impurity and an Oxygen vacancy in experiment.

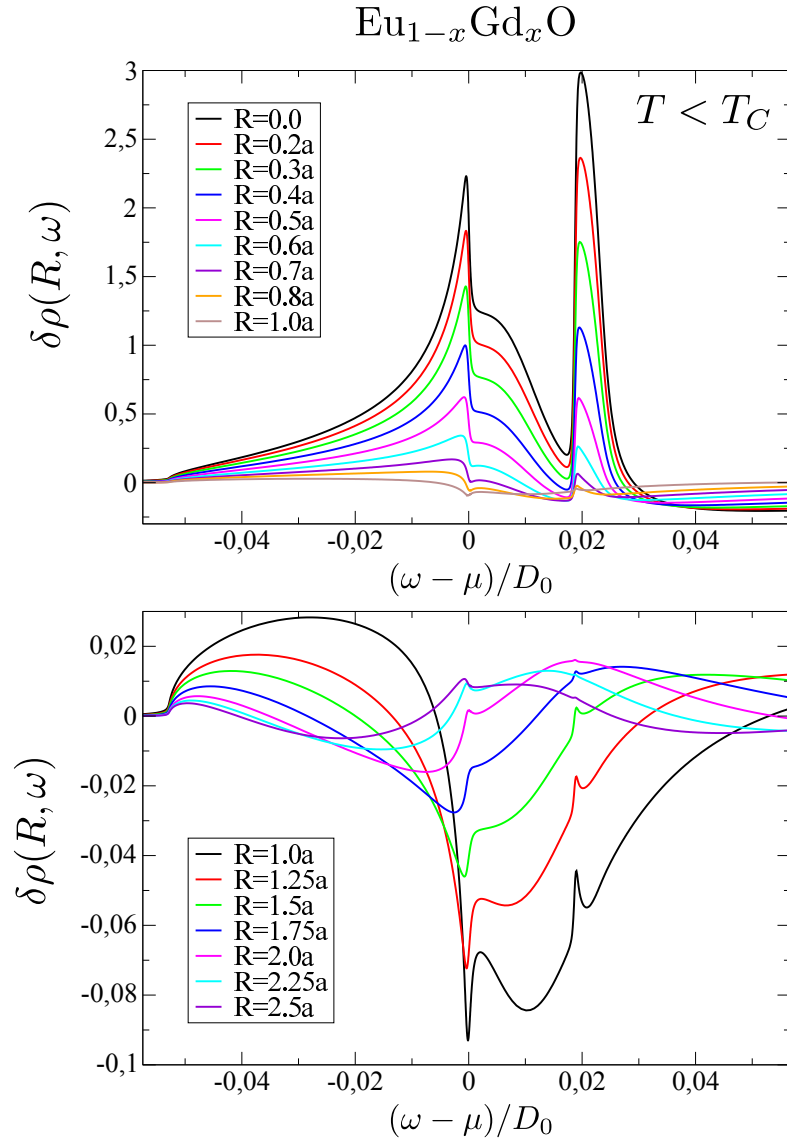


Figure 10.1.: Corrections to the conduction band density of states $\delta\rho(R, \omega)$, for various distances R to the impurity position in the low temperature phase ($T = 20\text{K}$) of bulk $\text{Eu}_{1-x}\text{Gd}_x\text{O}$ with $x = n_i = 0.01$.

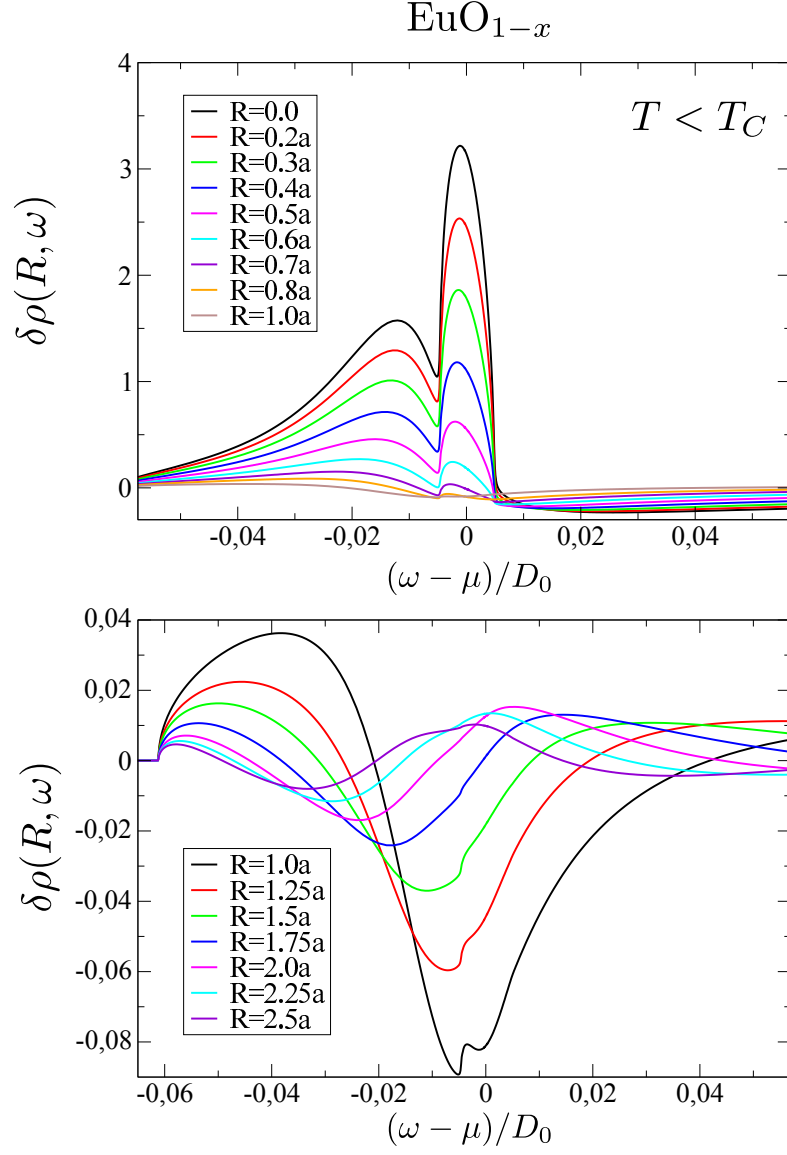


Figure 10.2.: Corrections to the conduction band density of states $\delta\rho(R, \omega)$, for various distances to the impurity position in the low temperature phase ($T = 20\text{K}$) of bulk EuO_{1-x} with $x = n_i = 0.01$, $U = 0.002D_0$ and $E_d = -0.01D_0$.

10. Prediction of STS spectra

As the temperature is increased towards T_C , the spin degeneracy is lifted and the two peaks merge into a single one. In figure 10.3 we depict $\delta\rho$ at $R = 0$ for various temperatures across the phase transition. In the Oxygen case, the spin degenerate peak is roughly twice as large in comparison to the Gadolinium case since the number of excess electrons is doubled. The spatial dependence of $\delta\rho$ in the high temperature phase is similar to the one in the low temperature phase, i.e. the strength of the spin degenerate peak decreases with the distance R and a Fano dip emerges at greater distances.

In order to demonstrate the influence of finite size effects on the STS spectra, we show $\delta\rho$ at $R = 0$ in the low temperature phase for different layers in a film of isolated $\text{Eu}_{1-x}\text{Gd}_x\text{O}$ (see figure 10.4). Although only the outer layer can be probed in experiment, this helps us to assess the effect of variations in the charge carrier density and the magnetic moment as they occur near the surface of a probe. The reduction of the magnetization towards the surface can be seen in the decrease of the distance between the two peaks in $\delta\rho$ with increasing layer index α . Moreover, we observe an increase in the population of the impurity towards the outer layers which is associated with the conduction band depletion at the surface (cf. figure 7.2). Despite the surface induced changes in $\delta\rho$, the characteristic appearance of the two sharp peaks is preserved. Therefore, we expect that even in very thin films one should be able to observe the spin split peak structure. Moreover, in principle our results provide a means to distinguish a Gadolinium impurity from an Oxygen vacancy. However, as the splitting is around $0.02D_0 = 0.16\text{eV}$ and the peak width is roughly $0.01D_0 = 0.08\text{eV}$, this may prove challenging with respect to the experimentally accessible resolution.

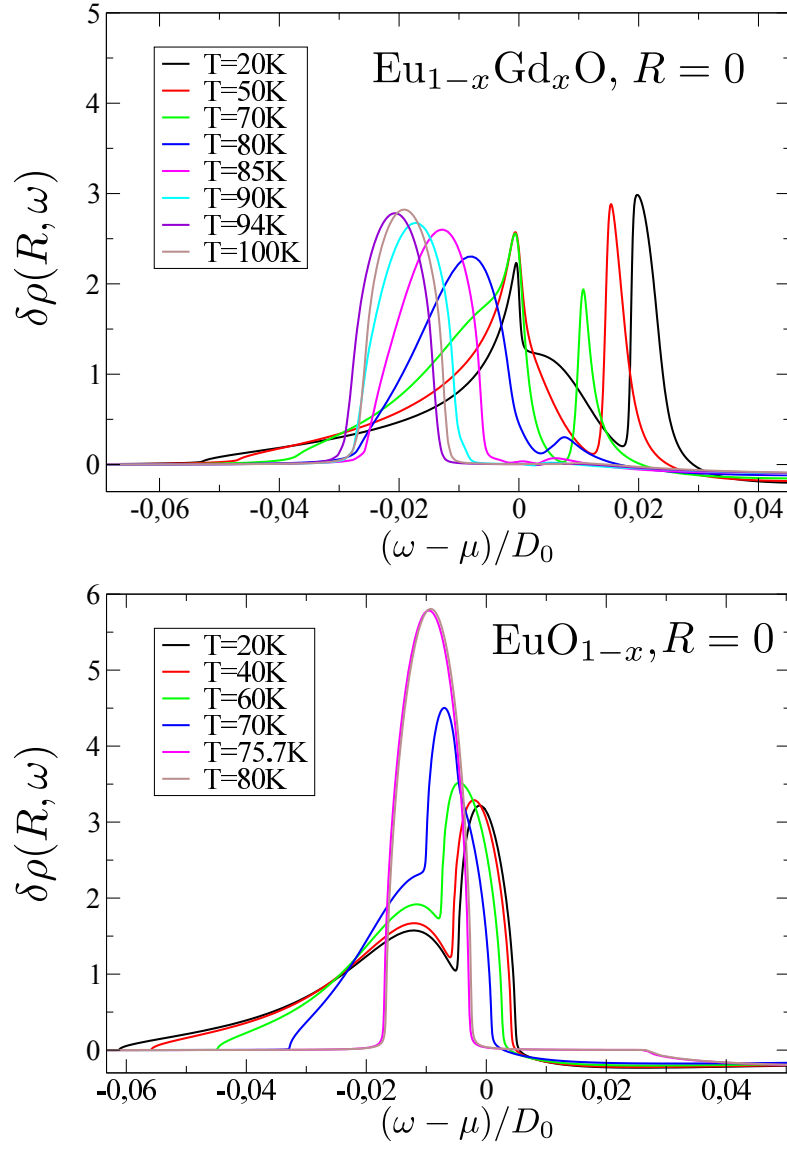


Figure 10.3.: Corrections to the conduction band density of states $\delta\rho(R = 0, \omega)$ at the position of an impurity for various temperatures across the phase transition in bulk $\text{Eu}_{1-x}\text{Gd}_x\text{O}$ (top) and bulk EuO_{1-x} with $U = 0.002D_0$ and $E_d = -0.01D_0$ (bottom). The doping concentration is $x = n_i = 0.01$ in both cases.

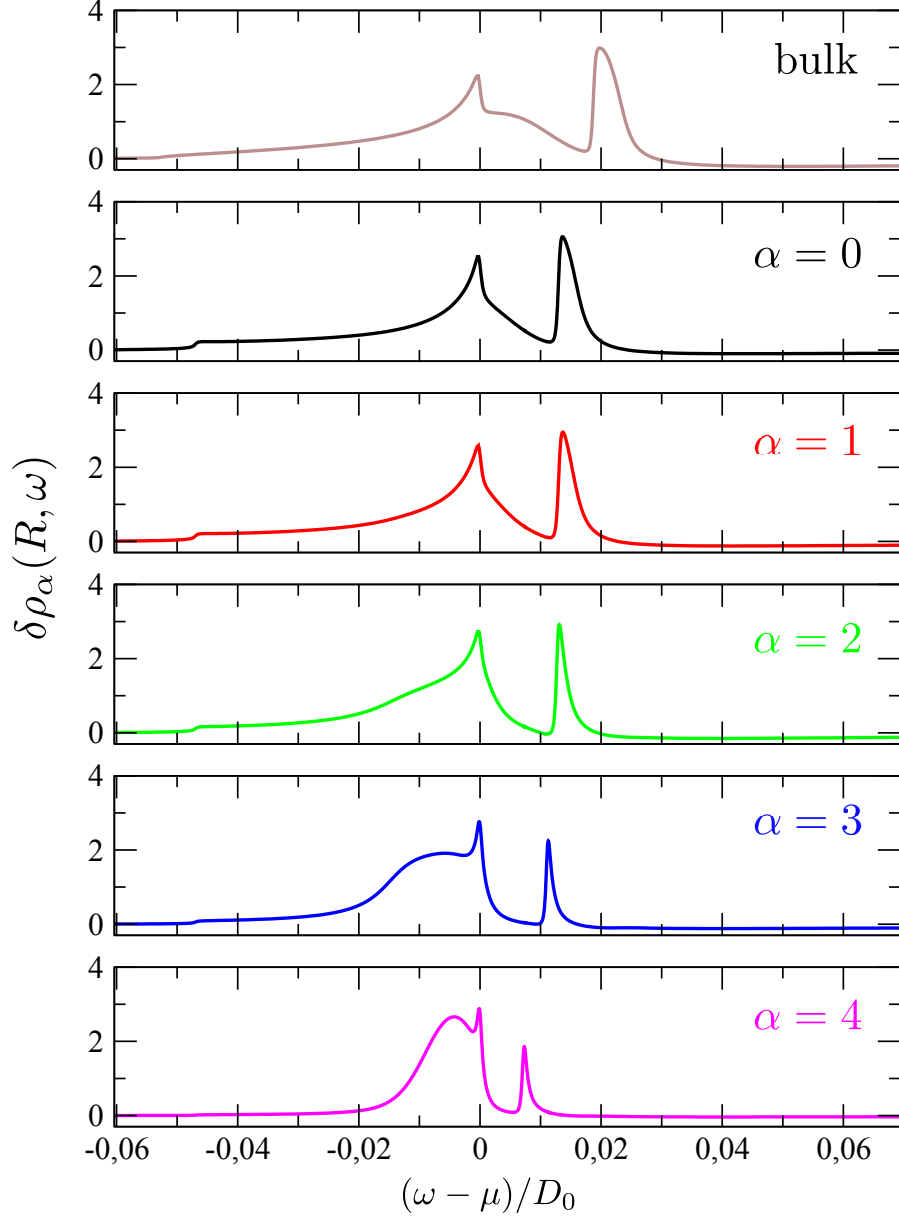


Figure 10.4.: Corrections to the conduction band density of states $\delta\rho_\alpha$ for various layer indices α in the low temperature phase ($T = 20\text{K}$) of a mirror symmetric film of $\text{Eu}_{1-x}\text{Gd}_x\text{O}$. The film thickness is $N = 9$ and the doping concentration is $x = n_i = 0.01$. For comparison, we also show the results for the corresponding bulk system.

11. Conclusion

In this work, we developed a theory for the simultaneous ferromagnetic semiconductor-metal transition in heterostructures and bulk systems of electron doped Europium monoxide. The theory is based on work of Arnold and Kroha [18] for bulk $\text{Eu}_{1-x}\text{Gd}_x\text{O}$, which in the present work was extended in order to describe systems with spatial inhomogeneities in one direction. In addition, we adapted the impurity part of the theory for the description of Oxygen deficient Europium monoxide. In order to obtain a more realistic theory for the magnetic interaction in spatially inhomogeneous systems, the non-local character of RKKY interactions between localized magnetic moments was integrated. By omitting certain parts of the model Hamiltonians ((4.1) and (4.6)), we were able to simulate metallic and ferromagnetic materials. This proved useful for comparisons to electron doped EuO systems, as well as for the modeling of different types of substrate films in heterostructures. In order to apply the correct work function difference for the latter, it was necessary to solve the theory for the isolated subsystems of a heterostructure. We implemented a highly stable and flexible computer program for the numerical solution of the theory, which comprises all different cases in a single program [63]. This includes the calculation of bulk and multilayer systems, Gadolinium impurities and Oxygen vacancies, long range RKKY and nearest neighbor magnetic interaction as well as non-interacting systems like metals and ferromagnets. Moreover, we provided a simple interface for initiating the numerical calculations and managing their results [65].

During our investigation of bulk $\text{Eu}_{1-x}\text{Gd}_x\text{O}$ systems, we could demonstrate that the theory qualitatively predicts the simultaneous phase transition as well as the increase of the transition temperature with the doping concentration. Moreover, we found that the saturation effect in the doping induced T_C enhancement is a result of the increasing localization of electrons in the impurity states, which is in agreement with experiments of Mairoser et. al. [15]. In both $\text{Eu}_{1-x}\text{Gd}_x\text{O}$ and EuO_{1-x} systems, the Curie temperature is reduced as the bare impurity level is lowered due to the enhanced occupation of the impurity level in this case. This mechanism represents a possible explanation for the absence of doping assisted T_C enhancement in Oxygen deficient Europium monoxide. It might also be explained by the absence of magnetic impurities, as we were able to demonstrate by varying the on-site Coulomb repulsion U and comparing to the results for the Gadolinium case. By investigating EuO_{1-x} systems with weak on-site Coulomb repulsion U as well as $\text{Eu}_{1-x}\text{Gd}_x\text{O}$ systems with $U \rightarrow \infty$, we covered the crossover from a doubly occupied to a singly occupied impurity state. In the latter case, low lying spin fluctuations lead to a transfer of spectral weight towards the Fermi energy due to the onset of a Kondo resonance. As a result, the semiconducting gap is closed at elevated temperatures which leads to an increase of the Curie temperature. This picture is supported by our findings that the Curie temperature increases with the on-

11. Conclusion

site Coulomb repulsion U in Oxygen deficient EuO. As U is increased, the impurity becomes more likely to be single occupied and therefore magnetic. The strong impact of low lying spin fluctuations onto the T_C enhancement was exposed by comparing the Curie temperature in $\text{Eu}_{1-x}\text{Gd}_x\text{O}$ to the one of EuO_{1-x} with the same doping concentration. Despite the fact that the conduction band occupation in the former is reduced by a factor of two in comparison to the latter, its Curie temperature is substantially increased.

Besides bulk systems, we investigated thin films of $\text{Eu}_{1-x}\text{Gd}_x\text{O}$ and the implications of finite size effects onto the phase transition. As a general attribute of the conduction band in a finite size film, we observed an electron depletion at the interface to the vacuum. This leads to Friedel oscillations in the conduction band occupation, which are damped towards the inside of the film. Due to the strong dependence of the magnetic subsystem on the number of available itinerant electrons, these oscillations have a substantial impact on the Curie temperature. In particular, the electron depletion at the vacuum interface decreases the Curie temperature beyond the effect of missing coupling partners. As expected, this effect is even more pronounced in the case of long range RKKY interactions. On the other hand, the interface induced distortion of the conduction band occupation does not substantially change the gap position in the inside of the film. As a result, we observe a semiconductor-metal transition concomitantly with the ferromagnetic transition as well as a doping induced T_C enhancement similar to the bulk case.

In order to examine the influence of a metal interface, we performed a thorough analysis of metal- $\text{Eu}_{1-x}\text{Gd}_x\text{O}$ -metal heterostructures. As expected, the presence of a metal leads to the accumulation or depletion of conduction band electrons in the $\text{Eu}_{1-x}\text{Gd}_x\text{O}$ film, depending on the work functions in both materials. We demonstrated that there can be a significant T_C enhancement due to the increased amount of itinerant electrons in the system. In the case of the more precise inclusion of long range RKKY interaction we observed an increase of the Curie temperature up to around 20%. However, we found that the interface induced T_C enhancement is inevitably associated with a suppression of the semiconductor-metal transition. By examining a ferromagnet- $\text{Eu}_{1-x}\text{Gd}_x\text{O}$ -ferromagnet heterostructure, we found that the coupling to a high T_C ferromagnet can not considerably increase the Curie temperature in $\text{Eu}_{1-x}\text{Gd}_x\text{O}$.

Finally, we used the results of the self-consistent theory to predict the STS spectra in the vicinity of an impurity at the surface of an electron doped Europium monoxide sample. Here, we were able to identify the signatures of magnetic impurities by comparing the results for $\text{Eu}_{1-x}\text{Gd}_x\text{O}$ and EuO_{1-x} .

A. Conductivity calculation

A.1. Current operator for the bulk model

During the calculation of the current operator for the bulk model (cf. (5.139)), we use the commutator of the electron density and the bulk Hamiltonian (4.1),

$$[\rho(\mathbf{q}, t), H] = \sum_{\mathbf{k}, \sigma} (\varepsilon_{\mathbf{k}} - \varepsilon_{\mathbf{k}-\mathbf{q}}) c_{\mathbf{k}-\mathbf{q}\sigma}^\dagger(t) c_{\mathbf{k}\sigma}(t).$$

We prove this relation here, employing the following commutator relations for fermionic operators:

$$[c_i^\dagger c_j, c_k^\dagger c_l] = c_i^\dagger c_l \delta_{jk} - c_k^\dagger c_j \delta_{il} \quad (\text{A.1})$$

$$[c_i^\dagger c_i, c_j^\dagger c_j] = 0 \quad (\text{A.2})$$

$$[c_i^\dagger c_i, c_j] = -\delta_{ij} c_i \quad (\text{A.3})$$

$$[c_i^\dagger c_i, c_j^\dagger] = \delta_{ij} c_i^\dagger. \quad (\text{A.4})$$

We begin by considering the electron density operator in real space $\rho(\mathbf{r})$. In order to establish a connection to the operator basis of discrete Wannier states, we consider the conduction electron and impurity density operators at lattice site i , $\rho_{c,i} = \sum_{\sigma} c_{i\sigma}^\dagger c_{i\sigma}$ and $\rho_{d,i} = \sum_{\sigma} d_{i\sigma}^\dagger d_{i\sigma}$, respectively. The relation to the continuous electron density operator is given by

$$\begin{aligned} \rho(\mathbf{r}) &= \sum_i \delta(\mathbf{r} - \mathbf{R}_i) \rho_{c,i} + \sum_{\{i\}} \delta(\mathbf{r} - \mathbf{R}_i) \rho_{d,i} \\ &= \rho_c(\mathbf{r}) + \rho_d(\mathbf{r}), \end{aligned}$$

where the second sum runs over the positions of the randomly distributed impurity sites. The conduction band contribution to the electron density reads

$$\begin{aligned} \rho_c(\mathbf{r}) &= \sum_{\sigma} \sum_i \frac{1}{N} \sum_{\mathbf{p}} e^{i(\mathbf{r}-\mathbf{R}_i)} \frac{1}{\sqrt{N}} \sum_{\mathbf{k}} e^{-i\mathbf{k}\mathbf{R}_i} c_{\mathbf{k}\sigma}^\dagger \frac{1}{\sqrt{N}} \sum_{\mathbf{q}} e^{i\mathbf{q}\mathbf{R}_i} c_{\mathbf{q}\sigma} \\ &= \frac{1}{N} \sum_{\mathbf{p}} e^{i\mathbf{p}\mathbf{r}} \underbrace{\left(\sum_{\mathbf{q}\sigma} c_{\mathbf{q}-\mathbf{p}\sigma}^\dagger c_{\mathbf{q}\sigma} \right)}_{\rho_c(\mathbf{p})}, \end{aligned} \quad (\text{A.5})$$

A. Conductivity calculation

and the impurity contribution is given by

$$\rho_d(\mathbf{r}) = \frac{1}{N} \sum_{\mathbf{p}} e^{i\mathbf{p}\mathbf{r}} \underbrace{\left(\sum_{\{i\}\sigma} e^{-i\mathbf{p}\mathbf{R}_i} d_{i\sigma}^\dagger d_{i\sigma} \right)}_{\rho_d(\mathbf{p})}. \quad (\text{A.6})$$

Hence, we have an expression for the momentum dependent electron density operator $\rho(\mathbf{q}) = \rho_c(\mathbf{q}) + \rho_d(\mathbf{q})$ and we can proceed with the calculation of the commutator. The contribution from the magnetic part of the Hamiltonian after mean-field approximation (5.69) reads

$$[\rho(\mathbf{q}), H_{cf}] = \left[\sum_{i\sigma} e^{-i\mathbf{q}\mathbf{R}_i} c_{i\sigma}^\dagger c_{i\sigma} + \sum_{\{i\}\sigma} e^{-i\mathbf{q}\mathbf{R}_i} d_{i\sigma}^\dagger d_{i\sigma}, -J_{cf} \sum_{j\lambda\lambda'} \mathbf{S}_j c_{j\lambda}^\dagger \tau_{\lambda\lambda'}^z c_{j\lambda'} \right] \stackrel{(\text{A.2})}{=} 0.$$

The commutators with the first and third part of the impurity part of the Hamiltonian (4.3) vanish due to (A.2) and we are left with

$$\begin{aligned} [\rho(\mathbf{q}), H_{cd}] &= V \sum_{\lambda\sigma} \sum_j \sum_{\{i\}} \left[c_{j\lambda}^\dagger c_{j\lambda}, c_{i\sigma}^\dagger d_{i\sigma} + d_{i\sigma}^\dagger c_{i\sigma} \right] e^{-i\mathbf{q}\mathbf{R}_j} \\ &\quad + V \sum_{\lambda\sigma} \sum_{\{j\}} \sum_{\{i\}} \left[d_{j\lambda}^\dagger d_{j\lambda}, c_{i\sigma}^\dagger d_{i\sigma} + d_{i\sigma}^\dagger c_{i\sigma} \right] e^{-i\mathbf{q}\mathbf{R}_j} \\ &= V \sum_{\lambda\sigma} \sum_j \sum_{\{i\}} \left\{ \underbrace{\left[c_{j\lambda}^\dagger c_{j\lambda}, c_{i\sigma}^\dagger \right]}_{\stackrel{(\text{A.4})}{=} \delta_{ij} \delta_{\sigma\lambda} c_{i\sigma}^\dagger} d_{i\sigma} + d_{i\sigma}^\dagger \underbrace{\left[c_{j\lambda}^\dagger c_{j\lambda}, c_{i\sigma} \right]}_{\stackrel{(\text{A.3})}{=} -\delta_{ij} \delta_{\sigma\lambda} c_{i\sigma}} \right\} e^{-i\mathbf{q}\mathbf{R}_j} \\ &\quad + V \sum_{\lambda\sigma} \sum_{\{j\}} \sum_{\{i\}} \left\{ c_{i\sigma}^\dagger \underbrace{\left[d_{j\lambda}^\dagger d_{j\lambda}, d_{i\sigma} \right]}_{\stackrel{(\text{A.3})}{=} -\delta_{ij} \delta_{\sigma\lambda} d_{i\sigma}} + \underbrace{\left[d_{j\lambda}^\dagger d_{j\lambda}, d_{i\sigma}^\dagger \right]}_{\stackrel{(\text{A.4})}{=} \delta_{ij} \delta_{\sigma\lambda} d_{i\sigma}^\dagger} c_{i\sigma} \right\} e^{-i\mathbf{q}\mathbf{R}_j} \\ &= 0. \end{aligned}$$

The only non-vanishing contribution stems from the conduction band part of the Hamiltonian (4.2). It is given by

$$\begin{aligned} [\rho(\mathbf{q}), H_0] &= [\rho_c(\mathbf{q}), H_0] \\ &= \sum_{\mathbf{p}\mathbf{k}} \sum_{\sigma\lambda} (\varepsilon_{\mathbf{k}} - \mu) \underbrace{\left[c_{\mathbf{p}-\mathbf{q}\sigma}^\dagger c_{\mathbf{p}\sigma}, c_{\mathbf{k}\lambda}^\dagger c_{\mathbf{k}\lambda} \right]}_{\stackrel{(\text{A.1})}{=} c_{\mathbf{p}-\mathbf{q}\sigma}^\dagger c_{\mathbf{k}\lambda} \delta_{\mathbf{p}\mathbf{k}} \delta_{\sigma\lambda} - c_{\mathbf{k}\lambda}^\dagger c_{\mathbf{p}\sigma} \delta_{\mathbf{p}-\mathbf{q},\mathbf{k}} \delta_{\sigma\lambda}} \\ &= \sum_{\mathbf{k}\sigma} (\varepsilon_{\mathbf{k}} - \varepsilon_{\mathbf{k}-\mathbf{q}}) c_{\mathbf{k}-\mathbf{q}\sigma}^\dagger c_{\mathbf{k}\sigma}. \end{aligned}$$

In the first step, we have used that $[\rho_d(\mathbf{q}), H_0] = 0$ holds due to (A.2). This closes the proof.

A.2. Current operator for the multilayer model

In the following, we will prove relation (5.160), which is used during the derivation of the current operator in the multilayer case. It reads

$$\begin{aligned} [\rho(\mathbf{q}_{\parallel}, \alpha), H] = & \frac{1}{a} \sum_{\mathbf{k}_{\parallel}\sigma} \left(\varepsilon_{\mathbf{k}_{\parallel}}^{\alpha} - \varepsilon_{\mathbf{k}_{\parallel}-\mathbf{q}_{\parallel}}^{\alpha} \right) c_{\mathbf{k}_{\parallel}-\mathbf{q}_{\parallel}\alpha\sigma}^{\dagger} c_{\mathbf{k}_{\parallel}\alpha\sigma} \\ & + \frac{1}{a} \sum_{\mathbf{k}_{\parallel}\sigma} \left(t_{\alpha} c_{\mathbf{k}_{\parallel}-\mathbf{q}_{\parallel}\alpha\sigma}^{\dagger} c_{\mathbf{k}_{\parallel}\alpha-1\sigma} + t_{\alpha+1} c_{\mathbf{k}_{\parallel}-\mathbf{q}_{\parallel}\alpha\sigma}^{\dagger} c_{\mathbf{k}_{\parallel}\alpha+1\sigma} \right. \\ & \left. - t_{\alpha} c_{\mathbf{k}_{\parallel}-\mathbf{q}_{\parallel}\alpha-1\sigma}^{\dagger} c_{\mathbf{k}_{\parallel}\alpha\sigma} - t_{\alpha+1} c_{\mathbf{k}_{\parallel}-\mathbf{q}_{\parallel}\alpha+1\sigma}^{\dagger} c_{\mathbf{k}_{\parallel}\alpha\sigma} \right), \end{aligned}$$

where the multilayer Hamiltonian is given by (4.6). We begin by considering the electron density operator at the continuous space variable $\mathbf{r} = (\mathbf{r}_{\parallel}, r_{\perp})$. The connection to the conduction band and impurity electron density at discrete space position, $\rho_{c,i\alpha} = \sum_{\sigma} c_{i\alpha\sigma}^{\dagger} c_{i\alpha\sigma}$ and $\rho_{d,i\alpha} = \sum_{\sigma} d_{i\alpha\sigma}^{\dagger} d_{i\alpha\sigma}$, is given by

$$\begin{aligned} \rho(\mathbf{r}_{\parallel}, r_{\perp}) &= \sum_{i\beta} \delta(r_{\perp} - \beta) \delta(\mathbf{r}_{\parallel} - \mathbf{R}_{\parallel i}) \rho_{c,i\beta} + \sum_{\{i\beta\}} \delta(r_{\perp} - \beta) \delta(\mathbf{r}_{\parallel} - \mathbf{R}_{\parallel i}) \rho_{d,i\beta} \\ &= \rho_c(\mathbf{r}) + \rho_d(\mathbf{r}), \end{aligned}$$

where we sum over the randomly distributed impurity sites in the second term. Since we want to evaluate the electron density at a discrete perpendicular position α rather than at the continuous one r_{\perp} , we write

$$\begin{aligned} r_{\perp} &\rightarrow \alpha \\ \delta(r_{\perp} - \beta) &\rightarrow \frac{\delta_{\alpha\beta}}{a}. \end{aligned}$$

With this, we obtain

$$\rho_c(\mathbf{r}_{\parallel}, \alpha) = \frac{1}{N_{\parallel}} \sum_{\mathbf{p}_{\parallel}} e^{i\mathbf{p}_{\parallel}\mathbf{r}_{\parallel}} \underbrace{\left(\frac{1}{a} \sum_{\mathbf{q}_{\parallel}\sigma} c_{\mathbf{q}_{\parallel}-\mathbf{p}_{\parallel}\alpha\sigma}^{\dagger} c_{\mathbf{q}_{\parallel}\sigma} \right)}_{\rho_c(\mathbf{p}_{\parallel}, \alpha)} \quad (\text{A.7})$$

for the conduction band electron density similar to (A.5), and

$$\rho_d(\mathbf{r}_{\parallel}, \alpha) = \frac{1}{N_{\parallel}} \sum_{\mathbf{p}_{\parallel}} e^{i\mathbf{p}_{\parallel}\mathbf{r}_{\parallel}} \underbrace{\left(\frac{1}{a} \sum_{\{i\beta\}\sigma} \delta_{\alpha\beta} e^{-i\mathbf{p}_{\parallel}\mathbf{R}_{\parallel i}} d_{i\beta\sigma}^{\dagger} d_{i\beta\sigma} \right)}_{\rho_d(\mathbf{p}_{\parallel}, \alpha)}$$

for the impurity electron density (cf. (A.6)). On the other hand, from (A.7) we can derive

$$\rho_c(\mathbf{p}_{\parallel}, \alpha) = \frac{1}{a} \sum_{i\sigma} e^{-i\mathbf{p}_{\parallel}\mathbf{R}_{\parallel i}} c_{i\alpha}^{\dagger} c_{i\alpha}.$$

A. Conductivity calculation

Now, we can calculate the commutator beginning with the mean-field Heisenberg lattice contribution (5.78):

$$\begin{aligned}
[\rho(\mathbf{q}_{\parallel}, \alpha), H_{cf}] &= \left[\sum_{i\sigma} e^{-i\mathbf{q}_{\parallel} \mathbf{R}_{\parallel i}} c_{i\alpha\sigma}^{\dagger} c_{i\alpha\sigma}, -J_{cf} \sum_{\beta} \langle S_{\beta} \rangle \sum_{j\lambda\lambda'} c_{j\beta\lambda}^{\dagger} \tau_{\lambda\lambda'}^z c_{j\beta\lambda'} \right] \\
&+ \left[\sum_{\{i\beta\}\sigma} \delta_{\alpha\beta} e^{-i\mathbf{q}_{\parallel} \mathbf{R}_{\parallel i}} d_{i\alpha\sigma}^{\dagger} d_{i\alpha\sigma}, -J_{cf} \sum_{\beta} \langle S_{\beta} \rangle \sum_{j\lambda\lambda'} c_{j\beta\lambda}^{\dagger} \tau_{\lambda\lambda'}^z c_{j\beta\lambda'} \right] \\
&\stackrel{(A.2)}{=} 0.
\end{aligned}$$

In a similar fashion, it can be shown that the commutator with the electrostatic part of the Hamiltonian (4.11) vanishes,

$$[\rho(\mathbf{q}_{\parallel}, \alpha), H_{\phi}] = 0.$$

Analogously to the bulk case, the commutators of $\rho(\mathbf{q}_{\parallel}, \alpha)$ with the first and third part of the impurity Hamiltonian (4.12) vanish due to (A.2) and we are left with

$$\begin{aligned}
[\rho(\mathbf{q}_{\parallel}, \alpha), H_{cd}] &= \frac{V}{a} \sum_{\lambda\sigma} \sum_j \sum_{\{i\beta\}} \left[c_{j\alpha\lambda}^{\dagger} c_{j\alpha\lambda}, c_{i\beta\sigma}^{\dagger} d_{i\beta\sigma} + d_{i\beta\sigma}^{\dagger} c_{i\beta\sigma} \right] e^{-i\mathbf{q}_{\parallel} \mathbf{R}_{\parallel j}} \\
&+ \frac{V}{a} \sum_{\lambda\sigma} \sum_{\{j\gamma\}} \sum_{\{i\beta\}} \left[d_{j\gamma\lambda}^{\dagger} d_{j\gamma\lambda}, c_{i\beta\sigma}^{\dagger} d_{i\beta\sigma} + d_{i\beta\sigma}^{\dagger} c_{i\beta\sigma} \right] \delta_{\gamma\alpha} e^{-i\mathbf{q}_{\parallel} \mathbf{R}_{\parallel j}} \\
&= \frac{V}{a} \sum_{\lambda\sigma} \sum_j \sum_{\{i\beta\}} \left\{ \underbrace{\left[c_{j\alpha\lambda}^{\dagger} c_{j\alpha\lambda}, c_{i\beta\sigma}^{\dagger} \right]}_{\stackrel{(A.4)}{=} \delta_{ij} \delta_{\alpha\beta} \delta_{\sigma\lambda} c_{i\beta\sigma}^{\dagger}} d_{i\beta\sigma} + d_{i\beta\sigma}^{\dagger} \underbrace{\left[c_{j\alpha\lambda}^{\dagger} c_{j\alpha\lambda}, c_{i\beta\sigma} \right]}_{\stackrel{(A.3)}{=} -\delta_{ij} \delta_{\alpha\beta} \delta_{\sigma\lambda} c_{i\beta\sigma}} \right\} e^{-i\mathbf{q}_{\parallel} \mathbf{R}_{\parallel j}} \\
&+ \frac{V}{a} \sum_{\lambda\sigma} \sum_{\{j\gamma\}} \sum_{\{i\beta\}} \left\{ c_{i\beta\sigma}^{\dagger} \underbrace{\left[d_{j\gamma\lambda}^{\dagger} d_{j\gamma\lambda}, d_{i\beta\sigma} \right]}_{\stackrel{(A.3)}{=} -\delta_{ij} \delta_{\beta\gamma} \delta_{\sigma\lambda} d_{i\beta\sigma}} + \underbrace{\left[d_{j\gamma\lambda}^{\dagger} d_{j\gamma\lambda}, d_{i\beta\sigma}^{\dagger} \right]}_{\stackrel{(A.4)}{=} \delta_{ij} \delta_{\beta\gamma} \delta_{\sigma\lambda} d_{i\beta\sigma}^{\dagger}} c_{i\beta\sigma} \right\} \delta_{\alpha\gamma} e^{-i\mathbf{q}_{\parallel} \mathbf{R}_{\parallel j}} \\
&= 0.
\end{aligned}$$

Finally, we consider the only non vanishing contributions, which stem from the parallel and perpendicular part of the conduction band Hamiltonian (4.8) and (4.9). The contribution from the former reads

$$\begin{aligned}
[\rho(\mathbf{q}_{\parallel}, \alpha), H_{\parallel}] &= [\rho_c(\mathbf{q}_{\parallel}, \alpha), H_{\parallel}] \\
&= \frac{1}{a} \sum_{\mathbf{p}_{\parallel} \mathbf{k}_{\parallel}} \sum_{\beta} (\varepsilon_{\mathbf{k}_{\parallel}}^{\beta} - \mu) \underbrace{\left[c_{\mathbf{p}_{\parallel} - \mathbf{q}_{\parallel} \alpha \sigma}^{\dagger} c_{\mathbf{p}_{\parallel} \alpha \sigma}, c_{\mathbf{k}_{\parallel} \beta \lambda}^{\dagger} c_{\mathbf{k}_{\parallel} \beta \lambda} \right]}_{\stackrel{(A.1)}{=} c_{\mathbf{p}_{\parallel} - \mathbf{q}_{\parallel} \alpha \sigma}^{\dagger} c_{\mathbf{k}_{\parallel} \beta \lambda} c_{\mathbf{p}_{\parallel} \mathbf{k}_{\parallel}} \delta_{\mathbf{p}_{\parallel} \mathbf{k}_{\parallel}} \delta_{\alpha\beta} \delta_{\sigma\lambda} - c_{\mathbf{k}_{\parallel} \beta \lambda}^{\dagger} c_{\mathbf{p}_{\parallel} \alpha \sigma} \delta_{\mathbf{p}_{\parallel} - \mathbf{q}_{\parallel}, \mathbf{k}_{\parallel}} \delta_{\alpha\beta} \delta_{\sigma\lambda}} \\
&= \frac{1}{a} \sum_{\mathbf{k}_{\parallel} \sigma} (\varepsilon_{\mathbf{k}_{\parallel}}^{\alpha} - \varepsilon_{\mathbf{k}_{\parallel} - \mathbf{q}_{\parallel}}^{\alpha}) c_{\mathbf{k}_{\parallel} - \mathbf{q}_{\parallel} \alpha \sigma}^{\dagger} c_{\mathbf{k}_{\parallel} \alpha \sigma}.
\end{aligned}$$

A.3. Diagrammatic evaluation of the current-current correlation function

Before being able to calculate the perpendicular contribution, we need to Fourier transform to momentum space,

$$\begin{aligned} H_{\perp} &= \sum_{\alpha i \sigma} \left(t_{\alpha} c_{i\alpha\sigma}^{\dagger} c_{i\alpha-1\sigma} + t_{\alpha+1} c_{i\alpha\sigma}^{\dagger} c_{i\alpha+1\sigma} \right) \\ &= \sum_{\mathbf{k}_{\parallel} \alpha \sigma} \left(t_{\alpha} c_{\mathbf{k}_{\parallel} \alpha \sigma}^{\dagger} c_{\mathbf{k}_{\parallel} \alpha-1\sigma} + t_{\alpha+1} c_{\mathbf{k}_{\parallel} \alpha \sigma}^{\dagger} c_{\mathbf{k}_{\parallel} \alpha+1\sigma} \right). \end{aligned}$$

With this, the commutator reads

$$\begin{aligned} [\rho(\mathbf{q}_{\parallel}, \alpha), H_{\perp}] &= [\rho_c(\mathbf{q}_{\parallel}, \alpha), H_{\perp}] \\ &= \sum_{\substack{\mathbf{k}_{\parallel} \sigma \\ \mathbf{p}_{\parallel} \beta \lambda}} \left\{ \frac{t_{\beta}}{a} \underbrace{\left[c_{\mathbf{k}_{\parallel} - \mathbf{q}_{\parallel} \alpha \sigma}^{\dagger} c_{\mathbf{k}_{\parallel} \alpha \sigma}, c_{\mathbf{p}_{\parallel} \beta \lambda}^{\dagger} c_{\mathbf{p}_{\parallel} \beta - 1 \lambda} \right]}_{\substack{(A.1) \\ = c_{\mathbf{k}_{\parallel} - \mathbf{q}_{\parallel} \alpha \sigma}^{\dagger} c_{\mathbf{p}_{\parallel} \beta - 1 \lambda} \delta_{\mathbf{k}_{\parallel} \mathbf{p}_{\parallel}} \delta_{\alpha \beta} \delta_{\sigma \lambda} \\ - c_{\mathbf{p}_{\parallel} \beta \lambda}^{\dagger} c_{\mathbf{k}_{\parallel} \alpha \sigma} \delta_{\mathbf{k}_{\parallel} - \mathbf{q}_{\parallel}, \mathbf{p}_{\parallel}} \delta_{\alpha \beta - 1} \delta_{\sigma \lambda}}} \right. \\ &\quad \left. + \frac{t_{\beta+1}}{a} \underbrace{\left[c_{\mathbf{k}_{\parallel} - \mathbf{q}_{\parallel} \alpha \sigma}^{\dagger} c_{\mathbf{k}_{\parallel} \alpha \sigma}, c_{\mathbf{p}_{\parallel} \beta \lambda}^{\dagger} c_{\mathbf{p}_{\parallel} \beta + 1 \lambda} \right]}_{\substack{(A.1) \\ = c_{\mathbf{k}_{\parallel} - \mathbf{q}_{\parallel} \alpha \sigma}^{\dagger} c_{\mathbf{p}_{\parallel} \beta + 1 \lambda} \delta_{\mathbf{k}_{\parallel} \mathbf{p}_{\parallel}} \delta_{\alpha \beta} \delta_{\sigma \lambda} \\ - c_{\mathbf{p}_{\parallel} \beta \lambda}^{\dagger} c_{\mathbf{k}_{\parallel} \alpha \sigma} \delta_{\mathbf{k}_{\parallel} - \mathbf{q}_{\parallel}, \mathbf{p}_{\parallel}} \delta_{\alpha \beta + 1} \delta_{\sigma \lambda}}} \right\} \\ &= \frac{1}{a} \sum_{\mathbf{k}_{\parallel} \sigma} \left\{ t_{\alpha} c_{\mathbf{k}_{\parallel} - \mathbf{q}_{\parallel} \alpha \sigma}^{\dagger} c_{\mathbf{k}_{\parallel} \alpha - 1 \sigma} - t_{\alpha+1} c_{\mathbf{k}_{\parallel} - \mathbf{q}_{\parallel} \alpha + 1 \sigma}^{\dagger} c_{\mathbf{k}_{\parallel} \alpha \sigma} \right. \\ &\quad \left. + t_{\alpha+1} c_{\mathbf{k}_{\parallel} - \mathbf{q}_{\parallel} \alpha \sigma}^{\dagger} c_{\mathbf{k}_{\parallel} \alpha + 1 \sigma} - t_{\alpha} c_{\mathbf{k}_{\parallel} - \mathbf{q}_{\parallel} \alpha - 1 \sigma}^{\dagger} c_{\mathbf{k}_{\parallel} \alpha \sigma} \right\}. \end{aligned}$$

This proves the above relation.

A.3. Diagrammatic evaluation of the current-current correlation function

In this part, we perform the evaluation of the Matsubara sum needed for the calculation of the current-current correlation functions (5.145), (5.167) and (5.172). Denoting the

A. Conductivity calculation

upper and lower fermion lines by some placeholder quantum numbers a and b , we have

$$\begin{aligned}
\Pi_{ab}(i\omega_n) &= \text{bubble diagram with upper arc labeled } a, i\omega_m \text{ and lower arc labeled } b, i\omega_m + i\omega_n \\
&= \frac{1}{\hbar\beta} \sum_m G_a(i\omega_m) G_b(i\omega_m + i\omega_n) \\
&= - \oint_C \frac{dz}{2\pi i} G_a(z) G_b(z + i\omega_n) \\
&= - \int_{-\infty}^{\infty} \frac{d\epsilon}{2\pi i} f(\epsilon) \{ G_a(\epsilon + i0^+) - G_a(\epsilon - i0^+) \} G_b(\epsilon + i\omega_n) \\
&\quad - \int_{-\infty}^{\infty} \frac{d\epsilon}{2\pi i} \underbrace{f(\epsilon - i\omega_n)}_{f(\epsilon)} G_a(\epsilon - i\omega_n) \underbrace{\{ G_b(\epsilon + i0^+) - G_b(\epsilon - i0^+) \}}_{2i\text{Im}G_b^R(\epsilon) = -2\pi i A_b(\epsilon)} \\
&= \int_{-\infty}^{\infty} d\epsilon f(\epsilon) [A_a(\epsilon) G_b(\epsilon + i\omega_n) + G_a(\epsilon - i\omega_n) A_b(\epsilon)] \tag{A.8}
\end{aligned}$$

Here, we used that ω_n is a bosonic Matsubara frequency and we transformed the integration path in the second step according to figure A.1.

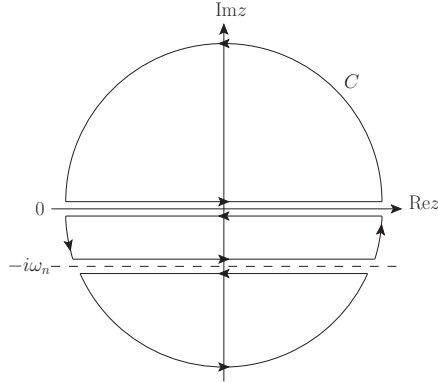


Figure A.1.: Integration contour for the evaluation of the Matsubara sum in the pair bubble diagram of the conductivity

A.3. Diagrammatic evaluation of the current-current correlation function

The imaginary part of the retarded current-current correlation function reads

$$\begin{aligned}
\text{Im}\Pi_{ab}^R(\omega) &= \text{Im}\Pi_{ab}(\omega + i0^+) \\
&= \int_{-\infty}^{\infty} d\varepsilon f(\varepsilon) \left(A_a(\varepsilon) \underbrace{\text{Im}G_b(\varepsilon + \omega + i0^+)}_{-\pi A_b(\varepsilon + \omega)} + \underbrace{\text{Im}G_a(\varepsilon - \omega - i0^+)}_{\pi A_a(\varepsilon - \omega)} A_b(\varepsilon) \right) \\
&= \pi \int d\varepsilon f(\varepsilon) A_a(\varepsilon - \omega) A_b(\varepsilon) - \pi \underbrace{\int d\varepsilon f(\varepsilon) A_a(\varepsilon) A_b(\varepsilon + \omega)}_{\int d\varepsilon f(\varepsilon - \omega) A_a(\varepsilon - \omega) A_b(\varepsilon)} \\
&= \pi \int d\varepsilon [f(\varepsilon) - f(\varepsilon - \omega)] A_a(\varepsilon - \omega) A_b(\varepsilon) .
\end{aligned} \tag{A.9}$$

B. Local scattering

We derive the contribution to the momentum dependent conduction electron self-energy (5.1) in the case of a local and position independent self-energy in real space, i.e. $\Sigma_\sigma(\mathbf{r}, z) = \Sigma_\sigma(z)$. The Dyson equation reads

$$\begin{aligned}
G_{c\sigma}(\mathbf{r}, \mathbf{r}', z) &= \overleftrightarrow{\mathbf{r} \mathbf{r}'}^{z, \sigma} \\
&= \overleftrightarrow{\mathbf{r} \mathbf{r}'}^{z, \sigma} + \overleftrightarrow{\mathbf{r} \mathbf{r}''}^{z, \sigma} \text{ (loop)} \overleftrightarrow{\mathbf{r}'' \mathbf{r}'}^{z, \sigma} \\
&= G_{c\sigma}^0(\mathbf{r}, \mathbf{r}', z) + \sum_{\mathbf{r}''} \underbrace{G_{c\sigma}^0(\mathbf{r}, \mathbf{r}'', z)}_{\frac{1}{N} \sum_{\mathbf{k}} e^{i\mathbf{k}(\mathbf{r}-\mathbf{r}'')} G_{c\sigma}^0(\mathbf{k}, z)} \underbrace{\Sigma_\sigma(z)}_{\frac{1}{N} \sum_{\mathbf{p}} e^{i\mathbf{p}(\mathbf{r}''-\mathbf{r}') G_{c\sigma}(\mathbf{p}, z)}} \underbrace{G_{c\sigma}(\mathbf{r}'', \mathbf{r}', z)}_{\frac{1}{N} \sum_{\mathbf{p}} e^{i\mathbf{p}(\mathbf{r}''-\mathbf{r}') G_{c\sigma}(\mathbf{p}, z)}} \\
&= G_{c\sigma}^0(\mathbf{r}, \mathbf{r}', z) + \frac{1}{N^2} \sum_{\mathbf{k} \mathbf{p}} \underbrace{\sum_{\mathbf{r}''} e^{i\mathbf{r}''(\mathbf{p}-\mathbf{k})} e^{i\mathbf{k}\mathbf{r}} e^{-i\mathbf{p}\mathbf{r}'}}_{N\delta_{\mathbf{k}\mathbf{p}}} G_{c\sigma}^0(\mathbf{k}, z) \Sigma_\sigma(z) G_{c\sigma}(\mathbf{p}, z) \\
&= \frac{1}{N} \sum_{\mathbf{k}} e^{i\mathbf{k}(\mathbf{r}-\mathbf{r}')} \underbrace{\left(G_{c\sigma}^0(\mathbf{k}, z) + G_{c\sigma}^0(\mathbf{k}, z) \Sigma_\sigma(z) G_{c\sigma}(\mathbf{k}, z) \right)}_{G_{c\sigma}(\mathbf{k}, z)}. \tag{B.1}
\end{aligned}$$

From this, one can conclude that the momentum dependent self-energy from (5.1) and (5.2) is given by $\Sigma_\sigma(\mathbf{k}, z) = \Sigma_\sigma(z)$.

In the multilayer case, we consider a local self-energy in real space, which depends on the perpendicular position but not on the parallel position, i.e. $\Sigma_\sigma^\alpha(\mathbf{r}_\parallel, z) = \Sigma_\sigma^\alpha(z)$. The

B. Local scattering

Dyson equation in this case reads

$$\begin{aligned}
G_{c\sigma}^{\alpha\beta}(\mathbf{r}_{\parallel}, \mathbf{r}'_{\parallel}, z) &= \overleftrightarrow{\mathbf{r}_{\parallel}, \alpha \quad \mathbf{r}'_{\parallel}, \beta}^{z, \sigma} \\
&= \overleftrightarrow{\mathbf{r}_{\parallel}, \alpha \quad \mathbf{r}'_{\parallel}, \beta}^{z, \sigma} + \overleftrightarrow{\mathbf{r}_{\parallel}, \alpha \quad \mathbf{r}'_{\parallel}, \beta}^{z, \sigma} \circlearrowleft_{\mathbf{r}''_{\parallel}, \gamma}^{z, \sigma} \\
&= G_{c\sigma}^{\alpha\beta, 0}(\mathbf{r}_{\parallel}, \mathbf{r}'_{\parallel}, z) + \sum_{\mathbf{r}''_{\parallel}, \gamma} G_{c\sigma}^{\alpha\gamma, 0}(\mathbf{r}_{\parallel}, \mathbf{r}''_{\parallel}, z) \Sigma_{\sigma}^{\gamma}(z) \underbrace{G_{c\sigma}^{\gamma\beta}(\mathbf{r}''_{\parallel}, \mathbf{r}'_{\parallel}, z)}_{\frac{1}{N_{\parallel}} \sum_{\mathbf{p}_{\parallel}} e^{i\mathbf{p}_{\parallel}(\mathbf{r}''_{\parallel} - \mathbf{r}'_{\parallel})} G_{c\sigma}^{\gamma\beta}(\mathbf{p}_{\parallel}, z)} \\
&= G_{c\sigma}^{\alpha\beta, 0}(\mathbf{r}_{\parallel}, \mathbf{r}'_{\parallel}, z) + \frac{1}{N_{\parallel}^2} \sum_{\mathbf{k}_{\parallel}, \mathbf{p}_{\parallel}} \left\{ \underbrace{\sum_{\mathbf{r}''_{\parallel}} e^{i\mathbf{r}''_{\parallel}(\mathbf{p}_{\parallel} - \mathbf{k}_{\parallel})} e^{i\mathbf{k}_{\parallel}\mathbf{r}_{\parallel}} e^{-i\mathbf{p}_{\parallel}\mathbf{r}'_{\parallel}}}_{N_{\parallel} \delta_{\mathbf{k}_{\parallel}, \mathbf{p}_{\parallel}}} \cdot \sum_{\gamma} G^{\alpha\gamma} 0_{c\sigma}(\mathbf{k}_{\parallel}, z) \Sigma_{\sigma}^{\gamma}(z) G_{c\sigma}^{\gamma\beta}(\mathbf{p}_{\parallel}, z) \right\} \\
&= \frac{1}{N_{\parallel}} \sum_{\mathbf{k}_{\parallel}} e^{i\mathbf{k}_{\parallel}(\mathbf{r}_{\parallel} - \mathbf{r}'_{\parallel})} \underbrace{\left(G_{c\sigma}^{\alpha\beta, 0}(\mathbf{k}_{\parallel}, z) + \sum_{\gamma} G_{c\sigma}^{\alpha\gamma, 0}(\mathbf{k}_{\parallel}, z) \Sigma_{\sigma}^{\gamma}(z) G_{c\sigma}^{\gamma\beta}(\mathbf{k}_{\parallel}, z) \right)}_{G_{c\sigma}^{\alpha\beta}(\mathbf{k}_{\parallel}, z)}.
\end{aligned} \tag{B.2}$$

Therefore, the momentum dependent self-energy in (5.19) and (5.22) reads $\Sigma_{\sigma}^{\alpha}(\mathbf{k}_{\parallel}, z) = \Sigma_{\sigma}^{\alpha}(z)$.

C. Mirror symmetric systems

In this section, we discuss the implications of mirror symmetry for the self-consistent theory. First of all, we restrict ourselves to an odd number of monolayers $N = 2\tilde{N} - 1$ and we introduce an alternative layer index $\tilde{\alpha}$ whose origin is shifted with respect to the symmetry plane (see figure C.1).

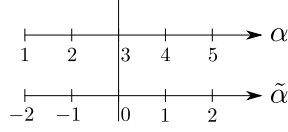


Figure C.1.: Nomenclature for mirror symmetric multilayer systems. The shown example corresponds to $\tilde{N} = 3$.

Due to mirror symmetry, the elements of the inverse Green's function matrix (5.19) obey the following relations:

$$\begin{aligned} d_{\tilde{N}+\alpha} &= d_{\tilde{N}-\alpha} & \text{for } \alpha \in (0, \dots, \tilde{N} - 1) \\ t_{\tilde{N}+\alpha+1} &= t_{\tilde{N}-\alpha} & \text{for } \alpha \in (0, \dots, \tilde{N} - 2) \end{aligned} \quad . \quad (\text{C.1})$$

For instance in the case of $N = 5$, it reads

$$\hat{G}_{c\sigma}^{-1}(\mathbf{k}_{\parallel}, z) = \begin{pmatrix} d_1 & -t_2 & & & \\ -t_2 & d_2 & -t_3 & & \\ & -t_3 & d_3 & -t_3 & \\ & & -t_3 & d_2 & -t_2 \\ & & & -t_2 & d_1 \end{pmatrix},$$

where the diagonal elements are given by

$$d_{\alpha} := z - \varepsilon_{\mathbf{k}_{\parallel}}^{\alpha} + \mu - \Sigma_{c\sigma}^{\alpha}(z).$$

As a direct consequence of (C.1), the minors from section 5.1.2 fulfill

$$\Theta_{N+1-\alpha} = \Phi_{\alpha},$$

for all α . With this, the elements of the Green's function matrix (5.20) become

$$G_{c\sigma}^{\alpha\beta}(\mathbf{k}_{\parallel}, z) = \begin{cases} (-1)^{\alpha+\beta} t_{\beta+1} t_{\beta+2} \cdots t_{\alpha} \frac{\Theta_{\beta-1} \Theta_{N-\alpha}}{\Theta_N} & \text{for } \alpha > \beta \\ \frac{\Theta_{\alpha-1} \Theta_{N-\alpha}}{\Theta_N} & \text{for } \alpha = \beta \end{cases} \quad . \quad (\text{C.2})$$

C. Mirror symmetric systems

It is obvious that by this procedure we can restrict ourselves to the calculation of the conduction electron self-energy in the right hand layers, i.e. $\alpha \in (\tilde{N}, \dots, N)$ or $\tilde{\alpha} \in (0, \dots, \tilde{N}-1)$. Since the calculations in the self-consistent theory with the greatest impact on the computation time are of linear order, we can decrease the overall calculation time by nearly a factor of two by exploiting the mirror symmetry.

In the following, we will discuss the consequences of mirror symmetry for the Heisenberg mean-field theory of section 5.3.2. It implies

$$\langle S \rangle_{\tilde{\alpha}} = \langle S \rangle_{-\tilde{\alpha}}.$$

Therefore, we only need to calculate a system of \tilde{N} layers with indices $\tilde{\alpha} \in (0, \tilde{N}-1)$ and adjust the boundary conditions. In the case of nearest neighbor coupling (5.85), the boundary condition is given by an additional spin $\langle S \rangle_{-1}$ at layer $\tilde{\alpha} = -1$ with

$$\langle S \rangle_{-1} = \langle S \rangle_1.$$

In contrast to this, in the case of inverse cubic coupling of section 5.3.2 or the long range RKKY interaction of section 5.3.3, the interlayer summation in the mean-field equation (5.84) becomes

$$2 \sum_{\beta \neq \alpha(\tilde{\alpha})} J_{4f}^{\alpha(\tilde{\alpha})\beta} \langle S_{\tilde{\beta}(\beta)} \rangle.$$

Here, $\tilde{\alpha}$ is restricted to the right hand side of the system $\tilde{\alpha} \in (0, \tilde{N}-1)$, but the summation over β runs over all N layers. In addition, we utilize the mapping

$$\tilde{\alpha}(\alpha) = \begin{cases} \alpha - N + 1 & \text{for } \alpha \geq N - 1 \\ N - 1 - \alpha & \text{for } \alpha < N - 1 \end{cases}$$

and its inverse

$$\alpha(\tilde{\alpha}) = \tilde{\alpha} + N - 1.$$

Similar to the Heisenberg lattice, the Poisson equation needs to be solved only on the right hand side of the system. The symmetry dictates

$$\phi_{\tilde{\alpha}} = \phi_{-\tilde{\alpha}}.$$

Therefore, the boundary conditions for the electrostatic problem (5.114) become

$$\phi_{-1} = \phi_1 \quad \text{and} \quad \phi_{N+1} = 0.$$

D. Kramers-Kronig-relations

In the self-consistent theory for electron doped Europium monoxide (chapter 5) as well as for the NCA equations (chapter 3), we use the imaginary part of the Green's function, i.e. the spectral density. The real part is only calculated if needed. The corresponding Kramers-Kronig relation for a retarded Green's function $G^R(\omega) = G(\omega - i0^+)$ reads [61]

$$\text{Re}G^R(\omega) = \mathcal{P} \int \frac{d\varepsilon}{\pi} \frac{\text{Im}G^R(\varepsilon)}{\omega - \varepsilon}.$$

A similar equation holds for the self-energies. In order to circumvent the numerical evaluation of the principal value, we write

$$\text{Re}G^R(\omega) = \int_{\omega_-}^{\omega_+} \frac{d\varepsilon}{\pi} \frac{\text{Im}G^R(\varepsilon) - \text{Im}G^R(\omega)}{\omega - \varepsilon} + \text{Im}G^R(\omega) \underbrace{\mathcal{P} \int \frac{d\varepsilon}{\pi} \frac{1}{\omega - \varepsilon}}_{-\log \frac{\omega_+ - \omega}{-\omega_- + \omega}},$$

where we have assumed that the Green's function vanishes for $\omega < \omega_-$ and $\omega > \omega_+$. Numerically, these limits are defined by the upper and lower limit of the integration grid. The analytical integral in the second term is calculated once at the beginning of the numerical calculation and stored for later use. Since the integrand in the first term vanishes for $\varepsilon = \omega$, a special choice of the numerical integration weights is needed in order to ensure the smoothness of the resulting function $\text{Re}G^R(\omega)$. For a given integration grid $\{\varepsilon_i\}$, with $i = 1, \dots, N$, $\varepsilon_1 = \omega_-$, $\varepsilon_N = \omega_+$, and $\varepsilon_j = \omega$, we choose

$$\Delta\varepsilon_i = \begin{cases} \varepsilon_{i+1} - \varepsilon_i & \text{for } i < j \\ 0 & \text{for } i = j \\ \varepsilon_i - \varepsilon_{i-1} & \text{for } i > j \end{cases}$$

as weights for the numerical integration. With this, the resulting real part of the Green's function at the grid position ω_j reads

$$\text{Re}G^R(\omega_j) = \frac{1}{\pi} \sum_i \frac{\text{Im}G^R(\varepsilon_i) - \text{Im}G^R(\omega_j)}{\omega_j - \varepsilon_i} \Delta\varepsilon_i - \log \frac{\omega_N - \omega_j}{-\omega_1 + \omega_j}.$$

Note that hereby each value of ω_j corresponds to a different set of integration weights.

E. Numerical integration of multiple peaked functions

In this section we discuss the details of the numerical integration as it occurs in the self-consistent theory for electron doped EuO (chapter 5) as well as in the solution of the single impurity Anderson model with $U \rightarrow \infty$ within the framework of the non-crossing approximation (chapter 3). In both cases, one has to deal with the numerical integration of functions which possess multiple peaks or features whose position may or may not be known in advance. Moreover, the position of these peaks or features as well as the peak heights and widths will change during the iterative solution of the self-consistent equations. Therefore, one needs an integration grid which resolves all peaks and features properly and is capable of handling crossing peak positions. This is provided by the numerical integration grid library, called *integrid*, which was developed specifically for this purpose [43]. The mathematical formulas used for the logarithmic and tangential integration grid regions are based on the ones given in [42]. The details of the grid creation procedure together with the usage instructions can be found in the integrid user's guide [43].

For the self-consistent theories, we use an equidistant integration base grid which may be interrupted by multiple logarithmic grid regions. A logarithmic grid region consists of three grid regions: one below (I), one around (II) and one above (III) the center point ω_k , which is the point with the highest grid point density (see figure E.1). Region I and

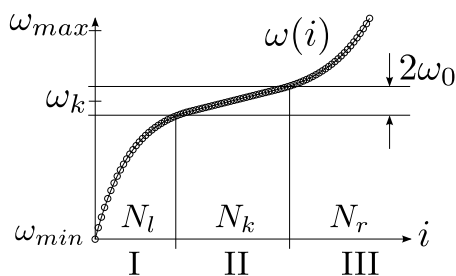


Figure E.1.: Logarithmic grid region.

III are exponential and region II is linear. The half width of the linear region ω_0 also controls the 'sharpness' of the exponential grid regions. The number of grid points in region I and III is N_l and $N_r + 1$, respectively. Both numbers will also influence the 'sharpness' of the exponential grid regions. The resolution of the linear grid region $d\omega_k$ equals the maximal resolution in the exponential grid regions and determines the number

E. Numerical integration of multiple peaked functions

of grid points in region II, N_k (see [43]). The logarithmic grid region is defined as

$$\omega(i) = \begin{cases} -\exp(-c_1(i - i_1)) + \omega_k & i \in \{0, \dots, N_l - 1\} \\ \omega_k - \omega_0 + d\omega_k(i - N_l - 1) & i \in \{N_l, \dots, N_l + N_k - 1\} \\ \exp(c_2(i - i_2 - N_l - N_k)) + \omega_k & i \in \{N_l + N_k, \dots, N_l + N_k + N_r\} \end{cases}, \quad (\text{E.1})$$

where the four boundary conditions

$$\begin{aligned} \omega(0) &= \omega_{min} & \omega(N_l - 1) &= \omega_k - \omega_0 \\ \omega(N_l + N_k) &= \omega_k + \omega_0 & \omega(N_l + N_k + N_r) &= \omega_{max} \end{aligned} \quad (\text{E.2})$$

determine the four parameters i_1 , i_2 , c_1 and c_2 (see [43]). It turns out to be more convenient to use the maximal resolution $d\omega_{min}$ at ω_k and the minimal resolution at the boundaries $d\omega_{max}$ instead of N_l , N_r and ω_0 . The corresponding relations reads

$$\begin{aligned} \omega_0 &= \frac{\omega_1 d\omega_{min}}{d\omega_{max}} \\ N_l = N_r &= \log\left(\frac{\omega_1}{\omega_0}\right) \frac{\omega_1}{d\omega_{max}}, \end{aligned}$$

where we have symmetrized the logarithmic grid region by setting $\omega_k = (\omega_{max} + \omega_{min})/2$ and introduced the half width $\omega_1 = (\omega_{max} - \omega_{min})/2$. In order to ensure a smooth behavior as two logarithmic grid regions intersect each other, we fix $\omega_1 = 0.1D_0$ and $d\omega_{max} = 0.01D_0$. For the sufficient resolution of a Lorentz-like peak of width Γ , we use $d\omega_{min} = \Gamma/N_p$, where N_p is a number between 20 and 100 depending on the desired quality of the peak resolution. The peak width and position in the imaginary part of a Green's function with a simple pole can be estimated by the self-energy. Nevertheless, it turns out to be necessary to track the peaks position and width during the iteration procedure and adjust the grid if necessary. This is done in the following way. The peak position $\tilde{\omega}_k$ is found simply as the maximum point of the function. Beginning from the peak position one proceeds to the left and to the right and scans the function values for a threshold of 10% of the peak height. This defines the width Γ . If the cluster point of the current grid region ω_k differs from the current peak position $\tilde{\omega}_k$ by more than 0.1Γ , the whole integration grid is recreated with the updated logarithmic grid region at $\tilde{\omega}_k$.

Publications

- *Thickness-dependent magnetic properties of oxygen-deficient EuO*
M. Barbagallo, T. Stollenwerk, J. Kroha, N.-J. Steinke, N.D.M. Hine, J.F.K. Cooper, C.H.W. Barnes, A. Ionescu, P.M.D.S. Monteiro, J.-Y. Kim, K.R.A. Ziebeck, C.J. Kinane, R.M. Dalgliesh, T.R. Charlton, S. Langridge
Phys. Rev. B 84, 075219 (2011)
- *Efficient construction of maximally localised Wannier functions: locality criterion and initial conditions*
Tobias Stollenwerk, Dmitry V. Chigrin, and Johann Kroha
J. Opt. Soc. America B 28, 1951 (2011)
- *Local photonic modes in periodic or random, dielectric and lasing media*
Tobias Stollenwerk, Regine Frank, Andreas Lubatsch, Oleg Zaitsev, Sergei V. Zhukovsky, Dmitry N. Chigrin, and Johann Kroha
J. Appl. Phys. B 105 (1), 163-180 (2011)

Bibliography

- [1] B. T. Matthias, R. M. Bozorth, and J. H. Van Vleck. Ferromagnetic interaction in EuO. *Phys. Rev. Lett.*, 7:160–161, 1961.
- [2] D. E. Eastman, F. Holtzberg, and S. Methfessel. Photoemission studies of the electronic structure of EuO, EuS, EuSe and GdS. *Phys. Rev. Lett.*, 23:226, 1969.
- [3] A. Mauger and C. Godart. The magnetic, optical and transport properties of representatives of a class of magnetic semiconductors: The Europium chalcogenides. *Phys. Rep.*, 141:51, 1986.
- [4] W. Nolting and A. Ramakanth. *Quantum Theory of Magnetism*. Springer-Verlag, 2009.
- [5] P. G. Steeneken, L. H. Tjeng, I. Elfimov, G. A. Sawatzky, G. Ghiringhelli, N. B. Brookes, and D.-J. Huang. Exchange splitting and charge carrier spin polarisation in EuO. *Phys. Rev. Lett.*, 88:047201, 2002.
- [6] M. R. Oliver, J. A. Kafalas, J. O. Dimmock, and T. B. Reed. Pressure dependence of the electrical resistivity of EuO. *Phys. Rev. Lett.*, 24:1064–1067, 1970.
- [7] M. R. Oliver, J. O. Dimmock, A. L. McWhorter, and T. B. Reed. Conductivity studies in Europium oxide. *Phys. Rev. B*, 5:1078–1098, 1972.
- [8] Y. Shapira, S. Foner, and T. B. Reed. EuO. i. resistivity and hall effect in fields up to 150 koe. *Phys. Rev. B*, 8:2299–2315, 1973.
- [9] Y. Shapira, S. Foner, R. L. Aggarwal, and T. B. Reed. EuO. ii. dependence of the insulator-metal transition on magnetic order. *Phys. Rev. B*, 8:2316–2326, 1973.
- [10] T. Penney, M. W. Shafer, and J. B. Torrance. Insulator-metal transition and long-range magnetic order in EuO. *Phys. Rev. B*, 5:3669–3674, 1972.
- [11] S. G. Altendorf, A. Efimenko, V. Olina, H. Kierspel, A. D. Rata, and L. H. Tjeng. Oxygen off-stoichiometry and phase separation in EuO thin films. *Phys. Rev. B*, 84:155442, 2011.
- [12] J. Schoenes and P. Wachter. Exchange optics in Gd-doped EuO. *Phys. Rev. B*, 9:3097, 1974.
- [13] T. Matsumoto, K. Yamaguchi, M. Yuri, K. Kawaguchi, N. Koshizaki, and K. Yamada. Preparation of Gd-doped EuO_{1-x} thin films and the magnetic and magneto-transport properties. *J. Phys.*, 16:6017, 2004.

Bibliography

- [14] H. Ott, S. J. Heise, R. Sutarto, Z. Hu, C. F. Chang, H. H. Hsieh, H.-J. Lin, C. T. Chen, and L. H. Tjeng. Soft x-ray magnetic circular dichroism study on Gd-doped EuO thin films. *Phys. Rev. B*, 73:094407, 2006.
- [15] T. Mairoser, A. Schmehl, A. Melville, T. Heeg, Canella, P. Böni, W. Zander, J. Schubert, D. E. Shai, E. J. Monkman, K. M. Shen, D. G. Schlom, and J. Mannhart. Is there an intrinsic limit to the charge-carrier-induced increase of the curie temperature of EuO? *Phys. Rev. Lett.*, 105:257206, 2010.
- [16] S. G. Altendorf, N. Hollmann, R. Sutarto, C. Caspers, R. C. Wicks, Y.-Y. Chin, Z. Hu, H. Kierspel, I. S. Elfimov, H. H. Hsieh, H.-J. Lin, C. T. Chen, and L. H. Tjeng. Spectroscopic observation of strain-assisted T_C enhancement in EuO upon Gd doping. *Phys. Rev. B*, 85:081201, 2012.
- [17] P. Sinjukow and W. Nolting. Fully self-consistent determination of transport properties in Eu-rich EuO. *Phys. Rev. B*, 69:214432, 2004.
- [18] M. Arnold and J. Kroha. Simultaneous ferromagnetic metal-semiconductor transition in electron-doped EuO. *PRL*, 100:046404, 2008.
- [19] T. S. Santos, J. S. Moodera, K. V. Raman, E. Negusse, J. Holroyd, J. Dvorak, M. Liberati, Y. U. Idzerda, and E. Arenholz. Determining exchange splitting in a magnetic semiconductor by spin-filter tunneling. *Phys. Rev. Lett.*, 101:147201, 2008.
- [20] J. Klinkhammer, D. F. Förster, S. Schumacher, H. P. Oepen, T. Michely, and C. Busse. Enhanced curie temperature of ultra thin textured EuO films on graphene. *Appl. Phys. Lett.*, 2013. submitted.
- [21] M. Müller, G.-X. Miao, and J. S. Moodera. Thickness dependence of ferromagnetic and metal-insulator transition in thin EuO films. *J. Appl. Phys.*, 105:07C917, 2009.
- [22] M. Barbagallo, N. D. M. Hine, J. F. K. Cooper, N.-J. Steinke, A. Ionescu, C. H. W. Barnes, C. J. Kinane, R. M. Dalgliesh, T. R. Charlton, and S. Langridge. Experimental and theoretical analysis of magnetic moment enhancement in oxygen-deficient EuO. *Phys. Rev. B*, 81:235216, 2010.
- [23] M. Barbagallo, T. Stollenwerk, J. Kroha, N.-J. Steinke, N. D. M. Hine, J. F. K. Cooper, C. H. W. Barnes, A. Ionescu, P. M. D. S. Monteiro, J.-Y. Kim, K. R. A. Ziebeck, C. J. Kinane, R. M. Dalgliesh, T. R. Charlton, and S. Langridge. Thickness-dependent magnetic properties of oxygen-deficient EuO. *Phys. Rev. B*, 84:075219, 2011.
- [24] A. Melville, T. Mairoser, A. Schmehl, T. Birol, T. Heeg, B. Hollander, J. Schubert, C. J. Fennie, and D. G. Schlom. Effect of film thickness and biaxial strain on the curie temperature of EuO. *Applied Physics Letters*, 102(6):062404, 2013.
- [25] M. Arnold. *Ferromagnetic Semiconductor-Metal Transition in Europium Monoxide*. PhD thesis, Universität Bonn, 2008.

- [26] P. Wachter. The optical electrical and magnetic properties of the europium chalcogenides and the rare earth pnictides. *C R C Critical Reviews in Solid State Sciences*, 3(2):189–241, 1972.
- [27] S. G. Altendorf. Growth, electronic structure, and properties of electron-doped EuO thin films. PhD thesis, 2011.
- [28] A. Schmehl. private communication.
- [29] D. F. Förster, J. Klinkhammer, C. Busse, S. G. Altendorf, T. Michely, Z. Hu, Y.-Y. Chi, L. H. Tjeng, J. Coraux, and D. Bourgault. Epitaxial Europium oxide on Ni(100) with single-crystal quality. *Phys. Rev. B*, 83:045424, 2011.
- [30] R. Schiller and W. Nolting. Thickness dependent Curie temperatures of ferromagnetic Heisenberg films. *Solid State Communications*, 110:121, 1999.
- [31] P. W. Anderson. Localized magnetic states in metals. *Phys. Rev.*, 124:41, 1961.
- [32] A. C. Hewson. *The Kondo Problem to Heavy Fermions*. Cambridge University Press, 1993.
- [33] J. Kroha and P. Wölfle. Fermi and non-fermi liquid behavior of local-moment systems within a conserving slave boson theory. In *Magnetism and Electronic Correlations in Local-Moment Systems: Rare-Earth Elements and Compounds: Proceedings of the Workshop Berlin, Germany*. World Scientific Publishing Company, Incorporated, 1998.
- [34] P. Coleman. New approach to the mixed valence problem. *Phys. Rev. B*, 89:3035, 1984.
- [35] J. Kondo. Localized magnetic states in metals. *Prog. Theo. Phys.*, 32:37, 1964.
- [36] J. R. Schrieffer and P. A. Wolff. Relation between the anderson and kondo hamiltonians. *Phys. Rev.*, 149:491, 1966.
- [37] W. Metzner and D. Vollhardt. Correlated lattice fermions in $d = \infty$ dimensions. *Phys. Rev. Lett.*, 62:324, 1989.
- [38] A. Georges, G. Kotliar, W. Krauth, and M. J. Rozenberg. Dynamical mean-field theory of strongly correlated fermion systems and the limit of infinite dimensions. *Rev. Mod. Phys.*, 68:13, 1996.
- [39] A. Georges and G. Kotliar. Hubbard model in infinite dimensions. *Phys. Rev. B*, 45:6479, 1992.
- [40] G. Baym and L. P. Kadanoff. Conservation laws and correlation functions. *Phys. Rev.*, 124:287, 1961.
- [41] G. Baym. Self-consistent approximations in many-body systems. *Phys. Rev.*, 127:1391, 1962.

Bibliography

- [42] M. H. Hettler, J. Kroha, and S. Hershfield. Nonequilibrium dynamics of the anderson impurity model. *Phys. Rev. B*, 58:5649, 1998.
- [43] Tobias Stollenwerk. Integrid - a highly versatile integration grid library for c++. <http://github.com/tstollenw/integrid>.
- [44] Tobias Stollenwerk. Solution of the single impurity anderson model in non-crossing approximation. <http://github.com/tstollenw/nca>.
- [45] M. Potthoff and W. Nolting. Surface metal-insulator transition in the hubbard model. *Phys. Rev. B*, 59:2549, 1999.
- [46] Bronstein, Semendjajew, Musiol, and Mühlig. *Taschenbuch der Mathematik*. Verlag Harri Deutsch, 2000.
- [47] M. Potthoff and W. Nolting. Effective mass at the surface of a fermi liquid. *Physica B*, 259-261:760, 1999.
- [48] M. Potthoff and W. Nolting. Metallic surface of a mott insulator – mott insulating surface of a metal. *Phys. Rev. B*, 60:7834, 1999.
- [49] J. K. Freericks. *Transport in mulilayered nanostructures*. Imperial College Press, London, 2006.
- [50] J. K. Freericks. Crossover from tunneling to incoherent (bulk) transport in a correlated nanostructure. *Appl. Phys. Lett.*, 84:1383, 2004.
- [51] J. K. Freericks. Dynamical mean-field theory for strongly correlated inhomogeneous multilayered nanostructures. *Phys. Rev. B*, 70:195342, 2004.
- [52] A. N. Tahvildar-Zadeh, J. K. Freericks, and B. K. Nikolić. Thouless energy as a unifying concept for josephson junctions tuned through the mott metal-insulator transition. *Phys. Rev. B*, 73:075108, 2006.
- [53] R. A. Usmani. Inversion of jacobi’s tridiagonal matrix. *Computers Math. Applic.*, 27:59, 1994.
- [54] The GNU MPFR library. <http://www.mpfr.org/>.
- [55] H. Bruus and K. Flensberg. *Many-Body Quantum Theory in Condensed Matter Physics: An Introduction*. Oxford graduate texts in mathematics. Oxford University Press, USA, 2004.
- [56] T. R. McGuire, B. E. Argyle, M. W. Shafer, and J. S. Smart. Ferromagnetism in divalent Europium salts. *Appl. Phys. Lett.*, 1:17, 1962.
- [57] T. R. McGuire, B. E. Argyle, M. W. Shafer, and J. S. Smart. Magnetic properties of some divalent Europium compounds. *J. Appl. Phys.*, 34:1345, 1964.

- [58] T. R. McGuire and M. W. Shafer. Exchange interactions in compounds. *J. Appl. Phys.*, 35:984, 1964.
- [59] M. A. Ruderman and C. Kittel. Indirect exchange coupling of nuclear magnetic moments by conduction electrons. *Phys. Rev.*, 96:99, 1954.
- [60] S. Burg, V. Stukalov, and E. Kogan. On the theory of indirect exchange in EuO. *Phys. Status Solidi B*, 249:847, 2011.
- [61] W. Nolting. *Viel-Teilchen-Theorie. Grundkurs Theoretische Physik*. Springer, Berlin, 2005.
- [62] R. Schaback and H. Wendland. *Numerische Mathematik*. Oxford graduate texts in mathematics. Springer, 2004.
- [63] Tobias Stollenwerk. Numerical solution of a self-consistent theory for electron doped Europium monoxide. <http://github.com/tstollenw/euo>.
- [64] H. Lüth. *Solid Surfaces, Interfaces and Thin Films*. Advanced Texts in Physics. Springer Verlag, 2001.
- [65] Tobias Stollenwerk. Database and management scripts for the numerical solution of a self-consistent theory for electron doped Europium monoxide. <http://github.com/tstollenw/euoscripts>.
- [66] J. O. Dimmock and A. J. Freeman. Band structure and magnetism of Gadolinium metal. *Phys. Rev. Lett.*, 13:750, 1964.
- [67] Bongsoo Kim, A. B. Andrews, J. L. Erskine, Kwang Joo Kim, and B. N. Harmon. Temperature-dependent conduction-band exchange splitting in ferromagnetic HCP gadolinium: Theoretical predictions and photoemission experiments. *Phys. Rev. Lett.*, 68:1931, 1992.
- [68] W. Nolting, T. Dambeck, and G. Borstel. Temperature-dependent electronic structure of Gadolinium. *Zeitschrift für Physik B Condensed Matter*, 94(4):409, 1994.
- [69] O. Újsághy, J. Kroha, L. Szunyogh, and A. Zawadowski. Theory of scanning tunneling spectroscopy of kondo ions on metal surfaces. In Venkat Chandrasekhar, Chris Haesendonck, and Alfred Zawadowski, editors, *Kondo Effect and Dephasing in Low-Dimensional Metallic Systems*, volume 50 of *NATO Science Series*, pages 245–248. Springer Netherlands, 2001.

Index

- Anderson model, 15, 27, 30
 - Perturbation theory, 54
- Charge distribution, 30, 67, 73
- Conduction band
 - bulk, 27, 28, 31
 - multilayer, 28, 30, 35
- Conductivity, 76
 - bulk, 78, 79
 - Linear response theory, 76
 - multilayer, 83
 - Numerical calculation, 93
 - parallel, 84
 - perpendicular, 84
- Europium monoxide, 9
 - Electronic structure, 9
 - Magnetism, 10
 - Model, 27, 28
- Heisenberg lattice, 28, 30, 57
 - Mean field approximation, 57, 59
- Impurities
 - Dilute, 42
 - Gadolinium, 53, 71, 97, 135
 - Oxygen, 54, 71, 102, 135
- Kramers-Kronig relation, 155
- Mirror symmetry, 153
- Non-crossing approximation, 18
- Numerical integration, 25, 40, 74, 157
- Poisson equation, 30, 68, 73
- Pseudo-particle representation, 16
- Resistivity
 - bulk, 79
 - parallel, 84
- RKKY interaction, 63, 104
- Scanning tunneling spectroscopy, 135
- Self-consistent theory, 70
- Single-site-T-matrix approximation, 46, 52
- Work function, 69